Title
Frequency comb generation in dispersion engineered Si3N4 microresonators and their applications

Author
Liu, Hao

Publication Date
2022

Peer reviewed|Thesis/dissertation

UNIVERSITY OF CALIFORNIA

Los Angeles

Frequency comb generation in dispersion engineered Si_3N_4 microresonators and their applications

A dissertation submitted in partial satisfaction

of the requirements for the degree

Doctor of Philosophy in Electrical & Computer Engineering

by

Hao Liu

2022

ABSTRACT OF THE DISSERTATION

Frequency comb generation
in dispersion engineered Si_3N_4 microresonators
and their applications

by

Hao Liu
Doctor of Philosophy in Electrical & Computer Engineering
University of California, Los Angeles, 2022
Professor Chee Wei Wong, Chair

Optical frequency combs, unique light sources that coherently link optical frequencies with microwave electrical signals, have heralded several scientific frontiers such as frequency metrology, optical clockwork, precision navigation, and high speed communication over the past decades. Parametric oscillation in ultrahigh Q microresonators, facilitated by the high quality factors and the small mode volumes, is an alternative physical process that offers the opportunity of optical frequency comb generation in compact footprints with smaller weight and lower power consumption. In particular, the observation of dissipative Kerr soliton (DKS) formation and soliton-induced Cherenkov radiation offers a reliable route towards self-referenced broadband optical frequency microcomb. DKS is localized attractor where the Kerr nonlinearity is compensated by the cavity dispersion and the cavity loss is balanced by the parametric gain. Thus the cavity dispersion and the pump-resonance detuning are two determining parameters in the existence of DKS in ultrahigh Q microresonators. Among numerous material platforms, Si_3N_4 planar waveguide system draws great

attention for its high nonlinearity, wide transparent window, low propagation loss and its CMOS-compatibility. For Si_3N_4 microresonators, dispersion is typically engineered by designing waveguide geometry. However, conventional method of using multi-mode waveguide results in additional perturbation to the Kerr frequency comb generation dynamics. Furthermore, despite of all the advantages, DKS suffers from low conversion efficiency, restrict pump-resonance detuning requirement and difficult dispersion design, which could be supplemented by normal dispersion frequency microcomb. In this thesis, I focus on frequency microcomb studies in novel designs of tapered Si_3N_4 planar waveguide geometry achieving higher-order-mode suppression. I not only work on unravelling the fundamental dynamics of DKS in anomalous dispersion regime, but I also investigate a novel pulse formation mechanism in normal dispersion device. Benefiting from their high intrinsic phase coherence and individual comb line powers, I further extend my research to absolute distance metrology with a single soliton comb that achieves nm-level precision, and terabits/s free-space optical communication with a flat normal dispersion comb.

The dissertation of Hao Liu is approved.

Gunter Steinmeyer

Yahya Rahmat-Samii

Sudhakar Pamarti

Mona Jarrahi

Chee Wei Wong, Committee Chair

University of California, Los Angeles

2022

To my unconditionally supportive parents

TABLE OF CONTENTS

LIST OF FIGURES

LIST OF TABLES

ACKNOWLEDGMENTS

Firstly, I would like to thank Prof. Chee Wei Wong with my most sincere gratitude for offering me the precious opportunity to join his lab when I was in master program in 2015 and supervising my PhD study till now. prof. Wong is a truly remarkable advisor for his passion and enthusiasm in science as well as his wide spectrum in knowledge which inspires me throughout my whole PhD time, and for his patience and tolerance towards my mistakes. In addition, Prof. Wong has guided me to various scientific research projects which truly enlarge my scope to photonics research. Secondly, I would like to show my appreciation to the Chinese Scholarship Council which financially supports me for the first three years of my PhD study and helps me go through the most tough time of my PhD time in the financial aspect.

My special thanks must go the Dr. Shu-Wei Huang, who is now a professor in University of Colorado, Boulder. Dr. Huang leads me to the world of photonics research. He has taught me valuable skills in optical experiments, and offered me many ideas in my PhD studies. He is a truly excellent scientist, whom I can always count on. His profound knowledge, scope in science, rigor in research and patience to apprentice set up a role model for me, and inspire me continuously, even after he left our group. I would also like to thank Dr. Wenting Wang for expanding my vision in photonics research. During my PhD study, we have numerous scientific discussions, and he could always come up with brilliant ideas. We have collaborated in several projects, which are demonstrated in chapter 4 and 8. I have learnt a lot from him, especially in engineering skills. He is not only an amazing working mate, but also a great lifetime friend to me. I am also thankful to Dr. Yoon-Soo Jang. I am very glad that we have worked together on the spectrally-resolved interferometry, demonstrated in chapter 7, which is reproduced from *Y.-S. Jang, H. Liu, J. Yang, M. Yu, D.-L. Kwong, and C. W. Wong, "Nanometric Precision Distance Metrology via Hybrid Spectrally Resolved and Homodyne Interferometry in a Single Soliton Frequency Microcomb," Phys. Rev. Lett., vol. 126, no. 2, p. 023903, Jan. 2021.*, with permission. Dr. Jang is knowledgeable, rigorous yet humble

and he help me reveal more possibilities of the application of frequency microcomb. I would also thank all other collaborators that I have worked with for the permission to reproduce materials from our work. Without them, this thesis could never be finished.

I am also thankful for Dr. Abhinav Vinod and Jaime Flor Flores. We joined the group roughly at the same time. Throughout these years, we have numerous discussions in assorted topics. I have truly learnt a lot from them. I would also express my appreciation to all the former and current group members including but not limited to Dr. Yongjun Huang, Dr. Zhenda Xie, Dr. Baicheng Yao, Dr. Jinghui Yang, Dr. Jiagui Wu, Dr. Yongnan Li, Dr. Bowen Li, Dr. Jingkang Lim, Dr. Hangbo Yang, Dr. James Mcmillan, Dr. Xiang Cheng, and Kai-Chi Chang that I have worked with in these years for always being available to teach me experimental skills, inspire me in my research, as well as share knowledge with me from different fields. It is a genuinely wonderful experience to work with so many brilliant and talented scientists and researchers.

I would also like to show my appreciation to Prof. Mona Jarrahi, Prof. Sudhakar Pamarti, Prof. Yahya Rahmat-Samii and Prof. Gunter Steinmeyer for serving on my committee and for their valuable suggestions to my PhD research. Especially, I would like to express my sincere gratitude to Prof. Mona Jarrahi and Prof. Gunter Steinmeyer for supporting me in numerous scholarship applications. I would also like to thank Deeona Columbia, Ryo Arreola, and Tricia Senate for making my PhD study and working as a GSR so much easier. Also, I want to thank Dr. Stephanie Krilov for offering me so many TAships in the Physics department, which helps me a lot financially.

Although doing research is exciting, PhD study sometimes could be really exhausting. Finding the work-life balance becomes really important for me to keep it up. So I would like to thank my very good friend and gym buddy, Dr. Han Yan, and all my badminton mates for all those sweat and joy as well as the confidence and fulfillment in sports. In the past two years, the pandemic is really hard to everyone. So I am really grateful to have my lovely wife, Dr. Yingmu Zhang's accompany during the lockdown. Without her, I could never

imagine how I would survive emotionally during the hardest time. I am also very luck to become close friend with Wenting Wang, Zhangji Zhao, Xinghe Jiang, Xiang Cheng, and Haitao Chen during my last year in UCLA. They make me not alone at the very end of my PhD journey.

At last, I would like to thank my parents. Without their unconditionally support and faith in me, none of these could ever happen. I owe every achievement in my life to them.

Since I first stepped in UCLA in 2014, I have spent almost 8 years in UCLA. Pursuing PhD for me is a long and rocky journey, however when I look back, I cherish every moment happened here. Every journey has its final, do not rush.

VITA

2010–2014 B.S. (Optical Engineering), Zhejiang University, Hangzhou, China.

2014–2016 M.S. (Electrical Engineering), University of California, Los Angeles, USA.

2016–2017 Junior Development Engineer, Electrical Engineering Department, UCLA.

CHAPTER 1

Introduction

Optical frequency combs, unique light sources that coherently link optical frequencies with microwave electrical signals, have heralded several scientific frontiers such as frequency metrology, optical clockwork, precision navigation, and high speed communication over the past decades [1, 2]. Parametric oscillation in ultrahigh Q microresonators [3, 4], facilitated by the high quality factors and the small mode volumes, is an alternative physical process that offers the opportunity of optical frequency comb generation in compact footprints [5] with smaller weight and lower power consumption. The recent demonstration of octave spanning parametric oscillation [6, 7], low-phase noise photonic oscillator [8, 9, 10, 11], stabilized optical frequency microcomb [12, 13, 14], and mode-locked femtosecond pulse train [15, 16, 17, 18, 19] have triggered great excitements. In particular, the observation of dissipative Kerr soliton formation and soliton-induced Cherenkov radiation [20] offers a reliable route towards self-referenced broadband optical frequency microcomb. Dissipative solitons are localized attractors where the Kerr nonlinearity is compensated by the cavity dispersion and the cavity loss is balanced by the parametric gain [21]. Thus the cavity dispersion and the pump-resonance detuning are two determining parameters in the existence of dissipative solitons in ultrahigh Q microresonators.

Generation of microresonator-based optical frequency comb, or Kerr frequency comb, has been studied in various material platforms [10, 22, 23, 24, 25, 26, 27, 28, 29, 20]. Among those platforms, Si_3N_4 planar waveguide system draws great attention for its high nonlinearity, wide transparent window, robust coupling mechanism, low propagation loss and

its CMOS-compatibility for potential monolithic electronic and feedback integration. For Si_3N_4 microresonators, dispersion is typically engineered by the design of waveguide geometry. However, conventional method of using multi-mode waveguide will result in additional perturbation to the Kerr frequency comb and dissipative soliton generation dynamics [30, 31, 27, 32, 33]. Hence, in my research, I focus on frequency microcomb studies in novel designs of tapered Si_3N_4 planar waveguide geometry achieving higher-order-mode suppression. I not only work on unravelling the fundamental dynamics of dissipative Kerr solitons in anomalous dispersion regime, but I also investigate a novel pulse formation mechanism in normal dispersion device. Benefiting from their high intrinsic phase coherence and individual comb line powers, I further extend my research to absolute distance metrology with a single soliton comb and free-space optical communication with a flat normal dispersion comb. The thesis is organized as follow:

In chapter 2, I will introduce a novel design of Si_3N_4 microresonator in which single mode operation, high quality factor, and anomalous dispersion are attained simultaneously [34]. The novel microresonator is consisted of uniform single mode waveguides in the semi-circle region, to eliminate bending induced mode coupling, and adiabatically tapered waveguides in the straight region, to avoid excitation of higher order modes. The intrinsic quality factor of the microresonator reaches 1.36×10^6 while the group velocity dispersion remains to be anomalous at -50 fs^2/mm. With this novel microresonator, we demonstrate that broadband phase-locked Kerr frequency combs with flat and smooth spectra can be generated by pumping at any resonances in the optical C-band. In this collaboration work, I mainly focus on the device characterization, experimental demonstration of the smooth and phase=locked microcomb as well as simulation of the microcomb dynamics using Lugiato-Lefever equation.

In chapter 3, I will unravel the transitional dynamics of frequency microcombs from chaotic background routes to femtosecond mode-locking in real time, enabled by our ultrafast temporal magnifier metrology and improved stability of dispersion-managed dissipative Kerr solitons generated in an 88 GHz Si_3N_4 microresonator [35]. Through our dispersion-managed

planar microresonator, we further observe a stability zone that is more than an order-of-magnitude larger than its prior static homogeneous counterparts, providing a novel platform for understanding ultrafast dissipative dynamics and offering a new path towards high-power frequency microcombs. In this co-authored work, I mainly contribute to the theoretically investigation of the intracavity dynamics of the stretched pulse in the tapered cavity using coupled nonlinear Schrödinger equation, device characterization and the frequency-resolved optical gating measurement.

In chapter 4, I will demonstrate thermally stabilized frequency microcomb formation in a dispersion-managed microresonator at the different mode-locking states featured with the negligible center frequency shift and broad frequency bandwidth. Subsequently, femtosecond timing jitter in the microcombs are characterized, supported by precision metrology on the timing phase, relative intensity noise and instantaneous linewidth. We contrast the fundamental noise for a range of 89 GHz microcomb states, from soliton crystals to multiple solitons and single-soliton regimes, determined by pump-resonance detuning. For the single-soliton state, we report a close-to-shot-noise-limited relative intensity noise of -153.2 dB/Hz and a quantum-noise-limited timing jitter power spectral density of 0.4 as^2/Hz, at 100 kHz offset frequency. This is enabled by a self-heterodyne linear interferometer with 94.2 zs/$Hz^{1/2}$ timing resolution, 50.6 mHz/$Hz^{1/2}$ RF frequency resolution, and 6.7 μV/Hz frequency discrimination sensitivity. We achieve a timing jitter at 1.7 ± 0.07 fs when integrated from 10 kHz to 1 MHz ($\approx$ 32.3 fs when integrated from 10 kHz up to 44.5 GHz Nyquist). Measuring and understanding the fundamental noise parameters in these high-clock-rate frequency microcombs are essential to advance soliton physics and precision microwave-optical clockwork. In this collaboration work, I experimentally demonstrate all the DKSs states, and theoretically analyze the dynamics of the DKS states with Lugiato-lefever equation incorporated with avoided-mode crossing.

In chapter 5, a novel method to deterministically generate double DKS with fixed azimuthal angle assisted by the dual-pump driven scheme in a 88 GHz Si_3N_4 microresonator

will be demonstrated. Via the dual-pump scheme, not only has the single soliton been repeatably generated, double DKS with deterministic azimuthal angle has also been realized through backward tuning. The effects of pump wavelength tuning and pump power on the azimuthal angle are investigated. A direct bridge between the azimuthal angle and the avoided mode crossing induced modulated CW background is established. This work not only provides insight to DKS dynamics in dual-pump scheme, but also improves the versatility of double-DKS based applications in microwave photonics.

In chapter 6, I will discuss the observations of square pulse formation in chip-scale frequency combs, through stimulated pumping at one free-spectral-range and in silicon nitride rings with +55 fs^2/mm normal group velocity dispersion (GVD). Tuning of the platicon frequency comb via a varied sideband modulation frequency is examined in both spectral and temporal measurements. Determined by second-harmonic auto-correlation and cross-correlation, we observe bright square platicon pulse of 17 ps pulsewidth on a 19 GHz flat frequency comb. With auxiliary-laser-assisted thermal stabilization, we surpass the thermal bistable dragging and extend the mode-locking access to narrower 2 ps platicon pulse states, supported by nonlinear dynamical modeling and boundary limit discussions.

In chapter 7 A spectrally-resolved laser dimensional metrology via a free-running soliton frequency microcomb, with nanometric-scale precision will be discussed [36]. Spectral interferometry provides information on the optical time-of-flight signature, and the large free-spectral range and high-coherence of the microcomb enable tooth-resolved and high-visibility interferograms that can be directly readout with optical spectrum instrumentation. We employ a hybrid timing signal from comb-line homodyne, microcomb, and background amplified spontaneous emission spectrally-resolved interferometry – all from the same spectral interferogram. Our combined soliton and homodyne architecture demonstrates a 3-nm repeatability over a 23-mm non-ambiguity range achieved via homodyne interferometry, and over 1,000-seconds stability in the long-term precision metrology at the white noise limits. In this co-authored work, I focus on the stable single soliton generation with dual-driven

scheme and then investigate the Allan deviation of the 88 GHz repetition rate.

In chapter 8, I will demonstrate terabits/s-scale coherent data communications in a free-space atmospheric link, via a platicon frequency microcomb and through wavelength- and polarization-division multiplexing towards multiple-access networks. Spanning more than 64 optical carriers at 115 GHz channel spacing, we report the first free-space link with a frequency microcomb, with up to 10.2 Tbit/s aggregate data transmission with 20 Gbaud symbol rate per carrier and over 160 m atmospheric distances, even under log-normal turbulent conditions. With 16-state quadrature amplitude modulation, we demonstrate the retrieved constellation maps line-by-line across the broad microcomb, achieving communication bit-error rates below the hard- and soft-decision thresholds for forward-error correction. Secondly, to enable multiple-access networks, we demonstrate a single-input single-output (SISO) free-space link, further improving the raw bit-error rates. In SISO configuration we achieve an aggregate data rate up to 5.2 Tbit/s, alongside a field-tested 1.3 bit/s/Hz spectral efficiency in our microcomb atmospheric link. We quantify experimental power penalties of $\approx$ 3.8 dB at the error-correction threshold, with respect to the theoretical additive white Gaussian noise limit. Thirdly, we further demonstrate for the first time the master-slave carrier phase retrieval with frequency microcombs, the effects of turbulence-induced intensity scintillation and pointing error fluctuations in the end-to-end symbol error rates. Through channel fading models of low-visibility fog and smoke, log-normal atmospheric turbulence and non-zero bore-sight pointing errors, we compare our link measurements to the fundamental modelled channel scaling. High-order modulation scaling is subsequently examined for the free-space microcomb testbed. This demonstration provides a platform for broadband connectivity, terrestrial and backhaul links, and ground-satellite links. In this collaboration work, I am in charge of the experimental demonstration of the 115 GHz normal dispersion microcomb, and theoretically study the mechanism of the microcomb with Lugiato-Lefever equation incorporated with avoided-mode crossing. Furthermore, I implement the 160-m free space link with active feedback control to minimize the pointing error. I also contribute

to the digital signal processing of the Terabits/s data communication.

CHAPTER 2

High-order-mode-suppressed Dispersion Engineered Si_3N_4 microresonator

2.1 Introduction

Optical frequency combs, unique light sources that coherently link optical frequencies with microwave electrical signals, have made a broad impact on frequency metrology, optical clockwork, precision navigation, and high speed communication over the past decades [1, 2]. Parametric oscillation in ultrahigh Q microresonators [3, 4], facilitated by the high quality factors and the small mode volumes, is an alternative physical process that offers the opportunity of optical frequency comb generation in compact footprints [5]. The recent demonstration of octave spanning parametric oscillation [6, 7], low-phase noise photonic oscillator [8, 9, 10, 11], stabilized optical frequency microcomb [12, 13, 14], and mode-locked femtosecond pulse train [15, 16, 17, 18, 19] have triggered great excitements. In particular, the observation of dissipative soliton formation and soliton-induced Cherenkov radiation [20] offers a reliable route towards self-referenced broadband optical frequency microcomb. Dissipative solitons are localized attractors where the Kerr nonlinearity is compensated by the cavity dispersion and the cavity loss is balanced by the parametric gain [37]. Thus the cavity dispersion and the pump-resonance detuning are two determining parameters in the existence of dissipative solitons in ultrahigh Q microresonators.

Generation of microresonator-based optical frequency comb, or Kerr frequency comb, has been studied in various material platforms [10, 22, 23, 24, 25], including Si_3N_4 planar waveg-

uide system that is especially suitable for monolithic electronic and feedback integration. For Si_3N_4 microresonators, dispersion is typically engineered by the design of waveguide geometry. Anomalous dispersion, required for bright dissipative soliton formation, is achieved using multi-mode waveguides in the optical C/L-band wavelength range. Besides, scattering loss in multi-mode waveguides is reduced, leading to higher quality factors and lower comb generation threshold [38]. Coupling between different transverse mode families in the multi-mode waveguides results in periodic disruption of dispersion and quality factor, introducing additional perturbation to the Kerr frequency comb and dissipative soliton generation dynamics [30, 31, 27, 32, 33]. Such effect manifests itself as characteristic amplitude modulation in the Kerr frequency comb spectrum or detrimental destabilization of the dissipative cavity soliton, depending on the strength and position of the mode coupling [27, 33]. Careful choice of pump mode to avoid the mode crossing region and increase of cavity's free spectral range (FSR) are thus necessary for dissipative soliton formation in conventional Si_3N_4 microresonators.

In this chapter, we report a novel design of Si_3N_4 microresonator in which single mode operation, high quality factor, and anomalous dispersion are attained simultaneously. No higher order mode is observed throughout the optical C/L-band in the transmission spectrum. A high resolution coherent swept wavelength interferometer is implemented to determine the intrinsic quality factor and the group velocity dispersion (GVD, β_2) of the microresonator. They are measured at 1.36×10^6 and -50 fs^2/mm, respectively. We demonstrate that phase-locked Kerr frequency combs can be generated by pumping at any resonances in the optical C-band. The spectra spanning more than 20 THz (full width at -20 dB) are smooth without periodic amplitude modulations.

2.2 Dispersion engineered microresonator design

For applications such as high speed communication and astrospectrograph calibration, it is beneficial to have a broadband optical frequency comb with a smooth and flat spectral shape [39, 40]. Such an unstructured spectrum is difficult to attain in a multi-mode microresonator (Figure 2.1), especially in Si_3N_4 microresonators where mode coupling is facilitated by the strong sidewall scattering [38]. Reducing the waveguide cross-section to $1 \times 0.8\,\mu m^2$ is a solution to eliminate higher order modes, but it results in larger optical mode overlap with the waveguide boundaries and consequently lowers the achievable quality factor. Compared to the multi-mode microresonator ($Q_I = 1,560,000$), the microresonator made of a $1 \times 0.8\,\mu m^2$ waveguide only has an intrinsic quality factor of 830,000 (Table I). Such decrease in the intrinsic quality factor leads to a reduction of cavity-enhanced Kerr effect by 3.5 times ($(1,560,000/830,000)^2$) [10]. Furthermore, such single mode waveguide features positive GVD and large third-order dispersion (TOD, β_3) for all optical communication wavelengths (Figures 2a and 2b), inhibiting the Kerr frequency comb generation.

microresonator type	**loaded** Q	**intrinsic** Q
single-mode waveguide with a uniform width of 1 μm	0.6 M	0.83 M
multi-mode waveguide with a uniform width of 2 μm	1.1 M	1.56 M
single-mode waveguide with varying widths from 1 to 2 μm	1.0 M	1.36 M

Table 2.1: Intrinsic and loaded quality factors of different types of microresonators. For a fair comparison, all other parameters of the microresonators are kept the same.

2.2.1 Higher order mode suppression

Our strategy to suppress higher order modes while maintaining high quality factor and anomalous dispersion is two-fold (Figure 2.2c). First, a uniform single mode waveguide ($1 \times 0.8\mu m^2$) is included in the semi-circle region where the waveguide is curved, as bending

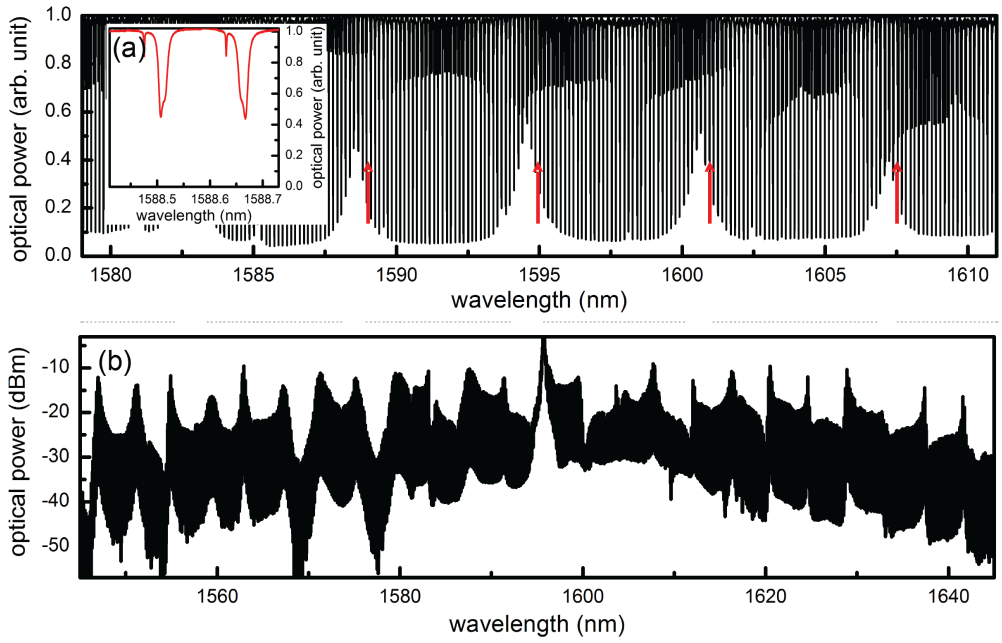

Figure 2.1: Kerr frequency comb from a multi-mode microresonator. a, Cold cavity transmission of a multi-mode microresonator. The waveguide cross-section is uniform at $2 \times 0.8 \mu m^2$ along the whole microresonator. Five modal families (3 TE and 2 TM) are identified and mode hybridization between the first two TE modes leads to periodic disruptions in dispersion and quality factor (red arrows). Inset: Zoom-in view of the cavity resonances around 1588.6 nm. b, Example Kerr frequency comb spectrum, showing a periodic amplitude modulation in its spectral shape due to the mode hybridization.

introduces significant mode coupling if a multi-mode waveguide is used. The diameter of the semi-circle is 200 μm. Second, the microresonator is enclosed by adding straight waveguides with adiabatically tapered width to join the two semi-circles. Each straight waveguide is 800 μm long with the width tapered linearly from 1 μm at the two ends to 2 μm at the middle, ensuring selective excitation of the fundamental mode in the otherwise multi-mode waveguide segment. The GVD and TOD of the uniform waveguides with different widths and the tapered waveguide calculated with a commercial full-vector finite-element-mode solver (COMSOL Multiphysic), taking into consideration both the waveguide dimensions and the material dispersion [41], which are summarized in Figure 2.2a,b. To account for the tapered

geometry, waveguide dispersions are calculated for various widths (1 to 1.2 μm with a step of 25 nm and 1.25 to 2 μm with a step of 50 nm). Dispersions as a function of waveguide width obtained from a cubic spline interpolation are also shown in the insets. The fitted functions are then used to calculate the path-averaged dispersions $\overline{\beta_2} = \frac{\int \beta_2(L)dL}{L_{cav}}$ and $\overline{\beta_3} = \frac{\int \beta_3(L)dL}{L_{cav}}$, where dL=400 nm. The tapered waveguide accounts for > 70% of the cavity length, thus the quality factor is minimally compromised (Table 2.1) and the average GVD remains to be anomalous in this novel Si_3N_4 microresonator (Figure 2.2a). The average TOD is calculated as -155 fs^3/mm (Figure 2.2b) and its perturbative effect on the dissipative cavity soliton is evaluated by introducing the normalized TOD coefficient $d_3 = \sqrt{\frac{\beta_1\omega_0}{Q_L}}\frac{\beta_3}{3|\beta_2|^{3/2}}$, where β_1 is the group velocity and Q_L is the loaded quality factor [42]. In the designed microresonator, d_3 = –0.016 $\ll$ 1 and thus it is still in the GVD-dominant regime that is beneficial for symmetric Kerr frequency comb generation. By numerically solving the Lugiato-Lefever Equation (LLE), which describes the dynamics of dissipative cavity solitons [43], it is shown that a stable 50-fs long pulse can be generated from the designed microresonator (Figure 2.2d). Further details about LLE could be find in Appendix B.

2.2.2 Device fabrication and characterization

The microresonator was fabricated with CMOS-compatible processes: first, a 5 μm thick under-cladding oxide was deposited to suppress substrate loss. An 800 nm thick Si_3N_4 layer was then deposited via low-pressure chemical vapor deposition, patterned by optimized deep-ultraviolet lithography, and etched via optimized reactive ion dry etching. Annealing at a temperature of 1150 °C was then applied to the chip for 3 hours to reduce the waveguide propagation loss. Finally the silicon nitride spiral resonators were over-cladded with a 3 μm thick oxide layer.

Characterization of the fabricated microresonator is summarized in Figure 2.3. A high resolution coherent swept wavelength interferometer (SWI) was implemented to characterize the cold cavity properties, Q and GVD, of the microresonator [17] (See detailed information

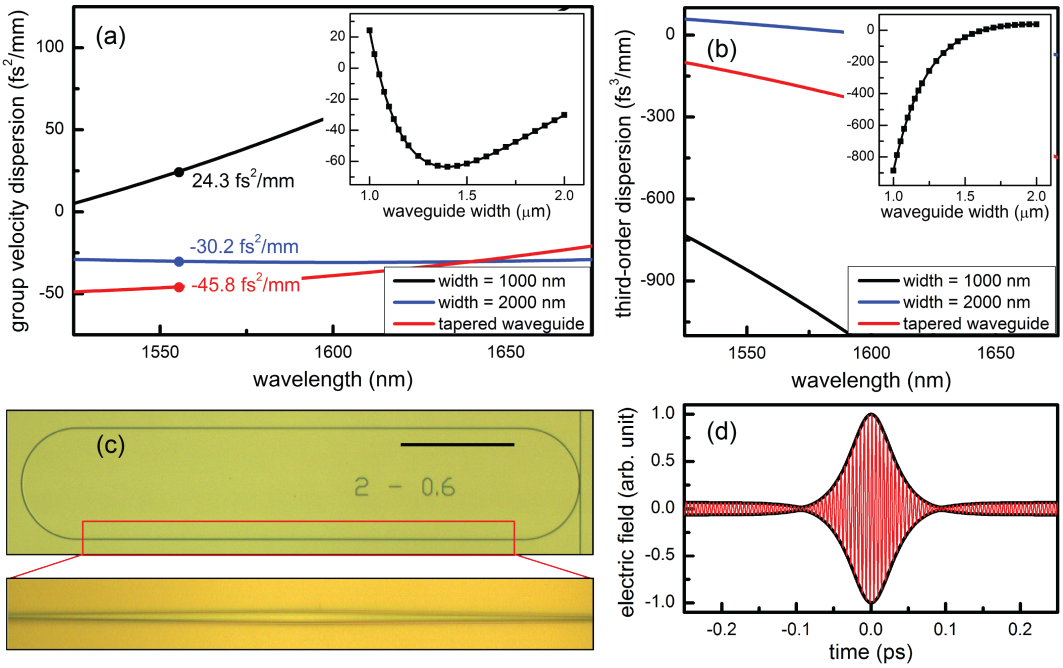

Figure 2.2: Design of a single-mode, high Q, and anomalous dispersion microresonator. a,b, GVD and TOD of the uniform waveguides with different widths and the tapered waveguide. c, An optical micrograph of the designed single-mode microresonator. The waveguide in the semi-circle regions has a uniform width of 1 μm, supporting only the fundamental modes. On the other hand, the 800 μm long straight waveguide has a tapered width from 1 μm at the end to 2 μm at the middle of the waveguide. The total cavity length is 2.2 mm. Scale bar: 200 μm. d, Dissipative cavity soliton with a FWHM duration of 50 fs is obtained by numerically solving the LLE.

in Appendix A.1.1). The wavelength of a tunable external cavity diode laser (ECDL) was linearly tuned from 1530 nm to 1590 nm at a scan speed of 60 nm/s. The laser was set to be purely TE polarized by inserting a polarizer with an extinction ratio of > 100 before the coupling optics. Similarly, an analyzer was used at the output to guarantee exclusive collection of either TE polarized (Figure 2.3a) or TM polarized (Figure 2.3c) transmission spectra. To minimize the thermally induced resonance shift, the on-chip temperature was actively controlled to ensure the temperature drift in 1 second was within 1 mK.

Figure 2.3a shows the cold cavity transmission of the microresonator, calibrated with 51

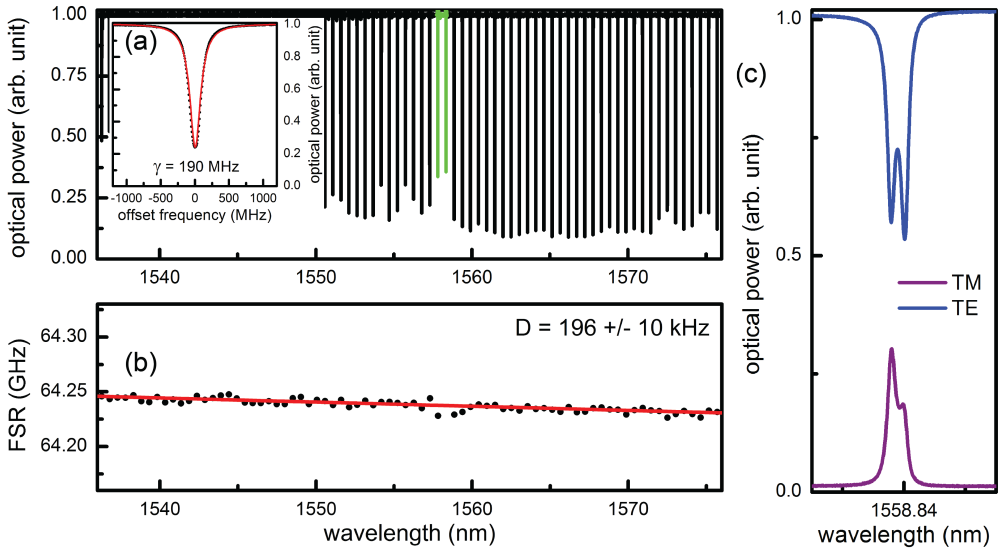

Figure 2.3: Characterization of the single-mode, high Q, and anomalous dispersion microresonator. a, Cold cavity transmission of the designed single-mode microresonator, measured with the high resolution coherent swept wavelength interferometer (detailed in appendix A). Higher order modes are not observed in the microresonator, but the weak TE and TM coupling around 1558 nm results in a 10% reduction in the cavity loading (green lines and inset on the right). Inset on the left: resonance at 1556 nm is undercoupled with a loaded Q of 1,000,000. b, Wavelength dependence of the FSR, measuring a non-equidistance of the modes, $D = -\frac{\beta_2 c \omega_{FSR}^2}{n}$, of 196±10 kHz. The extracted GVD is anomalous at -50±2.6 fs^2/mm. The slight dispersion disruption around 1558 nm is negligible in the Kerr frequency comb formation, evidenced by the smooth spectral shapes shown in Figure 2.4. c, At a different temperature ($\Delta T = 7$ °C) where the TE and the TM resonances become closer to degeneracy, stronger polarization coupling results in further reduction in the cavity loading. The input is TE polarized and the output is analyzed by either a TE or a TM polarizer, showing the hybridized modes are superposition of both polarization states.

absorption features of the HCN gas cell, and no higher order transverse modes are observed throughout the optical C/L bands in the spectrum. The inset shows the resonance at 1556 nm, which is undercoupled with a loaded Q over 1,000,000 and intrinsic Q about 1,360,000. 10 transmission spectra were taken and independently fitted to determine the mean value of the GVD and the error bar of the measurements. Figure 3b shows the wavelength dependence of the free spectral range (FSR), measuring a FSR of 64.24 GHz and a mode non-equidistance of 19±10 kHz at 1556 nm. The GVD extracted from the measurements is anomalous at -50 ± 2.6 fs^2/mm.

2.3 Smooth and flat phase-locked Kerr frequency comb generation

For Kerr frequency comb generation, the microresonator is pumped with an on-chip power up to 1.7 watts. A flat and smooth phase-locked Kerr frequency comb can be generated by pumping at any resonances in the optical C-band, thanks to the absence of quality factor disturbance induced by mode coupling. Figure 2.4 shows three example spectra pumping at 1551.83 nm, 1556.48nm, and 1561.58 nm. Importantly, the spectral shapes resemble one another and periodic amplitude modulations are not observed, distinctly different from Figure 2.1 where the comb spectrum is structured by the mode coupling characteristics. Tuning speed of the pump frequency has been shown to be a critical parameter to drive the Kerr frequency comb into low-phase noise soliton state, circumventing the thermal effect of the microresonator [16]. To find the proper tuning speed, pump power transmission is monitored while pump frequency is scanned, via control of the piezoelectric transducer, across a cavity resonance with tuning speeds varying from 1 nm/s to 100 nm/s. When the tuning speed is higher than 40 nm/s, a characteristic step signature of low-phase noise soliton state is observed. Figure 2.5a shows the pump power transmission with the pump frequency tuning speed set at 60 nm/s. Coherence of the Kerr frequency comb is characterized by measuring the RF amplitude noise with a scan range much larger than the cavity linewidth [18, 27, 44].

Pump mode is removed with a fiber WDM filter to avoid saturation of the photodetector. Figure 2.5b shows RF amplitude noise of the Kerr frequency comb at different states, showing the transition from a high-phase noise state (state 1) to the low-phase noise soliton state (state 2). In state 3, the pump is off-resonance and Kerr frequency comb is not generated. At the proper pump-resonance detuning, the RF amplitude noise drops by more than two orders of magnitude (state 1 to state 2) and reaches the background noise of the detector (state 3). The RF amplitude noise measurements confirm the generation of phase-locked Kerr frequency combs.

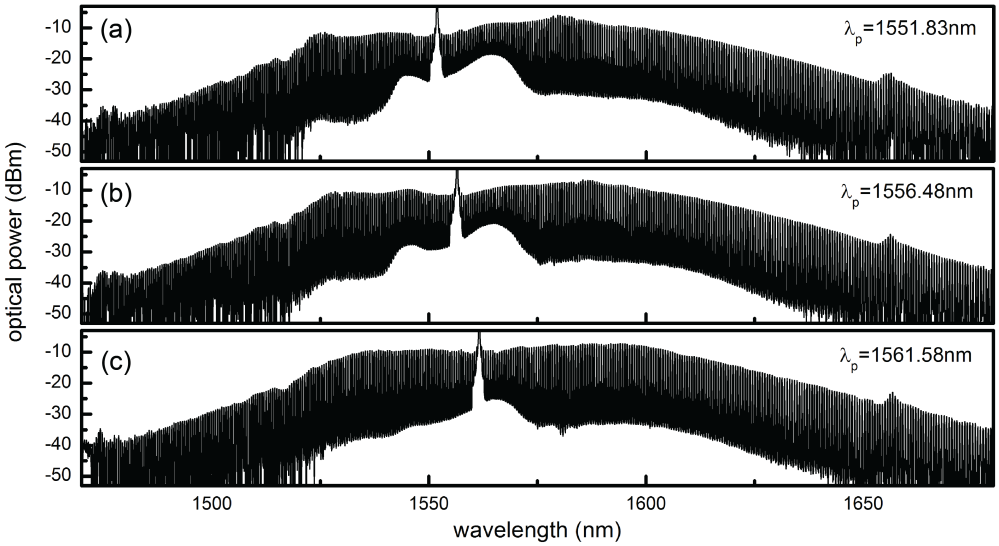

Figure 2.4: Smooth and flat Kerr comb generation at different pump wavelengths. In the designed single-mode microresonator, phase-locked Kerr frequency combs can be generated by pumping at any resonances in the C-band. Three example spectra are shown here. a, $\lambda_p = 1551.83$nm. b, $\lambda_p = 1556.48$nm. c, $\lambda_p = 1561.58$nm. Moreover, the spectral shapes are smooth without periodic amplitude modulations, distinctly different from Figure 2.1.

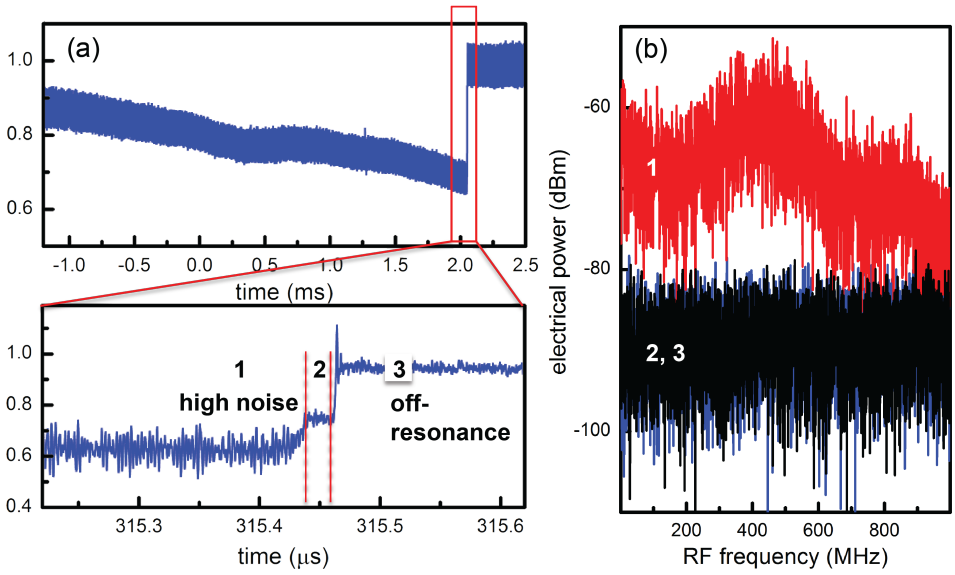

Figure 2.5: Phase-locked Kerr frequency comb generation. a, Pump power transmission as the pump wavelength is scanned across a cavity resonance at a speed of 60 nm/s. The observation of the step signature is characteristic of the low-phase noise soliton state (state 2). b, RF amplitude noise of the Kerr frequency comb at different states (1: high-phase noise, 2: low-phase noise) along with the detector background (3), showing the transition in and out of the low-phase noise state. The scan range of 1 GHz is more than five times the cavity linewidth.

2.4 Summary

In summary, we demonstrate a novel design of Si_3N_4 microresonator which can be used to attain single mode operation, high quality factor, and anomalous dispersion all simultaneously. The microresonator is consisted of uniform single mode waveguides in the semi-circle region, to eliminate bending induced mode coupling, and adiabatically tapered waveguides in the straight region, to ensure selective excitation of the fundamental mode. The intrinsic Q of the microresonator is 1.36×10^6, 1.6 times larger than that of a single mode microresonator with a uniform waveguide cross-section. More importantly, the GVD of the novel microresonator remains to be anomalous at -50 fs^2/mm. With the novel microresonator, we demonstrate the generation of phase-locked Kerr frequency combs pumped at any resonances

in the optical C-band. The spectra spanning more than 20 THz (full width at -20 dB) are smooth without periodic amplitude modulations.

CHAPTER 3

Dispersion-managed Dissipative Kerr Soliton

3.1 Introduction

Optical frequency combs, first demonstrated in Mode-locked lasers, are unique light sources that coherently link optical frequencies with microwave electrical signals and have largely influenced studies in frequency metrology, optical clocks, precision navigation, and high-speed communication in recent decades [2]. The dissipative Kerr soliton, a local attractor that doubly balances the parametric gain and cavity loss as well as the Kerr nonlinearity and dispersion [37], has drawn significant attention in frequency comb studies in recent years. These investigations have led to the discoveries of extensive soliton and soliton molecule dynamics [45, 46, 47, 48]. In particular, efforts in the breathing pulse evolution along the cavity length – through dispersion management – could broaden the scope of mode-locking physics and solve the high-energy pulse break-up problem induced by an excessive accumulated nonlinear phase, a serious limit in traditional cavities where pulses propagate statically [49, 50, 51].

The miniaturization of frequency comb generation into chip-based microresonators offers an opportunity to examine dissipative Kerr soliton generation in compact footprints [21], which not only provides a promising testbed to examine fascinating nonlinear dynamics [52] but also offers a reliable route for frequency microcombs [53] towards implementations in low-phase noise photonic oscillators[9], broadband optical frequency synthesizers [13, 54], integrated dual-comb spectroscopy [55], coherent terabit communications [56], coherent laser

ranging [57, 58], and spatio-temporal control of solitons [59]. In a normal procedure, dissipative soliton states can be generated when the driving laser frequency or power is tuned in the Kerr-active microresonator from blue detuning to red detuning, initiating spontaneous cavity modulation instability, followed by Turing pattern generation [60, 61, 62], a transition into spatial-temporal chaos, and the eventual passage into the breather soliton, soliton molecules or crystals, and single soliton states. As previous studies of cavity dynamics in fiber optics could be boosted by real-time measurement technology [63, 64, 65], the study of these abundant transition dynamics in a microcavity can benefit from a time magnifier system due to its ability to characterize non-repetitive and arbitrary waveforms in real time with sub-picosecond temporal resolution in a single shot [66, 67]. Complementing the techniques of direct detection [68] and electro-optic comb scanning [69], temporal magnification can help surpass the electronic limits when studying microresonator dynamics at very high repetition rates of several tens of GHz or more. In steady state, static dissipative solitons have been observed and characterized in both the anomalous [16] and normal dispersion regimes [17, 15]. Dispersion-managed dissipative solitons have also been theoretically studied in Kerr active resonators [70], including cases with shorter pulse widths for higher pulse energies. Specifically, dispersion-managed microresonators [34] can exhibit improved output pulse stability via the reduced timing jitter converted from pulse center frequency fluctuations due to the near-zero net GVD. In addition, a dispersion-managed dissipative Kerr soliton is more resistant to breather soliton instabilities, increasing the attainable pulse energy from a passive resonator [70]. Operation in the stretched-pulse regime with near-zero GVD has been demonstrated to be beneficial in femtosecond Mode-locked fiber lasers for achieving a narrow linewidth, low phase noise, and attosecond timing jitter [71], which are important merits for advancing microwave photonics [72] and coherent pulse synthesis [73]. A similar timing jitter reduction from decreasing the net cavity dispersion is also theoretically predicted in Kerr-active resonators [74].

Here, we report the real-time transitional dynamics and enhanced stability of dispersion-

managed dissipative solitons. Our oscillator is designed asymmetrically with adiabatic tapering where single-mode operation, a high quality factor, and dispersion management are attained simultaneously [34]. This design enables the enhanced stable formation of dispersion-managed dissipative solitons. Subsequently, through our ultrafast temporal magnifier (UTM) approach [67], we are able to map – in real-time –transitional portraits of femtosecond mode-locking from noisy chaotic backgrounds. We illustrate the complex bifurcation dynamics of these tuned dissipative solitons. Third, through correlated transmission measurements, we show that our dispersion-managed dissipative solitons exist in a stability zone that is an order-of-magnitude larger than that in prior static homogeneous oscillators and sustain more pulse energy.

3.2 Dispersion-managed dissipative Kerr solitons in a tapered microresonator

3.2.1 88 GHz dispersion-managed Si_3N_4 microresonator design and characterization

A scanning electron microscopy (SEM) image of the dispersion-managed microresonator is shown in Figure 3.1a. The device consists of a waveguide with varying widths to provide the oscillating GVD along the cavity length, and the detailed design of the waveguide width is shown in Figure 3.1b. Figure 3.1d shows the GVD and nonlinear coefficient varying along the cavity length. Since the effect of the varying nonlinear coefficient is negligible compared to the changing GVD, we only consider the impact of GVD management in this work. Such an oscillating GVD results in the periodic stretching and compression of dispersion-managed dissipative Kerr solitons (DM-DKSs) and is more resistant to breather soliton instability, increasing the attainable pulse energy from a passive resonator [15] (see Appendix B.1). In our current design, the microresonator waveguide width first changes from 1 μm at the coupling region to 4 μm in the middle of the microcavity and then changes back to 1 μm in

the second half of the microcavity, resulting in a GVD oscillation from -59 fs^2/mm to +58 fs^2/mm.

The Si_3N_4 microresonator design not only provides an oscillating GVD along the cavity length but also suppresses higher-order mode families, which suppresses the mode-crossing-induced perturbation to dissipative soliton generation, leaving only the rare mode-crossing caused by TE-TM mode hybridization from the fabrication imperfection [70]. Both the bus waveguide and the cavity waveguide in the coupling region are designed to be strictly single-mode, thereby ensuring selective excitation of the fundamental mode and suppressing other transverse mode families. The cavity transmission around the pump mode is plotted in Figure 3.1e, with no observable higher-order transverse modes in the transmission spectrum. Near-critical coupling is attained, with a loaded Q of 1.9×10^6 and a cavity loading of 90% for the pump mode. The microresonator free spectral range is measured to be $\approx$ 88 GHz. The GVD and TOD shown in Figure 3.1c are calculated with COMSOL, taking into consideration both the cavity geometry and the material dispersion. The path-averaged GVD is slightly anomalous at -2.6 fs^2/mm, leading to intracavity pulse dynamics in the stretched-pulse regime. To verify the near-zero path-averaged GVD, both SWI and a high-resolution frequency-comb-assisted diode laser spectroscopy [75] are employed to characterize the cold cavity properties of our designed Si_3N_4 microresonator (See Appendix A.1). With active control of the on-chip temperature, passive shielding against acoustic noise and an absolute wavelength calibration with the hydrogen cyanide gas standard, the method provides a GVD accuracy of 0.4 fs^2/mm, determined as the standard deviation calculated from 10 independent measurements. The mean value of the net cavity GVD from the 10 measurements is -6.4 fs^2/mm (Figure 3.1f).

3.2.2 Dispersion-managed dissipative Kerr soliton: theoretical analysis

In order to accurately depict the intracavity dynamics of DM-DKS, instead of mean-field LLE, we solve coupled nonlinear Schrödinger equation numerically to describe the DM-DKS

formation physics:

$$\begin{aligned} A^{m+1} &= \sqrt{TP_{in}} + \sqrt{1-T}A^{m}\exp -j\delta \\ \frac{\partial}{\partial z}A^{m} &= -\frac{\alpha}{2}A^{m} - \frac{j}{2}\beta_2(z)\frac{\partial^2}{\partial t^2}A^{m} + j\gamma(z)|A^{m}|^2A^{m} \end{aligned} \tag{3.1}$$

where $m, \beta_2, \alpha, T, \gamma$, and δ are the number of roundtrips, GVD, cavity loss, coupling loss, Kerr nonlinear coefficient, and pump-resonance detuning, respectively. The cavity length is discretized into a total of 120 steps, and at each step, β_2 and γ are re-evaluated based on the local waveguide geometry. Figure 3.2a plots the numerically solved DM-DKS evolution within the microcavity. The asymmetry of the pulse width and peak power shown in Figures 3.2b is due to the chirp change (see the detailed simulation result and discussion in Appendix B.1). For each round trip, the DM-DKS experiences a cycle of stretching and compression between 32.3 fs and 29.9 fs (Figure B.1).

3.2.3 Dispersion-managed dissipative Kerr soliton: experimental realization

Tuning the pump frequency into the cavity resonance from the blue side with a scan speed of 3.5 THz/s, a stable DM-DKS can be observed, with a typical optical spectrum shown in Figure 3.3a. The 3 dB bandwidth of the measured spectrum is 4.78 THz, and the transform-limited FWHM pulse duration is 92 fs. Notably, the measured DM-DKS spectrum fits well with a Gaussian profile (red line) rather than the squared hyperbolic shape (blue line), indicative of stretched-pulse operation [70]. The inset plots the numerically simulated comb spectrum, which also shows a better match with a Gaussian profile than a sech^2 profile. Furthermore, the TOD effect is augmented due to the near-zero GVD, resulting in the observed asymmetry in the optical spectrum and carrier frequency shift (green dashed line) from the pump. A stable pulse train and low-noise operation is confirmed by an RF amplitude noise spectrum measurement (Figure 3.3b), showing that the noise level approaches the detector background, and a frequency-resolved-optical-gating (FROG) measurement (Figure 3.3c), showing consistently low retrieval errors below 10^{-2}. A singlet DM-DKS pulse with a

negative chirp, in qualitative agreement with the numerical simulation, is retrieved from the FROG spectrogram. We note that a quantitative comparison cannot be made due to the limited bandwidth of the C-band Er-doped fiber amplifier used in our FROG measurement (see Appendix A.3.1).

Figure 3.4a shows the total transmission of the microresonator with respect to the pump resonance detuning when the pump frequency is scanned across the resonance at a speed of 2.1 THz/s. The transmission deviates from a Lorentzian lineshape and follows a triangular profile defined by the combined effect of the thermal and nonlinear resonance shifts, resulting in optical bistability that eventually leads to dissipative Kerr soliton formation. At the edge of the resonance, multiple discrete transmission steps are observed, which have been identified as important attributes of dissipative Kerr soliton (Figure 3.4b). As solitons are formed, excessive optical power is ejected from the cavity, resulting in a stepwise increase in the total transmission.

3.3 Real-time dynamics measurement with an ultrafast temporal magnifier

While the temporal structure of the intracavity field is detailed at the sub-picosecond time scale, the evolution and transition dynamics are portrayed at a much slower sub-microsecond time scale, which is associated with the cavity photon time of the microresonator. The orders-of-magnitude difference in the time scale between the two time dimensions poses an experimental challenge for capturing a comprehensive picture of the dynamics. Here, we demonstrate that UTMs are invaluable solutions that can fully characterize the evolution and transitional dynamics of dissipative Kerr solitons. A UTM is the time-domain counterpart of a high-speed digital microscope system, utilizing the space-time duality principle where diffraction in space and dispersion in time share the same mathematical expression [67]. Incorporating suitable GDDs (D_1 and D_2) before and after the four-wave mixing stage

in a highly nonlinear fiber (HNLF), a temporal magnification of 72× and a time resolution of 600 fs are attained in our UTM, enabling a detailed depiction of the dissipative soliton's temporal structure. The evolution and transition dynamics, on the other hand, are sampled optically with a synchronized and stabilized femtosecond Mode-locked fiber laser (MenloSystems GmbH). The frame rate of the first UTM is 250 MHz, higher than the cavity resonance linewidth of 100 MHz, and is determined by the laser repetition rate stabilized to an Rb-disciplined crystal oscillator.

The schematic setup of the UTM is depicted in Figure 3.5 (Appendix A.6). UTM is implemented though four-wave mixing (FWM) in a 50-m highly nonlinear fiber (HNLF). The HNLF (OFS) had a zero-dispersion wavelength (ZDW) of 1556 nm and a dispersion slope of 0.019 ps/(nm^2·km). The nonlinear coefficient is 11.5 W^{-1} km^{-1}. The FWM pump is derived from a stabilized femtosecond Mode-locked fiber laser, and its spectral component from 1554 nm to 1563 nm is first filtered out by wavelength-division multiplexing (WDM2) and subsequently amplified by a C-band erbium-doped fiber amplifier (EDFA-C) to 50 mW. Before the signal and the pump are combined via WDM3 into the FWM stage, they are chirped by D_1 and D_f, respectively, through two spools of SMF-28. The generated idler is filtered out via WDM4 and then chirped by the output dispersion D_2 through a spool of DCF. Finally, the filtered and chirped idler is amplified by an L-band erbium-doped fiber amplifier (EDFA-L) to 100 μW before it is sent to a 25 GHz amplified photodetector (PD2) and an 80 GS s^{-1} real-time oscilloscope for detection. For the correlation measurements, the ECDL laser frequency scan and the oscilloscope data acquisition system are synchronized using a multi-channel pattern generator. All of the electronics are commonly referenced to an Rb-disciplined crystal oscillator for accurate timing.

At a frame rate of 25 MHz for the second UTM and with a 190 ps single-shot record length, we can record a complete intracavity field of 16 roundtrips in real time, but missing the information between each measurement. Then, multiple frames are stitched to reconstruct the soliton evolution through the whole transmission step. As long as the intracavity field

pattern evolves much slower than 25 MHz, our technique could provide valuable information about the intracavity waveform evolution.

To compare the difference in the transition dynamics and stability zone between static and dispersion-managed dissipative Kerr solitons, we synchronize both the transmission and UTM measurements with pump frequency scanning and focus on the dynamics around these transmission steps.

3.3.1 Stability zone and temporal dynamics: static dissipative Kerr soliton

A representative result of static soliton formation in a homogeneous microresonator is summarized in Figure 3.6a. The Si_3N_4 microresonator consists of a 1.2×0.8 μm^2 uniform waveguide, with a loaded Q of 1.5×10^6, a cavity loading of 86%, and a measured GVD of -33.1 fs^2/mm (Figure 3.1c). At the first transmission step where the cavity loading decreases to 45% (corresponding to a transmission of 55%), a doublet soliton state is reached and remains stable for a 160 kHz change in the pump resonance detuning before the second transmission jump. A further reduction in the cavity loading to 30% results in the formation of a singlet soliton state, which nevertheless only exists in a small stability region of 30 kHz. An on-chip pump power of 30 dBm is used in this example, but similar behaviour is noted for pump powers of 24 dBm and 27 dBm. However, no stable soliton states are observed from the UTM when the on-chip pump power exceeds 30 dBm.

3.3.2 Stability zone and temporal dynamics: dispersion-managed dissipative Kerr soliton

In comparison, representative results of dispersion-managed soliton formation with distinctly different features are summarized in Figures 3.6b and 3.6c. First, a stable singlet soliton is observed at both power levels of 30 dBm (Figure 3.6b) and 32 dBm (Figure 3.6c), with a better success rate in achieving the singlet soliton state at higher power. The on-chip

pump power of 32 dBm is limited by the available power of our high-power erbium-doped fiber amplifier. Second, while the transition from chaos to low-noise stable solitons is still associated with a transmission step, the transition from a multiple soliton state to a singlet soliton state no longer results in a further ejection of excessive intracavity power. Rather, monotonic increases in the cavity loading from 38% to 52% (Figure 3b) and from 36% to 57% (Figure 3.6c) are observed. When the on-chip pump power is 30 dBm, triplet solitons are first observed after the transmission step (Figure 3.6b-I), and their interaction gradually results in a transition to a singlet soliton state at the end of the transmission step (Figure 3.6b-II). Both characteristics illustrate the advantage of the dispersion-managed Kerr soliton in concentrating more energy into a singlet soliton pulse. Furthermore, the stability zone of DM-DKS including both the multiple and singlet soliton cases are extended to 340 kHz (Figure 3.6b) and 400 kHz (Figure 3.6c), more than double the stability zone of a static soliton. In particular, at a higher on-chip pump power of 32 dBm, the singlet soliton state can persist across the whole transmission step (Figure 3.6c), showing a remarkable increase in the singlet soliton stability zone by more than an order of magnitude (400 kHz as opposed to 30 kHz) at a higher pump power. The generation of this particularly stable singlet soliton state is found to be correlated with a cleaner transmission curve before the transition (grey region in Figure 3.6), with the root mean squared fluctuation decreasing from 20% to 10%.

3.3.3 Transition dynamics of dispersion-managed dissipative Kerr soliton evolution

To probe the real-time dynamics in this potentially chaotic regime, the UTM is slightly modified to increase the signal-to-noise ratio and reduce the TOD-induced aberration at the cost of lowering the measurement frame rate (red dashed box in Figure 3.5c). While the overall system GVD is increased by more than a factor of 5, the TOD is minimized by a proper combination of a dispersion-compensating fiber and a non-zero-dispersion-shifted fiber (see Appendix A.3.2). The output from the stabilized femtosecond Mode-locked fiber laser comb,

for optical sampling along the slow time axis, is pulse-picked with an electro-optic modulator (EOM) to reduce the repetition rate down to 25 MHz. An arbitrary waveform generator (AWG), electronically synchronized to the Mode-locked pulse train, serves effectively as a high-quality frequency divider and drives the EOM for pulse picking with a dynamic extinction ratio of more than 20 dB. With the modified UTM, we are able to measure the evolution of not only the low-noise stable solitons but also the chaotic oscillations before the stable transition (Figure 3.7). In the case where the singlet soliton remains stable across the whole transmission step (Figure 3.6c), the temporal structure before the transition appears to be less chaotic, resulting in a cleaner transmission curve. Despite intense and rapid soliton interaction dynamics (Figure 3.7b), a clear temporal pulse structure is still observed, which is quite different from the chaotic state (Figure 3.7d). The inset in Figure 4a shows a stability analysis of the dispersion-managed oscillator, showing that such a design could enlarge the single soliton zone with a high pump power (see Appendix B.1 for detailed discussion).

3.4 Summary

In summary, we discuss the observation of DM-DKS in an adiabatically tapered Si_3N_4 microring. The tuned GVD along the cavity length manifests itself in a Gaussian-like optical spectrum that has a more equalized pump-matching comb power than a $sech^2$ spectral shape, which is advantageous for applications such as astrospectrograph calibration and high-capacity coherent communication. Stretched-pulse operation with near-zero net cavity GVD is beneficial for reducing the timing jitter of frequency microcombs and advancing on-chip microwave photonics and precision metrology. We apply UTM metrology to observe and study the evolution dynamics of our dispersion-managed dissipative solitons. With this new approach, we portray the soliton transition dynamics and show that these dispersion-managed dissipative solitons exist in a stability zone that is an order-of-magnitude larger at a higher pump power than their static counterpart in traditional homogeneous oscillators and

sustain more pulse energy. The dispersion management demonstrated by the design of the waveguide geometry can be generalized and extended to other material systems, such silicon [76], high-refractive-index glass [77], aluminium nitride [78], AlGaAs [28] and lithium niobate [79], and unconventional spectral ranges, such as the ultraviolet [80] and mid-infrared ranges [81]; the same principle can also be applied to other types of microresonators by engineering whispering gallery mode cavity structures [82]. The dispersion-managed dissipative soliton microresonator provides a novel platform for understanding ultrafast dissipative cavity dynamics and offers a new path towards high-power frequency microcombs.

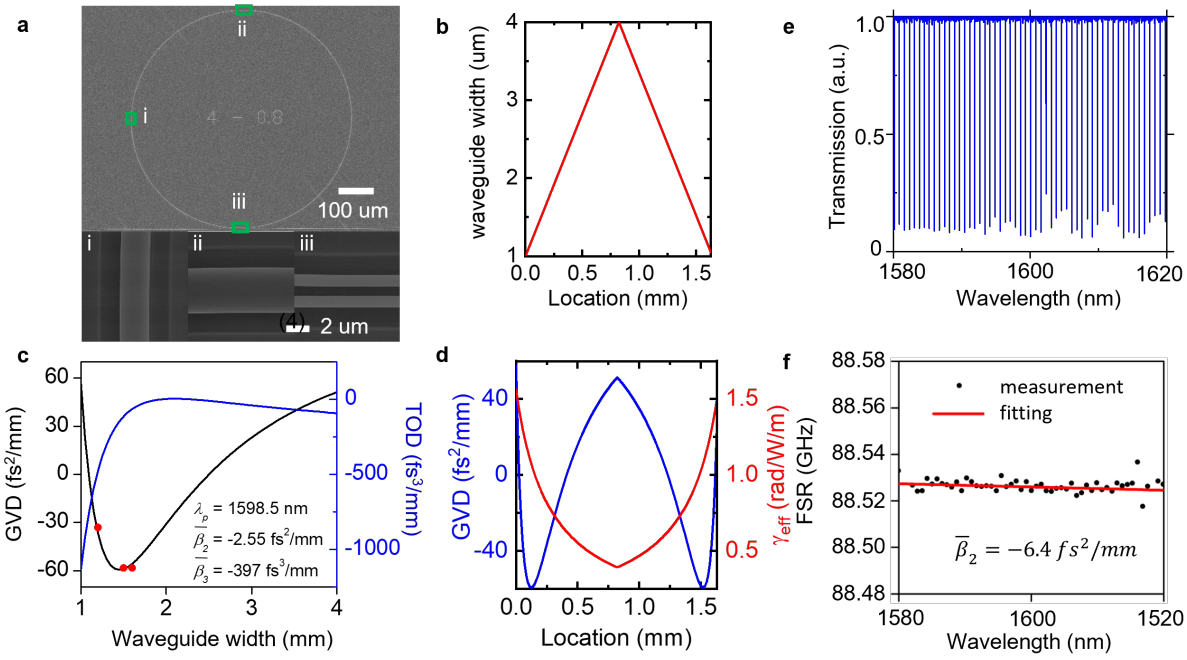

Figure 3.1: Characterization of an 88 GHz adiabatically tapered Si_3N_4 microring. a, SEM image of the dispersion-managed microring. The varying widths of the cavity waveguide provide an oscillating GVD and varying nonlinear coefficient. b, The waveguide width changes at different locations of the microring. c, COMSOL-modelled GVD and TOD of the Si_3N_4 waveguide with respect to the waveguide width, taking into consideration both the waveguide dimensions and the material dispersion. At the pump wavelength of 1598.5 nm, the path-averaged GVD and TOD are -2.6 fs^2/mm and -397 fs^3/mm, respectively. The red dots are the measured GVD for waveguides with widths of 1.2 μm, 1.5 μm, and 1.6 μm, showing good agreement with the simulation results. d, The GVD (blue curve) and nonlinear coefficient (red curve) at the pump wavelength (1598.5 nm) change at different locations of the microring. e, Cold cavity transmission of the tapered Si_3N_4 microring, measured with SWI. The existence of higher-order transverse modes is not observed across the wavelength region of interest. f, Wavelength dependence of the FSR, determining the residual non-equidistance of the modes, $D = (-\frac{\beta_2 \omega_{FSR}^2 c)}{2\pi n}$, of 54 ± 3 kHz. The extracted GVD is anomalous at -6.4±0.4 fs^2/mm, in good agreement with the simulation result.

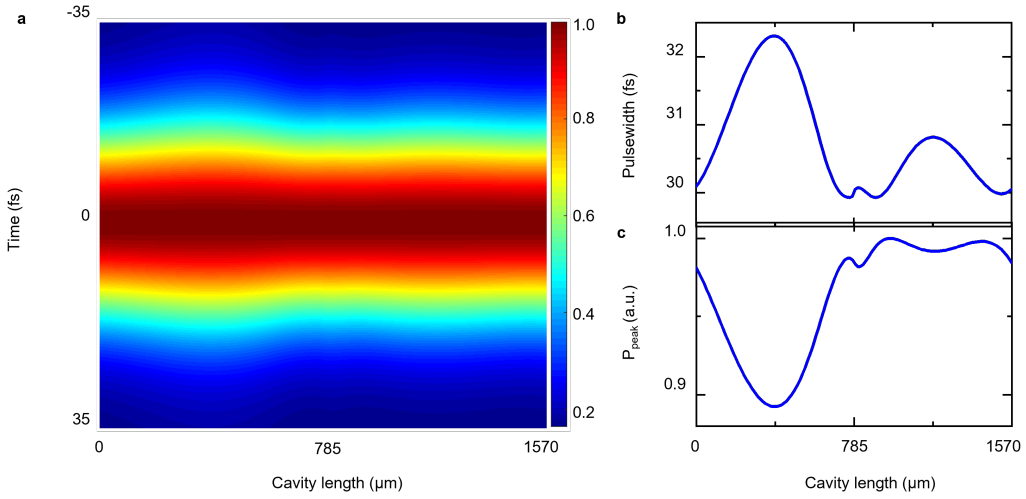

Figure 3.2: NLSE-modelled DM-DKS dynamics. a, 2D map of oscillating pulse width along cavity position due to dispersion management. The pulse width changes along the cavity length length. b, upper panel: The variation in the FWHM of the dispersion-managed dissipative soliton along the cavity length; lower panel: The variation in the peak power of the dispersion-managed dissipative soliton along the cavity length.

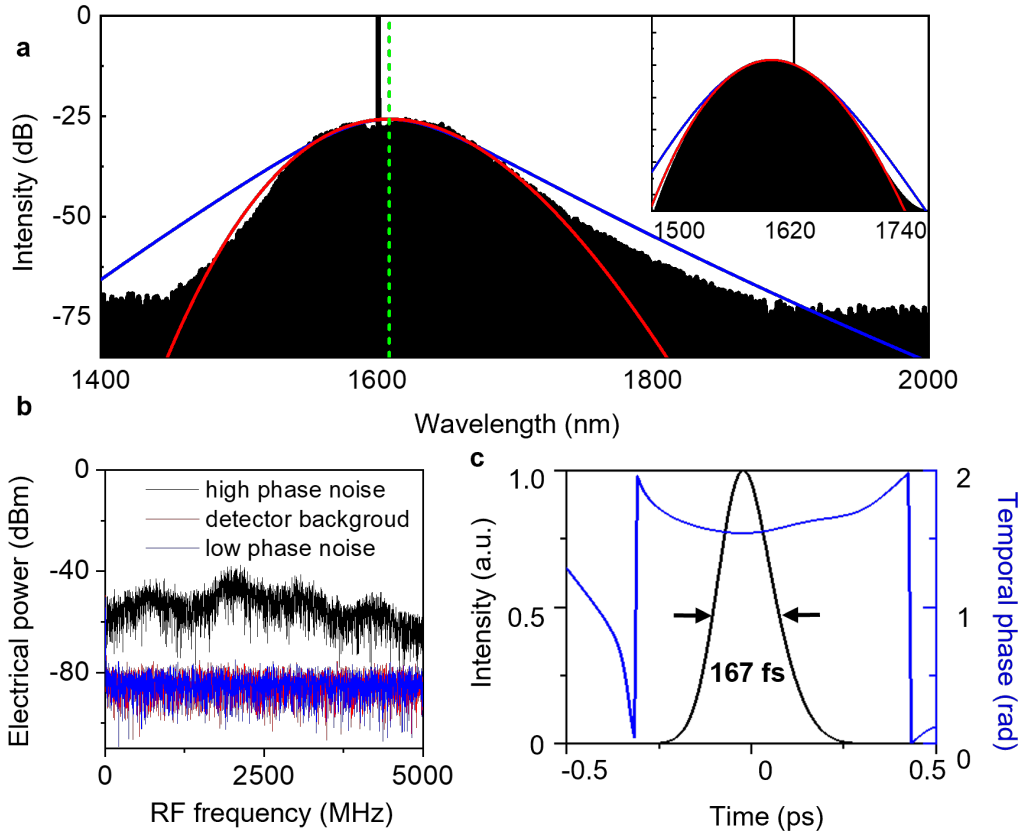

Figure 3.3: Experimental characterization of DM-DKS. a, Measured optical spectrum of the dispersion-managed dissipative soliton, which fits better to a Gaussian profile (red curve) than a sech^2 profile (blue curve). The 3 dB bandwidth of the measured spectrum is 4.78 THz, and the corresponding FWHM of the transformed-limited pulse is 92 fs. Inset: simulated comb spectrum, also showing a better match with a Gaussian profile than a sech^2 profile. b, RF amplitude noise of the Kerr frequency microcomb in different states, showing the transition into the low-phase noise state with amplitude noise reaching the detector background. The 5 GHz scan range is more than 50 times the cavity linewidth. c, Pulse shape (black line) and temporal phase (blue line) retrieved from the FROG measurement. The FWHM pulse duration is measured to be 167 fs.

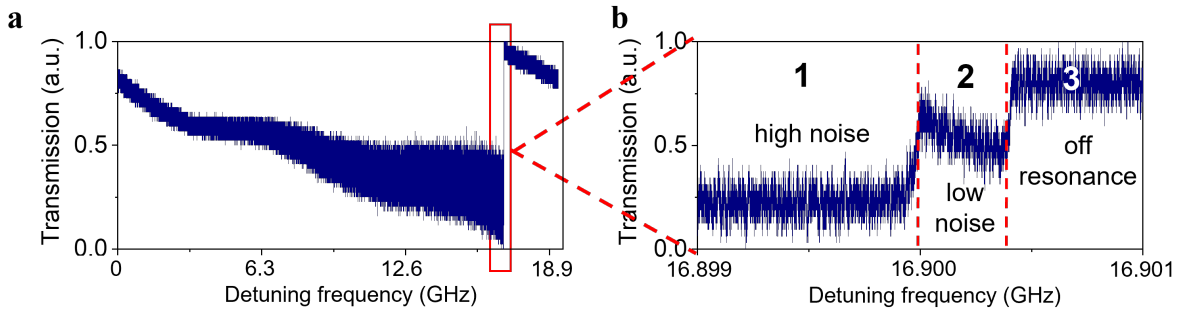

Figure 3.4: Pump power transmission at scanning speed of 2.1 THz/s. a,Total power transmission as the pump frequency is scanned across a cavity resonance at a speed of 2.1 THz/s for an on-chip pump power of 30 dBm. The step signature is characteristic of the low-phase noise soliton state (state 2). b, The dissipative Kerr soliton dynamics around these transmission steps are studied and portrayed with the UTM system.

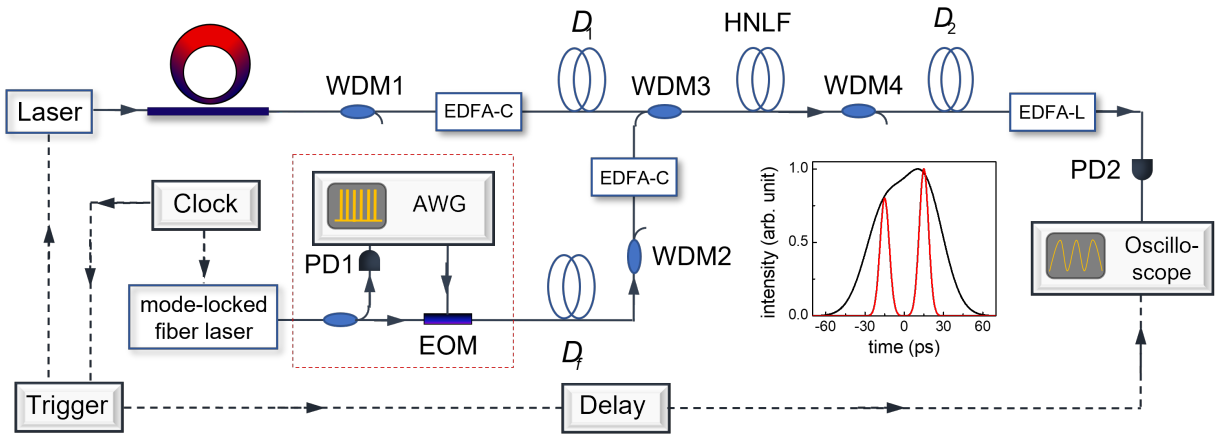

Figure 3.5: Schematic setup of the UTM system. Along the fast time axis, the temporal structure of the intracavity field is magnified and captured by a real-time oscilloscope. The temporal magnification and time resolution of the UTM system are 72× and 600 fs, respectively. Along the slow time axis, the evolution and transition dynamics are sampled optically with a stabilized femtosecond Mode-locked fiber laser. The frame rate of the UTM system is thus 250 MHz, limited by the repetition rate of the Mode-locked fiber laser. All of the electronics are commonly referenced to an Rb-disciplined crystal oscillator for accurate synchronization. Inset: two pulses separated by 30 ps, originally unresolved (black curve), are distinguishable via the UTM system. ECDL: external cavity diode laser. WDM: wavelength-division multiplexing. EDFA: erbium-doped fiber amplifier. AWG: arbitrary waveform generator. EOM: electro-optic modulator. PD: photodetector. D_1, D_2, and D_f are the dispersions for the UTMs (see A.1). To increase the SNR and reduce the aberration, the measurement frame rate is reduced to 25 MHz by picking 1 pulse out of 10 with an EOM driven by a synchronized AWG (red dashed box).

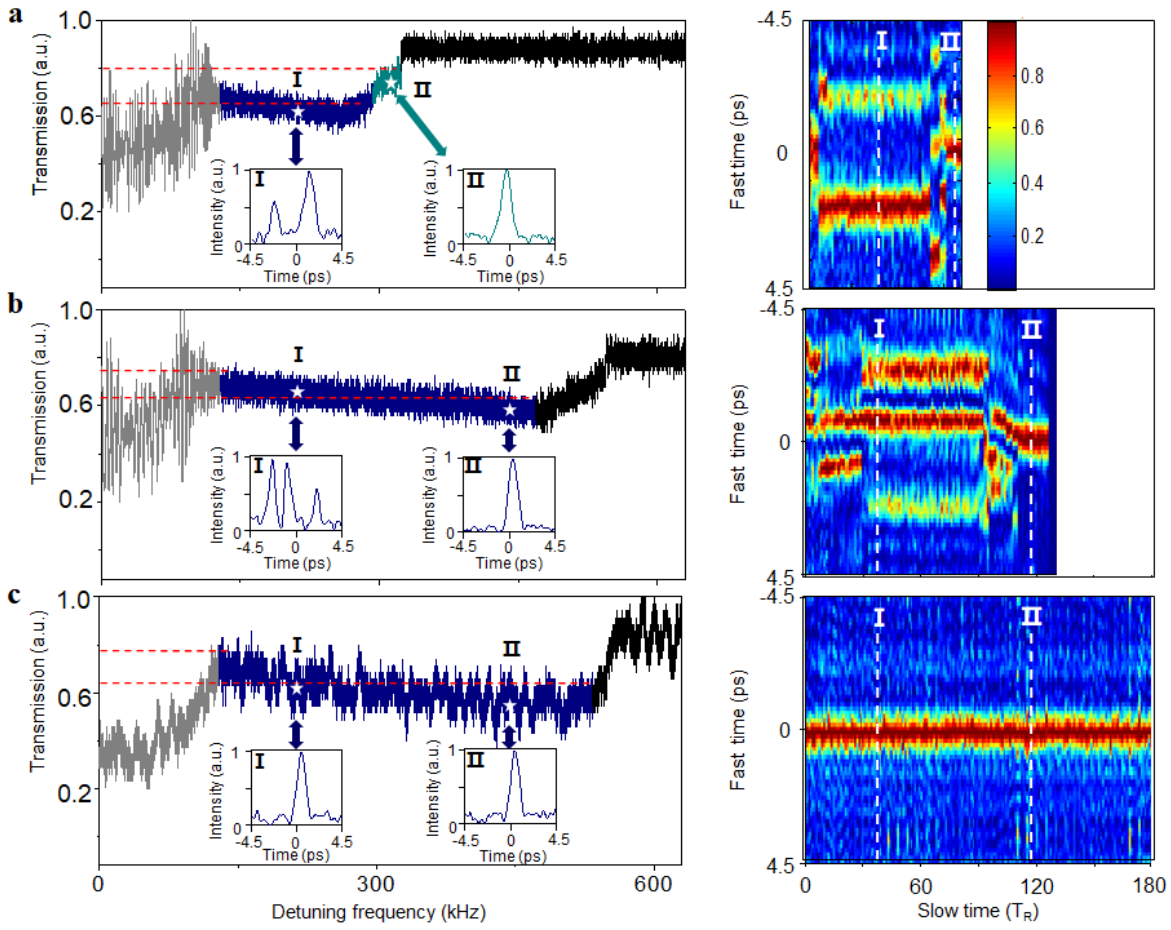

Figure 3.6: UTM-enabled comparison of the stability zone and temporal dynamics between static DS and DM-DKS. a, Total power transmission (left panel) and the 2D evolution portrait (right panel) of static DS formation in a homogeneous microring with a measured GVD of -33.1 fs^2/mm. A single soliton is only observed in the last transmission step and remains stable for the pump resonance detuning range of 30 kHz, where the cavity loading is reduced to 30%. The on-chip pump power is 30 dBm. b and c, Total power transmission (left panel) and the 2D evolution portrait (right panel) of DM-DKS in the tapered microring, showing increased stability zones at a higher pump power than static solitons. In panel b, the on-chip pump power is 30 dBm, and in panel c, the on-chip pump power increases to 32 dBm. At this pump power level, a low-noise stable soliton state is not observed in a homogeneous microresonator. Insets: measured pulse shapes at the pump resonance detuning denoted by the white dashed lines in the 2D mappings.

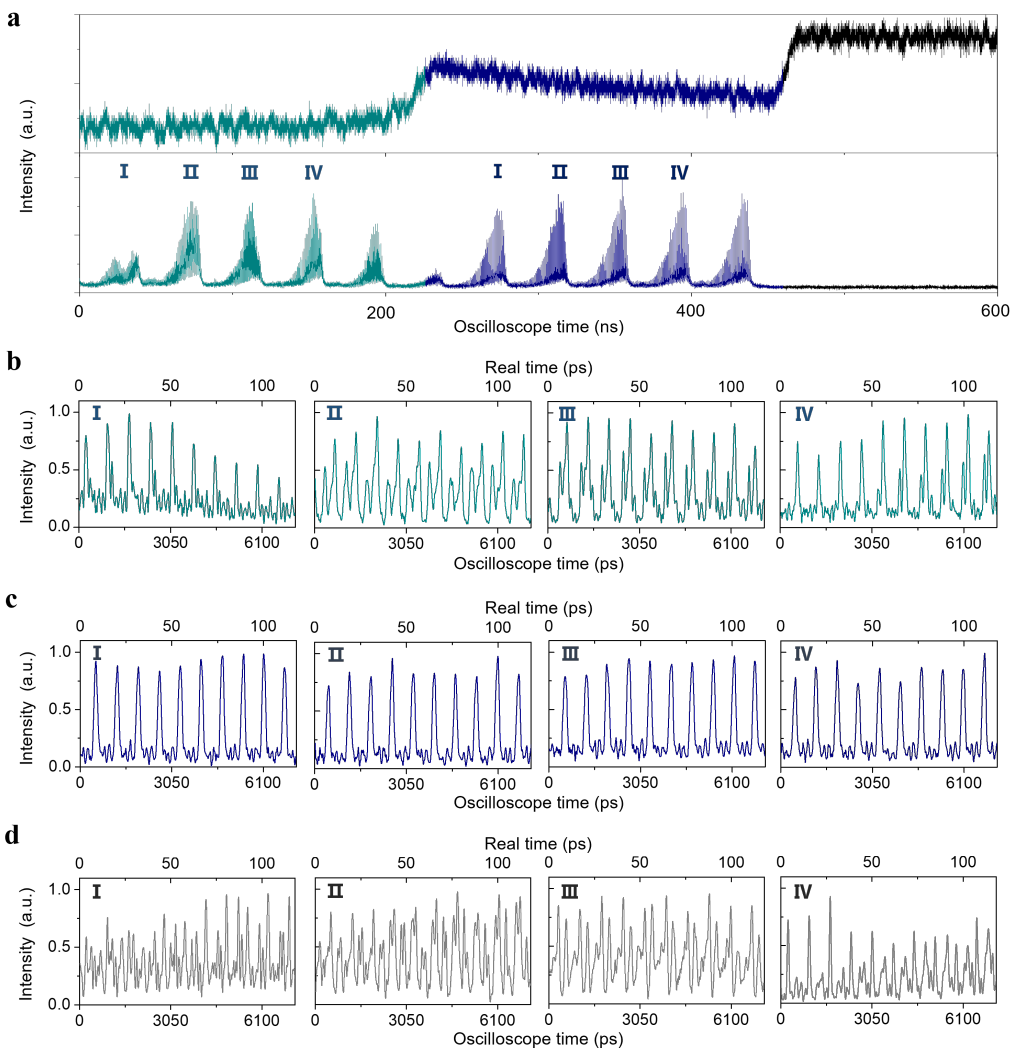

Figure 3.7: Transition dynamics of a DM-DKS. The on-chip pump power is 32 dBm, and the scan speed is 2.8 THz/s. a, Total power transmission (top panel) and magnified optical waveforms on the real-time oscilloscope (bottom panel). For the case where the singlet soliton state persists across the whole transmission step (c), the temporal pulse structure is still discernible before the transition despite intense and rapid soliton interaction dynamics (b). We note that real time is the oscilloscope time divided by MUTM. d, With the SNR-improved UTM, chaotic states could also be successfully recorded.

CHAPTER 4

Timing jitter investigation in 88 GHz dispersion-managed dissipative Kerr soliton via dual-pump scheme

4.1 Introduction

Laser frequency combs have impacted science and technology fields with their equidistant frequency spacings, serving as unique coherent microwave and optical clockworks [83, 84]. Recent emerging applications include, for example, optical clocks for space-borne networks [85, 86], precise laser ranging metrology for autonomous platforms [87] and low phase noise radio frequency generation [88, 89], all aided by low timing jitter mode-locked frequency combs. The observations of dissipative soliton microcombs in single microresonators [21, 16] or coupled-microresonators [90] with smooth spectral profiles and dispersive waves [20] offer opportunities to examine soliton comb dynamics in miniature platforms. There has been significant progress of soliton microcomb formation in different integrated microresonators such as Si_3N_4 [91], AlN [92], $LiNbO_3$ [93], and AlGaAs [94], benefiting from either ultra-high quality factors or large nonlinear coefficients. The recent demonstrations of electrically pumped turn-key soliton microcombs [95, 96, 97] and mode-locked microcombs [98] further reinforce the viability of the fully integrated frequency microcomb and pave the way for integrated functionalities such as terabit-per-second coherent transceivers [56, 99, 100], parallel coherent LiDAR [101], precision frequency metrology and control [13, 54], astrophysical spectrographs [102, 103], laser spectroscopy [104, 55, 105], distance ranging [36, 58, 57], low-noise

microwave generation [8, 106, 107], and convolutional processing networks [108, 109].

In soliton microcombs, the pump-resonance detuning noise [110] plays a critical role in the pump-to-repetition-rate noise transduction [111, 112, 113]. A low repetition rate phase noise (repetition rate timing jitter) regime exists at a detuning where soliton center frequency shift from dispersive-wave emission is balanced by nonlinear effects. The phase noise can be improved by injection locking pump laser to resonant cavities [98], pumping the microresonators with a narrow linewidth laser [114], optimizing high-order dispersion of the microresonators [115], and thermal stabilization with an auxiliary laser [116]. Quantum motion of the microresonators has also been observed recently through timing jitter characterization in counter-propagating soliton pairs after suppressing common-mode technical noise [117]. With close-to-zero net group velocity dispersion, dispersion-managed soliton microcombs have been theoretically and experimentally investigated in active resonators featuring shorter pulse width as well as better timing stability [35, 74, 70]. Therefore, the precise characterization of timing jitter in various microcombs is highly demanded. Direct photon-detection can characterize timing jitter when repetition rates are detectable, but it has limited timing jitter power spectral density (PSD) noise floor of $1 \times 10^{-6}\text{fs}^2/\text{Hz}$ at 1 MHz offset frequency [91]. It is sensitive to intensity-noise-to-phase-noise (IM-PM) conversion [118]. Linear fiber interferometry [107, 119] could provide a lower timing jitter PSD noise floor of $1 \times 10^{-9}\text{fs}^2/\text{Hz}$ which is free of the IM-PM conversion and shot noise limit.

Here we demonstrated a series of thermally intracavity-power-stabilized microcombs at different mode-locked states in 88 GHz dispersion-managed Si_3N_4 microresonators with negligible center frequency shift and broad frequency bandwidth. The demonstrated dispersion-managed (DM) microcombs not only expand the scope of soliton dynamics [21, 16, 20, 90], but also enable low-jitter soliton trains. Subsequently, we determine the intensity, timing and optical frequency fluctuations of the soliton microcombs at the single-soliton, multiple soliton, and soliton crystal states [120, 52]. Since the microcomb oscillators have high repetition rates, low pulse energy, and high pulse background, we present a linear interferometry

approach with tens of zeptosecond/$\text{Hz}^{\frac{1}{2}}$ timing jitter resolution to characterize its jitter. We note that the approach in [107, 119] is reference-free and independent of the repetition rate, expanding from prior silica microcomb [107] and fiber comb studies [119] to the 88 GHz pulse train timing jitter measurements of the silicon nitride DM-DKSs. The measurement of the fundamental timing jitter is based on: (1) time delay for the frequency discrimination and (2) optical carrier interference for the optical phase discrimination. We observe a relative intensity noise (RIN) of -153.2 dB/Hz at 100 kHz offset, with a corresponding integrated RIN of 0.034% from 100 Hz to 10 MHz for the single-soliton microcomb. The measured near-instantaneous linewidth of individual comb lines is 2.3 kHz. For the single-soliton microcomb, the quantum-noise-limited timing jitter PSD is determined as 0.4 as^2/Hz for 100 kHz offset, with an integrated jitter of 1.7 $\pm$ 0.07 fs from 10 kHz to 1 MHz. These measurement observations of the femtosecond-level jitter in chip-scale frequency microcombs advances a fundamental research platform towards chip-based optical-microwave clockwork, distributed timing standards, and precision metrology.

4.2 DM-DKS generation in a 89 GHz tapered microresonator via dual-pump scheme

The device design of the 89 GHz Si_3N_4 microresonator is similar to the one in chapter 3, however, due to fabrication imperfection, the exact GVD is different. The fundamental TE mode features a small anomalous path averaged GVD of -3.51 fs^2/mm at a pump wavelength of 1602 nm, simulated through COMSOL. The cavity GVD is experimentally characterized by the SWI with only two avoided mode-crossings across the entire wavelength range, shown in Figure 4.1. The measured free spectral range and GVD are $\approx$ 89 GHz and -4.39 fs^2/mm, respectively. The measured loaded and intrinsic quality factors are 1.8×10^6 and 3.4×10^6, respectively.

DM-DKSs are then generated in this microresonator via a dual driven scheme, which will

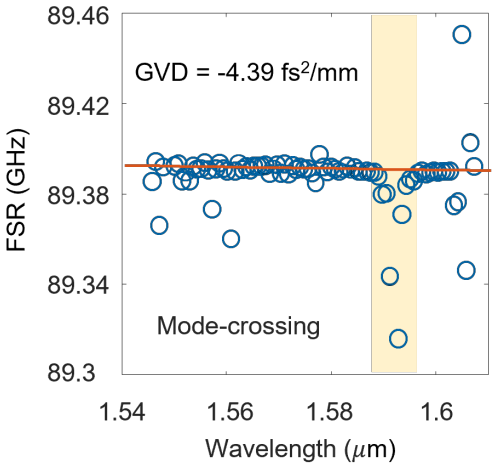

Figure 4.1: Measured GVD of the 89 GHz tapered microresonator. The measured GVD via SWI is $\beta_2 = -4.39 \text{fs}^2/\text{mm}$.

be further discussion in chapter 5. Figure 4.2a illustrates the optical spectrum of the single-soliton DM-DKS overlapped with the LLE modeled spectral profile. Modest spectral dips are observed resulting from two hybridized inter-polarization mode couplings at 1592.64 nm and 1659.72 nm are observed. The 1563.64 nm peak is the auxiliary pump laser. To illustrate the temporal performance of the microcomb, we measured the intensity A.C. trace with a non-collinear second-harmonic autocorrelator after pump suppression with a bandpass filter. Figure 4.2b shows the measured pulse width of the single-soliton at $\approx$ 305 fs for the filtered optical spectrum (autocorrelation trace background originating from the continuous-wave pump laser), along with the $\approx$ 11.2 ps pulse train. The modeled pulse width is included in the inset of Figure 4.2b. We also observed double-soliton and soliton crystal states in the microresonator. The corresponding measured optical spectra of the double-soliton and one defect soliton crystal are illustrated in Figure 4.2c and 4.2e overlapped by the LLE modeled spectral profiles, respectively. The soliton crystal optical spectrum indicates destructive interference between a single-soliton microcomb and a 12-FSR perfect soliton crystal microcomb. The spatiotemporal LLE modeled intracavity waveforms are depicted in Figure 4.2d and 4.2f where the soliton defect in the time domain is presented. The demonstrated

microcombs offer broader optical spectra consistent with the simulated results over multiple soliton types with near-single-mode operation with only two avoided mode crossings and negligible center frequency shift [121].

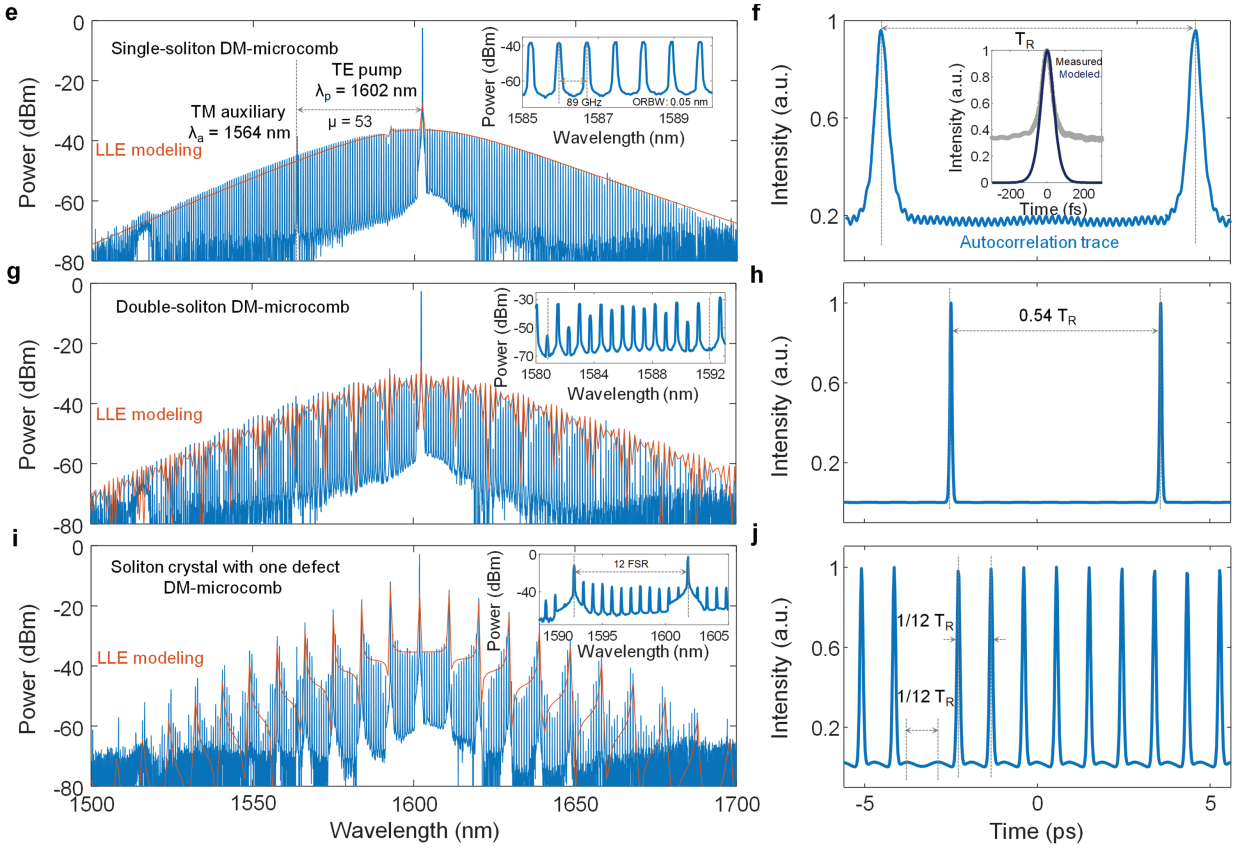

Figure 4.2: Examples of DM-DKS. a, c, and e, Measured optical spectra of the single-soliton, double-soliton and soliton crystal with one defect overlapped with the LLE model showing negligible center frequency shifts. Insets are zoomed optical spectra. b, Measured intensity A.C. trace of the single-soliton state. Inset is the measured and modeled pulse width. d and f, Modeled intracavity waveforms of double-soliton and soliton crystal states with a temporal separation of $0.54\mathrm{T_R}$ and $\frac{1}{12}\mathrm{T_R}$, respectively.

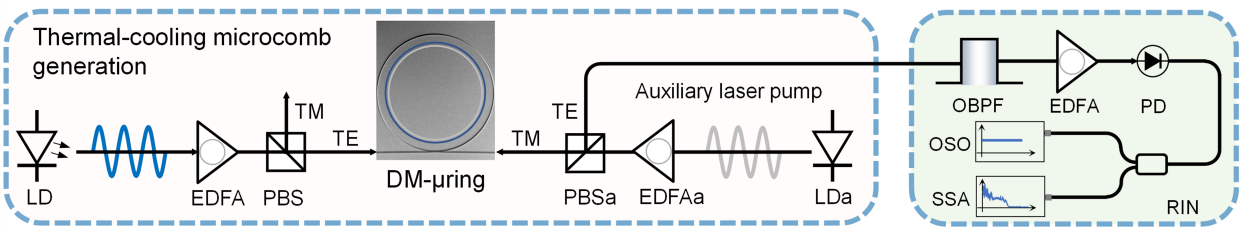

Figure 4.3: Experimental setup of the TE-TM dual-driven approach for the generation of thermally stabilized soliton microcomb and the relative intensity noise measurement. LD: laser diode; EDFA: erbium-doped fiber amplifier; PBS: polarization beam splitter; TE: transverse-electric; TM: transverse-magnetic, OBPF: optical bandpass filter; PD: photodiode; OSO: oscilloscope; SSA: signal source analyzer.

4.3 Relative intensity noise measurement

To obtain the DM-microcombs reliably and deterministically, Figure 4.3 illustrates the implemented TE-TM dual-driven pump approach (discussed in chapter 5). The forward-propagating pump laser is amplified and polarized into the transverse-electric (TE) polarization while the backward-propagating transverse-magnetic (TM) polarized auxiliary laser thermally stabilizes the microresonator intracavity total power. We generate the microcombs in a planar tapered dispersion-managed Si_3N_4 microresonator at the effective red-detuned regime of the pump resonance ν_0 through this dual-driven scheme based on dynamic photothermal stabilization. The orthogonal-polarized auxiliary laser is launched into the blue-detuned regime from the resonant mode ν_{53} in the counterpropagating direction to mitigate thermal transients during the microcomb transition from a high-noise chaotic state to a low-noise mode-locked state and thermally stabilize the pump-resonance detuning. The TM-polarized auxiliary laser experiences normal GVD avoiding the initiation of parametric oscillation [8]. The auxiliary laser is used to stabilize the microresonator intracavity power by optimizing the auxiliary laser power and phase detuning [116]. To quantify the soliton microcomb noise performance, we conduct intensity noise and comb line linewidth measurements at the different soliton microcomb states prior to the respective timing jit-

ter measurements. Coherence of the soliton frequency microcomb is examined via the RF intensity noise spectra over a microwave frequency span that is a few times of cold cavity resonance linewidth. While this distinguishes between the high and low noise comb states, it does not identify noise types nor sources.

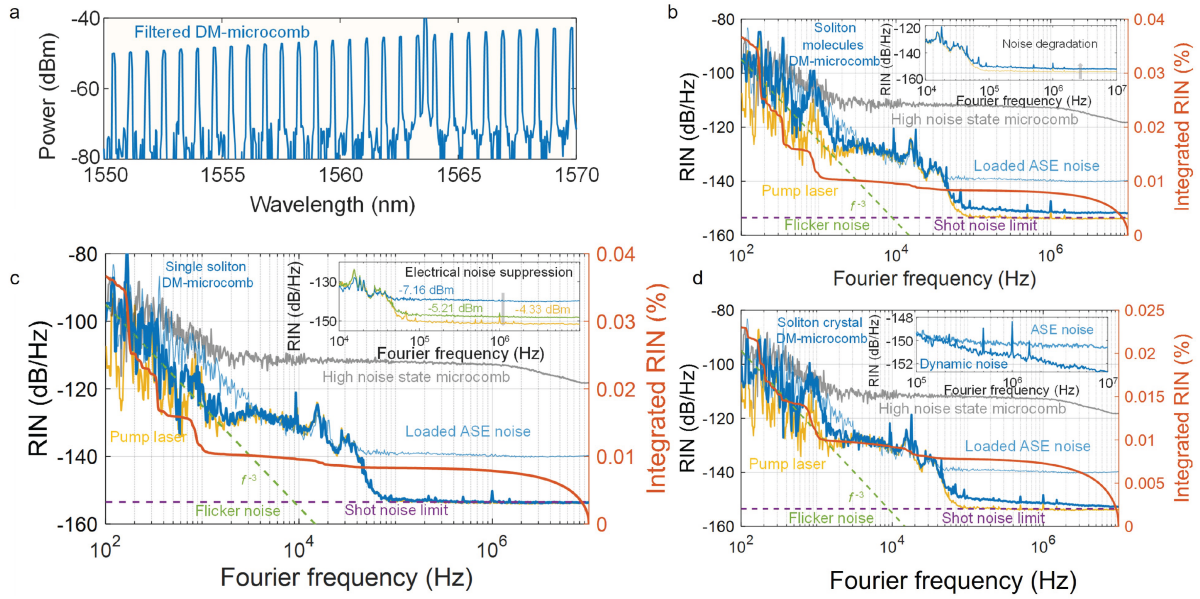

Figure 4.4: RIN measurements of different DM-DKS states. a, Filtered optical spectrum of the single-soliton DM microcomb. b, c, and d, Relative intensity noise power spectral density (PSD) and the corresponding integrated RIN of the microcombs at the different dynamical states along with the lower bound set by the pump laser. The RIN PSD of the chaotic DM-microcomb and the RIN PSD after loading broadband ASE noise are also illustrated. Inset of b: Electrical noise optimization by adjusting the incident optical power of the PD to explore the dynamic soliton intensity fluctuations at the different states. Inset of c: Noise degradation of the double-soliton DM-microcomb showing additional white high-frequency noise. Inset of d: Noise degradation of the soliton crystal DM-microcomb showing dynamic high-frequency noise.

To supplement the RF intensity noise measurements of the soliton microcombs, measurement of the relative intensity noise (RIN) is performed next. The filtered microcomb with pump mode removed is measured by a photodetector (Thorlabs PDA10CF) with optical

power of 210 μW. A multimeter and an oscilloscope are utilized to monitor the DC voltage (V_0). Then a signal source analyzer (Keysight E5052B) records the voltage fluctuation PSD $S_{\Delta I}(f)$. The filtered optical spectrum is shown as in Figure 4.4a. The measured RIN PSD [$S_{RIN}(f)$] of the 89 GHz mode-locked microcombs, calculated by normalizing the measured intensity fluctuation PSD [$S_{\Delta I}(f)$ in units of V^2/Hz] by the average detected intensity $|V_0|^2$, is shown in Figure 4.4b to 4.4d corresponding to the single-soliton, double-soliton, and one defect soliton-crystal microcombs. The black curves in Figure 4.4b to 4.4d are the RIN PSD of the spatiotemporal chaotic state [122] and the pump laser, indicating the upper and lower bounds of the soliton microcomb RIN PSD. The soliton microcomb RIN PSD drops with a 30-dB/decade slope ($1/f^3$) over the first offset frequency decade while the CW pump laser RIN PSD falls with a 20-dB/decade slope ($1/f^2$). The pump laser RIN PSD is measured at a non-resonant wavelength after the microresonator. The discrepancy between the two slopes is attributed to environmental noise sources such as free-space-to-chip coupling fluctuations. For the single-soliton state, the measured RIN is -153.2 dB/Hz at 100 kHz offset with a corresponding integrated RIN of 0.034% when integrated from 100 Hz to 10 MHz with the relation $RIN_{in} = \int_{f_1}^{f_2} S_{RIN}(f)df$, where f_1 and f_2 are the lower and upper offset frequency bounds. The measured RIN of the double-soliton state and the soliton crystal state are -149.8 dB/Hz and -148.6 dB/Hz respectively for a 100 kHz offset. The corresponding integrated RIN are 0.036% and 0.023% over the same integrated frequency range. The inset of Figure 4.4b shows the electrical noise suppression to facilitate the observation of the dynamical intensity noise of the microcombs by optimizing the incident power of the photodetector from -7.16 to -4.33 dBm. The insets of Figure 4.4c and 4.4d show the noise degradation of the double-soliton and soliton crystal microcombs which results from the conversion of phase fluctuations to intensity fluctuations in the intracavity spectral interference process.

4.4 Interferometric coherence envelope measurements of soliton microcomb instantaneous linewidths

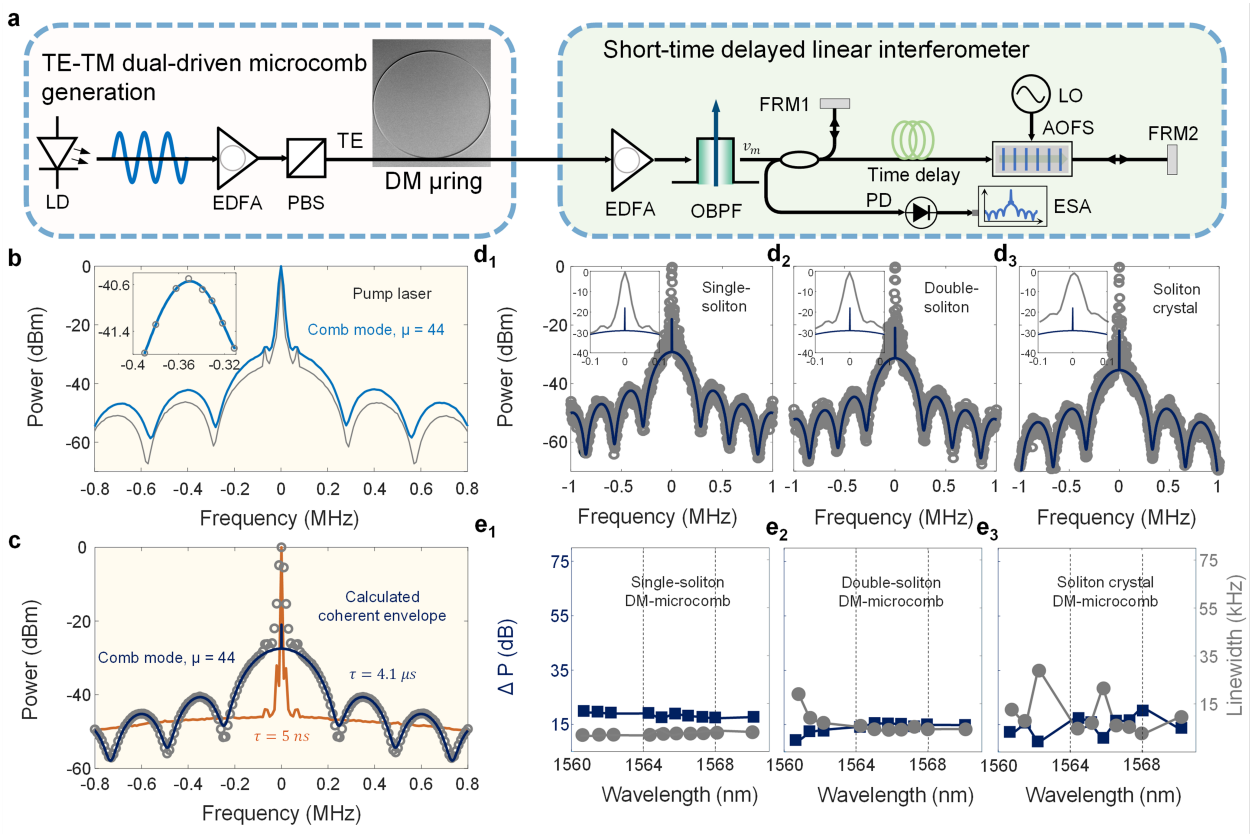

Figure 4.5: Near-instantaneous linewidth measurement of the DM-DKS. a, Experimental setup of the SDLI. FRM: Faraday rotator mirror, AOFS: acoustic optical frequency shifter, LO: local oscillator, ESA: electrical spectrum analyzer. b, Measured interferometric coherence envelope (ICE) of the pump laser and mode ν_{44}. Inset: peak detection. c, Measured ICE with different time delays to show spectral resolution and power dynamic range of the SDLI. d_1 to d_3, Measured ICE of one comb line of the single-soliton, double-soliton and soliton crystal states, respectively, with Linewidth distributions of the different comb lines from 1560 nm to 1570 nm in e_1 to e_3.

To further elucidate the noise characteristics of the soliton microcombs, here we investigate instantaneous linewidths of the generated individual comb teeth and soliton microcomb linewidth distributions. We built a short-time delayed linear interferometer (SDLI) based on

Michelson interferometry with heterodyne detection as shown in Figure 4.5a. This approach converts the frequency fluctuation $\Delta\mu_m = \Delta(f_p + mf_R) = \Delta f_p(1 + m \times \Delta f_R/\Delta f_p)$ of the microcomb lines into the second-peak and second-trough (SPST) power contrast difference (ΔP) of the coherent interference pattern in the SDLI which can be expressed as [123]:

$$\begin{aligned}\Delta P &= 10\log_{10} P_{peak} - 10\log_{10} P_{trough} \\ &= 10\log_{10}\frac{\left[1+\left(\frac{2}{n_0\Delta\nu\tau}\right)^2\right]\left[1+\exp\left(-2\pi n_0\Delta\nu\tau\right)\right]}{\left[1+\left(\frac{3}{2n_0\Delta\nu\tau}\right)^2\right]\left[1-\exp\left(-2\pi n_0\Delta\nu\tau\right)\right]}\end{aligned} \tag{4.1}$$

where τ is the delay time, n_0 is the fiber refractive index, and $\Delta\nu$ is the comb mode linewidth. The power spectrum of the SDLI is the product of the Lorentzian spectrum and the periodic modulation power spectrum. Figure 4.5b shows the measured interferometric coherence envelope power spectrum of the pump laser and one of comb lines with mode number $\mu = 44$ away from the pump. Polynomial curve fitting is used to detect the peaks and troughs of the interference envelope. Figure 4.5c shows the measured and calculated interferometric envelopes at different time delays to evaluate the spectral resolution and power dynamic range. The measured linewidth of the pump laser is 1.5 kHz when the time delay is 3.55 μs. The measured interferometric envelopes of the single-soliton, double-soliton, and soliton crystal states are presented in Figure 4.5d_1 to 3d_3 overlapped with the calculated envelopes at the same time delay showing the microcomb linewidths of 2.3 kHz, 3.0 kHz and 2.4 kHz, respectively. Next, we study the linewidth distribution of microcomb lines over the C-band from 1560 nm to 1570 nm to examine linewidth multiplication away from the pump in soliton frequency microcombs. Figure 4.5e shows the linewidth distribution for the different microcomb dynamical states with pump centered at $\approx$ 1602 nm and in the range of $\approx$ 10 nm. A slight increase in linewidth further away from the pump towards shorter wavelengths is observed in Figure 4.5e_2 due to the decrease in the comb line optical power from double-pulse spectral interference. The linewidth distribution is related to the unbounded timing jitter of the microcombs. In the soliton crystal state, the linewidth distribution has a larger

fluctuation which arises from the structured optical spectrum as shown in Figure 4.2e, due to the signal-to-noise ratio dependence of the measurement.

4.5 Self-heterodyne linear interferometry (SHLI) for soliton microcomb femtosecond jitter metrology

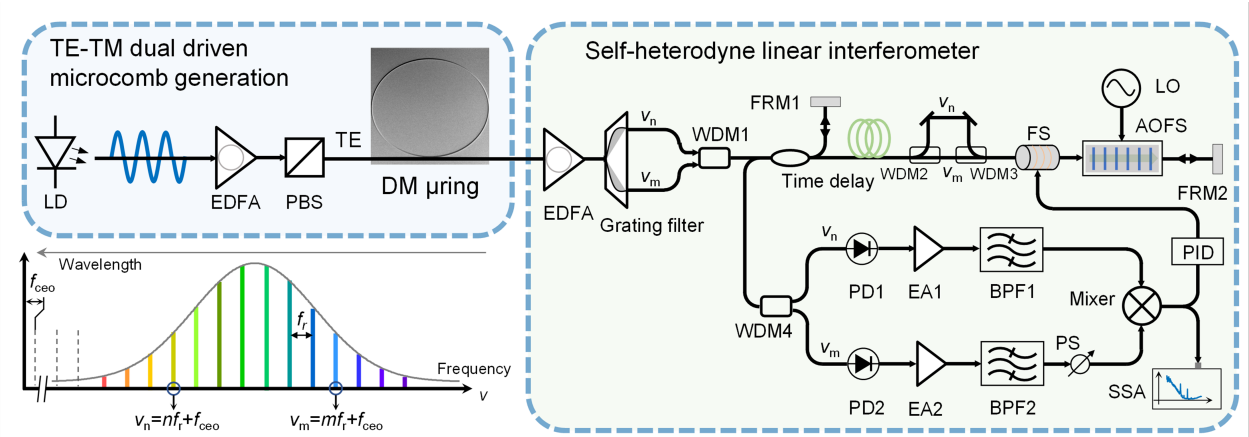

Figure 4.6: Schematic setup of the self-heterodyne linear interferometer (SHLI). WDM: wavelength division multiplexer; FS: fiber stretcher; EA: electronic amplifier; BPF: bandpass filter, PS: phase shifter; PID: proportional-integral-differential controller. Inset: schematic illustration of the self-heterodyne linear interferometry.

We next examine the timing jitter via a self-heterodyne linear interferometer (SHLI). Figure 4.6 illustrates the implemented SHLI architecture for precision timing jitter metrology. The interferometer consists of a reference arm and a time-delayed arm in which a fiber-coupled acousto-optic modulator (AOM) driven by a RF signal f_m allows heterodyne detection of phase fluctuation power spectral density (PSD, $S_\varphi[\mathrm{dBrad}^2/\mathrm{Hz}]$). A diffractive grating-based narrowband filter pair selects two microcomb lines at frequencies $\nu_n = n \times f_R + f_{CEO}$ and $\nu_m = m \times f_R + f_{CEO}$ as illustrated in the inset of Figure 4.6 separated by a $(m-n) \times f_R$ frequency difference, where f_R is the repetition rate and f_{CEO} is the carrier envelope offset frequency of the microcombs. Frequency noise $\Delta\nu(f)$ of the selected lines is subsequently

discriminated with delay time τ by the relation $\Delta\varphi(f) = 2\pi\Delta\nu(f)\tau$. The optical phase fluctuations $\Delta\varphi(f)$ are converted into optical intensity fluctuations by linear optical interferometry. At the fiber interferometer output, the two optical lines are demodulated by two photodetectors. The residual phase noise PSD originates from the frequency difference $(m-n) \times f_R$ of the two selected comb lines, proportional to delay time τ. Then, a double-balanced mixer is used to extract the timing jitter PSD and eliminate the common-mode noise induced by the carrier envelope offset signal and the driven microwave frequency signal (f_m). The frequency fluctuations of the two selected optical comb lines are converted into voltage fluctuations with the transfer function $\Delta\nu(f) \propto K_\varphi \frac{|1-\exp(-i2\pi f\tau)|}{|i\times f|}(m-n)\Delta f_R(f)$, where K_φ is the peak voltage at the double-balanced mixer output. The transfer function shows that the measured voltage fluctuation is proportional to $\frac{|1-\exp(-i2\pi f\tau)|}{|i\times f|}$, which implies there will be null points at the offset frequency $f = 1/\tau$ and its harmonics, providing the upper Fourier frequency limit of the timing jitter measurement.

The measured voltage fluctuation PSD is subsequently converted into frequency noise PSD and further into timing jitter PSD $S_{\Delta T_R}(f)$ with the relation

$$S_{\Delta T_R}(f) = \left(\frac{1}{2\pi f_R}\right)^2 \frac{1}{(m-n)^2}\frac{1}{f^2}\left(\frac{|i\times f|}{K_\varphi|1-\exp(-i2\pi f\tau)|}\right)^2$$

The detected voltage fluctuation at the mixer output is separated into two parts. The first part synchronizes the fiber interferometer to the frequency microcombs, avoiding free walk via a piezoelectric-transduced fiber stretcher (FS) through a loop filter with 1 kHz bandwidth. The second part is recorded by a signal source analyzer which gives the timing fluctuation PSD and the frequency fluctuation PSD of the soliton microcomb repetition rate. To precisely remove the common-mode noise resulting from dispersion and increase the interferometer signal-to-noise ratio, we utilize a delay control unit (DCU) which contains a motorized fiber delay line (MDL) and a pair of wavelength-division multiplexed (WDM) couplers. This timing-stabilized and dispersion-compensated fiber interferometer can be considered as a true time delay, which is an optical counterpart of the delay-line frequency discriminator in microwave metrology.

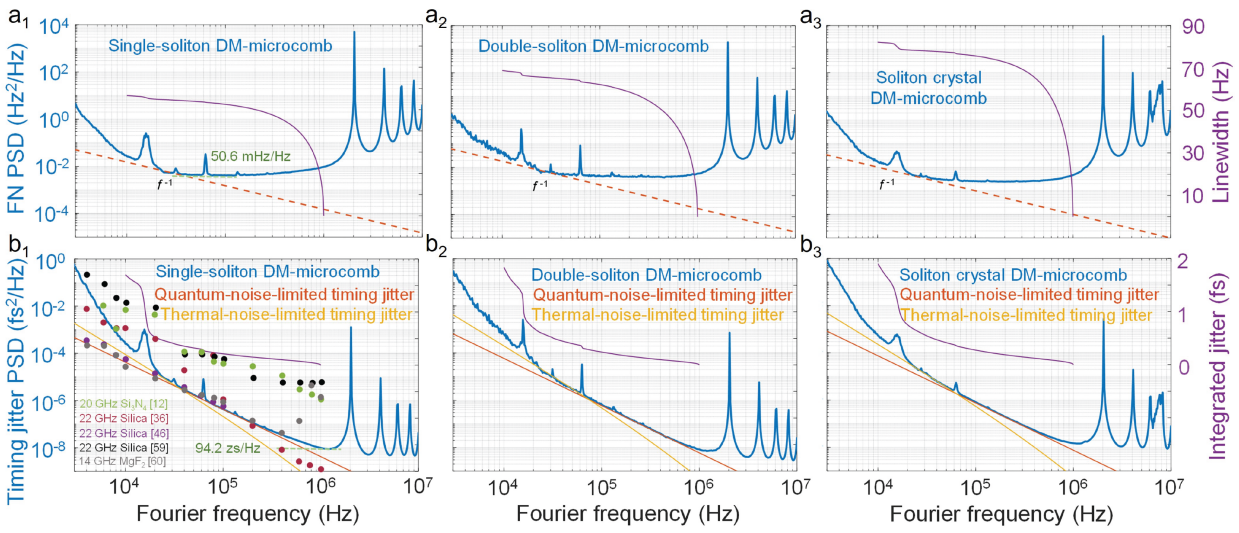

Figure 4.7: Repetition rate frequency noise and timing jitter measurement. a_1 to a_3, Measured frequency noise PSD at different soliton states with a 49-m stabilized fiber link. The orange dashed lines with 10 dB/decade slopes indicate repetition rate frequency free-walk induced by microresonator intracavity power fluctuations. The corresponding repetition rate tone linewidth integrated from 1 MHz to 10 kHz is denoted with purple curves. b_1 to b_3, Timing jitter PSD measurement of the soliton microcombs at different dynamical states with the calculated thermal noise and quantum noise limits. The corresponding integrated timing jitter is included.

We convert the measured voltage fluctuation PSD on the baseband into the repetition rate frequency noise $S_{\Delta f_R}(f)$ PSD to examine the frequency noise behavior as shown in Figure 4.7a_1 to a_3, and 4b3 of the soliton microcomb at the single-soliton, double-soliton, and soliton crystal states, respectively. The measured repetition rate frequency noise PSD are 2,556 mHz^2/Hz, 4,151 mHz^2/Hz and 4,168 mHz^2/Hz respectively at 100 kHz offset with a noise frequency resolution of 64 $mHz/Hz^{1/2}$ at the single-soliton microcomb. We observe that the repetition rate frequency noise features a 20-dB/decade slope below $\approx$ 20 kHz offset, indicating the repetition rate random walk frequency noise. Based on the noise power-law, soliton microcombs have a repetition rate flicker frequency walk from $\approx$ 20 kHz to 40 kHz offset, a white frequency noise from $\approx$ 40 kHz to 200 kHz offset, and a flicker and white phase

noise from ≈ 200 kHz to 1 MHz. The resulting integrated linewidths of the free-running repetition rate tone are shown in Figure 4.7a for the three microcomb dynamical states.

Figure 4.7b_1 to b_3 show the measured timing jitter PSD for the different soliton dynamical states. For the single-soliton comb, the measured quantum-noise-limited timing jitter PSD is 0.4 as^2/Hz at 100 kHz offset. The corresponding integrated timing jitter is 1.7 ± 0.07 fs when integrated from 10 kHz to 1 MHz as shown in the Figure 4.7b_1 which is close to the timing jitter in silica microresonator frequency microcombs measured with similar technology [107]. The integrated timing jitter from 10 kHz to 44.5 GHz Nyquist is ≈ 32.3 fs. The achieved femtosecond-level jitter is enabled by close-to-zero intracavity dispersion to minimize group delay fluctuations, suppressed Kerr nonlinearities within the tapered waveguide [47], and the thermally stabilized dual-driven approach. Our dispersion-managed microresonator stretches the soliton pulse within the cavity, effectively reducing the accumulated nonlinear phase shift during pulse propagation. The quantum-noise-limited timing jitter PSD of the two (double-soliton and soliton crystal) states at 100 kHz offset are at 0.66 as^2/Hz and 0.82 as^2/Hz, respectively. This corresponds to an integrated jitter of 1.9 ± 0.06 fs and 1.8 ± 0.09 fs. The dynamical noise is observed in the timing jitter PSD of the soliton crystal microcomb at the offset frequency around 8 MHz. Compared to direct photon detection for timing jitter PSD measurements [91], the SHLI method can effectively avoid the intensity-noise-to-phase-noise (IM-PM) conversion and shot-noise limit. The measured timing jitter PSD compares to prior works [91, 107, 117, 19, 124] as shown in Figure 4.7b_1.

For each of the microcomb soliton states, we observe that the timing jitter PSD drops with a 40-dB/decade slope within 3 to 20 kHz as shown in Figure 4.7b. Deviation of timing jitter PSD over low Fourier frequency is associated with intracavity power fluctuation leading to a $1/f^4$ slope with the relation $S^{T_R}_{\Delta T_R}(f) = \left(\frac{1}{2\pi f T_R}\right)^2 S_{T_R}(f)$ where intracavity power-induced round-trip fluctuations $S_{T_R} \propto f^{-2}$.

Figure 4.7b also includes theoretical cavity thermal bounds on the timing jitter PSD with yellow solid lines limiting the measured timing jitter PSD from 20 kHz to 40 kHz with a 25-

dB/decade slope ($1/f^2.5$), arising from thermorefractive variation. In the DM microresonator, the thermal-noise limited timing jitter PSD, originating from the thermodynamic fluctuations $\langle \delta T^2 \rangle = k_B T^2/CV\rho$, where V is the optical mode volume, k_B is the Boltzmann constant, T is the chip temperature, ρ is density, and C is specific heat capacity, is described with the model [125]:

$$S_{\Delta T_R}(f) = \frac{1}{(2\pi f_R)^2}\left(\frac{\nu_c}{n_0 f_R}\frac{dn}{dT}\right)^2 \frac{1}{f^2}\frac{k_B T^2}{\sqrt{2\pi^4 \varkappa \rho C f}}\frac{1}{R\sqrt{d_r^2 - d_z^2}}\frac{1}{\left[1+(2\pi f \tau_d)^{3/4}\right]^2} \tag{4.2}$$

where dn/dT is the thermorefractive coefficient, $\varkappa$ is the thermal coonductivity, R is the microresonator ring radius, $d_{r(z)} = \int d_{r(z)} dL/L_{cavity}$ is the half-width of the fundamental mode along the tapered DM microresonator, and $\tau_d = \frac{\pi^{1/3}}{4^{1/3}}\frac{\rho C}{\varkappa} d_r^2$. From 40 kHz to 600 kHz, the measured PSD falls with a quantum-noise limited 20-dB/decade slope($1/f^2$). The theoretical quantum-noise timing jitter limit without shot-noise shown in Figure 4.7b with orange solid lines follows the model [74]:

$$S_{\Delta T_R}(f) = \frac{1}{4\pi\sqrt{2} f_R^2}\sqrt{\frac{\gamma}{\Delta_0 D}}\frac{g}{\gamma^2}\left[\frac{1}{96}\frac{\gamma D}{\delta_0}\frac{\gamma^2}{f^2} + \frac{1}{24}\left(1+\frac{\pi^2 f^2}{\gamma^2}\right)^{-1}\frac{\gamma^2}{f^2}\frac{\Delta_0 D}{\gamma}\right] \tag{4.3}$$

where gamma is the half linewidth half height of the cavity resonance, $g = \frac{n_2}{n_0}\frac{\hbar\omega_c^2 c}{V n_0}$ is the nonlinear gain coefficient, $n_0(n_2)$ is the refractive index (nonlinear index) of the nitride resonator, $\omega_c = 2\pi\nu_c$ center angular frequency of the microcombs, c is the light speed in vacuum, $D = -\frac{\beta_2 \omega_R^2 c}{\gamma n_0}$ is the normalized dispersion and $\Delta_0 = \omega_0 - \omega_P$ is the resonance-pump detuning. Above 600 kHz, the measured PSD is limited to 8905 zs^2/Hz by the SHLI spectral resolution.

Based on soliton theory, the quantum-noise-limited timing jitter PSD model, especially in the high offset frequency more than 10 kHz, can analytically predict noise behaviors for different mode-locked states via the relation $S_{\Delta T_R}(f) \approx 0.5294\frac{\zeta}{(2\pi f)^2}\frac{h\nu}{E_p}\frac{\alpha_{tot}}{T_R}\tau_p^2$ [126], where $E_p \approx \frac{4\pi h \vartheta \nu_c}{D_1 \gamma_c}\sqrt{2 D_2 \Delta_0}$ is the intracavity pulse energy, $D_1/2/\pi$ is the cavity FSR, D_2 is related to cavity GVD, ϑ is the transmission of the microresonator, γ_c is the cubic nonlinearity parameter, $\tau_p \approx \frac{1}{D_1}\sqrt{\frac{D_2}{2\Delta_0}}$ is the intracavity pulse duration [110], ζ and α_{tot} are the

spontaneous emission factor and cavity loss. For the different soliton states, the quantum-noise-limited timing jitter PSD is inversely proportional to the resonance-pump detuning and proportional to square root of the cavity dispersion. The soliton microcomb center frequency fluctuation PSD $S_{\Delta T_R}(f)$ can also be converted into the timing jitter with the relation $S_{\Delta T_R}(f) \approx \left(\frac{D_2}{fT_R}\right)^2 S_{\Delta\nu_c}(f)$ where $\Delta\nu_c$ is the center frequency fluctuations induced by avoided-mode-crossings [112, 113], odd-order dispersion [115], or Raman effects [52]. In addition, the intracavity intensity fluctuations will introduce the extra timing jitter PSD with the relation of $S_{\Delta T_R}(f) = C \times (\eta P_{in})^2 \left(\frac{1}{f}\right)^2 S_{RIN}(f)$ where $\eta = df_R/dP_{in}$ is the transduction factor, P_{in} is the microresonator intracavity power, C is a constant [107, 116].

We note our noise measurements of the frequency microcombs below the offset frequency of 20 kHz are still higher than the microresonator theoretical thermodynamical limits. This is attributed to the strong free-running intracavity power fluctuations and pump-resonance detuning noise. Further active stabilization of the intracavity power and pump-resonance detuning [106, 113] can improve the timing jitter PSD at the low offset frequency. By increasing tapered waveguide width (increasing the effective resonant mode volume) and decreasing the cavity GVD, the jitter of the frequency DM-microcomb oscillator can be improved to sub-femtosecond timing imprecision.

4.6 Summary

In this study the fundamental noise of dispersion-managed soliton microcombs without a restoring force are examined in detail. Dispersion-managed microcombs are deterministically and reliably generated with a TE-TM dual-driven thermally stabilized approach at the single-soliton, double-soliton, and soliton crystal regimes. The RIN is determined to be -153.2 dB/Hz at 100 kHz offset for the single-soliton state and its short-term linewidth is $\approx$ 2.3 kHz at 3.55 μs delay time across the span of the individual comb lines, with both parameters bounded by the cw pump laser. The timing jitter PSD is 0.4 as^2/Hz at 100 kHz

offset and the corresponding integrated timing jitter is 1.7 ± 0.07 fs from 10 kHz to 1 MHz. To the best of our knowledge, we achieved femtosecond timing jitter for the first time in dispersion-managed microcombs. This performance permits our designed microresonators to serve as reference clock oscillators. The demonstrated results show the dynamic noise for the double-soliton and soliton crystal in the RIN PSD is important to understand intracavity soliton dynamics, with the single-soliton state having the lowest jitter, and with slight but quantifiable variations across the different soliton states. The effective cavity length fluctuation is the main noise source at low offset frequencies, and it originates from intracavity power fluctuations in the microresonator. In the dispersion-managed microcombs, we also note the negligible center frequency shift, preventing center-frequency-shift-related noise conversion processes. Understanding high-order dispersion in the dispersion-managed microresonators which facilitates additional noise coupling mechanisms could be explored in future studies. By feedback stabilizing pump laser intracavity power and frequency, the timing jitter of the dispersion-managed chip-scale soliton oscillator could be further reduced to sub-femtosecond imprecision.

CHAPTER 5

Observation of deterministic double DKS generation

5.1 Introduction

Over the past two decades, remarkable breakthroughs have been seen in the chip-scale frequency microcomb studies with ultrahigh-Q microresonators [25, 24, 26, 27, 28, 29, 20], from table-top demonstrations [9, 127] to small factor integrated platforms [54, 97, 95], thriving in both fundamental dynamics [127, 62, 52, 15, 128, 129, 112, 130, 116] and various applications, including spectroscopy [104], optical coherent tomography (OCT) [131, 132], low noise radio frequency generation [13, 133], frequency synthesis [54], distance ranging [36, 101], photonic convolution processing [109, 108], and high-speed optical communication [56, 99, 100]. Among these studies, dissipative Kerr solitons (DKS), which requires a delicate balance between loss and parametric gain, as well as Kerr nonlinear phase shift and anomalous dispersion [21], draws the most attention, for their self-referenced broadband optical frequency comb nature. DKS states include single DKS, multi DKS and soliton crystal states. Except for single DKS state, which has a sech^2 envelope, all the other DKS states' optical spectra are just the interference of several soliton pulses circulating around the cavity. The comb line intensity could be expressed as [20]: $I(\mu) = |\sum_{j=1}^{N} \exp(i\varphi_j \mu)|^2$. However, except for perfect soliton crystal state and double DKS states, other multi DKS states are difficult to identify merely from the spectra. Recently, the lotus-like double DKS state, due to its interference nature, has found its own application in microwave photonics area. However, although repeatable double DKS generation is realized, the azimuthal angle between the two soliton pulses is still stochastic [134].

Here we experimentally demonstrate a novel method to deterministically generate double DKS with fixed azimuthal angle assisted by the dual-pump driven scheme in a 88 GHz Si_3N_4 microresonator. Si_3N_4 platform is currently the most wildly applied platform due to its CMOS-compatible fabrication process, large Kerr nonlinearity, broad transparent window, low Raman nonlinearity and high-power handling capability [21]. However, just like the other platforms, such as AlGaAs, AlN, Si and SiO_2, Si_3N_4 also suffers from thermal effect, which makes it difficult to tune the pump laser to the effective red-detuned regime, where DKS states exist. In order to mitigate the fast thermal effect, power kicking and high-speed frequency scanning methods are proposed with abrupt change of power or frequency to bypass the thermal effect. The emergence of dual-pump scheme significantly simply the procedure to generate single DKS state [135, 136]. With the assist of an auxiliary pump at C band, the nonlinear thermal effect of Si_3N_4 is significantly mitigated, hence the once forbidden effective red-detuned regime could be easily accessed through manually wavelength tuning. Then a 88 GHz single DKS is repeatedly accessed, confirmed by the $sech^2$ optical spectrum shape, the amplitude noise measurement as well as the autocorrelation measurement. Furthermore, several double DKS states are demonstrated with different azimuthal angles. Next, we report a deterministic method to generate double DKS states with fixed azimuthal angle, directly accessed from single DKS state, with backward detuning. The fine tuning of the azimuthal angle via wavelength tuning and pump power variation are further investigated. Finally, the connection between the deterministic coarse dialing of double DKS states with different angle from 180° to 17° and the avoided mode crossing (AMX) is established.

5.2 Device characterization

In the experiment, a Si_3N_4 planar microresonator with 800 nm height is utilized for DKS generation. The width of the microresonator is tapered from 4 μm to 1 μm, where the light is coupled out to the bus waveguide. Unlike the common uniform waveguide design, such

taper design could effectively suppress higher order mode family, averting avoided mode crossing (AMX) induced by the coupling between different transverse mode families [34]. Furthermore, the taper design could also achieve higher Q factor, as well as offer an extra degree of freedom to engineer the net dispersion, which are discussed in our previous works [35]. Figure 5.1 shows the cold cavity transmission of the 88 GHz microresonator. A high speed SWI is applied to record more than 100 TE_{00} resonances over the whole C and L bands, with loaded Q factors higher than 1.5 million. The lower panel plots the FSR of all the recorded resonances, with retrieved GVD of -7 fs^2/mm. The blue dashed box circles out the AMX originating from the inevitable coupling between TE and TM mode families. A detailed depiction of the related resonance is in the lower left of the upper panel. Such AMX is critical in the deterministic double DKS generation, and will be discussed in detail later in this manuscript.

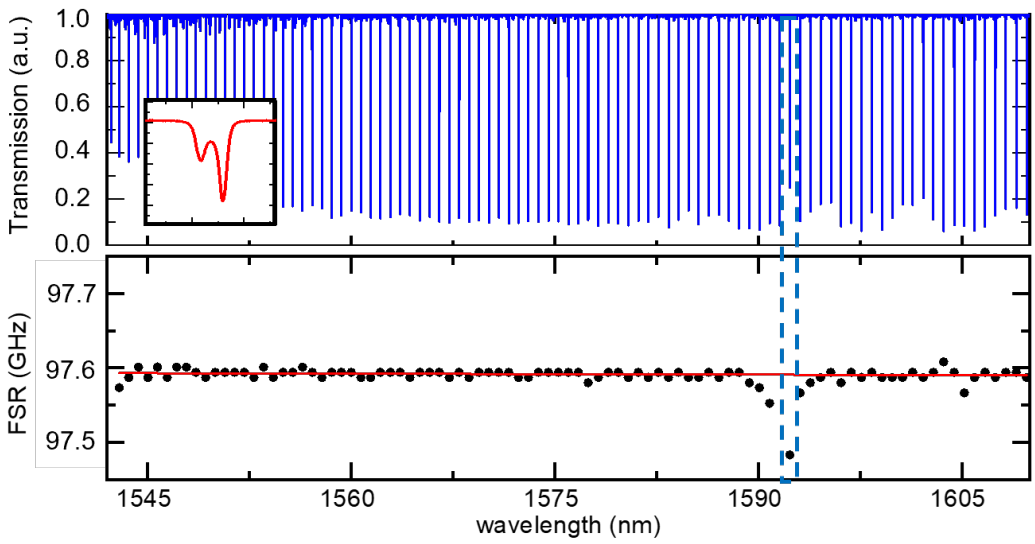

Figure 5.1: Dispersion characterization. Upper panel depicts the transmission of the tested 88 GHz Si_3N_4 microresonator. The inset shows the inevitable TE-TM mode coupling. The lower panel illustrates the FSRs of the resonances across 65 nm, with fitted anomalous GVD of -7 fs^2/mm. The dashed blue box circles the AMX attributed to the TE-TM mode coupling.

5.3 88 GHz DKS generation via dual pump scheme

Figure 5.2 demonstrates the schematic setup of the dual-pump driven method for single and double DKS generation.

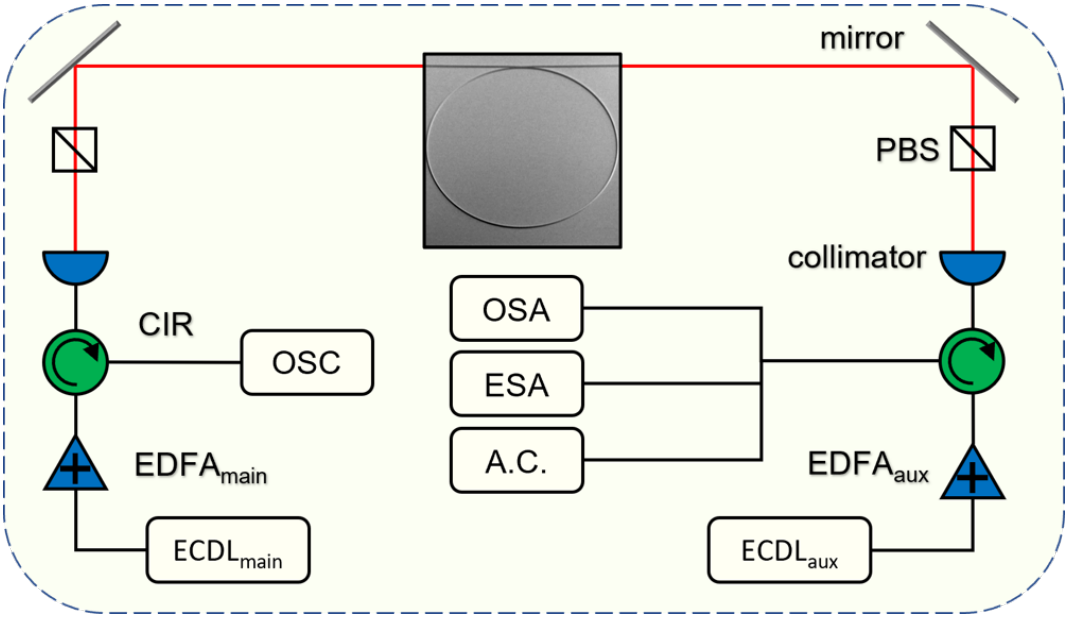

Figure 5.2: Schematic setup of dual-pump driven soliton generation. The main pump and the auxiliary pumps are launched into the 88 GHz Si_3N_4 microresonator in counterpropagating directions and separated via circulators (CIR). Both the main pump and the auxiliary pump are selected at TE polarization with PBS. The reflection path of the circulator on the auxiliary side is utilized for optical spectrum, amplitude noise and autocorrelation (A.C.) measurements. The reflection of the other circulator is used for monitoring the transmission of the auxiliary pump. OSC: oscilloscope; OSA: optical spectrum analyzer; ESA: electronic spectrum analyzer.

5.3.1 TE-TM dual pump scheme

The dual-pump driven method in our implementation utilizes two external cavity diode lasers (ECDL), which are amplified by two Er-doped fiber amplifiers (EDFA) and then launched in to the microresonator in counterpropagating directions. Both pumps are selected in TE

polarization with polarized beam splitters (PBS), due to anomalous dispersion and higher Q factor in TE mode. First, the auxiliary pump ($\mathrm{ECDL_{aux}}$) is tuned, from shorter wavelength to longer wavelength, into a resonance in C band (around 1565 nm in our case), and then stopped at the effective blue-detuned regime. Then the main pump ($\mathrm{ECDL_{main}}$) is launched into a resonance at around 1598 nm in the counterpropagating direction. Since both pumps are in the same polarization, in order to collect the transmission power of both main and auxiliary pumps, two high-power circulators are utilized. The reflection port of the left circulator in Figure 5.2 is used for monitoring the tuning of the auxiliary pump, while the reflection port of right circulator is split into three paths for optical spectrum, amplitude noise and autocorrelation measurements.

Figure 5.3 shows the scheme of dual-pump driven method. The upper left is the scenario that only involves single pump. The detuning between pump laser and the resonance is usually defined as $\Delta = \omega_0 - \omega_\mathrm{p}$, where ω_0 is the angular frequency of the cold cavity pump resonance and ω_p is the angular frequency of the pump laser. In the presence of thermal effect, an extra resonance shift introduced to the pump resonance frequency is approximately proportional to the product of the Q factor of the resonance and the power coupled to the cavity: $\Delta_\mathrm{T} \propto \mathrm{Q} \cdot \mathrm{P_c}$, where $\Delta_\mathrm{T} = \omega_0 - \omega_0'$ is the thermally induced resonance shift with the effective resonance frequency ω_0', Q is the quality of the pump resonance, and $\mathrm{P_c}$ is the power coupled into the pump resonance from the pump laser. Then the effective detuning could be written as: $\Delta_\mathrm{eff} - \omega_0 - \omega_\mathrm{p} - \Delta_\mathrm{T}$. When only a single pump is forwardly (shorter wavelength to longer wavelength) tuned into a resonance at the effective blue-detuned regime, due to the positive thermal-refractive coefficient in Si_3N_4, the resonance tends to shift to lower frequency (longer wavelength) as there is more power coupled into the resonance, and the effective detuning tends to become longer than without thermal effect. However, when pump laser is in the effective red-detuned regime, where DKS states exist, the pump resonance shifts to higher frequency (shorter wavelength) in forward tuning, which makes the effective detuning region much shorter than without thermal effect. Such phenomenon

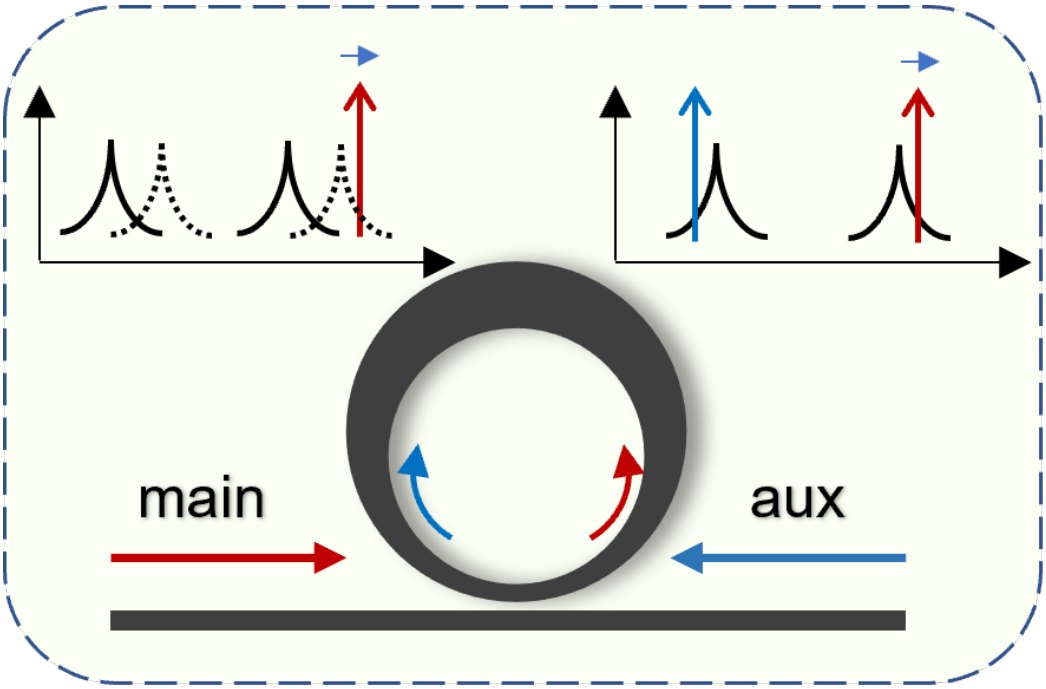

Figure 5.3: Principle of the dual-pump driven scheme. The main pump and the auxiliary pump are launched into the microresonator in the opposite direction. The upper left inset depicts single pump scheme, in which resonances will shift to shorter wavelengths when the pump is at effective red-detuned regime. The upper right inset illustrates the dual-pump scheme, in which all the resonances remain at the same position, when the main pump is tuned in the effective red-detuned regime, with the auxiliary pump set at the effective blue-detuned regime.

results in the thermal triangle in the pump scanning measurement.

Figure 5.4 upper panel plots the transition of the thermal triangle with the presence of a single pump. The characteristic step for DKS states is on the hundreds of kilohertz level when the pump is scanned at a scanning speed of 2.5 THz/s, which makes it extremely difficult to generate DKS states with manual tuning. In the presence of the auxiliary laser, the thermal induced resonance shift is dominated by both pump, i.e. $\Delta_T \propto Q_{main} \cdot P_{main_c} + Q_{aux} \cdot P_{aux_c}$, where Q_{aux} is the quality factor of the auxiliary pump resonance, and P_{aux_c} is the power coupled from the auxiliary pump. Since the auxiliary pump is set at the blue-detuned regime of the picked resonance, when the main pump is forwardly tuned into the resonance at blue-

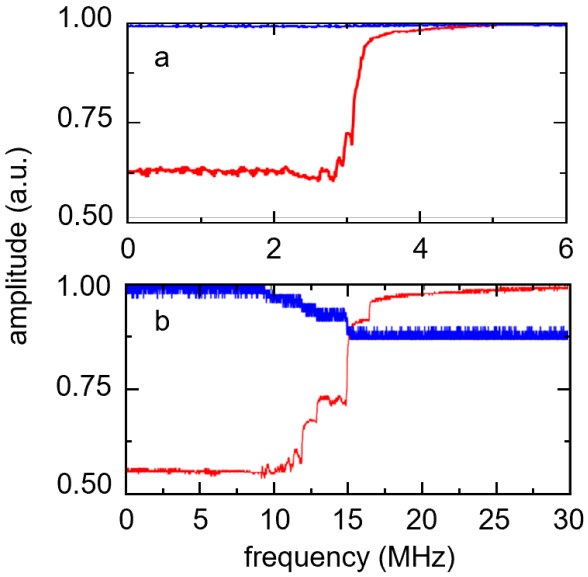

Figure 5.4: Pump power transmission of both pumps in single pump scheme and dual-pump regime. The upper panel shows that without the auxiliary pump, the soliton characteristic steps only maintain over tens of kHz. The lower panel illustrates that with the presence of the auxiliary pump, the soliton characteristic step is significantly extended to several MHz. Both measurements are implemented with laser scanning speed of 20 nm/s.

detuned regime, P_{main_c} increases and tends to redshift all the resonances, then the auxiliary pump is equivalently tuned away from the resonance, hence P_{aux_c} decreases, then Δ_T is mitigated. And when the main pump is forwardly tuned at the red-detuned regime, P_{main_c} decreases and all the resonances tend to be blue-shifted, so that the auxiliary pump is equivalently tuned towards the resonance, hence P_{aux_c} increases, then Δ_T is mitigated. So that the resonance will remain unchanged during the main pump tuning, with the appropriate choice of auxiliary resonance and auxiliary pump power. In a result, the resonances are thermally stabilized by the auxiliary pump. With the help of the thermal stabilization of the auxiliary pump and the cross-phase modulation (XPM) between the main and auxiliary pumps, the increase of effective detuning at the red-detuned regime is retarded, which manifest itself as a much longer characteristic step of DKS states during the pump transmission measurement

at the same scanning speed. The lower panel of figure 5.4 shows the corresponding measurement, from which we could see that the characteristic step is at several MHz level, which is boosted by more than 30 times. Such elongated characteristic step makes manually tuned DKS states possible.

5.3.2 Single DKS generation

Figure 5.5a is the optical spectrum of a single DKS state with signature sech^2 shape. The low noise state is confirmed with amplitude noise measurement up to 1 GHz, which is shown in the upper left inset. Furthermore, we implemented a non-colinear autocorrelation measurement on the single DKS state, shown in figure 5.5b. Although the fiber link is not optimized for zero link dispersion, the single pulse waveform with 11.28-ps period further confirms a 88 GHz single DKS generation.

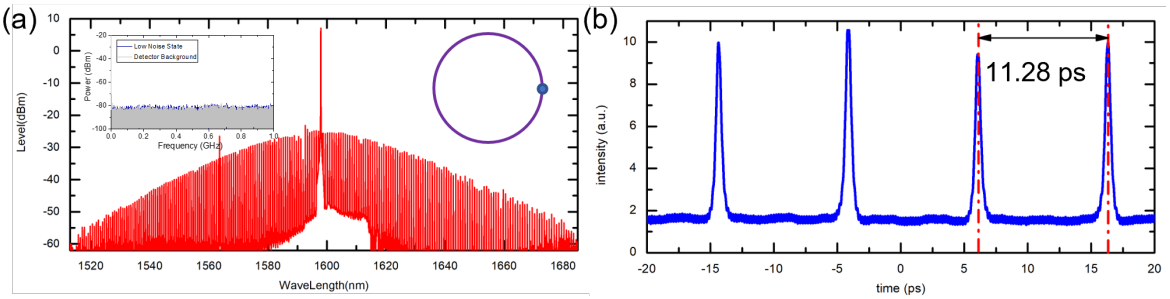

Figure 5.5: Typical single DKS. a, Single DKS optical spectrum. The upper left inset is the amplitude noise measurement (blue curve) of the DKS state compared with the detector background noise (gray curve). b, A.C. of the single DKS state. The 11.28 ps period proves the 88 GHz single pulse generation.

5.3.3 Double DKS generation with stochastic azimuthal angles

Figure 5.6a shows a typical double DKS state with distinguishable interference pattern. Through A.C. measurement shown in figure 5.6b, the time interval between the two solitons

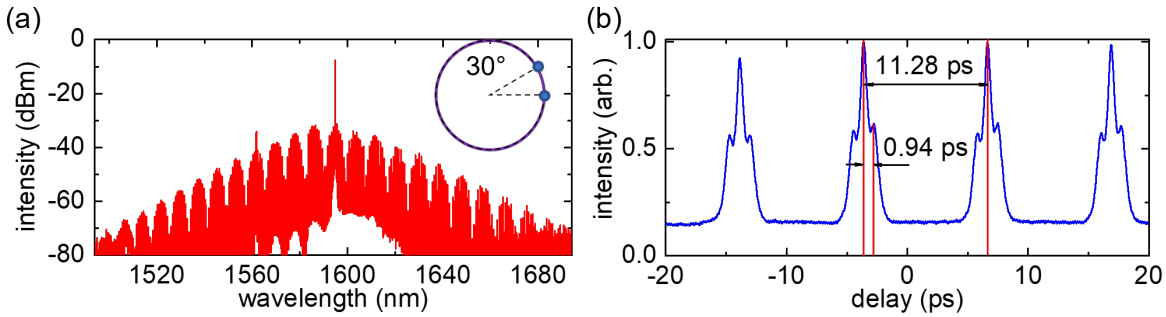

Figure 5.6: Typical double DKS. a, A double DKS state with azimuthal angle of 30°. b, A.C. measurement of the double DKS state in a. The 0.98-ps spacing between the peaks illustrates the 30° separation of the two pulses.

in the double DKS state is 0.98 ps. The retrieved azimuthal angle with respect to the 11.28-ps period is 30°. Figure 2(e) shows a unique double DKS state with azimuthal angle of 180°. The exact π phase difference results in a double FSR comb spectrum. Figure 2(f) shows another double DKS state with azimuthal angle of 21°, which has significantly wider lobe size than the 30° case. In the evolution process from multi DKS states to single DKS state, the pulses circulating along the microcavity diminish consecutively. Hence, theoretically a double DKS state could always be achieved in each comb evolution. However, the detuning range for each DKS state could vary in each evolution, consequently, the double DKS state cannot be generated in every trial. Furthermore, since the position of the pulses in the cavity is regulated by the modulated background due to the interference between the pump and the AMX, the azimuthal angle of the double DKS state is also stochastic [134].

5.4 Double DKS generation with deterministic azimuthal angles

In the presence of the auxiliary pump, bi-directional switching could be realized, similar to the photo-refractive effect in $LiNbO_3$ platform. Unlike previous work [137] in which backward tuning causes pulse number changing from higher number to lower number, the thermal stabilization via auxiliary pump could realize not only soliton burst [135], but also realize

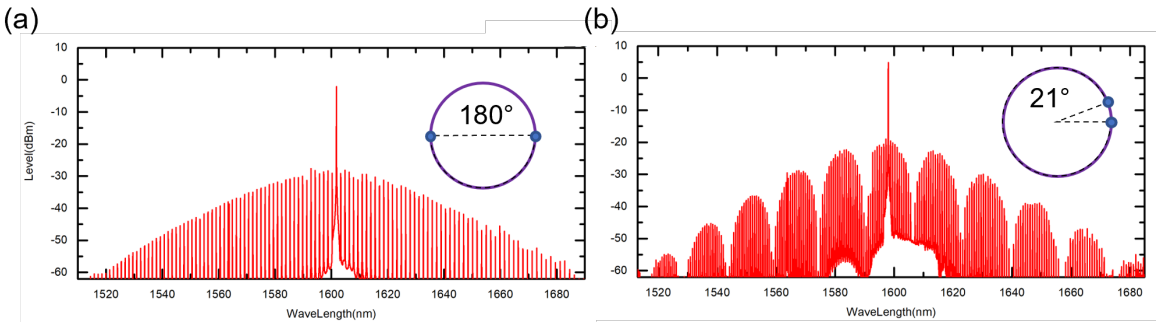

Figure 5.7: More double DKS examples. a, Typical double DKS state with azimuthal angle of 180°. Due to the π phase shift between the two pulses, the interference results in a double-FSR comb spectrum. b, A double DKS state with azimuthal angle of 21°. As the azimuthal angle decreases, the interference envelope would have a wider lobe width, which is a good indicator to roughly compare the azimuthal angle.

ascending switch of soliton numbers. Here in our work, we did not focus on soliton burst but we focused on the DKS state switching from single DKS state during backward tuning. Particularly, we found out that once the single DKS state is achieved, if one slowly tunes the main pump wavelength backwardly, the comb will always arrive at a double DKS state with the same azimuthal angle in a deterministic fashion, when the pump power and resonance are not changed. Since the double DKS states have recognizable modulated pattern due to the interference between the two soliton pulses, it is rather easy to retrieve the azimuthal angle from fitting. Hence, all the azimuthal angle information hereafter are retrieved from the spectral fitting of the double DKS state.

In the experiment, we notice that the main and auxiliary pump intensities need to be carefully chosen to achieve single DKS to double DKS switching. In our experimental scheme, the auxiliary pump is set at 27 dBm, and only when the main pump power is between 23 dBm and 25 dBm, could the deterministic double DKS generation be realized. Although the azimuthal angle between the two solitons in the double DKS state is fixed via backward tuning, it could still be slightly tuned through forward tuning.

5.4.1 Azimuthal angle control via pump wavelength detuning

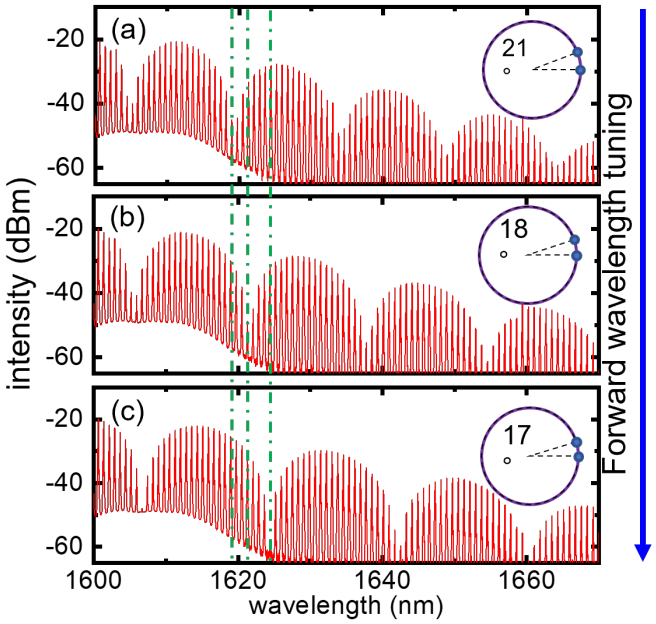

Figure 5.8: Azimuthal angle of double DKS tuning through pump wavelength tuning. a-c, The azimuthal angle between the two DKS pulses tends to decrease as forward wavelength tuning. Through finely and slowly tuning of the wavelength, the azimuthal angle is deterministically controlled over 4°.

Figure 5.8(a-c) shows the experimental results for the azimuthal angle tuning through forward tuning. First, The comb is manually tuned into a single DKS state, then a slow manual backward tuning is applied to the main pump until a double DKS state with azimuthal angle of 21° is achieved. Next, the main pump wavelength is slowly tuned forwardly, until a single DKS state is arrived again. During the process, A double DKS state with azimuthal angle of 18° and 17° are captured through an OSA, consecutively. However, since the forward tuning is applied manually and the OSA has a relatively slow capture time, a continuous variation of the azimuthal angle is not recorded, nor the smallest azimuthal angle is observed. This could be explained through the modulated background from the AMX. As mentioned previously, the pulse azimuthal position is regulated by the modulation on the

CW background introduced by the AMX. The time period of the modulated background is directly related to the frequency difference between the pump resonance and the maximum mode shift resonance. The larger the frequency difference, the shorter time period. Hence, during the forward tuning, as the frequency difference is increasing, the time interval of two adjacent potential well that could trap the soliton pulses gets closer. Therefore, the azimuthal angle in the double DKS state shows a descending trend along with forward tuning.

5.4.2 Azimutal angle control via pump power

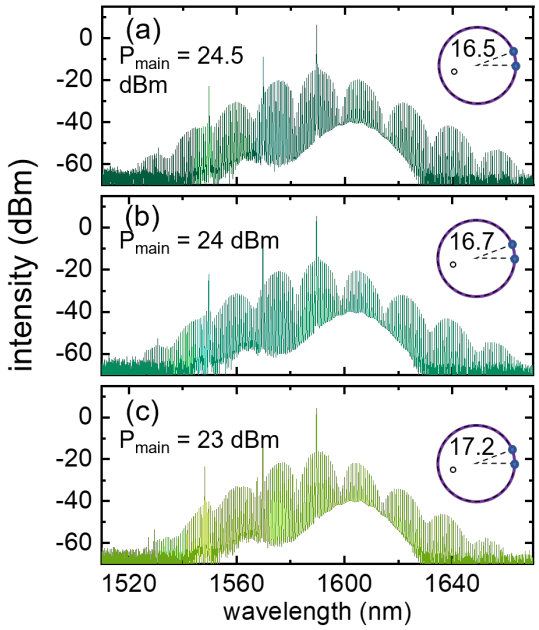

Figure 5.9: Azimuthal angle of double DKS tuning through pump wavelength tuning. a-c, The azimuthal angle between the two DKS pulses tends to decrease as forward wavelength tuning. Through finely and slowly tuning of the wavelength, the azimuthal angle is deterministically controlled over 4°.

Similarly, Once the deterministic double DKS is realized, by changing the main pump power, the azimuthal angle could also be tuned slightly. Figure 5.9(a-c) plot the correspond-

ing measurement results. In the similar auxiliary pump scheme, the main pump is set at 24.5 dBm. In the same procedure, a double DKS state with azimuthal angle of 16.5°. When the main pump power is decreased to 24 dBm, the azimuthal angle is then increased to 16.7°. Figure 5.9c shows that when the main pump is set at 23 dBm, the azimuthal angle is further increased to 17.2°. The azimuthal angle has an ascending trend as the pump power decreases.

5.4.3 Investigation in azimuthal angle with AMX

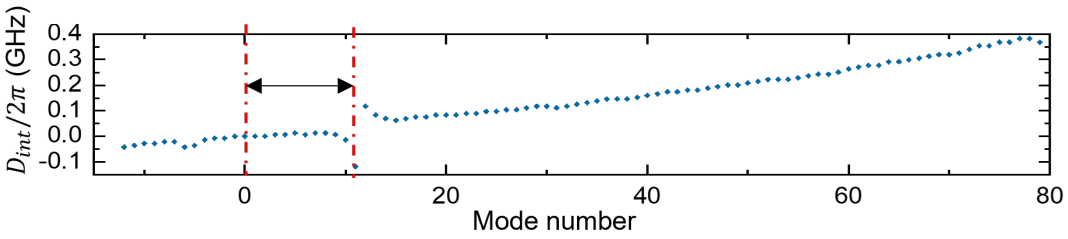

Figure 5.10: D_{int} vs mode number. The maximum AMX is located 11 FSR away from the pump mode (mode 0).

Next, we investigated the relationship between the deterministic azimuthal angle and the pump position with respect to the maximum mode shift induced by AMX. Figure 5.10 depicts the accumulative dispersion D_{int} vs mode numbers. The abrupt change is induced by AMX. Here we define the pump mode is mode 0, and the mode number where the maximum mode shift happens as N. In figure 5.10, N = 11, which means that the pump mode is 11-FSR away from the maximum mode shift induced by AMX. Figure 5.11a plots the optical spectrum of the double DKS state pumped at N = 11, generated via the backward tuning procedure. The azimuthal angle is 17.14° in a deterministic fashion. The angle is retrieved from spectral fitting, as previously mentioned. The fitting curve is plotted in red line on top of the optical spectrum. Figure 5.11b plots the deterministically generated double DKS state with azimuthal angle of 17.14° when N = 10. Figure 5.11(c-i) plots the double DKS states

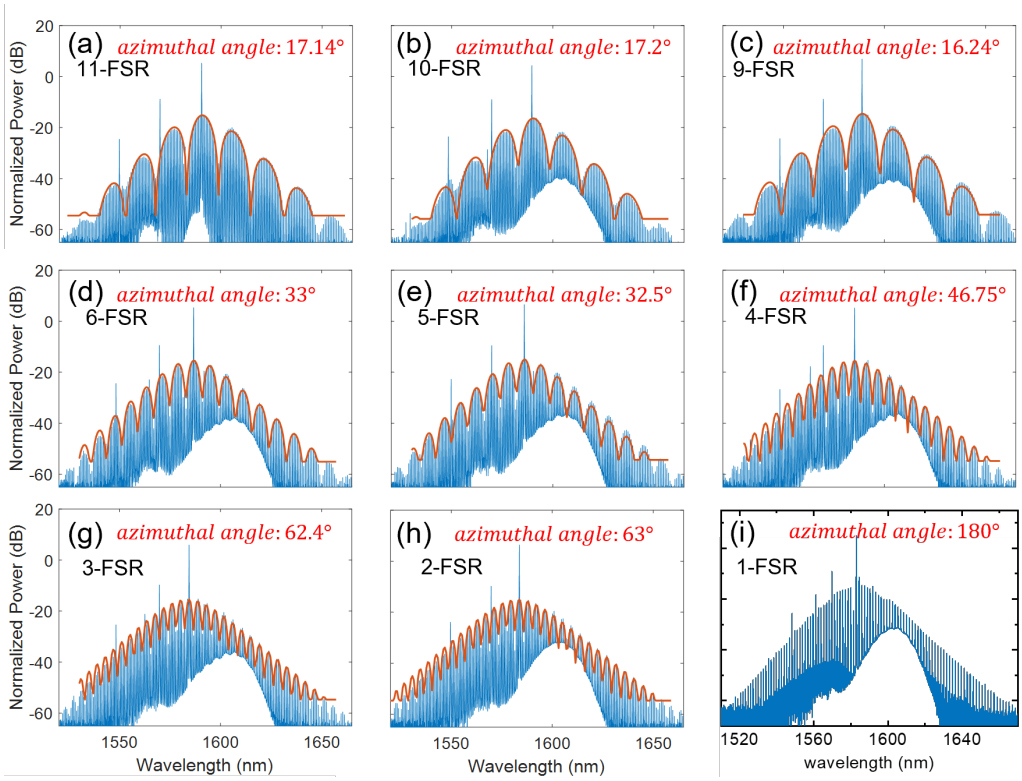

Figure 5.11: Optical spectra of different double DKS states pumped at different resonances with respect to the maximum AMX position. 11-FSR to 2-FSR cases show typical double DKS interference envelope, from which the azimuthal angles are fitted from the interference patterns. In the 1-FSR case, the optical spectrum shows a double FSR comb, indicating a 180° azimuthal angle.

when N = 9, 6, 5, 4, 3, 2 and 1. The azimuthal angles are 16.24°, 33°, 32.5°, 46.75°, 62.4°, 63° and 180°, respectively. Since the azimuthal angle in figure 5.11i is 180°, leading to a double-FSR comb spectrum, spectral fitting is not necessary, hence not plotted. Figure 5.12 summarizes the azimuthal angle for double DKS state generated at different pump mode. Due to unknown reasons, there are no deterministic double DKS generation at pump mode 7 and 8. For the other cases, double DKS states are generated as expected. Overall, the azimuthal angle shows a descending trend as the pump mode is away from the resonance with maximum mode shift, which matches with our prediction, shown in red curve. The prediction is based on single AMX point using two parameters model, however, in real implementation,

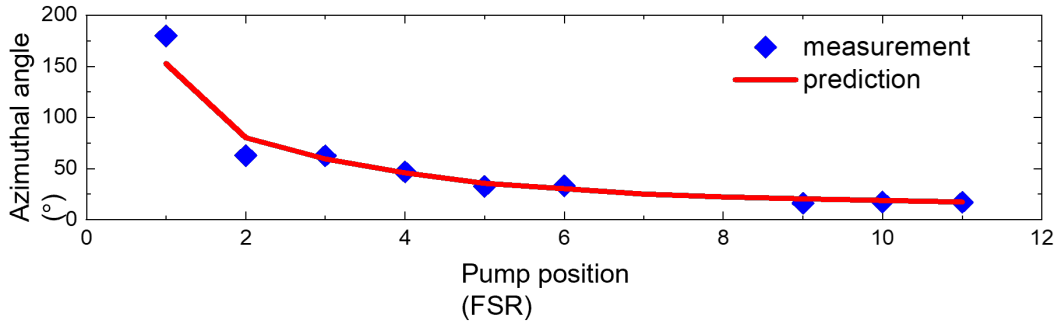

Figure 5.12: Summary of the azimuthal angles in different pump position cases. The result shows clear descending trend of the azimuthal angle with respect to increasing pump-AMX spacing.

the auxiliary pump will also contribute to the modulation of the CW background, leading to a more complex background field. This could account for the deviation of the measurement from the prediction.

5.5 Summary

In conclusion, through a TE-TE dual-pump driven method, we demonstrate a novel scheme to deterministically generate double DKS state with fixed azimuthal angle in a 88 GHz Si_3N_4 microresonator. Assisted by an auxiliary pump at C band, the thermal nonlinearity is significantly mitigated. Hence, the characteristic steps for DKS states are elongated, so that single soliton state could be repeatedly generated manually, which is difficult to achieve with single pump in our Si_3N_4 platform previously. Although no soliton burst is demonstrated in this work, we successfully observed bi-direction switching, in which the soliton number decreases in forward tuning while increases in backward tuning. Particularly, we demonstrated double DKS state generation through backward tuning from a single DKS state. Although similar phenomenon has been mentioned in a recent publish paper [136] during the preparation of this manuscript, to our best knowledge, we for the first time focus on the double DKS state's azimuthal angle control and establish a bridge between AMX

and the azimuthal angle. In the backward tuning from a single DKS state, the comb always arrives at a double DKS state with deterministic azimuthal angle, when pumped at the same resonance. However, once the double DKS is generated, the azimuthal angle could be fine tuned through forward tuning or pump power control. The azimuthal angle tends to decrease in forward tuning and increase when the pump power decreases. Furthermore, we demonstrated that the deterministic azimuthal angle is directly related to the modulated CW background induced by AMX. Therefore, by choosing different pump resonance with respect to the maximum mode shift that originates from AMX, we successfully dial the azimuthal angle from 180° to 17°. We believe that with appropriate control of the AMX, such as the method demonstrated in [138], the azimuthal angle could be further manipulated. This study not only enriches the understanding of DKS dynamics in dual-pump driven scheme, but also offer more versatility of the double DKS state in the application of microwave photonics, such as microcomb based reconfigurable RF filters [134].

CHAPTER 6

Stimulated generation of deterministic platicon frequency microcombs

6.1 Introduction

Over the past two decades, remarkable breakthroughs have been seen in the chip-scale frequency microcomb [5] studies with ultrahigh-Q microresonators [26, 25, 24, 27, 28, 29, 20], from table-top demonstrations [127, 9] to small factor integrated platforms [54, 97, 95], thriving in both fundamental dynamics [127, 62, 52, 15, 128, 129, 112, 130, 116] and various applications, including spectroscopy [104], optical coherent tomography (OCT) [131, 132], low noise radio frequency generation [13, 133], frequency synthesis [54], distance ranging [36, 101] and high-speed optical communication [56, 99, 100]. Most of these works are based on dissipative Kerr solitons (DKS) in anomalous GVD microresonators for self-referenced broadband optical frequency combs, which requires a delicate balance between loss and gain, as well as nonlinear phase and dispersion [21], and could limit the pulse energy if an ultrashort pulse and broadband spectrum are desired simultaneously. Since the material GVD of most platforms are normal in visible and near-infrared frequency range, the cavities are often engineered to achieve anomalous dispersion in pump resonances across a broad range [15, 139, 140]. Among these platforms, silicon nitride outstands due to its CMOS-compatible fabrication process, large Kerr nonlinearity, broad transparent window, low Raman nonlinearity and high-power handling capability [21]. The engineering of silicon nitride is commonly based on thick-nitride (> 600 nm) waveguide that supports multi

transverse modes to achieve anomalous dispersion while maintaining high quality factors for low threshold frequency microcomb generation [95, 141]. However, the inevitable coupling between different transverse mode families characteristically modulates the amplitude of the frequency microcomb spectrum and could detrimentally destabilize the dissipative Kerr soliton formation [27, 33]. Tapered waveguide is then proposed to achieve anomalous GVD and single mode operation simultaneously [34, 142], however, the operation for DKS remains non-trivial [95, 137, 135] with complex intracavity dynamics [129, 110, 112]. Furthermore, the ultralow loss thick-nitride waveguide fabrication needs special treatment [143], which is not offered in current commercial Si_3N_4 foundry process. Consequently, the adoption of DKS in standard PIC architectures through commercial foundries is still not possible [144]. Compared to the state-of-art ultralow-loss thick-nitride Si_3N_4 microresonator with 30-million Q [145], recent demonstration of ultra-thin silicon nitride microresonators have achieved 260-million Q with comparable free spectral range (FSR) [98], which significantly decreases the comb generation threshold. However, anomalous dispersion is forbidden in such scheme. Consequently, the study of novel methods to enhance normal dispersion frequency microcomb generation can simplify the microresonator frequency comb architecture and extend its operation into other frequency ranges.

Frequency microcomb generation in the normal GVD regime has recently been examined both theoretically and experimentally in a variety of platforms including crystalline resonators and integrated microresonators [15, 17, 146, 60, 147], as well as been demonstrated in many applications [99, 148, 149]. Its formation and nonlinear dynamics usually require shifted pump mode resonances [150], which can be achieved by avoided mode crossing caused by mode coupling between different mode families [30] or coupling between adjacent microresonators [151, 138], or self-injection locking [144, 152] to provide local anomalous dispersion [147, 27]. Among these prior studies, solitonic bright pulse with unique flat-top square pulse shape – or the platicon – has increasingly drawn attention in numerical studies [150, 153, 154]. These theoretical modeling studies on the platicon have shown its pulsewidth

can be continuously controlled in a broad range via the pump-resonance detuning (and hence the intracavity energy and nonlinear parametric gain). In addition, the conversion efficiency of pump power into comb power can be potentially higher in the platicon comb than in solitons, for the same GVD value [150]. Benefiting from its optical spectra's sharp edge and flat top features, the platicon can help increase the signal processing capabilities in optical domain for high-speed communication [155, 156, 157], with other applications in pulse shaping and amplification, nonlinear optical imaging, and production of high-brightness electron beams [158]. Although experimental demonstration of platicon frequency microcombs via self-injection locking has been recently demonstrated via self-injection locking [144] and pulse-pumping [159], the platicon generation via intensity-modulated pump [160], to the best of our knowledge, has not been demonstrated yet.

Here we experimentally demonstrate the generation of platicon frequency microcomb and its operating parameters in a chip-scale Si_3N_4 microresonator with normal dispersion, as a complimentary follow-up work of our previous demonstration [161]. Via an intensity-modulated pump [160], a platicon generation approach is demonstrated such that sophisticated schemes for introducing pump mode shift or self-injection locking could be avoided. A platicon frequency comb with 80 nm span (60 dB) and clean comb spacing beat note is achieved. The platicon has a flattop pulse duration deterministically tunable from 2 to 17 ps, observed and confirmed through optical spectra, intensity autocorrelation and dual-comb cross-correlation measurements. Controls of the frequency comb optical spectrum through TOD, pump-resonance detuning, and modulation frequency are studied and characterized.

6.2 Stimulated generation of deterministic platicon frequency microcombs: theorectical study

To understand and predict the nonlinear dynamics, we first start with a modified form of LLE which has an intensity-modulated external pump to numerically model the platicon

generation:

$$T_R \frac{\partial}{\partial t} A(t,\tau) = \sqrt{\alpha_c} A_P - \left[\frac{\alpha_c + \alpha_p}{2} + j\delta - jL_{cav} \sum_{\geq 2} \frac{\beta_k}{k!} \left(j\frac{\partial}{\partial \tau} \right)^k - j\gamma I(t,\tau) \right] A(t,\tau) \quad (6.1)$$

where T_R is the round-trip time, $A(t,\tau)$ is the envelope function of the platicon, t is the slow time corresponding to the evolution time over round trips, τ is the fast time describing the temporal structure of the wave, A_P is the external pump, α_p is the propagation loss, α_c is the coupling loss, and δ is the pump-resonance detuning, where ω_c and ω_p are the cavity resonance frequency and pump frequency, respectively. β_k describes the dispersion coefficient ($\beta_2 > 0$ indicates normal GVD and $\beta_2 < 0$ indicates anomalous GVD), and we only consider second and third order dispersion in this case. $\gamma = \frac{n_2 \omega_0}{c A_{eff}}$ is the Kerr nonlinearity, in which n_2 is the nonlinear refractive index and A_{eff} is the effective modal area of the pumping transverse mode. In our modified LLE, we assign $A_p = \sqrt{P\left\{1 + M\sin\left[\frac{2\pi t}{T_R}\left(\frac{\Delta}{\omega FSR} + 1\right)\right]\right\}}$ to describe the intensity-modulated external pump, where P is the pump power without modulation, M is the modulation depth ($0 \leq M \leq 1$), $\Delta = \omega_M - \omega_{FSR}$ is the deviation between the modulation frequency ω_M and the $\omega_{FSR} = \frac{2\pi}{T_R}$ of the pumped cavity resonance. The simulation starts from vacuum noise and is run for 1.5×10^5 roundtrips until the solution reaches steady-state. The simulation is based on our FSR of 19 GHz with normal GVD of +55 fs^2/mm and negative TOD of -948 fs^3/mm.

The formation of platicon with intensity-modulated pump can be explained by wave-breaking theory [162, 163, 164][67–69] as detailed below. Figure 6.1a shows the 2D evolution map of platicon temporal profile against the non-dimensional cavity resonance detuning δ, with four snapshots of the 2D illustrated in Figure 6.1b. Figure 6.1b1 (δ = -0.1) shows the sinusoidal envelope of the modulated pump input seeding the wave-breaking dynamics. Resulting from self-phase modulation, the pump ahead and behind the modulation minimum respectively experiences an instantaneous frequency up-shift and down-shift. In a normal GVD microresonator, such difference in the frequency shift leads to deceleration and accel-

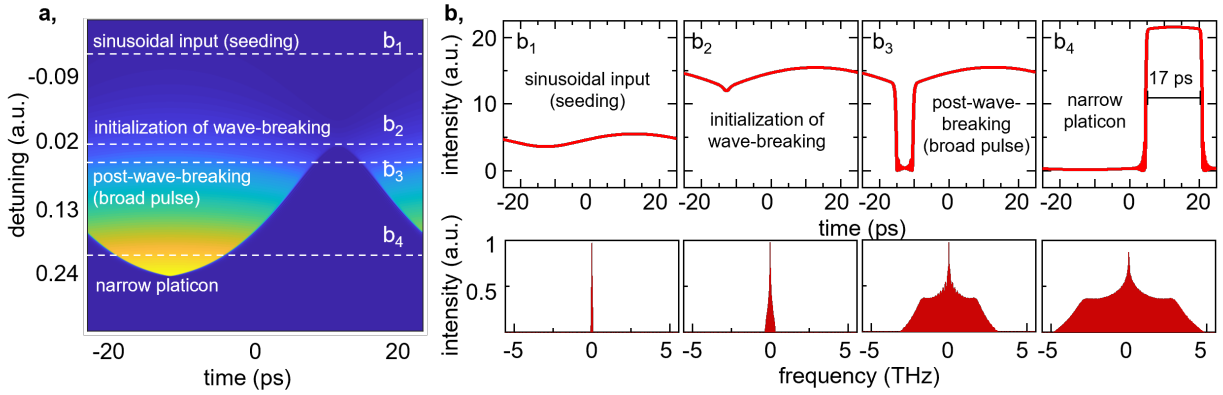

Figure 6.1: LLE modelling of platicon generation with intensity modulated pump. a, 2D evolution map of platicon temporal profile as a function of intracavity fast time and detuning. Four characteristic stages are selected to show the details of the evolution in panel b. b, Upper panels: temporal profiles of the platicon at different evolution stages, lower panels: frequency spectra corresponding each state. b_1: sinusoidal input (seeding); b_2: initialization of wave-breaking. Self-steepening shows that wave breaking is about to happen; b_3: post-wave-breaking. Wave breaking happens, and a broad square pulse is generated; b_4: a shorter narrow platicon is generated for increasing red detuning such as at $\delta = +0.2531$.

eration of the pump ahead and behind the modulation minimum. Consequently, evolution of the initially sinusoidal envelope would be directed outward around modulation maxima and inward around modulation minima, leading to self-steepening around modulation minima [164], such as shown in Figure 6.1b2 ($\delta = +0.0334$). The wave is thus compressed and four-wave mixing (FWM) of the front of the pulse further broadens the comb spectrum, wherein the wave-breaking initialization occurs. This subsequently results in a bright and wide square pulse generation (pulse maxima spanning over a longer timescale), as shown in Figure 6.1b3 ($\delta = +0.0598$). With further red detuning ($\delta = +0.2531$), the bright square pulse duration decreases down to 17 ps as shown in Figure 6.1b4. Thus, after occurrence of the wave-breaking, the platicon pulsewidth shortens with increasing pump-cavity resonance red detuning while the peak intensity of the pulse increases as well.

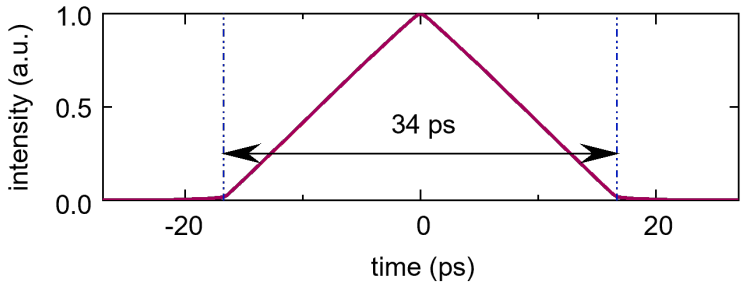

Figure 6.2: Simulated autocorrelation of the square pulse shown in Figure 1b$_4$. The width of the triangle is about twice of the width of the square pulse.

The corresponding simulated frequency comb spectra are shown in the lower row of each intermediate states. We note that, in the platicon state, the comb lines have a somewhat flat plateau away from the pump wavelength with roughly uniform intensities, before gradually decreasing to the noise floor. In our numerical modeling plots, the y-axis range is chosen such that it is comparable to the experimental dynamic range in our OSA. We put a 17-ps simulated platicon for better illustration of the square shape characteristics, however, the pulsewidth is theoretically controllable from tens of ps to sub-ps level, by varying the detuning. Since the 17 ps pulse has a square temporal structure, its computed autocorrelation is triangular as shown in Figure 6.2, with the bottom width of the triangle twice that of the platicon square pulsewidth. The triangular structure in the autocorrelation helps distinguish if a platicon is generated in time-domain.

6.3 Stimulated generation of deterministic platicon frequency microcombs: experimental investigation

6.3.1 Device characterization

In the experiments, we utilize a 19 GHz single-mode Si_3N_4 microresonator with Q factor of 1.2 million, and symmetrically top-bottom cladded with SiO_2. Through high-resolution

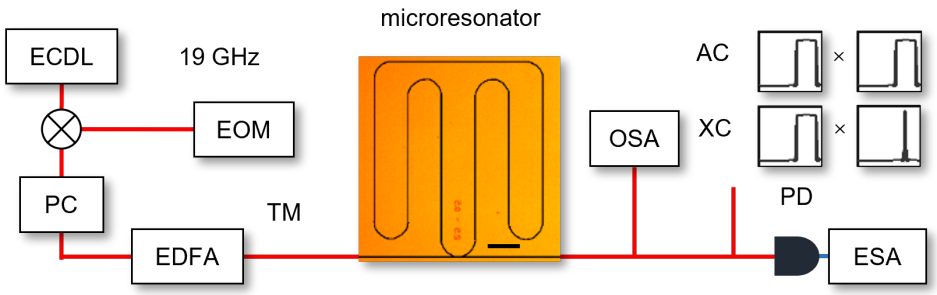

Figure 6.3: Schematic setup of platicon generation with intensity-modulated pump. The cw laser from the ECDL is first modulated by an EOM, and the modulation frequency is chosen to match the single FSR ($\approx$ 19.547 GHz). After amplification by an EDFA, the modulated pump is launched into the single mode microresonator, and the pump frequency is slowly red-tuned to generate the platicon. A polarization controller (PC) and a polarized beam splitter (not shown in the diagram) are utilized to optimize the intensity of TM polarization for TM mode operation. A 20-GHz high-speed photodetector (PD) is used to measure the amplitude and phase noises. An OSA is used to map the platicon spectrum. Then the time domain dynamics is examined by both auto-correlation (AC) and dual-comb cross-correlation (XC). The actual single mode microresonator is shown in the middle micrograph, whose straight waveguide is tapered from 2.5 μm to 1 μm to maintain high quality factor. The curved regions are 1 μm in width to maintain our single-mode frequency comb operation. Scale bar: 200 μm.

coherent SWI [48], the GVD is measured to be normal at 55 $\pm$ 2.5 fs^2/mm with TOD of -948 fs^3/mm, shown in Figure 6.4 . Figure 6.3 subsequently shows the schematic setup for our measurements: the pump from a tunable external cavity diode laser (ECDL) is sent into an electro-optical modulator (EOM) with 20-GHz bandwidth. The modulation frequency, provided by a local oscillator (LO), is set at 19.548 GHz to closely match the single FSR of the microresonator at pump wavelength, and the modulation depth is set so that the sideband intensity is about 3 dB lower than the pump. After amplification by an erbium-doped fiber amplifier (EDFA), the polarization of the modulated is carefully controlled by a fiber polarization controller (PC) and a polarized beam splitter to maximize the intensity of the pump projected into the TM mode. Then the modulated pump with an on-chip power

up to 1.4 W is launched into the microresonator. The output is collected by optical and electronic spectrum analyzers to measure the optical spectra, amplitude noises and radio frequency beat notes, respectively. Intensity autocorrelation (A.C.) and dual-comb cross-correlation (X.C.) measurements are conducted to analyze the time-domain performance of the platicon frequency comb.

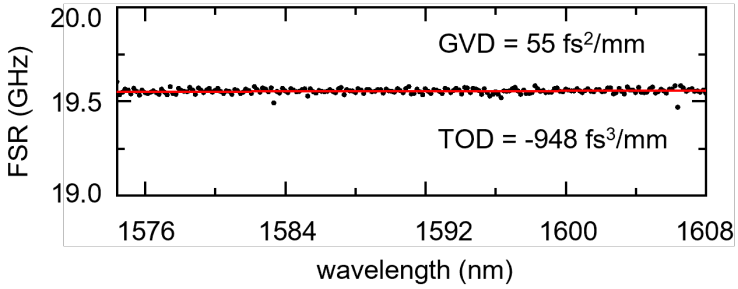

Figure 6.4: Dispersion characterization of the 19 GHz tapered microresonator. The fitted GVD is positive at 55 fs^2/mm, and the fitted TOD is negative at -948 fs^3/mm.

6.3.2 Evolution of the platicon frequency comb

We first experimentally study the evolution of the platicon frequency comb, with modulation frequency set at 19.548 GHz to be very close to single FSR. We red-tune the pump frequency in steps of 5 MHz to generate the platicon. The GVD and TOD measurement of the selected microresonator is shown in Figure 6.5a right inset. Figure 2a shows the triangular pump power transmission versus different pump-resonance detuning. States 1 (red) and 4 (black) are before and after the platicon generation, with their reference optical spectra (solely from the modulated pump) shown in the left inset of Figure 6.5a. The center pump is about 3 dB higher in power than the first sideband pair. As the pump laser is frequency tuned into the cavity resonance, the platicon frequency comb starts to evolve. At the beginning, cascaded FWM of the modulated pump leads to a weak growth of higher-order sidebands with characteristic rapid power decay for increasing mode numbers away from the pump. This is illustrated in the green curve of Figure 6.5b. With further tuning into the cavity

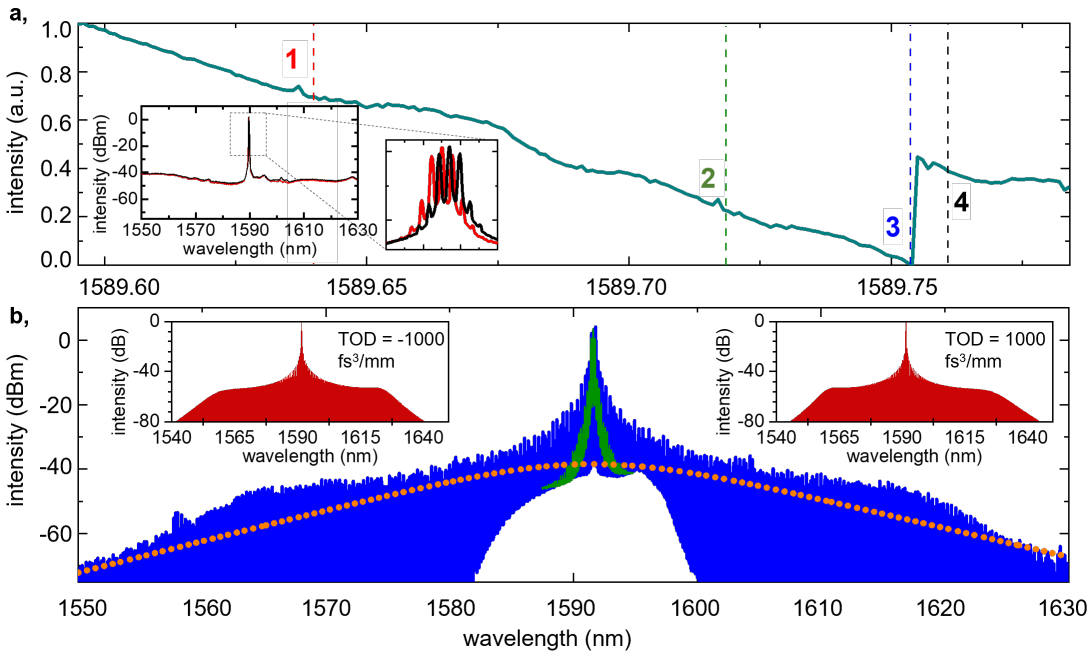

Figure 6.5: Dynamic detuning evolution and spectra of a modulated-pump platicon frequency comb. a, Pump transmission vs. detuning. The comb evolves to its critical point at state 3 (blue). Left inset: optical spectra of states 1 (red) & 4 (black), in which there are only modulated pump spectra. The first pair of sidebands are about 3 dB lower than main pump. Right inset: FSR measurement of the microresonator. b, Comb spectra at state 2 & 3. The comb just starts to evolve due to spontaneous FWM at state 2 (green curve) and the spectrum shape is more like a triangle other than the frequency spectrum of a platicon. At state 3, the frequency comb spectrum (blue curve) is at the critical point, spanning 80 nm. The shape coincides with the simulation, shown in the upper left inset. The upper right inset is comb spectrum simulation with positive TOD, as comparison. A typical single soliton comb spectrum envelope is included in dash pink line, indicating that platicon has higher comb line power at wavelength away from the pump.

resonance, the comb spectrum is dramatically broadened as shown in the blue curve of Figure 6.5b. The platicon spectrum shows the signature characteristic plateau and supported by our wave-breaking modeling shown earlier in Figure 6.1b. A typical single soliton spectrum envelope, clearly distinct from platicon is also included in Figure 6.5b as a light orange dashed line, which indicates that platicon could achieve higher comb line power at wavelengths away from the pump. The widest platicon comb spectrum generated by a single modulated pump is observed at the critical point of state 3, spanning over 80 nm and matches our numerical modelled estimate of 82 nm (left inset of Figure 6.5b). Subsequently, with further increase of the pump wavelength, the platicon comb is lost and the spectrum drops back to the modulated pump line, as shown earlier in state 4.

6.3.3 Investigation in modulation frequency mismatch Δ

To elucidate the underlying physics of the platicon formation, we next examined the impact of Δ on the platicon frequency comb spectrum. This is shown in Figures 3a to 3c (modeling) and Figures 3d to 3f (measurements). The platicon generation has certain tolerance on the value of Δ, effectively controlling the spectral symmetry and intensity distribution of the comb lines. We consider the modelled platicon spectral characteristics prior to the measurements and for the three cases of zero TOD, negative TOD and positive TOD. In the first and conceptual case of zero TOD, our modified LLE modeling shows that Δ will affect the comb line distribution, hence the symmetry of the comb spectra. Since the comb spectrum is perfectly symmetric at $\Delta = 0$, the impacts of Δ on the comb line distribution is symmetrical around the zero point. (details in Appendix B.3). We then examine the case of negative TOD at -1,000 fs^3/mm, matching our microresonator measurements (-948 fs^3/mm shown in Figure 6.4) and dispersion modelling (detailed in Appendix A.2.2). When Δ is negative, the spanning of comb spectrum on the left-hand side is significantly extended, hence more comb lines are generated on the shorter wavelength side since the modulation frequency better matches the higher frequency FSR (shorter wavelength) due to positive

GVD. This is shown in Figure 6.6a, for the case of Δ = -1,000 kHz. The comb span on the shorter wavelength side is almost 45-nm wider than the longer wavelength side, resulting in the platicon spectral asymmetry and more towards the blue-side.

Figure 6.6b shows that, when Δ = 0 kHz, the platicon comb is restored to a symmetric spectrum, spanning 80 nm. This arises because Δ balances out the effect of negative TOD. In Figure 6.6c, when Δ = 1,000 kHz, we see that the comb shape is asymmetric in an opposite manner (red-weighted) and has a distinctly narrower comb compared to the former two cases. This is due to the Δ and negative TOD both contributing to decreasing the phase matching bandwidth of the FWM. We note that, in each of the three Δ cases (Figure 6.6a to 6.6c), the general feature of the temporal square pulse is still captured in our simulations. Furthermore, we detailed the cases of zero and positive TOD, along with different Δ, in Appendix B.3, wherein the phenomenon is inverted and the platicon spectral asymmetry is at the opposite frequencies.Here, we use skewness from statistics for reference to describe the symmetry of platicon comb spectra (detailed in Appendix B.3). Figure 6.6g summarizes the skewness of the platicon comb spectra in both simulation and experiments. The experimental data points match well with the simulation curve.

Figures 6.6d to 6.6f show our platicon measurements for three different modulation frequencies with Δ of -1,000 kHz, 0 kHz and 1,000 kHz. The general structure of the comb matches the numerical predictions remarkably. In Figure 6.6d ($\Delta \approx$ -1,000 kHz) we observe the blue-weighted platicon comb spectrum; in Figure 6.6e the symmetric comb spectra is observed. In Figure 6.6f ($\Delta \approx$ 1,000 kHz), the red-weighted platicon is achieved. We note that with a 2 MHz change in the modulation frequency, the platicon comb span is tuned by 20 nm and with a controllable blue-red weightage distribution of the platicon frequency comb. We also note that the modulation frequency should not deviate too much from the single FSR, otherwise, the broadband platicon comb is no longer observable.

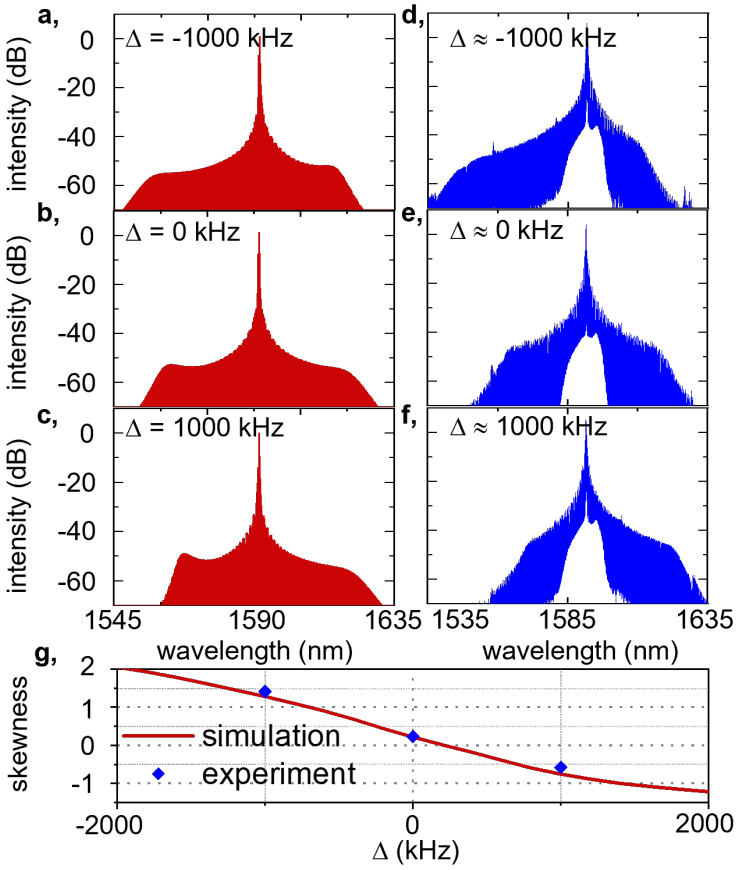

Figure 6.6: Deterministic platicon comb formation controlled by the sideband modulation frequency. a-c, Simulated frequency comb spectra with different modulation frequencies under a TOD of -1,000 fs^3/mm. a: Δ = -1000 kHz, b: Δ = 0 kHz, c: Δ = 1000 kHz. (d)-(f) Experimental frequency comb spectra with different modulation frequencies. d: 19.547 GHz ($\Delta \approx$ -1000 kHz), e: 19.548 GHz ($\Delta \approx$ 0 kHz), f: 19.549 GHz ($\Delta \approx$ 1000 kHz). All comb spectra span around 80 nm. (g) Comb skewness versus sideband modulation frequency Δ.

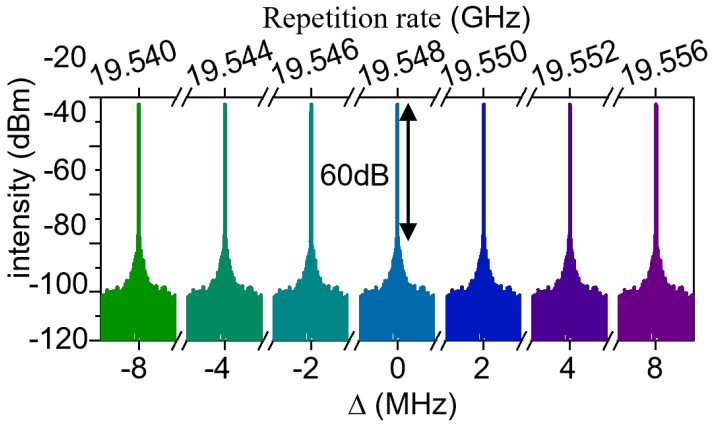

Figure 6.7: Heterodyne beat note of the platicon frequency microcomb at different modulation frequency. The x-axis is the offset frequency with respect to the FSR of pump mode. A 60-dB SNR is observed for each case. The RBW is 1 kHz.

6.3.4 Stability and time-domain characteristics analysis

Next we examine the stability of the platicon comb and its time-domain characteristic of the platicon at stage 3. It is worth mentioning that since the comb spacing is intrinsically locked to the modulation frequency and there are no sub-comb families, the amplitude noise remains intrinsically low, and the electrical beat note remains clean with high signal-to-noise-ratio (SNR) throughout the whole evolution. Figure 6.7 shows the measured power spectral density of the comb spacing beat note with a resolution bandwidth (RBW) of 1 kHz, centered at the $\approx$ 19.548 GHz modulation frequency. No other frequency components are observed. Differing from traditional dissipative Kerr solitons, the platicon is naturally mode-locked, avoiding modulation instability and high noise chaotic comb states. Figure 6.8 subsequently shows the platicon phase noise compared to the LO reference: at lower offset frequencies such as below 1 MHz, the platicon comb phase noise follows almost exactly the LO, with the platicon slightly worse than the LO in the flicker frequency ($1/f^3$) region below 180 Hz. This behaviour is similar to self-injection locking, where the noise performance of the optical microresonator follows the LO. However, starting from $\approx$ 1 MHz in our case, the

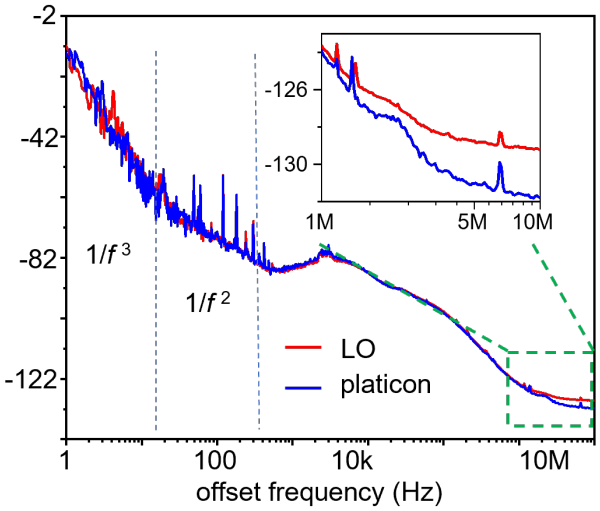

Figure 6.8: Phase noise measurements of the LO and platicon comb. The phase noise of platicon comb almost exactly follows the phase noise of the LO in the low frequency range, except in the $1/f^3$ range, the platicon is slightly better. But starting from 1 MHz, the platicon comb outperforms the LO, and suppresses the phase noise by up to 3 dB.

platicon comb surpasses the phase noise character of the reference LO by up to 3 dB. Since this offset frequency is much lower than the cavity resonance linewidth ($\approx$ 157 MHz), this phase noise suppression should not be from the filtering effect of the resonator, but rather a phase noise low-pass filtering effect of the frequency comb, similar to [124]. The 60-dB SNR of the platicon beat note suggests that the frequency comb is phase-locked and potentially mode-locked. To verify the mode-locking, we next examine the intensity autocorrelation of the platicon. For a square pulse, the time-domain autocorrelation is triangular in structure. The measured autocorrelation of in Figure 6.9 shows a triangular shape with bottom width of 34 ps, indicating that a bright square pulse of 17 ps. Since this is a wide pulse, we implemented a dual-comb cross-correlation to depict the pulse shape. Sampled over 100 pulses, the dual-comb cross-correlated pulsewidth τ_a is gauged to be around 17 ps, and the repetition period ($\tau_a + \tau_b$) is observed to be 51 ps. And further detailed in Appendix A.3.5.

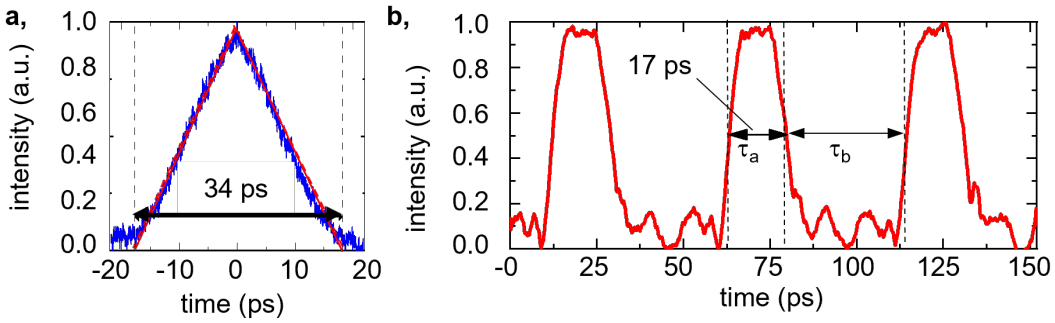

Figure 6.9: Time-domain characterization of platicon. a, Time-domain autocorrelation of the platicon comb. The bottom width of 34 ps of the triangle shape indicates a square bright pulse of 17 ps. b, Cross-correlation of the platicon pulse frequency comb. A 17 ps square bright pulse is directly observed.

6.3.5 Extended access to platicon frequency microcomb

As previously mentioned, the pulsewidth of the platicon square pulse can be controlled by varying the pump-resonance detuning. Nonlinear thermal effect of the microresonator, however, introduces thermal bistable dragging when sweeping the pump across the resonance – this hinders us from accessing the effective red detuning side of the resonance, where narrower square pulses can exist. Hence we implemented an auxiliary-laser-assisted thermal stabilization method [135][41] to overcome the thermal bistable dragging. Narrower deterministically-tuned pulsewidths are successfully achieved.

Figures 6.10a and 6.10b show the frequency comb spectra with pulsewidths of ≈ 4 ps and ≈ 2 ps respectively. Due to the limitation of our cross-correlation implementation (details in Appendix A.3.5), it is not suitable to directly measure the pulse widths of such narrow pulses, however, one can still roughly retrieve the pulsewidth through the unique frequency spectrum of the narrow square pulse, i.e. the two first-minima spacing. The strong modulation of the comb spectrum arises from the Fourier nature of square pulse, which manifests itself as a sinc function in the frequency domain. The size of the main dome (first-minima spacing and bounded by the two vertical dashed blue lines as shown) uniquely corresponds to the

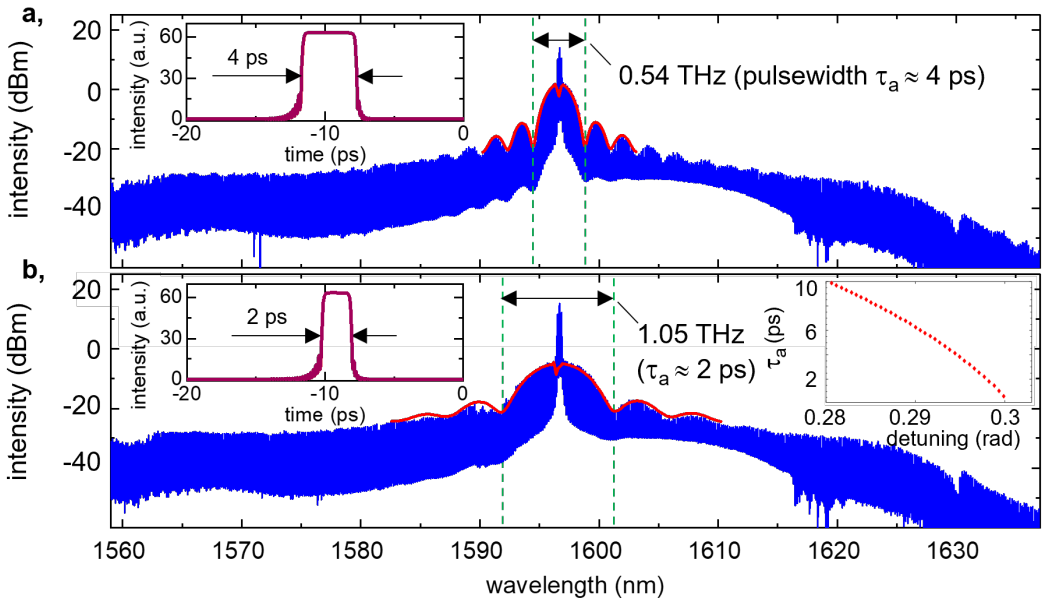

Figure 6.10: Extended access to platicon frequency microcomb. a, Comb spectrum of a 4-ps platicon square pulse. The spacing between the two first-minima is about 0.54 THz. The experimental measurement matches well with simulation platicon comb spectrum (red curve). The inset is the time-domain square pulse simulation corresponding to the red curve, which proves a 4-ps square pulse generation. b, Comb spectrum of a 2-ps platicon square pulse. The simulation of both frequency- and time-domain shows a 2-ps square pulse generation. Left inset is the time-domain profile. Right inset is a summary of the platicon pulsewidths versus δ, which indicates that narrow pulsewidth down to hundreds of fs could be achieved.

pulsewidth τ_a. Figure 6.10a shows a 0.54-THz spacing, which corresponds to a 4-ps square platicon. The frequency domain simulation (red envelope) matches the measurement almost exactly, which bridges the comb spectrum measurement to the corresponding time-domain simulation (inset figure). Figure 6.10b shows another achieved dual-pumped comb state with a 1.05-THz dome size, a Fourier shape that corresponds to the generation of a 2-ps square platicon. As previously discussed, the platicon pulse τ_a could be continuously changed by changing the detuning between the pump frequency and the resonance frequency. The inset of figure 6.10b shows the simulation of the pulse width vs. the detuning below 10 ps. The

narrowest pulse width achievable with current simulation parameters is 0.6155 ps. The inset figure shows that the pulse width becomes more sensitive to the detuning as the pulse width gets narrower. However, in the experiment, due to the frequency tuning resolution limit and the stability limit of the pump laser as well as the limit of the OSA acquisition time, 2-ps pulsewidth is the narrowest platicon pulse that can be captured by the OSA.

6.4 Summary

In this work we demonstrate the platicon frequency comb generation in normal GVD microresonators, with a single-FSR intensity-modulated pumping scheme. Initiated from the wave-breaking dynamics, we analyze the influence of modulation frequency and pump-resonance detuning on the platicon frequency comb properties. A phase-locked and mode-locked frequency comb is observed and the bright square pulse with widths from 2 ps to 17 ps is depicted using dual-comb cross-correlation. We demonstrate the comb symmetry deterministic control with the sideband modulation frequency, together with the third-order dispersion, along with the beat note power spectral density and phase noise character. With auxiliary-laser-assisted thermal stabilization, we not only extend access to forbidden region of platicon generation and narrower square pulse generation, but also simplify the estimation of the platicon pulse without time-domain measurement by bridging the platicon comb spectrum features to its pulsewidth. The microresonator would be a great platform for study of wave breaking regarding propagation loss and stimulated Raman scattering compared to fiber. This work has noteworthy influence on generating frequency comb in normal dispersion regime and with applications such as an intensity-flattened spectral comb for high-rate optical communications, nonlinear optical imaging with fiber endoscopes, pulse shaping and amplification, dual-comb and Raman spectroscopy, and novel on-chip microwave synthesizers.

CHAPTER 7

Nanometric precision distance metrology via hybrid spectrally-resolved and homodyne interferometry in a single soliton frequency microcomb

7.1 Introduction

With length as one of seven fundamental physical quantities, the ability to precisely determine distance to a target is especially important such as in observations of gravitational waves and futuristic space missions of multiple satellite flying formations [165]. With the current international system of units (SI) meter definition based on light vacuum path traveled in a time of 1/299,792,458 second [166, 167], laser-based distance measurement plays a pivotal role to advance length metrology with increasing precision. Most laser interferometers are based on the single-wavelength, with interferometric phase measurement to achieve sub-wavelength precision [168]. Inherently, a single-wavelength laser interferometer measures distance by accumulating a displacement from the initial to the target position, with the non-ambiguity range bounded at half the selected electromagnetic wavelength. To overcome this limitation, absolute distance measurement – which determines distance by a single operation – has been advanced in various platforms [169, 170, 87, 171, 172]. The advent of the frequency comb, which enables the whole optical frequency span to have traceability to well-defined frequency standards in the microwave or optical domains [173, 174, 84], brought about a breakthrough in absolute distance measurements [175]. The broad spectrum and ultrashort pulse of the frequency comb enable advanced laser distance metrology includ-

ing dual-comb interferometry [87, 176], synthetic-wavelength interferometry [177, 178, 179], spectrally-resolved interferometry (SRI) [180, 181, 182, 183], multi-wavelength interferometry [184, 185, 186], and cross-correlated time-of-flight measurements [171, 187]. Recently chip-scale microresonators have contributed to progress in laser frequency combs [5, 17, 62, 21] including the generation of different frequency microcombs [26, 15, 52, 188] temporal solitons [16, 128], integrated low-power microcombs [95], and optical frequency synthesizers [54]. These microcombs enable applications such as low-noise microwave generation [91, 8], optical communications [56], spectroscopy [104, 55], and distance measurement at $\approx$ 100 nm precision [58, 57, 101].

Here we describe spectrally-resolved laser ranging via a soliton frequency microcomb, with precision length metrology at the few nanometers scale. A single microcomb is utilized, of which the SRI (SRI) of the measurement and reference pulses engraves information on the optical time-of-flight. With the large (88.5-GHz) free-spectral range and high-coherence of our selected frequency microcomb, we directly read out the tooth-resolved and high-visibility interferogram via optical spectrum analyzers. We utilize a dual-pumping technique to stably generate the soliton mode-locking in a planar-waveguide Si_3N_4 microresonator, which is the same as in chapter 4. We describe the time-of-flight signal reconstruction via the integrated platform of comb-line homodyne interferometry, microcomb and background amplified spontaneous emission SRI, from the same spectral interferogram. The comb-line homodyne interferometry is unwrapped with the relatively-coarse microcomb, which is itself unwrapped with the low-coherence amplified spontaneous emission interferometry in the comb-background to achieve a 3-nm precision over a 23-mm non-ambiguity range. We sample the long-term distance metrology over 1,000-seconds stability and an Allan deviation up to 300-seconds, with a 3-nm measurement repeatability achieved from homodyne interferometry. The chip-scale single microcomb provides a platform to apply a hybrid microcomb and homodyne SRI architecture, achieving white noise-bounded high precision at long integration times and short distances, even comparable to a few-Hz stabilized fiber frequency combs. We

further demonstrate measurement linearity in example positional calibration and referenced against a three-dimensional (3D) precision gauge block for principle demonstration.

7.2 Measurement concept of soliton microcomb ranging by SRI

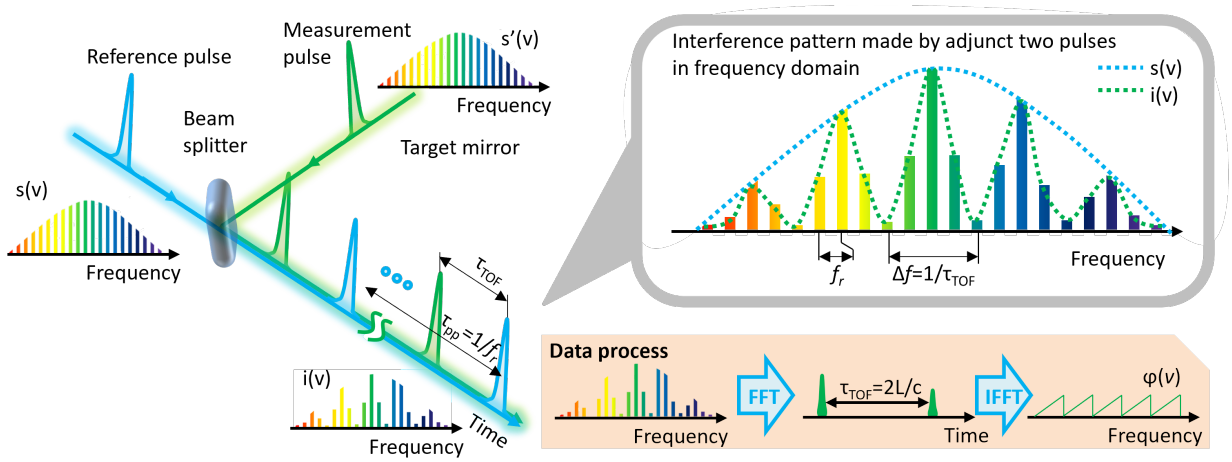

Figure 7.1: Architectural approach of the spectrally-resolved ranging via soliton microcomb. Reference and measurement pulses of the soliton frequency comb, separated by τ_{TOF}. The measurement pulse has a relative phase shift $\varphi(\nu) = 2\pi\nu \times \tau_{TOF}$ to the reference pulse, and it makes an interference in every frequency mode of the soliton frequency comb. The information of τ_{TOF} is thus engraved on the interference pattern in the frequency domain, monitored via the spectrometer. The wide free-spectral range of frequency microcombs enables its comb-tooth resolved spectral interferogram to be directly readout by readily-available optical spectrum analyzers.

Figure 7.1 shows our laser dimensional measurement concept with the soliton frequency microcomb. The time-delayed measurement pulse is described by relative phase delay $\Delta\varphi(\nu) = 2\pi\nu \times \tau_{TOF}$ to the reference pulse, with ν the optical carrier and τ_{TOF} the measurement-reference time-of-flight delay. With $s(\nu)$ the pulse spectrum, two separated pulses generate a frequency interference pattern as $i(\nu) = s(\nu)[1 + \cos\varphi(\nu)]$, engraving the time delay with $1/\tau_{TOF}$ period (Figure 1 right panel) with target distance L determination from $2n_{air}L = c_0\tau_{TOF}$, where c_0 is the vacuum speed of light and n_{air} the medium refractive

index. The time delay τ_{TOF} is directly determined by the peak position of the i(ν) Fourier-transform, expressed as $I(\tau) = FT\{i(\nu)\} = S(\tau) \otimes [\delta(\tau + \tau_{TOF})/2 + \delta(\tau) + \delta(\tau - \tau_{TOF})/2]$, where $\delta(\tau)$ is the Dirac delta function, $S(\tau)$ the s(ν) Fourier transform, and τ the time delay. Since s(ν) is a real function, its Fourier transform $S(\tau)$ is symmetric about $\tau = 0$ and repeated every $\tau = \tau_{pp} = 1/f_r$, where f_r is the repetition-rate and τ_{pp} the pulse-to-pulse temporal separation.

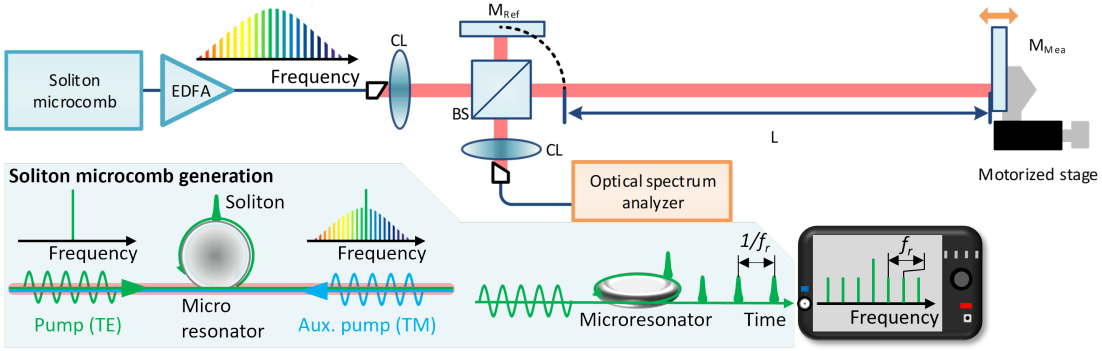

Figure 7.2: Soliton microcomb-based precision dimensional metrology via SRI. BS: non-polarizing beam splitter, M_{REF}: reference mirror, M_{MEA}: measurement mirror, EDFA: erbium-doped fiber amplifier, CL: free-space collimator lens. Left inset describes schematic for the TE-TM dual-pumped soliton microcomb generation.

Since the τ_{TOF} peak is symmetrical to $\tau_{pp}/2$, the measured τ_{TOF} folds at $\tau_{pp}/2$ and the measured distance has a triangle-shaped profile with increasing target distance [19]. Thus, the target distance is expressed as $2n_{air}L = c_o((m+1) \times \tau_{pp}/2 + \tau_{TOF}$ for even m, or $2n_{air}L = c_o(m+1) \times \tau_{pp}/2 - \tau_{TOF}$ for odd m, where m is an integer. In general, the calculated τ_{TOF} from (τ) peak detection is not precisely determined and is limited by the s(ν) bandwidth. We use a curve-fitting algorithm for precision peak detection and homodyne interferometry toward nanometer-level precision. Note that the non-ambiguity range(L_{NAR}) is determined from $f_r[L_{NAR} = c/(4f_r)]$ which corresponds to 850-μm (f_r = 88.5 GHz). For further precise measurement, we use the optical carrier phase from the inverse Fourier transformation of

$S(\tau)$. Then the target distance can be defined as $2n_{air}L = c_0/\nu(M_{homodyne} + \varphi(\nu))$, where $M_{homodyne}$ is the integer of the homodyne interferometry.

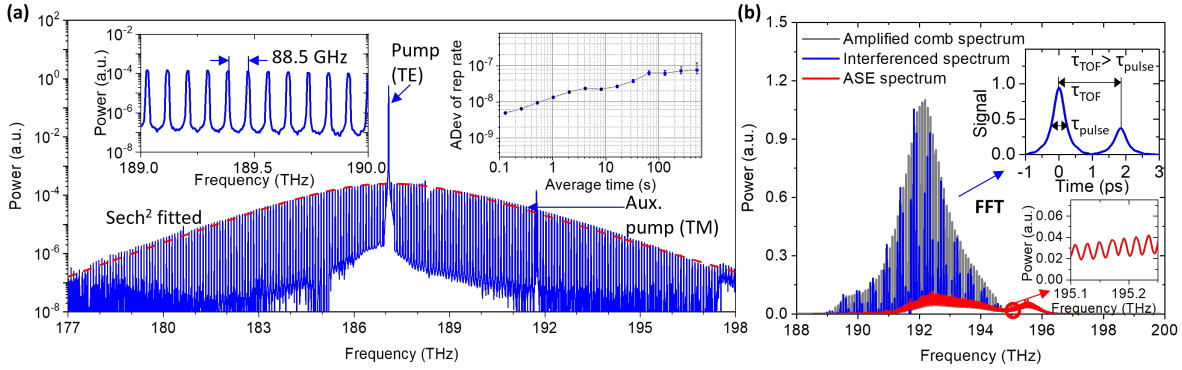

Figure 7.3: Soliton microcomb-based precision dimensional metrology. a, Example optical spectrum of the soliton microcomb from the high-Q Si_3N_4 microresonator, with the hyperbolic secant-square spectrum. Left inset: zoom-in illustration of the comb-tooth resolved spectrum. Right inset: Frequency stability of free-running repetition rate (f_r). b, Example measured high-coherence spectral interferogram (blue) from the reference and measurement pulses, along with the superimposed spectra of the C-band amplified soliton microcomb (gray). Red line shows the amplified spontaneous emission (ASE) noise induced by the EDFA from the same spectral interferogram of the blue line. Inset: zoom-in illustration of the low-coherence ASE spectral interferogram with the low-visibility interference.

Figure 7.2 depicts the setup for the microcomb-based dimensional metrology. A dissipative single-soliton is generated in a planar Si_3N_4 microresonator, with loaded quality-factor Q of 1.77×10^6, free spectral range (FSR) of 88.5 GHz, and anomalous GVD β_2 of -3 $\pm$ 1.1 fs^2/mm at 1595-nm. The stable single-soliton microcomb mode-locking is achieved with a counter-propagating dual-driven technique (discussed in chapter 5 and 4). Figure 7.3a shows the generated single-soliton microcomb, formed in the microresonator with Kerr nonlinearity. The soliton microcomb has a hyperbolic secant-square shape with a 1595-nm center wavelength and a 40-nm bandwidth. Such a broad spectrum fits well with SRI since the minimum measurable distance ($L_m$in) is limited by the Fourier-transform limited pulse

duration of light source (τ_{pulse}) as $2L_{min} = c_o \times \tau_{pulse}$ [180]. The right inset of Figure 7.3a shows the repetition rate (f_r) frequency stability Allan deviation, at about 5×10^{-8} level between 0.5 to 100-seconds.

Figure 7.2 shows the experimental setup for absolute distance measurement. A C-band section of the soliton comb is first amplified with an erbium-doped fiber amplifier up to 10 mW, centered at 192-THz with 2-THz bandwidth. A 50:50 beam splitter divides the soliton microcomb pulses into the reference and measurement arms for the interferometry and recombines upon the pulses return. The measurement mirror (M_{Mea}) is mounted on a motorized stage for translational motion. The recombined beam is collimated into a single-mode fiber, and sent into an optical spectrum analyzer with 50-pm resolution and 10-pm accuracy (or equivalently 6.3×10^{-6} wavelength inaccuracy with respect to the optical electromagnetic carrier). An example resulting spectral interference pattern is shown in the blue plot of Figure 7.3b. Since the microcomb has a large 88.5-GHz repetition-rate, the comb tooth-resolved interferogram can be directly read out with optical spectrum analyzer. In contrast, conventional fiber frequency combs rely on Fabry-Perot etalon-based mode filtering or virtually-imaged phase array spectrometers for comb tooth-resolved spectrograms. In Figure 7.3b, the background gray spectrum is the amplified C-band section of the original soliton microcomb for reference.

7.3 Absolute distance metrology by soliton microcomb-based SRI

To evaluate the measurement reliability, we measured a fixed distance over 1,000-seconds with a 1-second update rate. During the measurements, the air refractive index is fixed at 1.000247, which is calculated by the empirical equation under standard air [189][49]. Since the non-ambiguity range of microcomb-based SRI is limited by hundreds of micrometer, we extend the non-ambiguity range by introducing coarse measurement from ASE spectrum-based SRI [190, 191][50,51]. Since the spectrometer resolution is 50-pm ($\delta v_{spectrometer}$

= 6.14-GHz at 1560-nm), the maximum measurable range of ASE spectrum-based SRI (L_{MAX_ASE}) is 23.4-mm by relation of $L_{MAX\_ASE} = c_o/2n\delta v_{spectrometer}$. Further measurement range extension can be realized by introducing other coarse distance metrology [181, 186][20,25]. As shown in Figure 7.4b, the target distance ($L_{Mea} = c_o\tau_{TOF}/2$) and non-ambiguity range ($L_{NAR} = c_o\tau_{pp}/4$) is determined from the reconstructed time-domain signal, based on Fourier transform of the interference pattern in the frequency domain. Figure 7.4b shows the non-ambiguity range at 0.847424-mm. We see a large peak enhanced by summation of the ASE and microcomb spectrum, extending the measurement range.

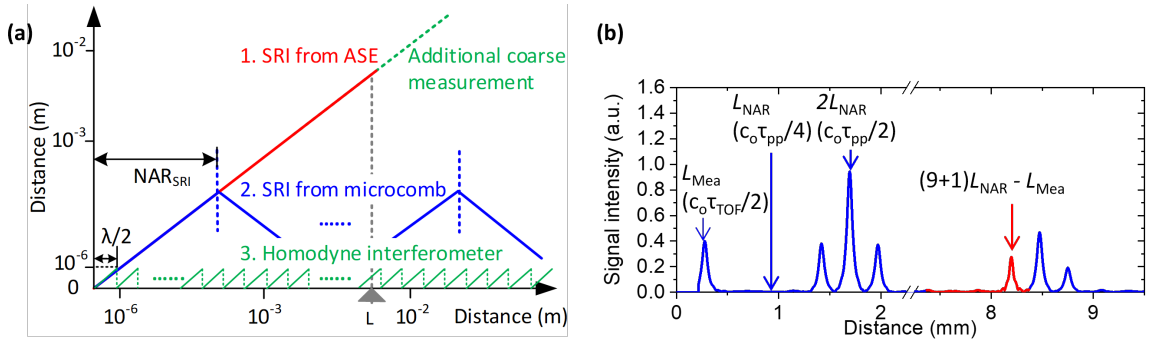

Figure 7.4: Distance measurement beyond the non-ambiguity range. a, Non-ambiguity range extension by the combined platform of ASE-noise-based spectral interferometry, soliton microcomb spectral interferometry and homodyne interferometry. To determine integer M of the homodyne interferometry, the coarse distance measurement from the microcomb (with $\lambda/2$, where $\lambda = c_o/v$.) is used. At the same time, to determine integer m of the microcomb, the ASE SRI is used. b, Time-domain signal reconstruction from the frequency domain interference. A typical signal-to-noise ratio of the time-domain signal is larger than 100.

We evaluate the measurement linearity by comparing with the encoder inside the motorized stage as shown in Figure 7.5. As shown in Figure 7.5(1), we model the positioning error with 3 types of spectral shapes with ideal interference pattern on the spectrum. Although amplified comb spectrum is narrower than original soliton microcomb spectrum, the positioning error of amplified comb spectrum case is better because of its smooth spectrum shape. The positioning errors of amplified comb, full microcomb and $sech^2$ spectrum with same spec-

tral bandwidth of amplified comb are estimated with standard deviations (1σ) of 124-nm, 560-nm and 23-nm, respectively. The measurements revealed a peak-to-valley discrepancy of $\pm$ 2.56-μm. We note that the comparison is limited by the motorized stage due to its low accuracy ($\approx \pm 5 - \mu$m). For further comparison, we compare the measurements between microcomb SRI and homodyne interferometry. The peak-to-valley discrepancy is $\pm$ 293-nm with standard deviation (1σ) of 185-nm. We also evaluated the translation motion exceeding the non-ambiguity range of 850-μm as shown in Figure 7.5inset. For comparison, the fiber comb-based SRI result is also plotted in light cyan. Beyond the non-ambiguity range, our measurement and the encoder match well within the encoder accuracy. We also measured a standardized gauge block cross-section with 3-mm height to validate the microcomb SRI for potential 3D surface measurement. The measurement repeatability taken over 5 consecutive measurements is determined to be 327-nm and 11.4-nm from microcomb SRI and homodyne interferometry respectively as the 1σ standard deviation. These results demonstrate that the microcomb SRI has a good potential for length and positioning calibration such as length standards and high-precision axial positioning.

As shown in Figure 7.6a and 7.6a up to 1,000-seconds, the measured distance from microcomb SRI is nearly constant without notable long-term drifts and has a standard deviation (1σ) of 81.6-nm. In contrast, the ASE spectrum-based SRI shows large fluctuations in the distance measurement due to its incoherence, but aids to extend the measurement range via non-commensurate periods in the time-domain. The ASE spectrum-based SRI measurement range is instead usually limited by the spectrometer optical resolution. An average value of the measured distance from microcomb-based SRI is found to be 8.197951-mm, and its accuracy is estimated to be 52-nm bounded by the optical spectrum analyzer. This accuracy can be enhanced by precisely measuring the repetition-rate f_r, instead of reading out solely the spectrum analyzer values. Measurement repeatability (in terms of Allan deviation) is calculated via the long-term measurement as shown in Figure 7.7. As noted in Figure 7.7, the measurement repeatability of microcomb-based SRI at 1-second

(without averaging) is found to be 80-nm. The measurement repeatability gradually improves to 11-nm, with a measurement fitted relation of 80-nm $\times\tau_{\text{avg}}^{-0.5}$. For longer averaging time more than 10-seconds, the measurement repeatability remains below 20-nm.

Homodyne interferometry provides a complementary approach to further improve the distance metrology precision at the nanometric level, since it employs the optical carrier frequency instead of the pulse train envelope in microcomb ranging. Using multiple comb lines, our comb-based homodyne interferometry counts the optical carrier phase, and its measured distance has a standard deviation (1σ) of 10.4-nm during the 1,000-seconds integration. We observed slowly-varying fluctuations (random walk), as shown in Figure 7.6a. (We note that for specific ranges, such as 900 to 1,000-seconds in this case, the standard deviation improves to 3.6-nm.) An average value of the measured distance from homodyne interferometry is found to be 8.197915-mm. As shown in Figure 7.7, the measurement repeatability of homodyne interferometry at 1-second is found to be 2.85-nm which deteriorated to 6.62-nm at 100-seconds. The measurement repeatability of microcomb-based SRI and homodyne interferometry are overlapping at more than 100-seconds of averaging because it is perhaps bounded by slowly-varying fluctuations on the optical path delay due to measurement path thermal expansion, air refractive index variations by slowly-varying environmental drift, or long-term fluctuations of the measured spectrum. If we remove long-term drift using high-pass filtering, the measurement stability can be enhanced to sub-nm at 100-seconds. The measurement repeatability is well-matched to each other, verifying that our measurement stability is not limited by the soliton microcomb. We note that the main limitations on the repeatability is the intensity fluctuations such as from the spectrum analyzer, microcomb, polarization and distance variations.

7.4 Summary

In this work, we have examined the scaling of the microcomb SRI with estimates of the microcomb stability (detailed in Figure S8). For distances smaller than 1-m, our precision limit is bounded by the measurement repeatability. For distances more than 1-m, the measurement precision will be bounded by the frequency stability of our free-running frequency microcomb which has been reported at the 10-8 to 10-9 level [13]. The scaling is square-root proportional with distance since for the longer distances the precision limit is bounded by the microcomb frequency instability ($\Delta f/f \sim \Delta L/L$). When locking the free-running microcomb to a Rb atomic clock or micro-photonic reference [12, 192, 193, 194], the frequency stability can be brought down to 10-12 at 100-seconds integration, further improving the long-distance precision of the single-soliton microcomb SRI. Our proposed scheme can be a platform for next-generation length standards via chip-scale laser frequency microcombs.

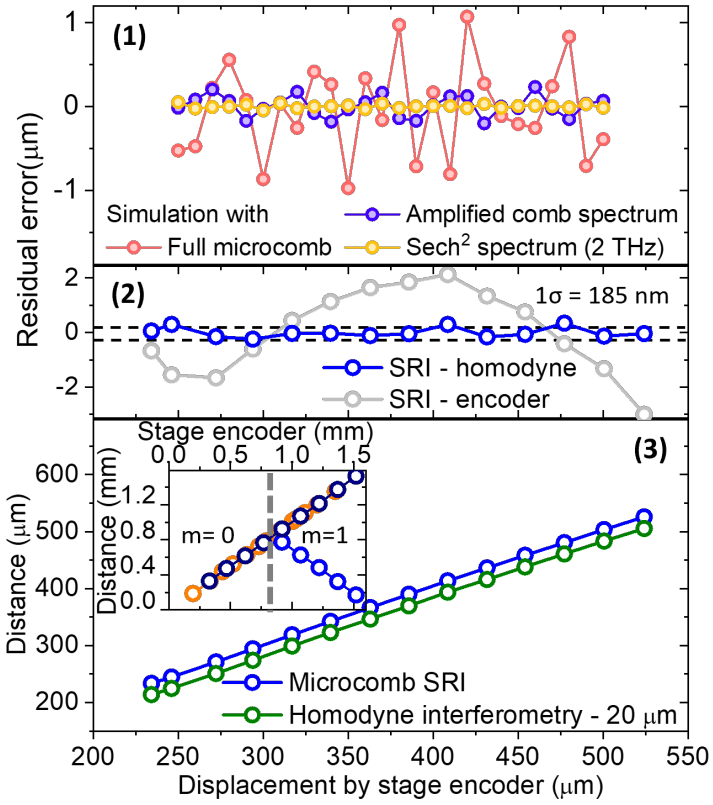

Figure 7.5: Measurement linearity of SRI. Measurement linearity is evaluated by measuring the target distance with 25-μm incremental translation of a motorized stage. Top panel is the modeled results of positioning error for different spectral shapes. Middle panel is the residual error comparing SRI, homodyne interferometry and the encoder. Bottom panel left inset shows the measured distance beyond the non-ambiguity range. The wrapped distance is unwrapped with calculated non-ambiguity in navy color. For comparison, a distance measurement from fiber-comb based SRI is also plotted in orange color.

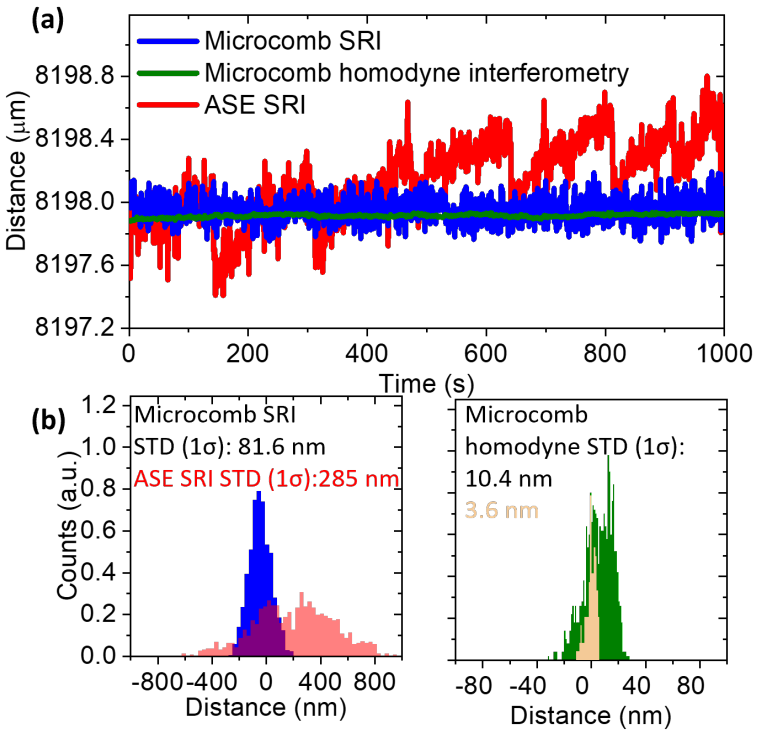

Figure 7.6: Nanometer-scale precision distance measurement: reliability evaluation. a, Long-term distance metrology sampled over 1,000-seconds. b, Left figure: histogram distribution of microcomb spectral interferometry and ASE spectral interferometry, with 1σ standard deviation of 81.6-nm (blue) and 285-nm (red) at 1,000-seconds measurement. Right: histogram distribution of homodyne interferometry, with 1σ standard deviation of 10.4-nm at 1,000-seconds measurement (green color). The 3.6-nm standard deviation is an example obtained from 900 to 1,000-seconds (yellow color).

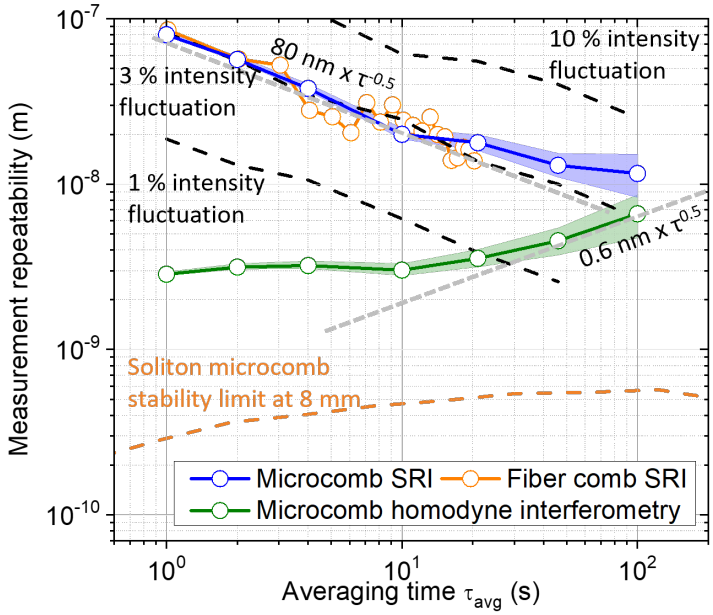

Figure 7.7: Nanometer-scale precision distance measurement: repeatability evaluation. Measurement repeatability verification through Allan deviation of the long-term ranging data. 3-nm measurement repeatability is achieved from drift-compensated homodyne interferometry. The white noise limit is denoted by the dashed gray line while flicker noise is not observed within our 100-seconds averaging time. Measurements from a few-Hz-stabilized fiber mode-locked laser frequency comb laser metrology are illustrated for comparison. Black dashed lines denote simulation results about intensity fluctuation induced measurement repeatability. Orange dashed line denotes the free-running soliton microcomb frequency instability-induced measurement repeatability at 8 mm.

CHAPTER 8

Free-space terabit/s coherent optical links via platicon frequency microcombs

8.1 Introduction

With the advent of wavelength-division multiplexing, fiber-based long-haul communications have seen dramatic improvements in land-based communication bandwidths and network topologies. This has transformed an ever-expanding data reach and demand in telecommunications, energy-efficient interconnects, high-definition remote conferences and virtual environments, medicine and health, large-scale computing, and high-energy particle physics experiments. The tremendous demand, however, has led to congestion in the last-mile wireless access networks of the allocated radio frequency (RF) GHz spectra, driving the need towards higher-frequency and optical carriers for wireless communications [195, 196, 197]. Optical wireless offers an intrinsically large THz-level bandwidth, without restrictions in spectrum usage, with ease of deployment, appreciably smaller-lighter receivers, and improved channel security. Furthermore, free-space optical communications provide for terrestrial and satellite links [198, 199, 200], enabling not only building-scale relay networks and backhaul links but also three-dimensional geostationary satellite networks for global broadband connectivity [201]. Working with multitude laser arrays for wavelength-division multiplexing, remarkable Tb/s free-space optical transmission has recently been demonstrated in feeder-link trials [202], including programmable wavelength-selectable switches for necessitated intensity equalization across the array, and in double-pass building-to-building links with electronic

control units [203]. Coherent detection [204], co-transmitted local oscillator tone in Kramers-Kronig transfer [205], and spatial-mode multiplexing [204, 206] have also been examined to further advance the free-space data transmission.

In a single frequency comb source with phase-locked discrete channels, the frequency microcomb has enabled massively parallel data transmission – in soliton [56], dark pulse [99], and high-data modulation formats [100] for example – embedded in fiber-based link demonstrations. The frequency microcomb phase coherence can simplify the error correction complexity due to its highly correlated stochastic phase and intensity fluctuations between the frequency comb carrier lines. The line-to-line phase correlations and reduction of inter-channel guard band requirements also simplifies the testbed implementations [207]. Through dual-interleaved soliton microcombs and the combined wavelength-multiplexing and polarization-multiplexing subspaces, aggregate data rates up to 55 Tb/s over 179 carriers have been examined in fiber [56]. Subsequently, spatial-mode multiplexing and higher-order digital data modulation further enabled 1.84 Pbit/s net data rates with 223 wavelength-multiplexed channels [208], and a 10.4 bit/s/Hz spectral efficiency [100], in the fiber subsystem testbeds. With the multiple orthogonally multiplexing schemes, aggregate data rates up to even 49.7 Tb/s per fiber core have been demonstrated with frequency microcombs [208] and up to 97.7 Tb/s per fiber core with bulk laser combs [209].

Here we report the first terabit/s-scale data communications in a free-space atmospheric link, via an intensity-equalized platicon frequency microcomb. Spanning over 64 optical carriers in both the wavelength- and polarization-multiplexed subspaces, an aggregate 10.2 Tbit/s coherent data transmission is achieved, at 20 Gbaud symbol rate per carrier, 115 GHz channel spacing and over 160 m atmospheric distances (indoor and outdoor hybrid link), even under log-normal turbulent conditions. 16-state quadrature amplitude modulation is examined, with the retrieved constellation maps characterized line-by-line across the efficient platicon microcomb and with stabilized free-space communication bit-error rates below the hard- and soft-decision thresholds for forward-error correction. Second, to enable multiple-

access networks, we examine the SISO communications, driving down the raw error rates to 6.5×10^{-5} over 10^6 symbols while preserving the overall intradyne signal quality. With our digital signal processing (DSP) algorithms and including hard-decision forward-error correction overheads, in our SISO we report an aggregate data rate up to total 5.2 Tbit/s data rate, a field-tested 1.3 bit/s/Hz spectral efficiency and a quantified 3.8 dB power penalty comparison with respect to the theoretical additive white Gaussian noise limits. Third, in our platicon microcomb free-space testbed, we quantify turbulence-induced intensity scintillation and pointing error fluctuations on the end-to-end symbol error rates, supported by our channel fading models. High-order modulation scaling, even in the presence of transceiver noise and channel non-idealities, are subsequently examined in our free-space microcomb testbed.

8.2 Microresonator-based platicon frequency microcomb generation

8.2.1 Device design and platicon comb generation

The designed Si_3N_4 microresonator has a $2 \times 0.8 \mu m^2$ waveguide cross-section with 200 μm radius, FSR of 115 GHz, loaded quality factor of Q ≈ 700,000, and GVD of ≈ $50 fs^2/mm$. The pump mode is chosen at around 1591 nm, where the adjacent mode (-1st mode) has a large mode shift due to higher-order mode coupling. To initiate the platicon microcomb, a CW ECDL (New Focus TLB 6730), amplified by an EDFA (BKtel) up to 36 dBm and then selected by a cube polarization beam splitter (PBS) for quasi-TM mode pumping, is slowly tuned into resonance from the blue-detuned regime of the pump mode and then the platicon microcomb is generated through cascaded four-wave-mixing. The quasi-TM mode is selected instead of the quasi-TE polarization due its normal group velocity dispersion to facilitate the platicon comb formation. A OBPF with a 3-dB bandwidth of ≈ 10 nm (Filter 1 in Figure 8.1a inset i) is used to suppress the ASE noise from the high power EDFA. Each

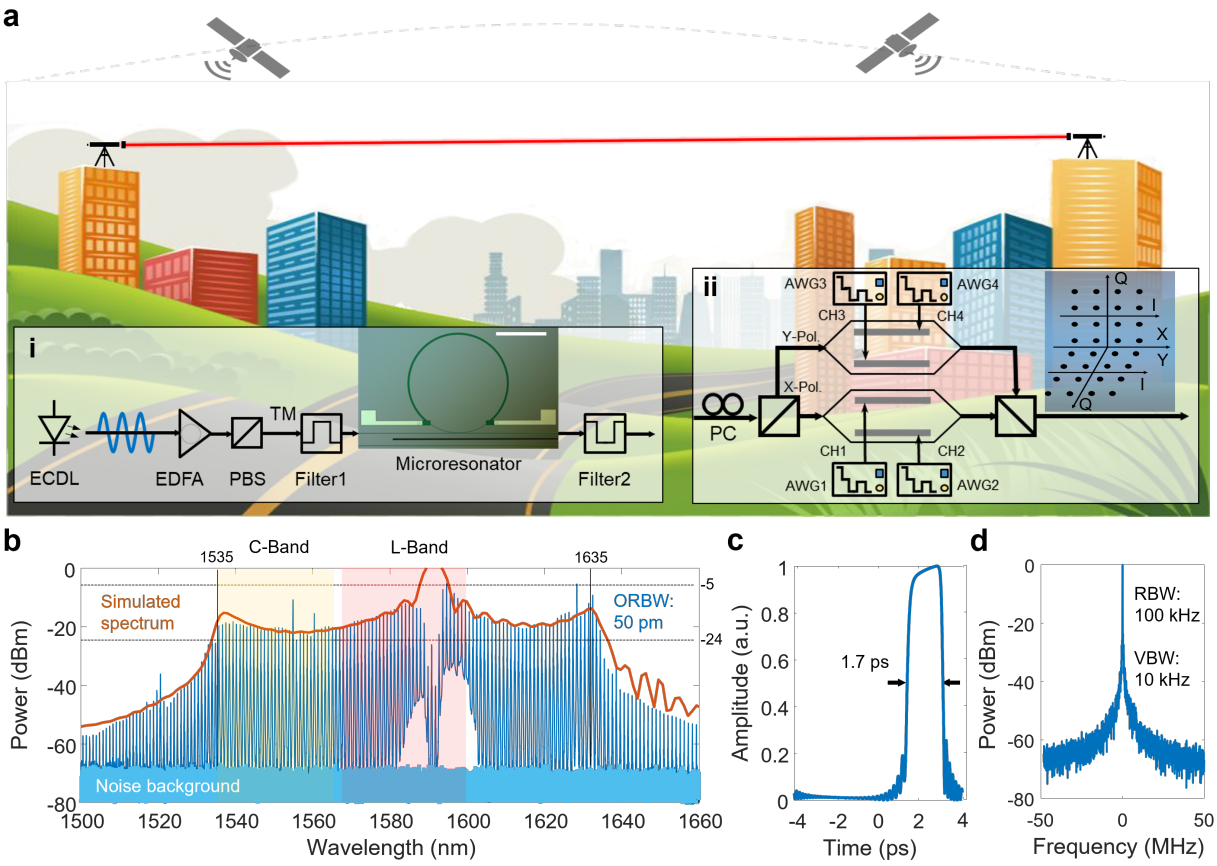

Figure 8.1: FSO wireless coherent communications with an atmospheric horizontal link using a platicon frequency microcomb. a, Conceptual illustration of the free-space line-of-sight optical link. Inset i: Frequency microcomb generation setup including an optical micrograph of the microresonator. Scale bar: 200 μm. Inset ii: PDM EO IQ optical transmitter along with four independent 50 GSa/s AWG. b, Measured platicon frequency microcomb at an ORBW of 50 pm, with LLE modeled spectrum in orange envelope. c, Modeled temporal pulse duration shows a 1.7 ps FWHM. d, Measured heterodyne RF beat note of extracted comb line against an external reference laser, in support of the low-noise square microcomb.

facet of the microresonator has 3-dB loss so that the on-chip power is 33 dBm which is used to generate frequency microcomb. The output power of ≈ 30 dBm is collected. Then the pump mode is suppressed via a narrow bandwidth fiber grating notch filter (Filter2 in Figure 8.1a inset ii) to avoid power saturation in downstream amplifiers and sent for the data transmission measurements. We tune the pump wavelength from blue-detuned side to approach the pump resonance, achieving the close-rectangular-shaped microcomb spectrum shown in Figure 8.1b with a conversion efficiency $\eta \approx 11\%$. The close-rectangular-shaped spectral roll-off factor is 7.4 dB/nm and 3.0 dB/nm for the long- and short-wavelength comb edges, respectively.

8.2.2 Platicon frequency microcomb characterization

A conceptual wireless optical communication scenario with a line-of-sight atmospheric link between two buildings is illustrated in Figure 8.1a, with the broadband coherent frequency microcomb source generation setup shown in inset i and the coherent data encoding schematic shown in inset ii. To ensure broadband operation, we carefully choose the normal dispersion frequency microcomb with a unique platicon dark-soliton spectral generation to preserve rectangular flattop comb line intensities over a 12.5 THz (100 nm) 19-dB bandwidth as illustrated in Figure 8.1b. This platicon microcomb provides more than 100 high-quality optical carriers with optical carrier-to-noise ratio (OCNR) of ≈ 50 dB, with a 115 GHz channel spacing for continuous stable operation without significant power drift and without dropping the low-noise comb state. We modulate the platicon microcomb input using polarization-diverse IQ modulators with four independent 50 GSa/s arbitrary waveform generators (AWG) as shown in inset ii of Figure 8.1a. Figure 8.1c shows the modeled pulse duration of 1.7 ps from the rectangle comb spectral envelope. Intensity fluctuations and linewidth broadening are examined by continuous-wave heterodyne beat note measurements, as shown in Figure 8.1d, between individual comb lines and a standalone narrow linewidth (≈ 100 kHz) ECDL, indicating the low-noise of the comb in support of free-space coherent communications. Fig-

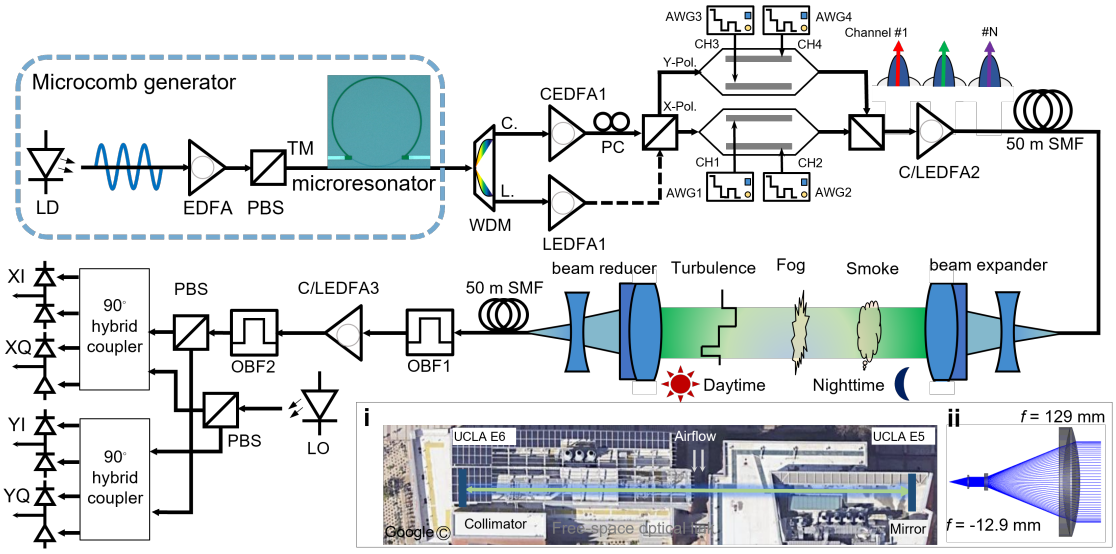

Figure 8.2: Data transmission setup, with polarization-division multiplexing (PDM) and wavelength-division multiplexing (WDM). Inset i: Aerial map of the free-space link field trial. Inset ii: Beam expander/reducer schematic diagram.

ure 8.2 shows the data transmission setup used to conduct the free-space PDM-WDM and the PDM-SISO coherent data transmission over a 160-m atmospheric horizontal link, based on the platicon frequency microcomb. The microcomb is spectrally split into the broad C- and L-bands with a fiber-based WDM, subsequently amplified by C- and L-band amplifiers independently to boost the average optical power of each spectral band. The microcomb has 29 C-band and 27 L-band carriers injected into the polarization-multiplexed IQ modulators. The aerial view inset i in the Figure 8.2 shows the field trial measurements of our free-space link. Detailed link design and stabilization are described in Appendix D. With amplifier compensation of the insertion and modulation loss, Figure 8.3a shows the raw output spectra for both the C-band ($\leq$ 4 dB power variation and $\geq$ 30 dB optical signal-to-noise ratio, $\mathrm{OSNR_{TX}}$) and L-band. The L-band spectrum shows lower OSNR around the 1591 nm pump wavelength, attributable to residual pump EDFA ASE noise. One figure-of-merit – the OSNR at the transmitter (OSNRTX) – is defined considering the carrier OCNR and ASE noise from the first C/L band EDFAs (CEDFA1/LEDFA1) before the free-space link. Our

platicon-comb transmitter subsystem has an average OSNRTX $\approx$ 30 dB over the example 56 C- and L-band carriers to enable the link.

8.2.3 Data communication system calibration and implementation

The microcomb output with power of 7.5 dBm is used for data transmission which is filtered by a 4 nm fiber grating notch filter to suppress the pump laser more than 40 dB. The filtered optical spectrum is split into C and L band with a power of -5.8 dBm and 4.2 dBm, respectively. The communication experiments were conducted as below. First, two commercial ECDLs are used to examine the data transmission system to achieve error-free communication with 105 symbols. Second, one of platicon microcomb lines is coupled in for the communication link. Third, to explore the power penalty originating from the frequency microcomb compared to the state-of-art EDCL, a noise loading measurement is carried out. Fourth, the back-to-back PDM-WDM communication is carried out without free-space transmission link to examine the validity of the optical carriers over C-band and L-band. Fifth, the PDM-WDM and PDM-SISO coherent data transmission are carried out for C/L-band and L-band respectively over a 160 m atmospheric horizontal free-space link. The raised-cosine filtering 16-QAM symbols are generated and loaded into four high-performance AWGs (Tektronix AWG 70001B) with a sampling rate of 50 GSa/s and a vertical resolution of 10-bits. By conducting the phase adjustment relative to the system clock to change the time skew between different AWGs (with reference to the demodulated eye-diagram), the four AWGs can be synchronized with precision of less than 2 ps. Subsequently, the data streams are loaded into the XI, XQ, YI, YQ of the PDM IQ modulator (Tektronix OM5110) with the optimized bias voltage of XI = 4.74 V, XQ = 1.84 V, YI = -2.48 V, YQ = 4.35 V, XP = 11.04 V and YP = 18.78 V. The loss, including the modulator insertion and modulation losses, is around 20 dB. Transmitter impairments are mitigated by monitoring the skewness of the demodulated constellation diagram via adjusting the relative time delay between I and Q arms. The relative time delay between X-polarization and Y-polarization

is minimized by checking the central alignment of the demodulated eye-diagram at the X- and Y-polarizations. Thereafter the bias voltages of the transmitter are optimized by examining bit error rate (BER) and error vector magnitudes (EVM) in real-time. A tunable OBPF (EXFO XTA-50) is used to center each optical carrier within a 3 nm bandwidth for data demodulation. The received optical signal is first polarization demultiplexed and then detected coherently with a tunable ECDL (Santec TLS-510) at the output power of 11 dBm. Two synchronized high-performance real-time oscilloscopes (Tektronix DPO70000SX) are used to digitize the waveforms at 100 GSa/s for XI, XQ, YI, YQ individually. This whole process is subsequently repeated over 64 example comb lines of the platicon frequency microcomb.

8.2.4 PM-16-QAM implementation

To increase the link spectral efficiency, we implement PM-16-QAM to encode the data stream on each frequency microcomb channel at a 20 Gbaud symbol rate. The PDM IQ modulators are driven by four independent high-performance 50 GSa/s 10-bit AWGs. The AWGs are programmed to generate four uncorrelated and timing-synchronized pseudo-random bit sequences (PRBS) with a length of 215 to drive the in-phase and quadrature-phase arms at the X- and Y-polarizations (termed as XI, XQ, YI, YQ) such that additional time delay is not required when introducing the data trace uncorrelation. The PRBS bit sequences are generated to synthesize the PM-16-QAM symbol sequences, which are used to modulate the microcomb carriers after raised-cosine (RC) phase shaping with a roll-off factor of 0.5 over a convolution length of 21 symbols and digital-to-analog conversion (DAC). We performed digital pre-compensation to mitigate non-idealities of the modulator, AWG, and coherent receiver in the frequency response. Additionally, we conducted the PDM-WDM system simulation to examine the adjacent channel data crosstalk with channel spacing of 115 GHz to emulate the practical WDM system.

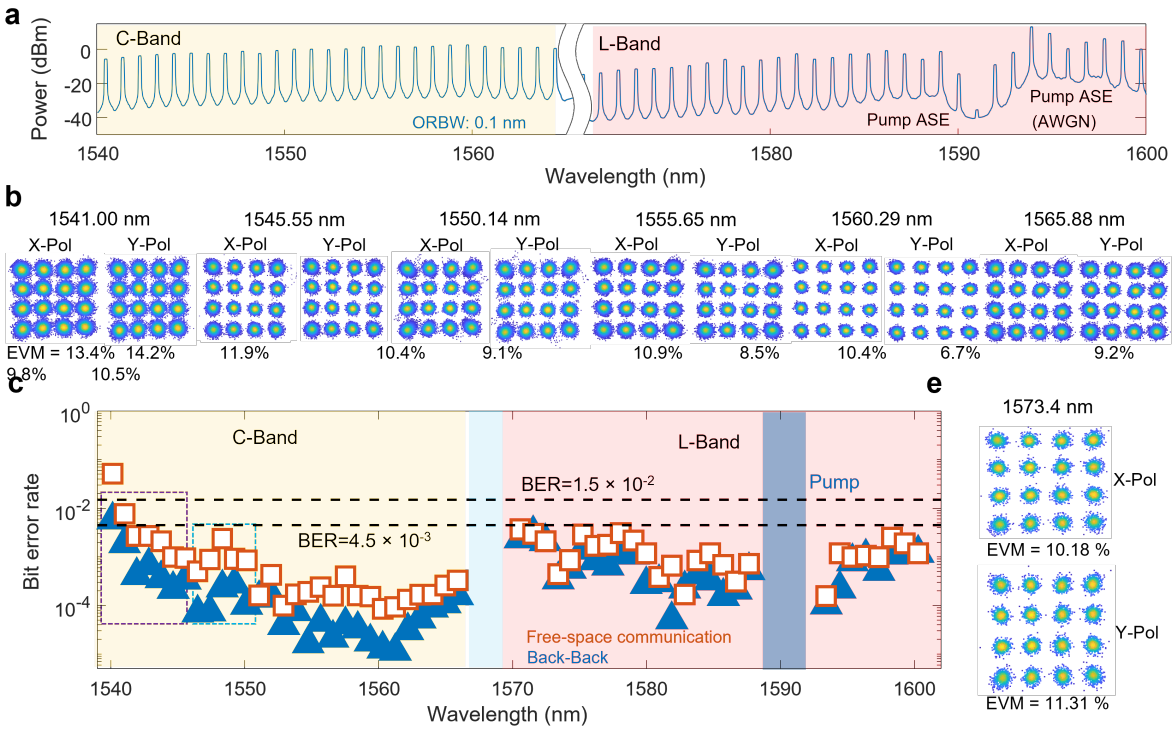

Figure 8.3: Coherent PDM-WDM data transmission over a 160 m horizontal free-space link for point-to-point data transmission. a, Measured optical spectrum of all C- and L-band channels with 100 pm ORBW. b, Example retrieved constellation diagrams of representative C-band channels for both XY polarization and the corresponding EVM. The measured constellation points are not elongated along the azimuthal direction indicating the absence of excessive phase noise. c, Measured BERs of each data channel covering C- and L-band for the free-space link (white squares) and back-to-back interconnect (blue triangles) with the error bars denoting the standard deviation. The BER thresholds are 4.5×10^{-3} and 1.5×10^{-2} for the hard-decision and soft-decision FEC, with 7% and 20% overhead respectively. The EDFA region listed in the left purple dashed box has lower transmitter optical carrier power. The light blue dashed-box region denotes environmental variations (pointing errors) during this particular measurement set. d, Example retrieved constellation diagrams of representative L-band PDM-WDM data transmission.

8.2.5 Free space data transmission link implementation

To demonstrate the free-space link between two buildings at UCLA, the transmitted optical signal at 200 mW (through a second set of C/L amplifiers, C/L EDFA2) is first beam-expanded into a 40 mm beam diameter by a 10× beam expander (Figure 8.2 inset ii) and reflected from a 2-inch silver mirror located in another building after considering eye safety ($\approx 0.004\text{W/cm}^2$ in our link, much lower than the IEC 60825 safety standards requirement of 4 W/cm2). The received optical signal is coupled back via a 10× beam reducer into a single-mode fiber which not only connects with the other fiber-based components but also blocks the environmental background radiation. After the 160-m building-to-building horizontal atmospheric data transmission, we implement a polarization-diverse dual-channel coherent receiver to examine the transmission quality channel-by-channel through a broadband tunable optical bandpass filter (OBPF) and a tunable ECDL.

To calibrate the polarization diversity of our communication link, we first characterize the polarization response of the system with two independent ECDLs and binary phase modulation to extract the system polarization Jones matrix. A third set of C/L-band amplifiers (C/L EDFA3) is used to compensate the free-space link loss and suppress the coherent receiver shot noise. Two synchronized real-time oscilloscopes with four channels are used to digitize the received electrical waveforms of XI, XQ, YI, and YQ, with a sampling rate of 100 GSa/s for off-line DSP. To enhance the platicon microcomb free-space link, DSP algorithms including matched filtering, IQ and XY-polarization time skew correction, offset frequency estimation, optical phase estimation, symbol decision, and demodulation mapping are examined in our link.

8.2.6 Data communication system performance characterization

Figure 8.3b represents example received constellations together with the measured error vector magnitude (EVM), covering the C-band in ≈ 4.5 to 5 nm spectral steps for both po-

larizations and with an average power of 6.9 mW per channel. The deviation of the measured constellations from ideality shows some anisotropy and increases along the radial direction due to power fluctuations of the complex waveforms. The retrieved constellation diagrams are not elongated along the azimuthal direction, indicating no excessive phase noise. We note that the nonlinear impairment and temporal walk-off from chromatic dispersion can be avoided, even when elevating the transmitted average power. Intradyne reception is carried out to examine the communication quality. To obtain the best data transmission quality, the EDFA pump currents are optimized by continuously examining the BER and quality factors Q^2_{dB} of the eye-diagram. As a quantitative characterization of data transmission quality, both the BER and EVM are used. EVM illustrates the effective distance of the received complex symbols with respect to their nominal positions in the constellation diagram, which form a Gaussian-shaped joint probability density function based on the real and imaginary parts of the error vector centered at the respective constellation points. With the small nonlinear and electronic noise in our subsystem, the EVM is related to the BER in our optical additive white Gaussian noise channel. We next conduct back-to-back data transmission with the optical carriers in the C- and L-band of the platicon microcomb after optimizing system parameters to minimize the microcomb phase and intensity fluctuation effects on the link.

Figure 8.3c illustrates the subsequently achieved free-space data transmission by adding the free-space link into the optimized communication system, while maintaining all the parameters and increasing only the output power via the second amplifier pairs (C/L EDFA2). Our increased transmitted average power, via C/L EDFA2, compensates for geometric loss of the free-space link, especially for longer distances, and relieves the power impairment originating from the turbulence-induced propagation beam spatial walk off and wander, and acoustic variation-induced pointing error (PE). Figure 8.3c shows the achieved BER, computed by comparing the decoded bit sequence with the transmitted ones. All comb lines, except the 1540.113 nm and 1541.002 nm channels, provide error-free communication be-

low the BER threshold of 4.5×10-3 (black dashed line). This allows a post-forward error corrected (FEC) BER below 10-15 for transmission over the 160 m free-space link using a hard-decision staircase FEC with a 7% overhead. Over the 29 C-band and 27 L-band channels, this yields an aggregate data rate capacity of 8.96 Tbit/s. The higher error rate channels still show BER below the threshold of 1.5×10^{-2} with a 20% overhead as shown with the black dashed line. After 7% and 20% overhead reduction for the channels, the aggregated data rate capacity is up to 8.29 Tbit/s and the corresponding net spectral efficiency, normalized by the channel spacing, is 1.28 bit/s/Hz. Figure 8.3d shows the representative constellation diagrams in the L-band at the 1573.4 nm channel, along with the corresponding EVM for the two polarization. Furthermore we note that, due to the large channel spacing, good frequency grid stability and associated QAM pulse shaping and matched filtering, the coherent inter-channel crosstalk is negligible in our link. Moreover, other studies [210] have demonstrated that an extinction ratio (ER) of more than 22.2 ± 1.5 dB between adjacent channels is sufficient for suppressing inter-channel crosstalk, aided by commercial tunable delay interferometer or programmable wave-shaping instruments. Our demonstrated free-space PDM-WDM coherent data transmission provides a platform for Tbit/s point-to-point wireless communications. It is worth noting that the WDM communication is demonstrated with one transmitter and hence to demonstrate the validity of coherent data demodulation for an uncorrelated data stream, we next conducted the PDM-SISO data transmission.

8.3 Coherent free-space single-input single-output data transmission

To demonstrate the multi-wavelength frequency microcomb towards multiple-access networks such as WDM passive optical network (WDM-PON), we examine the platicon microcomb for single-input single-output (SISO) data transmission, with the broadcasting network schematic illustrated in Figure 8.4. Advancing from PDM-WDM, the PDM-SISO approach

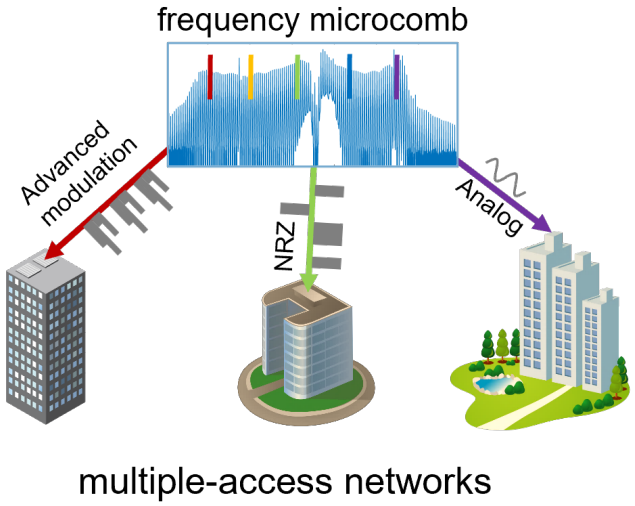

Figure 8.4: Conceptual illustration of the multiple-access network.

allows better noise tolerance due to the high power of the single comb line selected before the PDM IQ modulator and thus overcoming the impact from the residual pump ASE noise. This is a baseline testbed demonstration for multiple access networks and serves as a validation of coherent demodulation for temporally uncorrelated data streams with the developed DSP algorithm. We perform coherent SISO data transmission, including polarization diversity, now with a symbol length up to 10^6. Data transmission is achieved over the same free-space link and an individual optical carrier is selected out after the first EDFA (CEDFA1/LEDFA1) and the corresponding data demodulation performed individually to validate the DSP scheme.

Figure 8.5a shows the representative four-level eye-diagram of the XI component at 1580.93 nm, which elucidates the time delay between the two polarization clearly and visually. For the SISO link, the signal quality factor (Q^2_{dB}) can be calculated from the EVM by $Q^2_{dB} = 20 \times \log_{10}(\sqrt{\frac{1}{EVM}})$, with a Q^2_{dB} of 9.36 dB obtained for the 1580.93 nm example carrier. We note that across our optical carriers, Q^2_{dB} is typically $\approx$ 9.0 to 9.4 in our field trial. With the improved power amplification sensitivity of SISO (compared to WDM), representative constellation diagrams are shown in Figure 8.5b at 1590.53 and 1592.52 nm.

The achieved BERs are $6.5 \pm 5.63 \times 10^{-5}$ and $6.9 \pm 1.88 \times 10^{-4}$. Even with the lower OSNRs

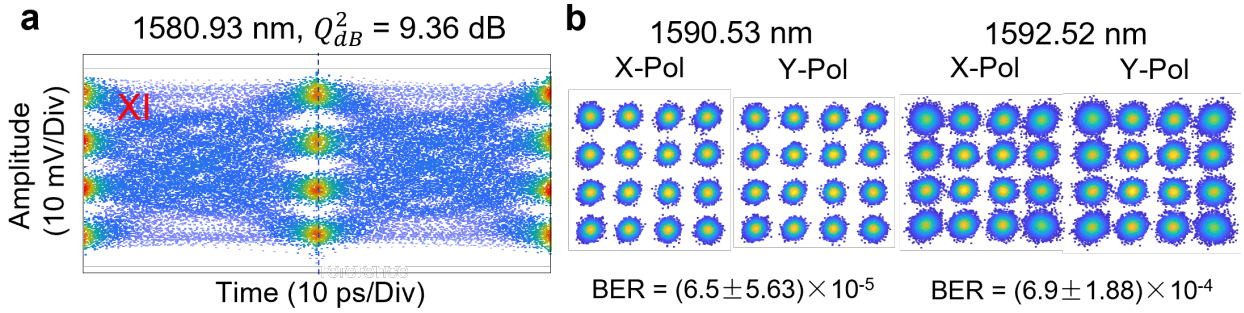

Figure 8.5: Eye diagram and constellation map of PDM-SISO data transmission. a, Representative dual-polarization four-level eye diagram with quality factor Q^2_{dB} of 9.36 dB for the in-phase component of the X-polarization (XI). b, Retrieved SISO constellation diagrams of two example channels (1590.535 and 1592.525 nm) adjacent to the pump laser with the corresponding BER.

in the L-band spectrum of the platicon microcomb, we were able to achieve BERs on the same order-of-magnitude as the PDM-WDM demonstration (1.6×10^{-4} at 1583 nm channel with lowest BER). Due to the small error occurrences with our 1 million symbols in SISO, we use the EVM metric instead of BER to rigorously quantify the data transmission quality. Figure 8.6 shows the resulting EVM distribution for the 35 SISO channels in the frequency comb L-band, along with a 16-QAM EVM threshold of 12.5% for error-free data transmission with the hard-decision FEC indicated by the dashed black line. The EVM for the dual polarization (X and Y) is below the threshold for all channels except the suppressed pump channel. The EVM at wavelengths above 1586 nm has fluctuations, which is related to the varying OSNR. An aggregated data rate up to 5.6 Tbit/s with 35 independent channels over the 160 m atmospheric free-space PDM-SISO link is obtained. Inclusive of the 7% overhead, the corresponding aggregated total data rate can go up to 5.21 Tbit/s, with a 1.29 bit/s/Hz spectral efficiency. The demonstrated PDM-SISO coherent data transmission not only shows the potential of the frequency microcomb source as a link but also provides a solution for free-space multiple-access networks.

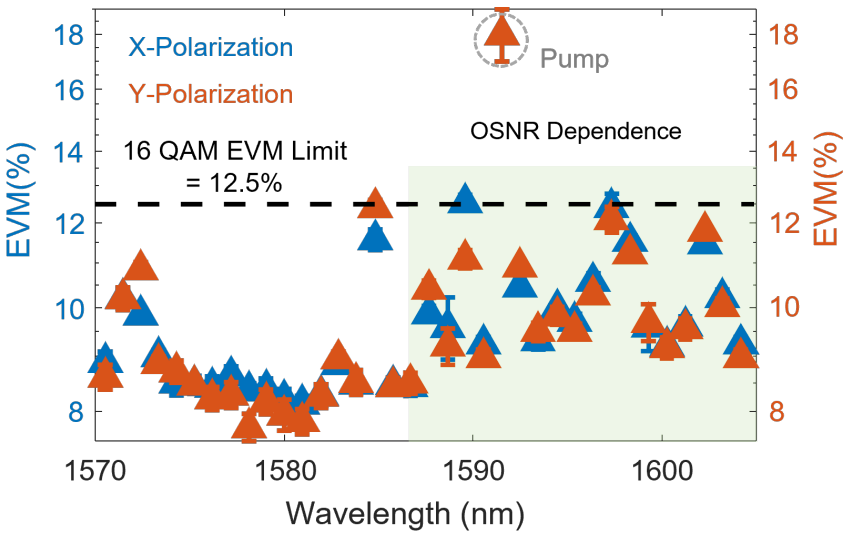

Figure 8.6: Measured EVM of each optical carrier channel with the error bar denoting the standard deviation over the L-band spectral range with the 16-QAM EVM threshold for error-free data transmission.

Figure 3e compares our platicon comb-based transceiver BER performance with state-of-art ECDLs and the theoretical BER limits determined by additive white Gaussian noise. We illustrate this for three arbitrary comb and ECDL wavelengths (1542.93, 1552.96 and 1561.32 nm; at 12.5 GHz spectral resolution in the optical spectrum analyzer) in back-to-back SISO data transmission. To examine the BER evolution measurement, the received OSNR is attenuated at 1.5-dB-step from 27 dB to 12 dB, which increases the ASE noise loading ratio. At the hard-decision FEC BER threshold of 4.5×10^{-3}, the comb-based transceiver has an $\approx$ 3.8 dB OSNR degradation (power penalty) with respect to the theoretical white noise BER limit for 16-QAM, while in comparison the ECDL-based transceiver has a 3.3 dB OSNR degradation. The additional 0.5 dB OSNR degradation from our platicon frequency microcomb is attributed to additive ASE noise from the first EDFA. This examination supports the platicon microcomb as a wireless backhaul data link in multi-wavelength multiple-access networks with high-order modulation and coherent detection.

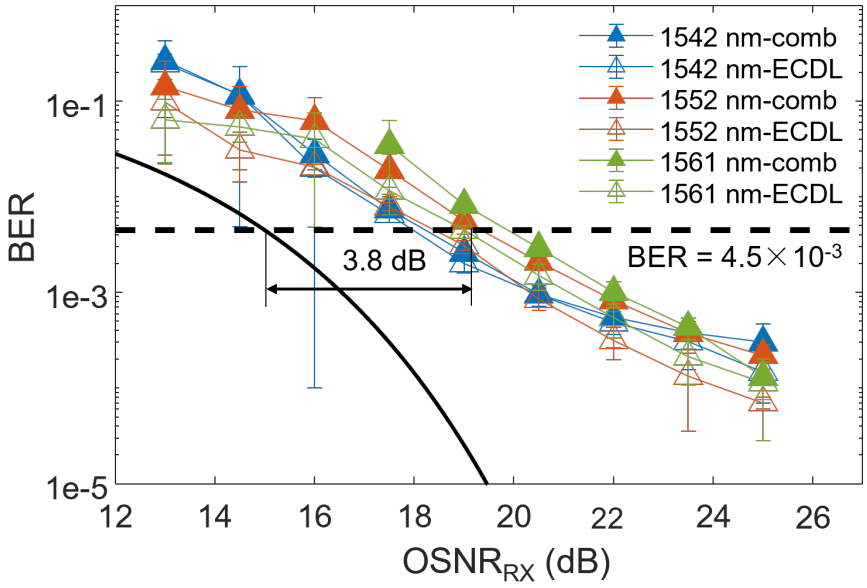

Figure 8.7: Measured BER versus OSNR before the coherent receiver of three independent 1542.93, 1552.96 and 1561.32 nm carriers derived from the platicon frequency microcomb (solid symbols). 16-QAM signaling at 20 Gbaud for both XY polarization together is implemented, and a single-wavelength standalone ECDL (empty symbols) is also illustrated for comparison. There is a 3.8-dB power penalty at the error-free data transmission threshold, compared to theoretical BER-OSNR. We observe an $\approx$ 1-dB degradation in the multi-channel microcomb compared to a single-wavelength ECDL. After considering the amplifier spontaneous noise from EDFA and the free-space link channel fading, the theoretically calculated BER curve fits with the experimental result.

8.4 Atmospheric turbulence-induced SER measurement and theoretical limits

In contrast to an independent array of DFB lasers, the chip-scale microcomb has lower optical power per comb line and lower OCNR which would limit the utmost free-space link reach, the choice of modulation format, and the maximum symbol rate. To mitigate this and the impact of ASE noise from cascaded optical amplifiers, it is essential to increase the comb line powers by optimizing the pump-to-comb-line conversion efficiencies. Figure 8.8 shows the parameter map in terms of conversion efficiency and the 20 dB optical bandwidth, to

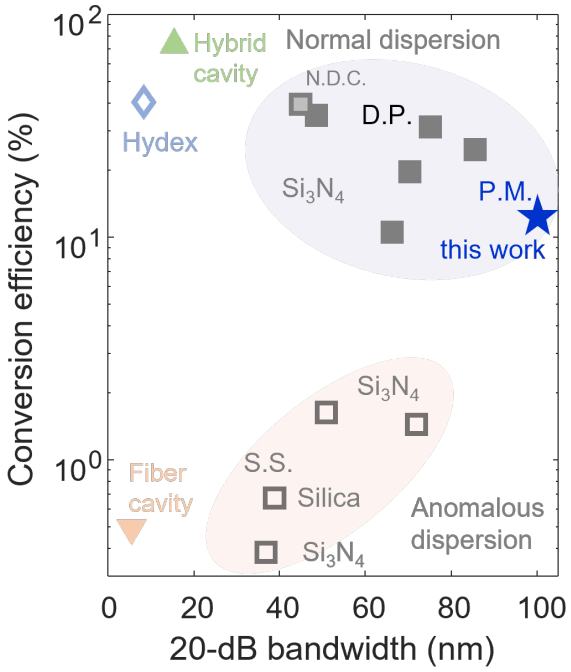

Figure 8.8: Comparison of microcombs' 20-dB optical spectrum bandwidth and conversion efficiency. Efficiency data from each reference; optical bandwidth via the comb spectrum from the maximum comb line. S.S.: single soliton [91, 19, 143, 143](from left-to-right). P.M.: platicon frequency microcomb [this work]. D.P.: dark pulse [211, 212, 99, 212, 213](from left-to-right) N.D.C.: normal dispersion comb [214]. Hybrid (fiber and microresonator) cavity with the laser cavity soliton [215], and Hydex with the soliton crystal with internal conversion efficiency [100].

compare between the different frequency microcomb candidates. Normal dispersion-based microcombs offer higher conversion efficiencies, including dark pulse microcombs and this work on the platicon microcombs, and has a general tradeoff between conversion efficiency and optical bandwidth.

To understand the atmospheric effects on our free-space testbed, Figure 8.9a shows the measured power fluctuations of the free-space link by monitoring the beam position with a quadrant position detector – this illustrates the beam position fluctuations before and after active feedback stabilization with 10× peak-peak beam position variation improvement. To

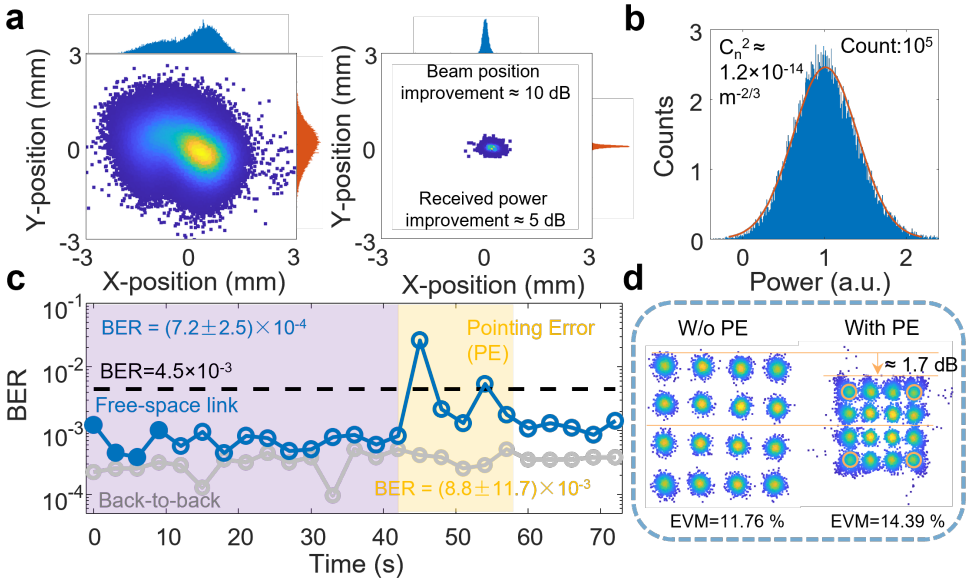

Figure 8.9: Pointing error optimization a, Measured free-space laser beam position along X-Y direction with a quadrant position detector. Left panel: free-running with asymmetrical beam position fluctuations. Right panel: corresponding beam position after active feedback control. b, Measured atmospheric turbulence-induced intensity scintillation (σ_I^2) of the free-space link field trial after suppressing pointing errors. c, Measured BER evolution showing the residual pointing error degradation of the free-space link, compared to a back-to-back baseline. d, Corresponding retrieved constellation diagrams of the first four (solid symbols in panel b) BER sampling segments and the fluctuating BER induced by PE shadowed by the light yellow color.

effectively suppress the pointing error in free-space, we implemented a tight beam-tracking lock system as detailed in Appendix D. To understand the BER dependence on the atmospheric turbulence-induced intensity scintillation, Figure 8.9b shows the measured power fluctuations of the free-space link after removing the pointing error with an active feedback propagation beam stabilization. The link availability and dropout period are investigated before and after engaging the active beam stabilization. The turbulence-induced intensity probability has a log-normal distribution. The scintillation index of the free-space atmospheric link, caused by the air refractive index variation in the atmosphere, is denoted by

the normalized variation of intensity fluctuations as $\sigma_{\mathrm{I}}^2 = \frac{\langle \mathrm{I}^2 \rangle - \langle \mathrm{I} \rangle^2}{\langle \mathrm{I} \rangle^2}$ where I is the received optical intensity. The corresponding refractive index structure parameter $\mathrm{C}_{\mathrm{n}}^2$ can be calculated by the Rytov variance

$$4\sigma_{\mathrm{I}}^2 \approx \sigma_{\mathrm{R}}^2 = 1.23\mathrm{C}_{\mathrm{n}}^2\mathrm{k}^{7/6}\mathrm{L}^{11/6}$$

for weak turbulence under the plane-wave model approximation [216], where k is the carrier wavenumber and L is the propagation distance. The measurement-obtained $\mathrm{C}_{\mathrm{n}}^2 = 4.8 \times 10^{-14}\mathrm{m}^{-2/3}$ at 1550 nm for the 160-m free-space testbed, which subsequently supports our communication model noted below.

Figure 8.9c examines the BER dependence on the atmospheric turbulence and the pointing error of the free-space link, by continuously transmitting the data sequence where the example 16th to 19th datapoint segments show significant BER fluctuation due to unlocked pointing error. The correspondingly reconstructed constellation diagrams are shown in Figure 8.9d without PE and with PE for the 1st to 4th and 16th to 19th datapoint segments: with the unlocked PE, there is a clear ≈ 1.7 dB amplitude degradation and the symbol walks randomly in the complex plane. With the measured link parameters on-hand, Figure 8.10 shows the dependence of the calculated theoretical 16-QAM SER on the SNR for different channel fading models: ideal channel, low visibility fog and smoke channel (F&S channel), atmospheric turbulence (AT) log-normal channel, and non-zero bore-sight PE channel. The symbol error probability of M-QAM is denoted as $\mathrm{SER} = 2(1 - 1/\sqrt{\mathrm{M}})\mathrm{erfc}(\mathrm{k}\sqrt{\mathrm{SNR}})$ where $\mathrm{k} = \sqrt{\frac{3}{2(\mathrm{M}-1)}}$ is the normalizing factor for different M-QAM. Adverse channel fading fundamentally limits the transmission reach of the free-space link. The average SER influenced by intensity scintillation of the free-space link is defined with $\mathrm{SER}_{\mathrm{FS}} = \int_0^\infty \mathrm{SER}\mathrm{f}_{\mathrm{I}}(\mathrm{x})\mathrm{dx}$, where x denotes the fractional power variation and $\mathrm{f}_{\mathrm{I}}(\mathrm{x})$ is the power density function of the random scintillation [217]. Atmospheric attenuation is calculated using the Beer-Lambert relation $\mathrm{f}_{\mathrm{I}}(\mathrm{x}) = \mathrm{f}_{\mathrm{FS}} = \mathrm{e}^{-\alpha_\lambda \mathrm{L}}$, where L is the link distance and attenuation coefficient $\alpha_\lambda = \frac{-\ln 0.05}{\mathrm{Vis}}(\frac{\lambda}{550})^{-\mathrm{q}}$ is related to the atmospheric visibility [218] with Vis and q the atmospheric visibility parameters. The intensity scintillation of the experimental free-space

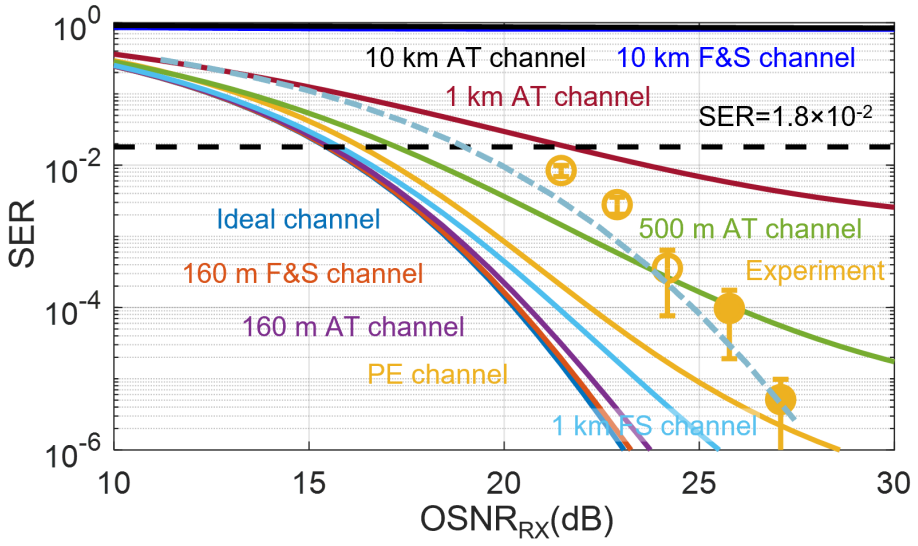

Figure 8.10: Modeled SER–SNR of the free-space link for different channel models and scaled reach range. F&S: fog and smoke, AT: atmospheric turbulence, PE: pointing error. Our experimental testbed data points are listed, with residual pointing error and turbulence as the primary and secondary sources of error in our microcomb free-space link demonstration.

link can be described by a log-normal distribution denoted as [216]

$$f_I(x) = f_{LN}(x) = \frac{1}{x2\sigma_I\sqrt{2\pi}} \exp \frac{\left(\ln x + \frac{2\sigma_I^2}{2}\right)^2}{8\sigma_I^2}$$

.

In a terrestrial free-space optical link, the light beam jitter variance along the horizontal and elevation axes are assumed to be identical, caused by the building motion and individual transmitter-receiver mechanical vibration. The non-zero bore-sight pointing error power density function is used to model the PE channel fading, defined as $f_I = f_{PE}(x) = \frac{\gamma^2}{A_0^{\gamma^2}} x^{\gamma^2-1}$ where $0 \leq x \geq A_0$, and A_0 ($\cong 1$) is the fraction of the collected power when pointing error $r = 0$, and where $\gamma = \frac{\omega_{eq}}{2\sigma_r} (\cong 0.874)$ is the ratio between the equivalent beam waist ω_{eq} and the PE displacement standard deviation σ_r at the receiver [216]. The Gaussian beam waist

propagating in atmospheric turbulence can be denoted as $\omega_z \approx \omega_0\sqrt{1+\varepsilon\left(\frac{\lambda z}{\pi\omega_0^2}\right)^2}$ where ω_0 is the beam waist at the transmitter for $z = 0$, $\varepsilon = 1+2\omega_0^2/\rho_0^2(z)$, and $\rho_0(z) = (0.55C_n^2k^2z)^{-3/5}$ as the spatial coherence length. For a circular detection aperture with radius a and Gaussian beam propagation, the equivalent beam width is expressed as $\omega_{eq} = \omega_z^2\frac{\sqrt{\pi}erf(h)}{2h\exp(-h^2)}$ where $h = \frac{\sqrt{\pi}a}{\sqrt{2}\omega_z}$ [216]. The subsequent SER-SNR dependence of the free-space link with different reach ranges of 160 m, 500 m, 1 km, and 10 km are plotted in Figure 8.10, based on the different channel fading models.

Figure 8.10 shows our experimental testbed measurements with the circle symbols to compare with the modelled SER-SNR dependences. The measured SER follows the aggregate (F&S, AT and non-zero bore-sight PE) fading models well, with the worst-case SER still below the 1.8×10^{-2} error correction bound. We also note that the $OSNR_{TX}$ before the coherent transmitter is determined by the comb line power of the platicon microcomb through the relation of

$$OSNR_{TX} = \frac{G \cdot P_{line}}{G \cdot P_{line} \,/\, OCNR_{line} + [2\pi n_{sp}\hbar\nu B_{ref}(G-1)]}$$

where P_{line} is the power level of the WDM carrier, G is the gain of the C- and L-EDFA after the C/L band WDM, n_{sp} is the spontaneous emission factor, $\hbar$ is the normalized Planck's constant, ν is the carrier optical frequency, and B_{ref} is the OSA resolution bandwidth [219]. The received SNR in the PDM-WDM system is then calculated by $SNR = \frac{B_{ref}}{B_s}OSNR_{RX}$, where B_S is the symbol rate and $OSNR_{RX}$ is related to the after-transmitter EDFAs noise figures and the $OSNR_{TX}$.

Figure 8.11 further shows the examination of the power penalty plots for higher-order advanced modulation including from 16-QAM to 256-QAM formats with polarization diversity. While the higher-order format affords a higher data rate naturally with our platicon microcomb, it has a tighter requirement on the $OSNR_{RX}$ (SNR) for a given SER threshold. Our measured testbed parameters are illustrated in Figure 8.11 too. Our measurements show an estimated power penalty resulting from the AT and PE effects as 1.0 ± 0.5 and 4.0 ± 1.0 dB

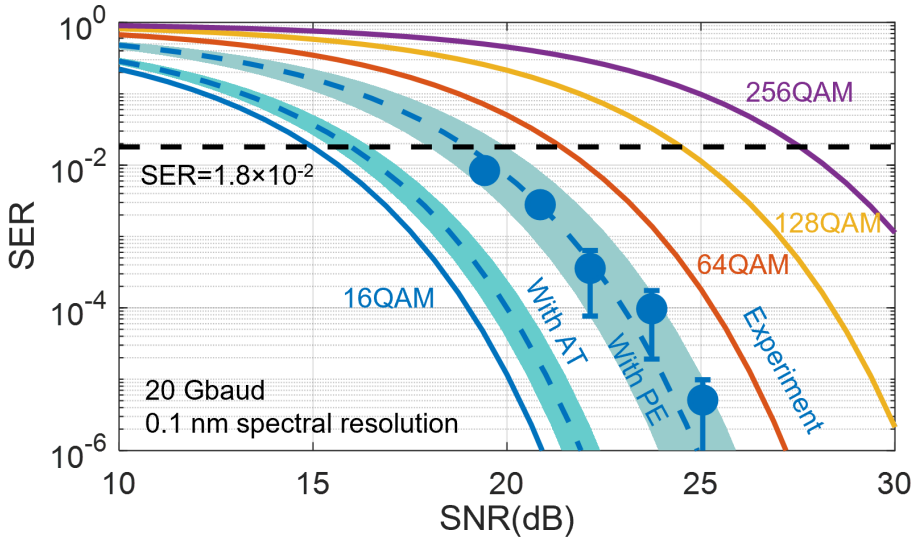

Figure 8.11: Power penalty for different advanced modulation formats. Modeled SER-SNR requirements, and scaling of the free-space link for different advanced modulation formats, signaling with 20 Gbaud each. Likewise, our testbed data points are listed with the same experimental conditions as Figure 8.10.

respectively. Based on our model, the SER over short-reach free-space link is bounded by the $OSNR_{TX}$ and system ASE noise floor. Conversely the long-reach link is bounded by channel fading including atmospheric attenuation and intensity scintillation such as from adverse weather conditions of rain, wind, snow, and fog. This demonstrated microcomb transceiver not only serves as a high-rate wireless backhaul for atmospheric free-space data transmission over short- or long-reaches, but also offer a compact high-rate solution for ground-to-satellite scenarios.

8.5 Summary

A chip-scale microcomb-based coherent transceiver for point-to-point atmospheric free-space data transmission is demonstrated. The spectral flatness and the pump- to-comb-lines power conversion efficiency of the microcomb is enhanced by the optimized waveguide spatial mode

interaction. First, 56 optical carriers spanning from 1540 nm to 1600 nm with the 115 GHz carrier spacing are examined for PDM-WDM coherent data transmission with the aggregated line data rate capacity up to 8.96 Tbit/s for error-free data transmission. The corresponding net spectral efficiency normalized to the channel spacing is 1.28 bit/s/Hz. To expand the point-point link into distributed wireless multiple-access network scenario, the PDM-SISO coherent data transmission is carried out with 35 independent channels. The PDM-SISO allows better noise tolerance and overcomes the impact from the residual pump ASE noise. An aggregated data rate capacity up to 5.6 Tbit/s is achieved, verified with the measured EVMs for the dual-polarization link below the error-free correction threshold of 12.5%. The effects of turbulence-induced intensity scintillation and pointing error fluctuations on the free-space data transmission link is characterized by continuous monitoring of the measured BER, with the BER degradation determined. Our link measurements are compared to theoretical limits induced by channel fading models of low-visibility fog and snow, log-normal atmospheric turbulence, and non-zero boresight pointing errors. Furthermore, the SNR requirements for the higher-order modulation scaling are described in both measurement and theory when considering the transceiver noise and channel non-idealities. The data transmission performance is bounded by the OSNRTX and system ASE noise floor for short reaches and contrastingly bounded by channel fading including atmospheric attenuation and intensity scintillation for long reaches. The communication data rate can be expanded by utilizing the EDFAs with broader gain bandwidth and using more advanced modulation format in the super-channel scheme. Due to strong correlation of stochastic frequency and phase variations of the optical carriers, joint phase estimation can be also explored. To further expand the data transmission coverage (10s km), the come line power of the platicon microcomb needs to be further improved. This demonstrated chip-scale transceiver serves as a potential platform for broadband connectivity, advanced Gaussian relay networks, and terrestrial and backhaul links.

APPENDIX A

Device design and characterization

A.1 Dispersion characterization method

A.1.1 Swept wavelength interferometry

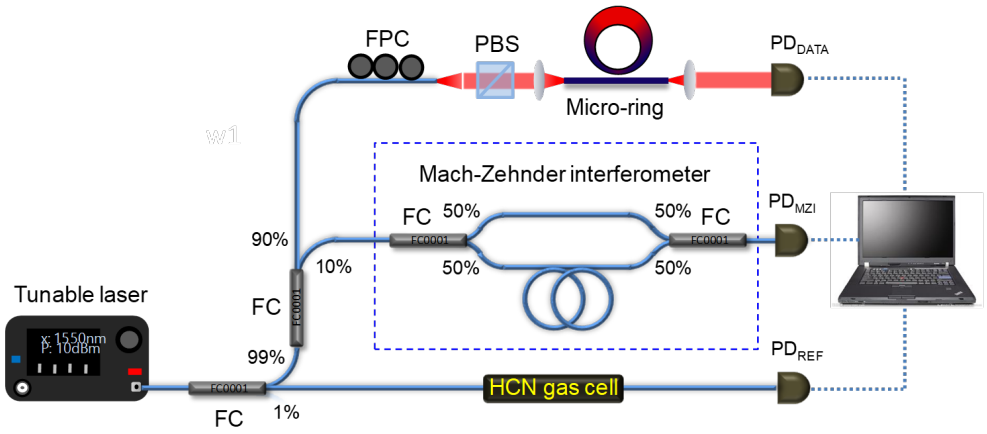

Figure A.1: Swept wavelength interferometer for dispersion measurement. The swept input laser is clocked with a highly-imbalanced MZI with 2.2 MHz optical frequency sampling resolution, and referenced against the optical transitions of an HCN reference gas cell. FC: fiber coupler; FPC: fiber polarization controller; PBS: polarization beam splitter; PD: photodetector; HCN: hydrogen cyanide.

Figure A.1 shows the schematic setup of the high resolution swept wavelength interferometer, which is applied for dispersion measurements of all the microresonator discussed in this thesis. Here we use the 88 GHz tapered microring resonator as an example. The microresonator transmission (Figure 3.1e), from which FSR values are determined, is measured

using a tunable laser swept through its full wavelength tuning range at a tuning rate of 60 nm/s. For absolute wavelength calibration, 1% of the laser output was directed into a fiber coupled hydrogen cyanide gas cell (HCN-13-100, Wavelength References) and then into a photodetector (PD_{REF}). The microresonator and gas cell transmissions are recorded simultaneously during the laser sweep by a data acquisition system whose sample clock is derived from a high-speed photodetector (PD_{MZI}) monitoring the laser transmission through an unbalanced fiber Mach-Zehnder Interferometer (MZI), which guaranteed uniform frequency sampling. The MZI has a path length difference of approximately 90 m, making the measurement optical frequency sampling resolution 2.2 MHz. The recorded resonances around the pump mode shows the critical coupling of our microresonator. It further proves that our tapered microresonator design not only engineers the dispersion, but also effectively suppresses transverse mode coupling. The absolute wavelength of each sweep is determined by fitting 51 absorption features present in the gas cell transmission to determine their subsample position, assigning them known traceable wavelengths and calculating a linear fit in order to determine the full sweep wavelength information. Each resonance is fitted with a Lorentzian line shape and the dispersion of the microring resonator is then determined by analyzing the wavelength dependence of the FSR.

A.1.2 frequency-comb-assisted diode laser spectroscopy

In order to further confirm the close-to zero net cavity dispersion of our design for the 88 GHz microring, we utilize a second dispersion measurement method, frequency comb assisted diode laser spectroscopy, shown in Figure A.2. A broadband tunable laser with tuning range of 80 nm around 1580 nm is used to generate RF beat notes with an erbium-doped-fiber-laser-based frequency comb (MenloSystems GmbH), which has repetition rate f_{rep} = 250 MHz, centered at 1560 nm, with accuracy of 10^{-14} and stability of 5×10^{-13} at 1 second. And its f_{ceo} is fully locked to an optical reference, which means all the comb modes are fixed at well-defined frequencies. The beat notes are detected by a photodetector (PD_{REF}) with

bandwidth of 150 MHz. Then the beat signal is selected by two narrow band-pass filters,

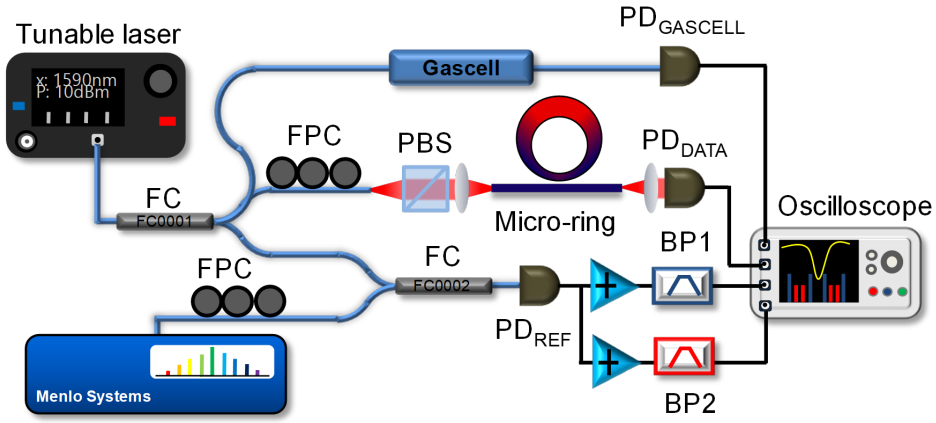

Figure A.2: Menlo-comb assisted dispersion measurement. BP1: 70 MHz, BP2: 35 MHz. FC: fiber coupler; FPC: fiber polarization controller; PBS: polarization beam splitter; PD: photodetector; BP: band-pass filter.

centered at 35 MHz and 70 MHz, respectively (bandwidth of 2.3 MHz), which gives out 4 frequency markers in each frequency comb line interval. By setting the scanning speed of the diode laser at 40 nm/s, the total 155,000 frequency markers are recorded by two ports of a high speed four-channel oscilloscope supporting 31,250,000 data points per channel, leading to a resolution of 352 kHz per data point. The remaining two channels are used for recording the transmission of the microcavity and 51 absorption lines of HCN gas cell. Then all the markers are located through an adaptive peak-finding algorithm, and a spline interpolation of the markers is used to retrieve the instantaneous frequency of the diode laser, while one absorption line of the gascell is used to calibrate the absolute frequency. Then the dispersion of the microring resonator is again determined by analyzing the wavelength dependence of the FSR. The mean value of the net cavity GVD of the tapered microring from the 10 measurements is -6.4 fs^2/mm.

A.2 Device design

A.2.1 88 GHz microresonator design

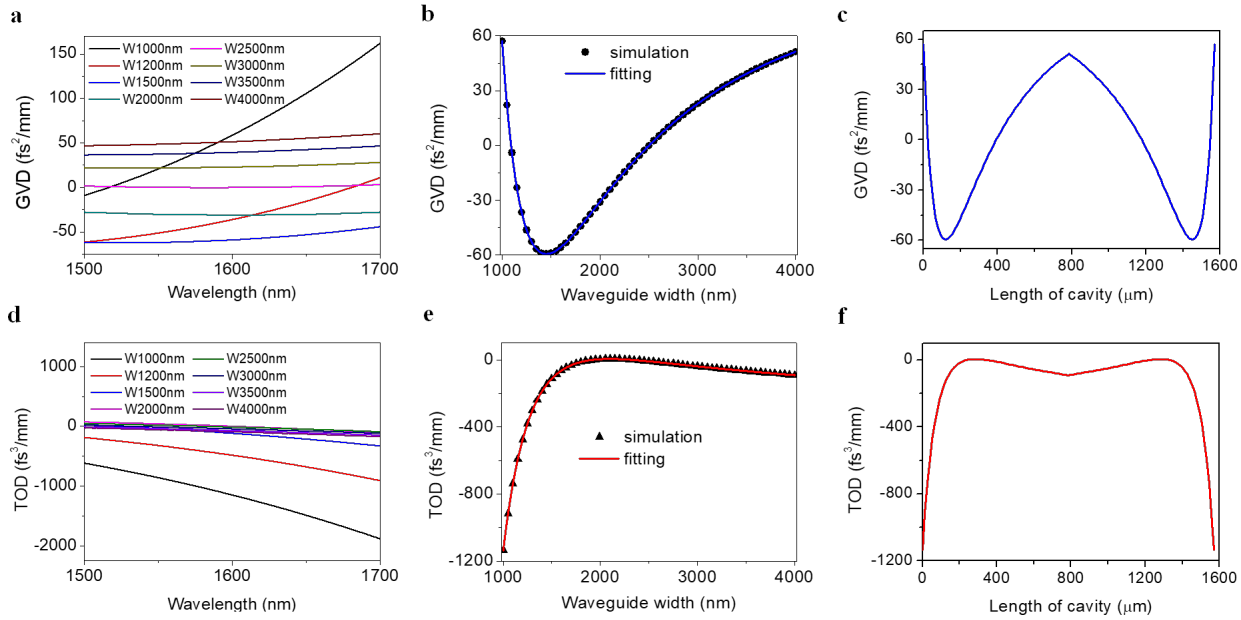

Figure A.3: Simulated GVD and TOD of the tapered microring for the fundamental mode TE_{00} of the 88 GHz tapered microring. a and d, The dispersions for different waveguide widths. b and e, The dispersions at pump wavelength (1598.5 nm) changed with the waveguide width of the microcavity. c and f, The dispersion at pump wavelength (1598.5 nm) changed with the length of the microcavity.

The microring has a diameter of 500 μm and tapered widths from 1 μm to 4 μm to provide variation in effective mode index, n_{eff}, and dispersion management along the cavity. The n_{eff} of the fundamental mode TE_{00} is modelled via COMSOL on 50 nm triangular spatial grid with perfectly-matched layer absorbing boundaries and 5 pm spectral resolution. Since the microring diameter is sufficiently large, the bending loss and the bending dispersion of the resonator waveguide are negligible in our microring resonators. Using the 4th order accurate central finite difference method, we numerically evaluate GVD and TOD in accordance with formulas: $\mathrm{GVD} = \frac{\lambda^3}{2\pi c_0^2}\frac{d^2}{d\lambda^2}n_{eff}$ and $\mathrm{TOD} = -\frac{\lambda^4}{4\pi c_0^3}\left(\lambda\frac{d^3}{d\lambda^3}n_{eff} + 3\frac{d^2}{d\lambda^2}n_{eff}\right)$. The GVD of the

fundamental mode (TE_{00}) of the microcavity proceeds from normal to anomalous, then back to normal when the waveguide width adiabatically increases from 1 μm to 4 μm, as shown in Figure A.3b. When light propagates through the tapered microring, the path-average dispersion, D_{ave}, is an arithmetic mean of dispersion in each segment:

$$D_{ave} = \frac{1}{C}\int_{resonator} D(\lambda, s)ds$$

, where C is the total length (i.e. circumference) of the microcavity; $D(\lambda, s)$ is the dispersion at wavelength λ, and segment at position s. The increment ds is set as 400 nm. Continuous function of the GVD and TOD with respect to waveguide width and length of the microcavity are obtained using a cubic spline interpolation of the COMSOL modeled discrete data points (blue and red line in Figures A.3b and A.3e). The fitted functions are then used to calculate the path-averaged dispersions based on equation above. The path-averaged GVD and TOD of the tapered microring at pump wavelength are -2.6 fs^2/mm and -397 fs^3/mm respectively.

A.2.2 19 GHz microresonator design

Figure A.4 shows the calculated GVD and TOD of fundamental TM mode in different waveguide width and tapered 19 GHz Si3N4 microresonator based on effective index simulation via COMSOL. The 19 GHz microresonator has 74% tapered straight waveguide and 26% bending waveguide. The straight tapered waveguide starts from 1 μm width to 2.5 μm width and then back to 1 μm width to seamlessly connect the bending waveguide. And the overall GVD for the tapered microresonator is around 50 fs^2/mm, which is close to our measurement, while the overall TOD is about -1,000 fs^3/mm at pumping wavelength.

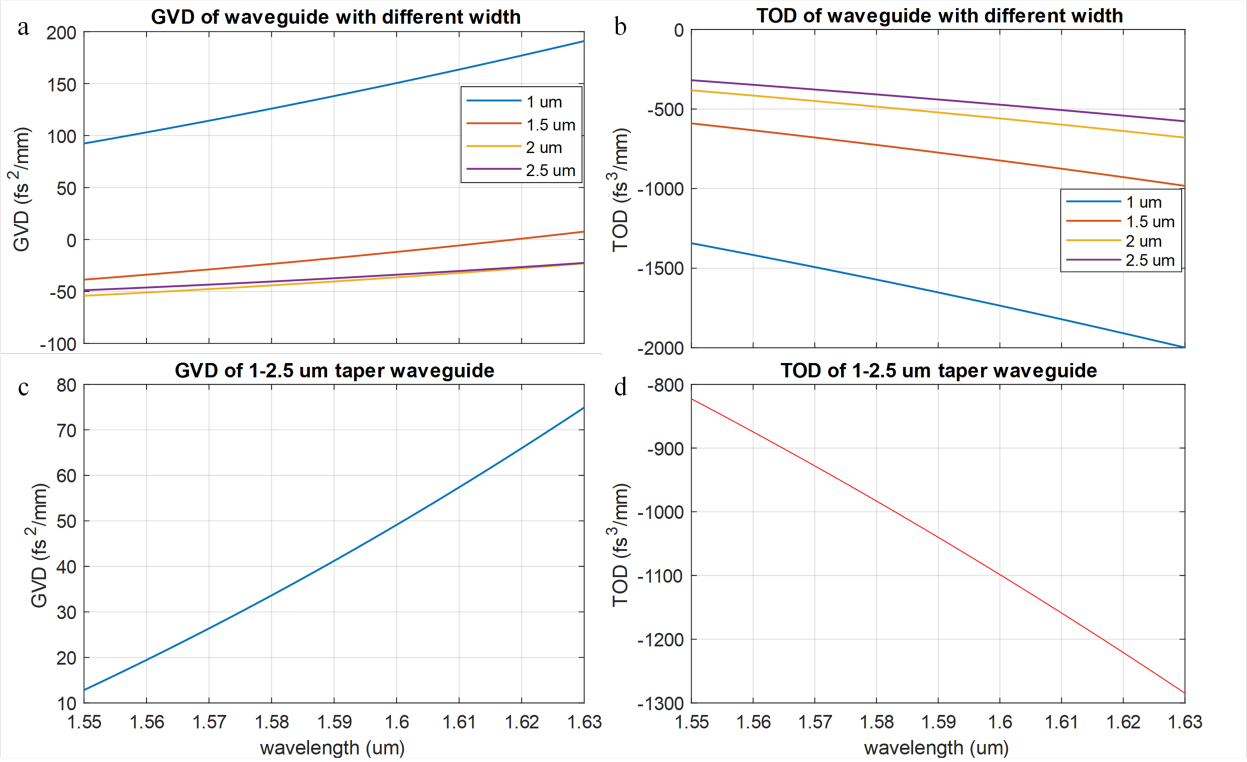

Figure A.4: Simulated GVD and TOD of the tapered microring for the fundamental mode TE_{00} of the 19 GHz tapered microresonator. a, GVD modelling for different waveguide width, at fixed waveguide height of 800 nm. b, TOD modelling for different waveguide width, at fixed waveguide height of 800 nm. c, Net GVD of the designed tapered waveguide. d, Net TOD of the designed tapered waveguide.

A.3 Microcomb characterization method

A.3.1 Pulse characterization with frequency-resolved optical gating

We measured the pulse duration via sub-femto-joule sensitive second-harmonic-generation (SHG) non-collinear frequency-resolved optical gating (FROG). Since the comb-line power of the soliton state was too low, a C-band erbium-doped fiber amplifier (EDFA-C) was applied after the comb was filtered out by a low-pass filter (LPF). The dispersion introduced by the amplifier and SMF connected the soliton generation setup, and the second-harmonic

generation (SHG) setup was carefully compensated by dispersion compensation fiber (DCF). Then, the SHG was sent into a Horiba 1000M series II spectrometer for the FROG measurement. Then, commercial FROG retrieval software (Swamp Optics, LLC.) was utilized to retrieve the temporal profile and phase information of the soliton state. To achieve the FROG measurements, the specific soliton state was maintained for at least 30 minutes to an hour.

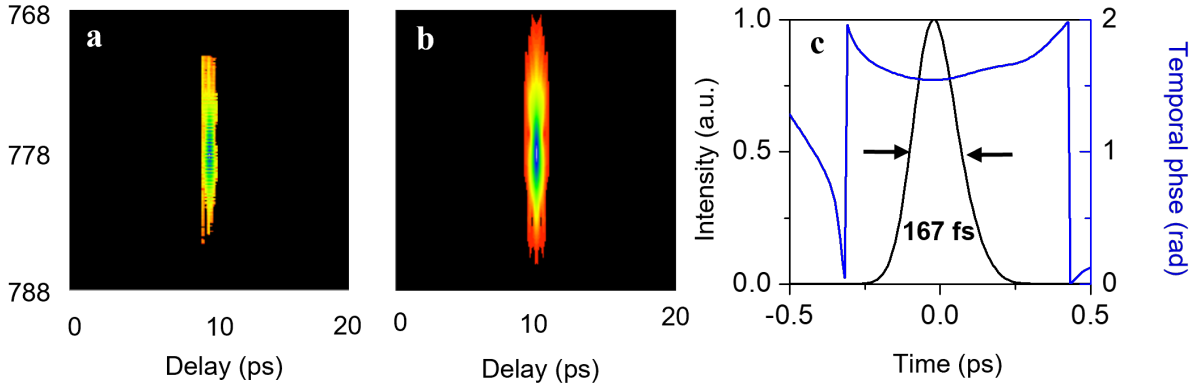

Figure A.5: Frequency-resolved-optical gating (FROG) measurement. a, Original FROG measurement after de-noising. b, FROG mapping retrieval via commercial software. c, Pulse shape (black line) and temporal phase (blue line) retrieved from the FROG measurement. The FWHM pulse duration is measured to be 167 fs. The residual chirp q is determined to be -0.1672.

Figure A.5 shows the data of FROG measurement. The retrieved mapping looks highly alike the original measurement after de-noising, showing a FROG retrieval error at 0.01. Since the 3-dB bandwidth of the filtered and amplified comb is $\approx$ 30 nm centered at 1560 nm, the retrieved $\approx$ 167 fs FWHM pulse duration shows a close-to-transform-limited Gaussian pulse. The residual chirp q is determined to be -0.1672, showing a slightly negative chirp, while, from simulation, the chirp q at the coupling region is -0.1325. Such small difference is inevitable due to limited combination of single mode fiber and DCF of the fiber link.

A.3.2 Ultrafast temporal magnifier

The UTM is based on the mathematical analogy between the diffraction of an electromagnetic beam and dispersive propagation of an electromagnetic pulse (Figure A.6). The total group delay dispersion (GDD), defined as the product of the GVD and the length of the dispersive medium, is analogous to the propagation distance which determines how much a beam is diffracted. An optical lens imparts a spatial quadratic spatial phase that is proportional to k/f, where the focal length f is a measure of the diffraction required for removal of the phase imparted by the lens. Similarly, one can create a time lens by imparting a quadratic temporal phase (linear frequency chirp $d\omega / dt$) to a waveform. A temporal focal GDD, D_f, is defined as the GDD required for removal of the quadratic phase imparted by the time lens. An UTM system is created by cascading an input GDD (D_1), a time lens, and an output GDD (D_2) in proper measure to satisfy the temporal imaging condition:

$$\frac{1}{D_1} + \frac{1}{D_2} = \frac{1}{D_f}$$

A waveform of arbitrary shape passing through this system emerges temporally rescaled with magnification:

$$M_{UTM} = -\frac{D_2}{D_1}$$

The parameters of the UTM components are shown in the Table A.1. To characterize the performance of the UTM system, a transform-limited femtosecond pulse with a bandwidth of 8 nm and a center wavelength of 1543 nm was used as the test input, as shown in Figure A.6. The pulsewidth of the test input was independently measured to be 450 fs by a second-harmonic generation autocorrelation setup. We used the UTM to measure the 2D mapping of the dissipative Kerr soliton dynamics. Our UTM was implemented though four-wave mixing (FWM) in a 50-m highly nonlinear fiber (HNLF). The HNLF (OFS) had a zero-dispersion wavelength (ZDW) of 1556 nm and a dispersion slope of 0.019 ps/(nm^2·km). The nonlinear coefficient was 11.5 $W^{-1} \cdot km^{-1}$. The FWM pump was derived from a stabilized femtosecond Mode-locked fiber laser, and its spectral component from 1554 nm to 1563

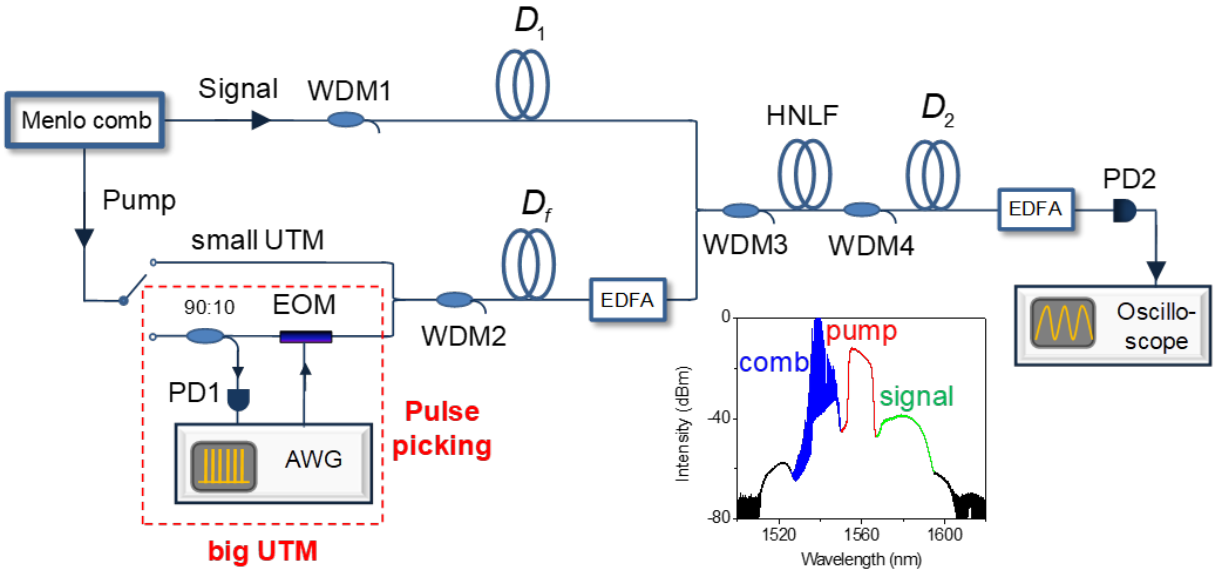

Figure A.6: Schematic setup for the UTM. To increase the SNR and reduce the aberration, the measurement frame rate is sacrificed to 25 MHz by picking 1 pulse out of 10 with an EOM driven by a synchronized AWG (red dashed box). Inset: the spectrum for the input comb, pump and output signal. Inset: The spectra of the UTM. The blue, red, and green is the input comb signal, pump and output signal, respectively.

nm was first filtered out by wavelength-division multiplexing (WDM2) and subsequently amplified by a C-band erbium-doped fiber amplifier (EDFA-C) to 50 mW. Before the signal and the pump were combined via WDM3 into the FWM stage, they were chirped by D1 and D_f, respectively, through two spools of SMF-28. The generated idler was filtered out via WDM4 and then chirped by the output dispersion D_2 through a spool of DCF. Finally, the filtered and chirped idler was amplified by an L-band erbium-doped fiber amplifier (EDFA-L) to 100 μW before it was sent to a 25 GHz amplified photodetector (PD2) and an 80 GS/s real-time oscilloscope for detection. For the correlation measurements, the ECDL laser frequency scan and the oscilloscope data acquisition system were synchronized using a multi-channel pattern generator. All of the electronics were commonly referenced to an Rb-disciplined crystal oscillator for accurate timing.

Device	**1st UTM**	**2nd UTM**
WDM1 μm	1538 - 1557 nm	1538 - 1557 nm
D_1 μm	-5.2 ps/nm	-27.45 ps/nm
WDM2	1554 - 1563 nm	1554 - 1563 nm
D_f μm	-9.5 ps/nm	-55.8 ps/nm
HNLF	HNL-DSF 50 m	HNL-DSF 50 m
D_2 μm	372 ps/nm	1.7 ns/nm
WDM4	1569 - 1610 nm	1569 - 1610 nm

Table A.1: Parameters of the UTM components.

A.3.3 Self-heterodyne linear interferometry

A diffraction grating pair is used to select the comb lines for the timing jitter PSD measurement. We first optimize the noise floor of the SHLI by improving the signal-to-noise ratio of the detected RF signal at 100 MHz. Secondly, we minimize the relative delay time between the two optical comb lines ($\nu_n = 190.11$ THz, $\nu_m = 192.55$ THz) and power difference of the two arms of SHLI, to enable the suppression of the common-mode noise. Thirdly, we optimize the delay time for the soliton microcomb based on two criteria: the first is to maximize the timing jitter measurement sensitivity and the second is to expand the measured Fourier offset frequency range. The fiber delay length was optimized to be 49 m. The detected RF power at the output of the two PDs are 14 and 19 dBm.

The fiber-delay-lined-based phase noise measurement is averaged measurement which is not a real-time measurement. The photodetected signal of each mode is filtered at f_{aom} and mixed by an RF mixer to reject the common-mode f_{ceo} noise. This down-converted RF mixer output contains the repetition-rate phase noise or timing jitter as a form of $\delta[\tau(m-n)f_{rep}]$. The frequency fluctuations of the two selected optical comb lines are converted into voltage

fluctuations with the transfer function

$$\Delta V(f) \propto K_{\varphi} \frac{|1 - e^{-i2\pi f\tau}|}{|i \times f|}(m - n)\Delta f_R(f)$$

where K_{φ} is the peak voltage at the double-balanced mixer output. In chapter 4, we used

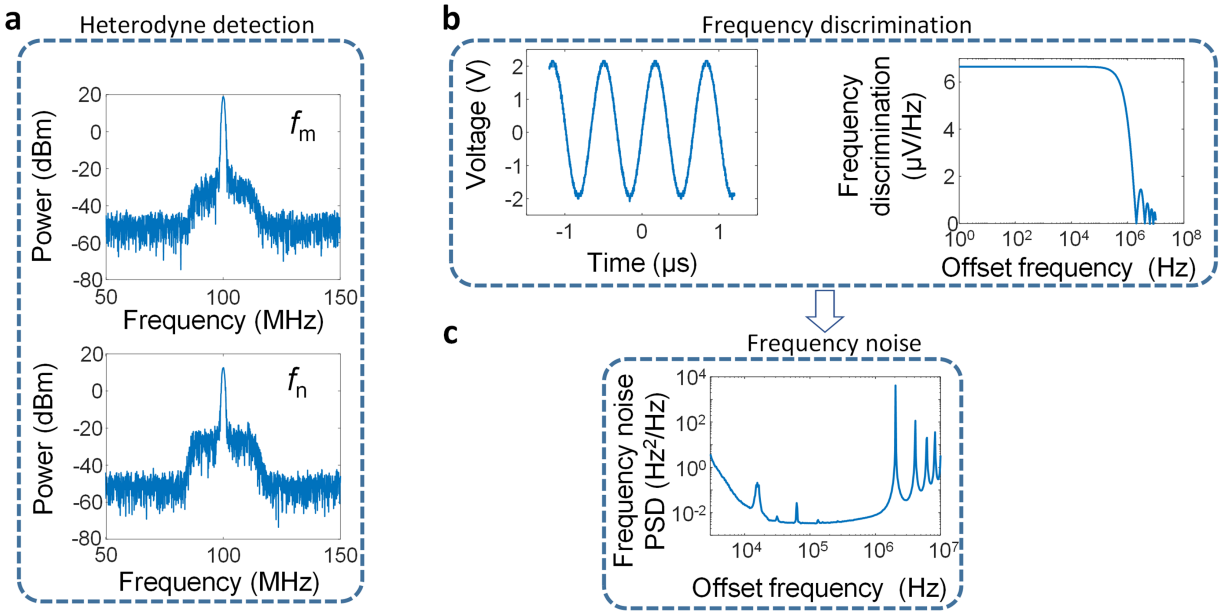

Figure A.7: Frequency discrimination and timing jitter measurement calibration. a, Example measured heterodyne beat note at the 100 MHz frequency. b, Frequency discrimination calibration of the system at 6.75 μV/Hz from 1 to 100-kHz offset. c, Measured frequency noise power spectral density of 3-Hz^2/Hz at 3-kHz offset and 3×10^{-3} Hz^2/Hz at 100-kHz offset.

49-meter fiber for timing jitter power spectral density measurement in the fiber Michelson interferometer. The time delay is around 0.49 μs corresponding to Fourier frequency of 2.04 MHz. This Fourier frequency set the upper offset frequency bound for our measurement. For the self-heterodyne linear interferometry timing jitter measurement technique, the heterodyne beat note, frequency discrimination calibration and the measured frequency noise are illustrated in the Figure A.7. The heterodyne detection beat note magnitude and delay time determines the frequency discrimination sensitivity via:

$$\Delta V(f) \,/\, \Delta f_R(f) \propto K_{\varphi} \frac{|1 - e^{-i2\pi f\tau}|}{|i \times f|}(m - n)$$

To characterize the system sensitivity, we carried out the experiment by setting m = n, wherein the noise floor is determined after common-mode noise rejection. The measured timing jitter measurement sensitivity is illustrated in Figure A.8 where we set the delay time to τ = 489 ns, 742 ns, and 1.24 μs. First, we calibrate the timing jitter sensitivity as shown in Figure A.8a which shows the timing jitter power spectral density noise floor of 1.6×10^{-10} fs^2/Hz. Over the same integrated frequency range of the timing jitter power spectral density, the integrated timing jitter is less than 0.1 fs. The system sensitivity calibration of sub-fs timing resolution shows the self-heterodyne linear interferometry could enable the femtosecond timing jitter characterization.

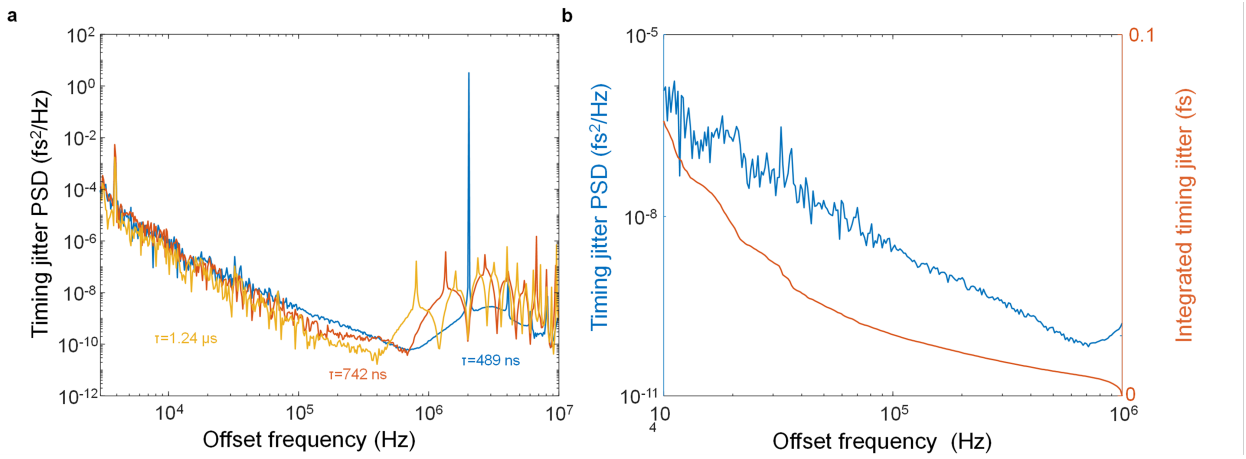

Figure A.8: The timing jitter measurement sensitivity. a, The determined timing jitter measurement sensitivity with different delay times. b, The determined timing jitter power spectral density and integrated timing jitter of the self-heterodyne linear interferometer noise floor.

A.3.4 88 GHz repetition rate measurement

To measure the ≈ 88.58 GHz microcomb repetition rate, which is beyond our direct electronic measurement capability, we implement an electro-optic modulation approach to measure the repetition rate via modulation sidebands. Fig. A.9 shows the experimental setup (panel a), measurement approach (panel b), and repetition rate (f_{rep}) measurement for free-running

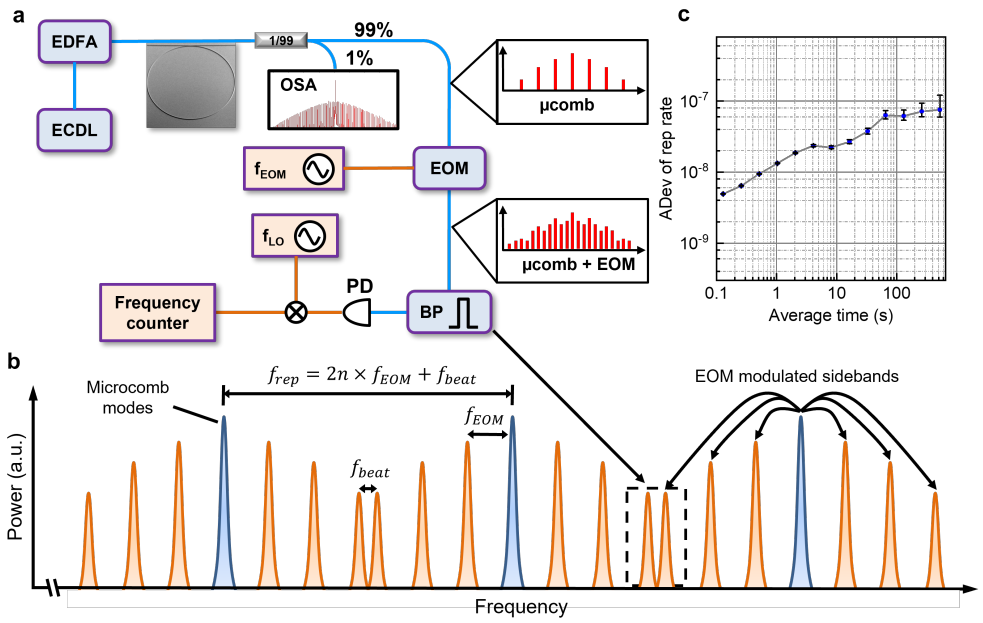

Figure A.9: 88 GHz repetition rate measurement. a, schematic setup. b, Mechanism of repetition rate measurement through EOM modulation. c, Frequency stability of soliton microcomb in terms of Allan deviation.

soliton microcomb (panel c). In a nutshell, the microcomb lines separated by 88.5 GHz (f_{rep}) are modulated by an electro-optic phase modulator (EOM), which is driven at 14.355 GHz (f_{EOM}) and generates several orders of optical sidebands between two adjacent comb lines. The EOM-driven sidebands from two adjacent comb lines generate a beat frequency (f_{beat}) at a low-frequency region ($\approx$ 2.45 GHz in our case), which lies within the detection range of our current electronics. The f_{rep} can thus be determined via the EOM driving frequency and beat frequency with $f_r = n \cdot f_{EOM} + f_{beat}$, where n is the sideband integer number (n = 3 in our case) as shown in Fig. A.9b. The beat frequency at low frequency is measured to determine the repetition rate at the high frequency region. In order to characterize the repetition rate stability, the beat frequency fbeat is down mixed with another local oscillator (f_{LO}) to tens of MHz level, and then directly measured by frequency counter for over 2,000-sec. The stability results are shown in Fig. A.9c. The repetition rate is $\approx$ 88.5799892 GHz

with total drift of 70 MHz over 2,000-sec. The Allan deviation is at the $\approx 7 \times 10^{-8}$ even when up to 400-sec integration time.

A.3.5 Dual-comb cross-correlation

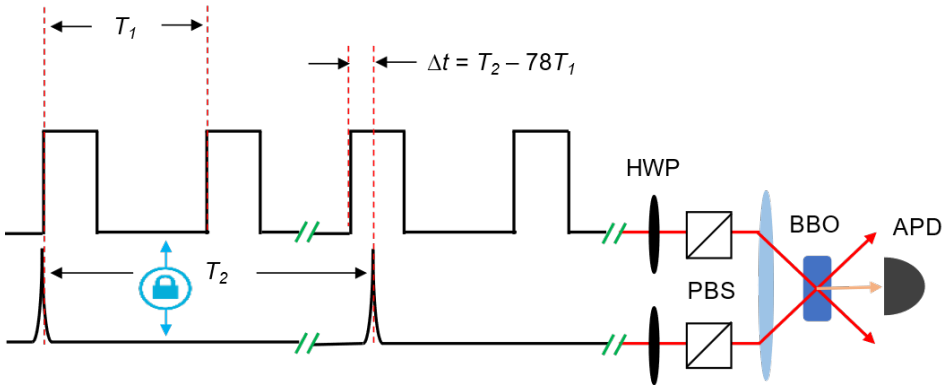

Figure A.10: Schematic setup for dual-comb cross-correlation. An ultrashort pulse with repetition rate of 250 MHz is utilized to probe the flat-top square pulse, and then the convolution is achieved through SHG.

Figure A.10 illustrates the principle of the dual-comb cross-correlation. The pump modulation frequency (and thus the platicon frequency comb spacing) and the Menlo fiber reference laser comb spacing are both referenced to the same Rb-disciplined crystal oscillator. By tuning the Menlo fiber laser comb spacing close to 78 times of the modulation frequency, dual-comb cross-correlation can be achieved due to the temporal walk-off between the picosecond platicon and the femtosecond reference pulse. The two locked pulse trains will have a time lag $\Delta t = T_2 - 78T_1$, after every 78 cycles of the square pulse train. With both stable pulses trains sent into two half-wave plates (HWPs) and polarization beam splitters (PBS) and then aligned into a bulk barium borate (BBO) for second-harmonic generation, the cross-correlation sampled signal is collected by a 700 Hz femto-joule avalanche photodiode (APD). A high-speed oscilloscope is then used to record the platicon temporal shape. Figure 6.9b of the main text shows the observed 17 ps flat-top pulse train. The rising edge

has a 10-to-90% rise time of 5.6 ± 0.48 ps, and the falling edge has a 90-to-10% fall time of 9.54 ± 0.82 ps, sampled over 100 pulses. Notably, such rising and falling time could not precisely reflect the real scenario. The resolution of the cross-correlation method is determined by the pulse width of the Menlo fiber laser comb. However, in order to suppress the nonlinear effect of the Menlo comb itself in the cross-correlation, the fs fiber laser is pre-chirped, which would substantially reduce the resolution of the cross-correlation method. Hence, instead of precisely measure the square pulse, the measurements here only qualitatively characterize the flat-top feature and the pulse width of the platicon pulse. The numerical modelled 17 ps platicon pulse reveals that the rising and falling edges to be 0.31 ps and 0.7 ps, respectively.

APPENDIX B

Theoretical analysis of microcomb dynamics

B.1 Dynamics in tapered microring

Figure B.1 summarizes the simulation results showing the intracavity evolution of pulse duration $\Delta\tau$ and the stable femtosecond pulse train coupled out of such stretched-pulse microcavity, modelled via coupled nonlinear Schrödinger equation described in chapter 3. We use the varied GVD (Figure A.3c) and TOD (Figure A.3f) to simulate the pulse dynamics. The circumference of the tapered-microcavity is finely divided into 120 segments with different GVD and TOD value, modelled in COMSOL, for different waveguide width, and the GVD and TOD is assumed uniform for each step. 2,001 modes centered at the pump are incorporate in the NLSE modeling. We also note that the mean-field approach could be examined for this cavity, even with the dispersion modulation, which would simplify the computational approach.

Our nonlinear simulation starts from vacuum noise and is run for 1.5×10^5 roundtrips until the solution reaches the steady state. For every round-trip, the dispersion-managed dissipative soliton (DM-DKS) experiences a full cycle of stretching and compression between 29.9 fs and 32.3 fs (Figure B.1a). Evanescent coupling occurs at position 0, and a stable 30.05-fs pulse train is coupled out of the stretched-pulse microcavity, and Figure B.1c shows the 10 consecutive pulses of the stable 30.5-fs pulse train coupled out of the microcavity. The output pulse train is stable even though the intracavity pulse is breathing.

The dynamic range of pulse stretch in the 88 GHz dispersion-managed tapered microcav-

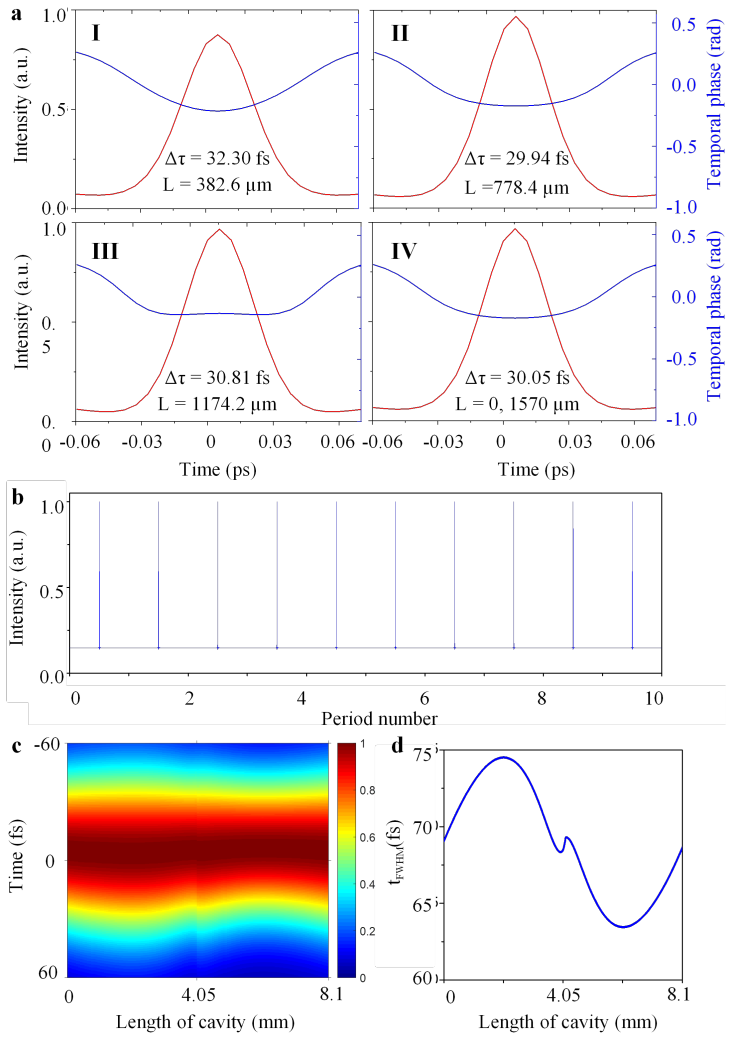

Figure B.1: Simulation of the DM-DKS in Si_3N_4 microring. a, Temporal intensity and phase at different positions in the cavity. The maximum $\Delta\tau$ of the pulse is 32.3 fs (at one fourth of the length of the cavity) and the minimum $\Delta\tau$ of the pulse is 29.93 fs (at around half of the length of the cavity). b, The stable output of the 30.05 fs pulse train. c, NLSE modeled dissipative Kerr soliton dynamics with oscillating pulse duration due to dispersion management in a 19 GHz microcavity. d, The variation of the pulse duration $\Delta\tau$ of the dispersion-managed dissipative soliton along the cavity.

ity is 1.08. The reason for such small pulsewidth variation (2.4 fs) is two-fold. One reason is that the pulse experiences negative chirp, zero chirp and positive chirp in a single roundtrip, which also causes the asymmetry in Figure 3.3a i&ii. The other reason is that the cavity length is relatively small, so the accumulated chirp is not enough for larger pulsewidth variation. To explain this, we apply the same cavity design in a larger cavity (8.1 mm, 19 GHz FSR). The simulated results are shown in Figure B.1c,d. The dynamic range of dynamic range of pulse stretch in the 19 GHz dispersion-managed taper microcavity is 1.17 and the pulsewidth variation range is 11 fs.

In order to theoretically study the enlarged soliton stability zone of dispersion-managed tapered microcavity, Numerical simulations of both dispersion-managed microcavity and uniform microcavity are performed to map out the stability zone of the solitons. The maps the soliton characteristic step zone with pump power vs. detuning, of both cavities is illustrated in Figure B.2. 10,000 roundtrips with a detuning step size of 10 μrad are performed for each pump power parameter. The white squares are simulation result we obtained. Then spline interpolation is applied to map the stability region. The black region shows chaotic state or off-resonance, the red region shows in such detuning step size, single soliton is successfully observed, and the purple region shows that no single soliton is observed but only single breather soliton is observed. In dispersion-managed resonator, single soliton is still successfully observed when the pump power is up to 260 mW while single soliton can only be observed below 80 mW in uniform resonator. In addition, the highest attainable pulse energy from single soliton in dispersion-managed microresonator is calculated 50% higher than the uniform microresonator case. Although uniform resonator has larger stability region, the tapered resonator is more resistant to breather soliton instability in higher pump power. It means that dispersion-managed tapered resonator could effectively enlarge single soliton stability zone in higher pump power, which matches our experimental observation.

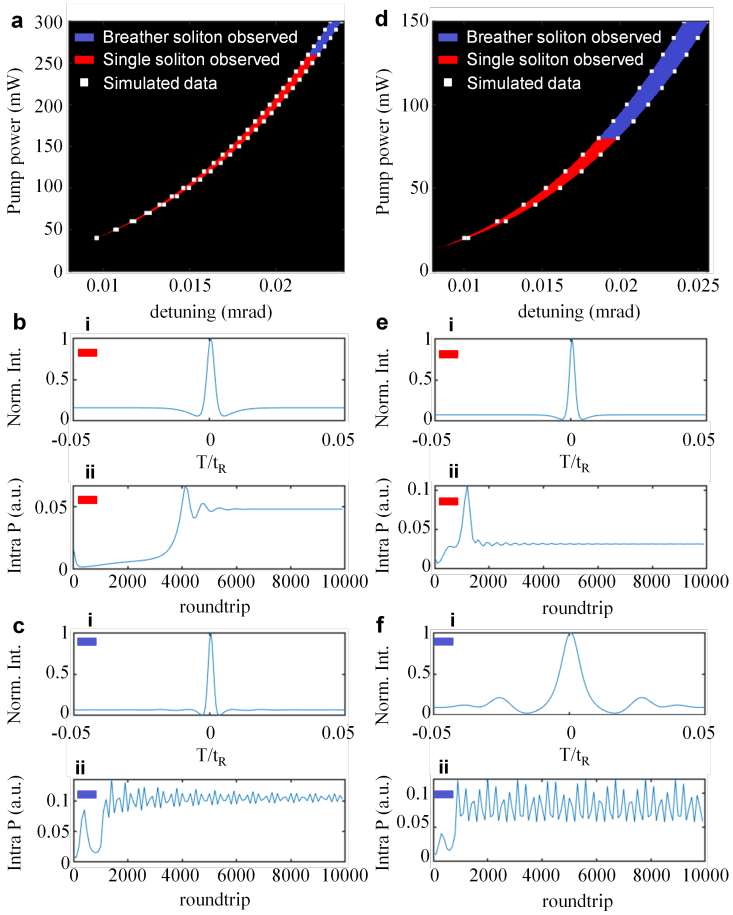

Figure B.2: Numerical simulation of soliton stability zone in dispersion-managed tapered cavity and uniform cavity. a, Soliton characteristic step mapping of dispersion-managed tapered cavity. b, Temporal waveform of single soliton and the intracavity power along 10,000 roundtrip times in tapered cavity. c, Temporal waveform of single breather soliton and the intracavity power along 10,000 roundtrip times in tapered cavity. The breathing frequency is around 126 MHz. d, Soliton characteristic step mapping of uniform cavity. e, Temporal waveform of single soliton and the intracavity power along 10,000 roundtrip times in uniform cavity. f, Temporal waveform of single breather soliton and the intracavity power along 10,000 roundtrip times in uniform cavity. The breathing frequency is around 126 MHz. i is temporal waveform and ii is intracavity power along roundtrips. The black region is no-soliton zone. The red region shows single soliton observed in a 10 μrad detuning step. The purple region shows no single soliton observed in a 10 μrad detuning step, where only single breather soliton is observed.

B.2 Lugiato-Lefever Equation

When the investigation is not focusing on the intracavity dynamics, the external-driven damped microcavity dynamics could be approximated by the mean field Lugiato-Lefever Equation:

$$\mathrm{T_R}\frac{\partial}{\partial \mathrm{t}}\mathrm{A}(\mathrm{t},\tau) = \sqrt{\alpha_\mathrm{c}}\mathrm{A_P} - \left[\frac{\alpha_\mathrm{c}+\alpha_\mathrm{p}}{2} + \mathrm{j}\delta - \mathrm{jL_{cav}}\sum_{\geq 2}\frac{\beta_\mathrm{k}}{\mathrm{k!}}\left(\mathrm{j}\frac{\partial}{\partial\tau}\right)^\mathrm{k} - \mathrm{j}\gamma\mathrm{I}(\mathrm{t},\tau)\right]\mathrm{A}(\mathrm{t},\tau) \quad \text{(B.1)}$$

where $\mathrm{T_R}$ is the round-trip time, $\mathrm{A_p}$ is the external pump, $\mathrm{A}(\mathrm{t},\tau)$ is the envelope function of the platicon, t is the slow time corresponding to the evolution time over round trips, τ is the fast time describing the temporal structure of the wave, $\mathrm{A_P}$ is the external pump, α_p is the propagation loss, α_c is the coupling loss, and δ is the pump-resonance detuning, where ω_c and ω_p are the cavity resonance frequency and pump frequency, respectively. β_k describes the dispersion coefficient ($\beta_2 > 0$ indicates normal GVD and $\beta_2 < 0$ indicates anomalous GVD), and we only consider second and third order dispersion in this case. $\gamma = \frac{\mathrm{n_2}\omega_0}{\mathrm{cA_{eff}}}$ is the Kerr nonlinearity, in which $\mathrm{n_2}$ is the nonlinear refractive index and $\mathrm{A_{eff}}$ is the effective modal area of the pumping transverse mode. When the absolute value of β_2 is large enough, the effect of higher order dispersions could be neglected, which is the case in chapter 2. However, when β_2 is close to zero, which is the case in chapter 4 and 5, β_3 need also to be considered. Furthermore, in order to incorporate the AMX-induced frequency shift, an additional frequency shift $\Delta\mathrm{n}$ is introduced to the nth mode, so that the mode frequency becomes: $\omega_\mathrm{n} = \omega_0 + \mathrm{D_1 n} + \frac{\mathrm{D_2 n_2}}{2} + \Delta_\mathrm{n}$. Δ_n is determined by the empirical two-parameters model: $\frac{\Delta_\mathrm{n}}{2\pi} = \frac{-\mathrm{a}/2}{\mathrm{n–b–0.5}}$, where a is the maximum mode frequency shift and n and b are the mode number and mode number for the maximum mode frequency shift, respectively. Thermal effects and the Raman effect are not considered for the simulation. From the cavity mode dispersion characterization, the cavity free-spectral range $\mathrm{D_1}\ /\ 2\pi =$ 88.52 GHz. Furthermore, we estimate the maximum frequency shift to be $\Delta_\mathrm{n}/2\pi = 130$ MHz

at 1581.5 nm determined by the spectral peak in the soliton microcomb optical spectrum. The estimated value is supported by comparing the simulated comb spectrum with the experimental result, which are in good qualitative agreement. 2,000 modes centered at the pump are incorporated in the LLE model. The simulation starts from vacuum noise and runs for 1×10^5 roundtrips until the solution reaches steady state.

B.3 Impact of Δ on the platicon generation with zero and positive TOD

In order to quantify the impact of the modulation frequency deviation Δ on the platicon microcomb, we introduce skewness, a measure to describe probability distribution of a real-valued random variable about its mean in statistics, to quantify the asymmetry of the comb line distribution. Here, we assign the comb line wavelength λ_i as the variable, where the pump wavelength λ_{pump} as the mean, and the value $P_i = \frac{I_i}{I_{total}}$ of the log-scale comb line intensity normalized to the total intensity as the probability for each comb line. Then the skewness is defined as: skewness $= \frac{\mu_3 - 3\mu\sigma^2 - \mu^3}{\sigma^3}$, where $\mu_3 = \sum_i \lambda_i^3 P_i$, $\mu = \sum_i \lambda_i P_i$, and $\sigma^2 = \sum_i \lambda_i^2 P_i - \mu^2$. In our cases, zero skewness indicates a perfectly symmetric comb spectrum, while negative skewness indicates more comb line power distributes on the longer wavelenght (lower frequency), and positive skew means more comb line power distributes on the shorter wavelength (higher frequency).

Figure S3(a-d) shows three simulated comb spectra of platicon at TOD = 0 fs^3/mm, with modulation frequency deviation Δ = -1000, 0, and 1000 kHz, as well as the skewness, consistent with Figure 6.6. Note that the comb spectra here have frequency as the x axis, while the skewness is flipped for direct comparison with Figure 3g, and it is why the comb line distribution looks controdictary to the skewness plot. The skewness plot is central symmetric, and we could see that when Δ=0, skewness is zero, which indicates a perfect symmetric comb spectrum. When the TOD remain the small amount as the real case introduced in the main

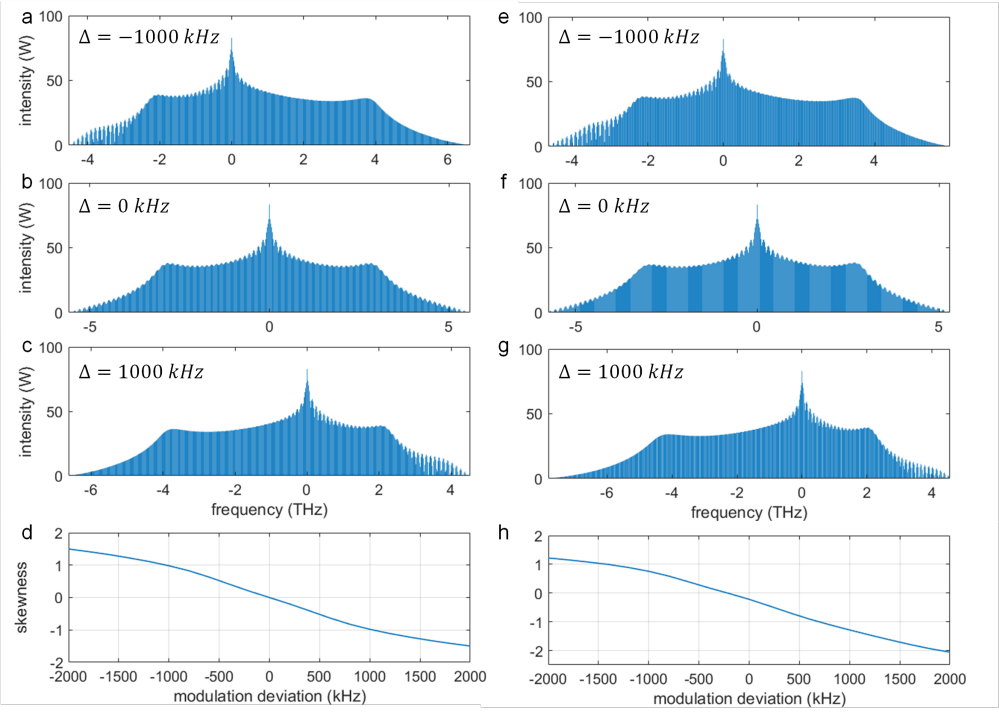

Figure B.3: Modeled platicon comb spectra and calculated skewness for Δ = -1000 kHz, 0 kHz, and 1000 kHz when TOD = 0 and 1000 fs^3/mm. a-c, modeled comb spectra for TOD = 0 fs^3/mm. d, Skewness for different Δ when TOD = 0 fs^3/mm. e-g, modeled comb spectra for TOD = 1000 fs^3/mm. h, Skewness for different Δ when TOD = 1000 fs^3/mm.

text, but with negative sign (TOD = 1000 fs^3/mm), the phenomenon is inverted compared to the negative case (Figure 6.6). The platicon comb is asymmetric to longer wavelength (lower frequency) when Δ=0, and the comb spectra will be more asymmetric when Δ is positive, comparing to the negative case.

APPENDIX C

microcomb-assisted hybrid spectrally-resolved and homodyne interferometry characterization

C.1 Data processing for the distance metrology

C.1.1 Fundamental minimum and maximum measurement range

To determine the distance, the reference and measurement pulse should be separated in the time domain. The minimum measurable distance (L_{min}) is determined by pulse duration used in the distance measurement. Lmin can be expressed as $L_{min} = c_o / (2\Delta\nu)$, where $\Delta\nu$ is a spectrum bandwidth. In our case, L_{min} is estimated to be 30 μm considering 5 THz spectrum bandwidth of soliton microcomb. The fundamental maximum measurable distance (L_{max}) is upper-bounded by the coherence length of the light source and can be expressed as $L_{max} = c_o / (2\delta\nu)$, where $\delta\nu$ is the linewidth of the light source. In our case, the L_{max} limit is estimated to be 1 km considering the 150 kHz linewidth of soliton microcomb.

C.1.2 Nonlinear curve fitting for precise peak detection

To precisely determine the peak position τ_{TOF} in time domain, we implement polynomial curve fitting near peak position as $I(\tau) = A\tau^2 + B\tau + C$. Data points for curve fitting are symmetrically chosen with 3 or 5 points around the peak position. The peak position is determined when its first derivative is equal to zero as $dI(\tau) / d\tau = 2A\tau + B = 0$. Thus the peak position is simply determined from $\tau = -B / 2A$.

C.2 Bounds on the measurement precision of homodyne interferometry

We found our measurement repeatability of the homodyne interferometry seems to be limited by environmental long-term drift including drift of refractive index of air and thermal expansion of the target distance. To evaluate ultimate measurement precision regardless of the long-term drift, we use 0.05 Hz high pass filter to minimize long-term drift effects on the precision. Figure C.1 shows comparison between raw data and high pass filtered data. For the high pass filtered case, a standard deviation (1σ) is improved to 3.9 nm and slowly-varying fluctuation disappears. If we assume that target is ideally fixed without long-term drift, measurement stability can be improved to be 0.15 nm at 100 seconds averaging time. Such measurement stability is close to commercial HeNe laser interferometry.

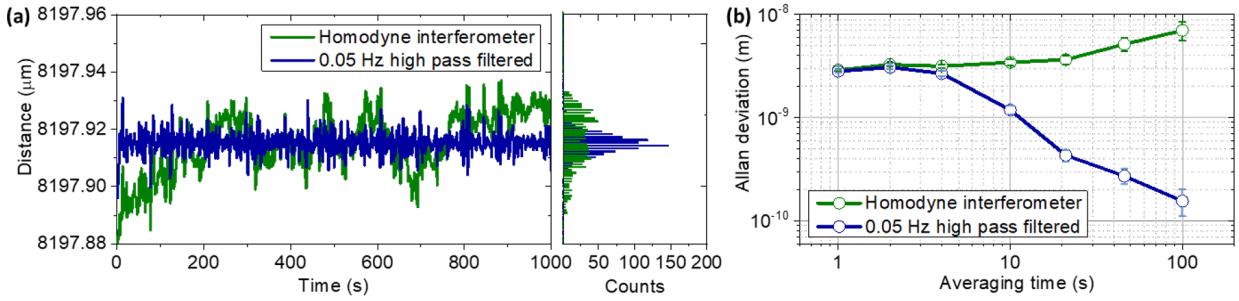

Figure C.1: Evaluation of measurement repeatability of homodyne interferometry. a, Time trace of homodyne interferometry during 1,000 seconds with raw data marked in yellow color. Its 0.05 Hz high pass filtered data is also plotted with gray color. Right inset shows those histogram b, Measurement precision in terms of Allan deviation, with 0.05 Hz high pass filtering to remove the long-term drift. Sub-nm measurement stability at 100 seconds averaging can be observed.

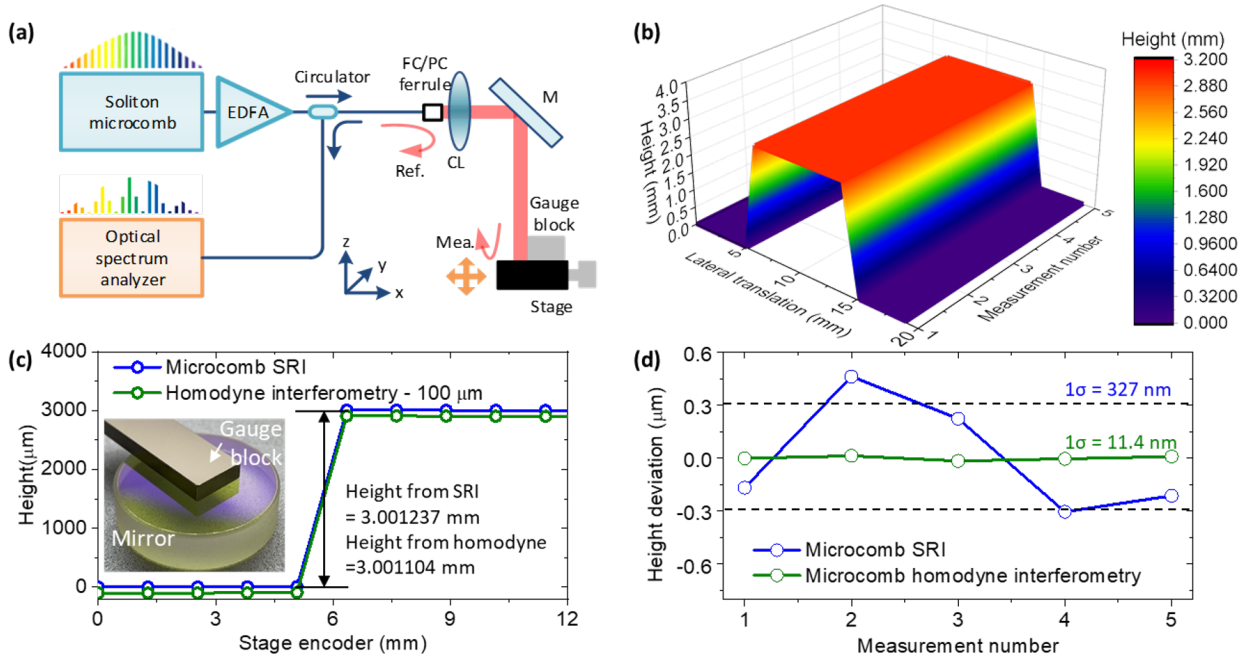

Figure C.2: Measurement of a reference gauge block cross-section via x-axis scanning. a, Measurement scheme for cross-section of gauge block with x-axis scanning stage. b, Reconstructed cross-section of a gauge block. c, The gauge block height is found to be 3.001237 mm and 3.001104 mm from soliton microcomb spectral interferometry and homodyne interferometry, matching well with reference specified height. d, Measurement repeatability of the gauge block height.

C.3 Position calibration of motorized stage and measurement range dependent imprecision by soliton microcomb-based SRI

To validate the microcomb SRI for potential 3D surface measurement, we measured a cross-section of a standardized gauge block, used for practical length metrology in 3D surface measurements and industry standards. We replaced the reference mirror in the interferometer part with the gauge block to measure the cross-section of the 3 mm height gauge block (Starrett RCM, 3.0 Al) that has a 300 nm uncertainty. The reference beam is made with a 4% Fresnel reflection from the end of FC/PC fiber ferrule. The transmitted beam is reflected from the target surface and sent to the optical spectrum analyzer along with the

reference beam. The gauge block is mounted on a flat mirror and the stage made an on-axis translation with 1.27 mm (0.05 inch) steps as shown in Figure C.2a. The distance at each step is recorded with 5 data points. The gauge block height is determined by the difference of the absolute distances between mirror and gauge block surface, with the same empirical air refractive index of 1.000247 as noted above. The measured cross-section of the gauge block is shown in Figure C.2b,c. The height of gauge block was found to be 3.001237 mm and 3.001104 mm from the microcomb SRI and homodyne interferometry respectively. We also found a different slope height between the mirror (1.413μm/mm) and gauge block surface (-1.817μm/mm). A tilting (cosine) error from imperfect plane-to-plane alignment may introduce the measurement error of 1.237 μm. As shown in Figure C.2d, the measurement repeatability taken over 5 consecutive measurements is determined to be 327 nm and 11.4 nm from microcomb SRI and homodyne interferometry, respectively as the 1σ standard deviation.

APPENDIX D

Platicon based free space communication implementation

D.1 Platicon frequency microcomb generation and characterization

Figure D.1 shows the experimental setup of the 115 GHz platicon frequency microcomb generation and characterization for the free space data transmission experiment. The normal dispersion microcomb is generated by pumping a silicon nitride microresonator with an ECDL. A FPC and a PBS are placed before the microresonator to optimize the pump polarization at the TM polarization. The pump light is amplified by an EDFA at an output power up to 36.5 dBm. After the EDFA, a free-space BPF is applied to suppress ASE noise. A pair of achromatic lenses is applied to couple light into and out of the microresonator, with approximate 3-dB loss per facet. Then the coupled-out light is collected into a series of fiber links through a free space collimator. The collected light is divided into several paths for further characterization and application, while the majority (99%) is sent for data transmission, and the remaining light is used for monitoring the optical spectrum, intensity noise (DC to 1 GHz) and output power, with OSA, ESA and power meter, respectively.

In the data transmission path, a fiber Bragg grating (FBG) notch filter with a 0.25 nm bandwidth is implemented to suppress the pump laser up to 40 dB. Inset i shows the resonant mode spectrum including the fundamental mode (quasi-TM_{00}) and higher order mode (quasi-TM_{10}). The platicon frequency microcomb is generated by sweeping the pump

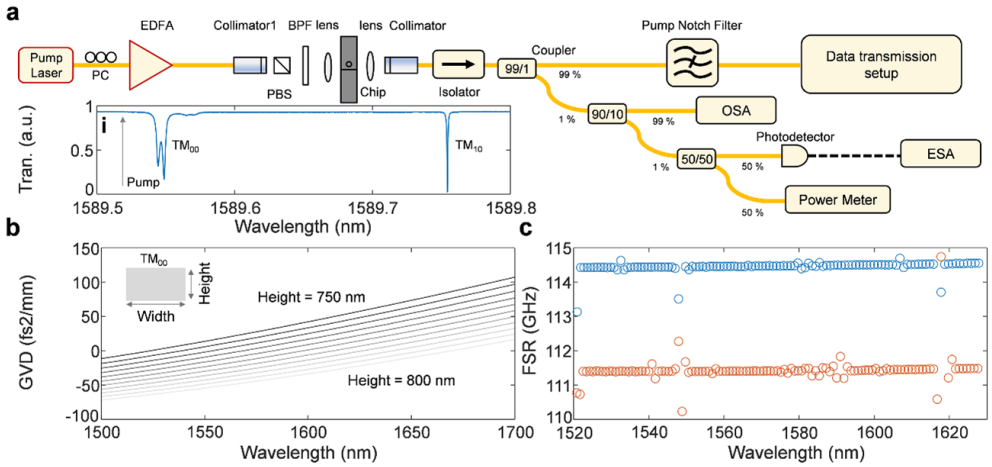

Figure D.1: Experimental setup of platicon frequency microcomb generation and the microresonator cavity mode dispersion design and characterization. a, Experimental setup of the 115 GHz platicon frequency microcomb generation and characterization. Inset i: the measured cavity mode spectrum with the avoided-mode crossing from transverse mode families coupling. b, Computed cavity mode dispersion from finite-element modeling for different waveguide heights. The waveguide width is fixed at 2 μm, while the waveguide height varies from 750 nm to 800 nm. c, Free spectral range characterization for the resonances of the different transverse mode families from swept-wavelength interferometry. The two transverse mode families, quasi-TM_{00} and quasi-TM_{10} have distinct FSRs, indicating that microcomb is excited in the quasi-TM_{10} mode family.

wavelength from shorter wavelength to longer wavelength towards quasi-TM_{10} resonance near AMX. The AMX facilitates the frequency microcomb generation in normal dispersion regime. Figure D.1b shows the calculated GVD by varying the waveguide height at the fixed waveguide width to explore the fabrication height uncertainty. The waveguide height is varied from 750 to 800 nm while the width is fixed at 2 μm. Figure D.1c depicts the dispersion characterization of the designed microresonator. Through the SWI and mode family identification processes, two quasi-TM mode families are identified, with FSRs of 111.5 GHz and 114.5 GHz, respectively. The 115 GHz microcomb line frequency spacing confirms that the microcomb is generated in the quasi-TM_{10} mode family. Second-order polynomial fitting is applied for both mode families to extract the GVD and TOD. The fitting results show that the quasi-TM_{00} mode family with $D_2 / 2\pi$ = –310 kHz and $D_3 / 2\pi$ = 8.6 kHz, and the quasi-TM_{10} mode family with $D_2 / 2\pi$ = –428 kHz and $D_3 / 2\pi$ = 6 kHz. Both mode families have normal GVD. By comparing the measured and calculated dispersion, we can pinpoint that our normal-dispersion microresonator has $\approx 2 \times 0.75 \mu m^2$ cross-section with an $\approx 6\%$ thickness or waveguide width uncertainty. Insets are the calculated Ey-field mode profiles from finite-element computation for a waveguide cross-section of $2 \times 0.75 \mu m^2$.

The Figure D.2 depicts the platicon frequency microcomb dynamics depending on the pump-resonance detuning. Figure D.2a and D.2b present the simulated and measured optical spectra. The microcomb starts from primary comb lines with 5-FSR away from the pump, then transit into a breathing state with breathing frequency of 400 MHz, then evolves into low noise states. With forward tuning of the laser wavelength, the microcomb remains low intensity noise, with increasing comb bandwidth. Figure D.2c shows the measured intensity noise power spectrum corresponding to the microcomb states in the Figure D.2b. Note that in the current microcomb evolution dynamics, no high noise states are observed in the simulation and experiment. When the AMX frequency shift is large enough, high noise state will start to occur. We note that for our data transmission measurements, the platicon microcomb low-noise state is stable for at least five to ten hours, without any active feedback

control or additional mechanisms. Only a high-precision temperature controller is needed to stabilize the chip and microring temperature.

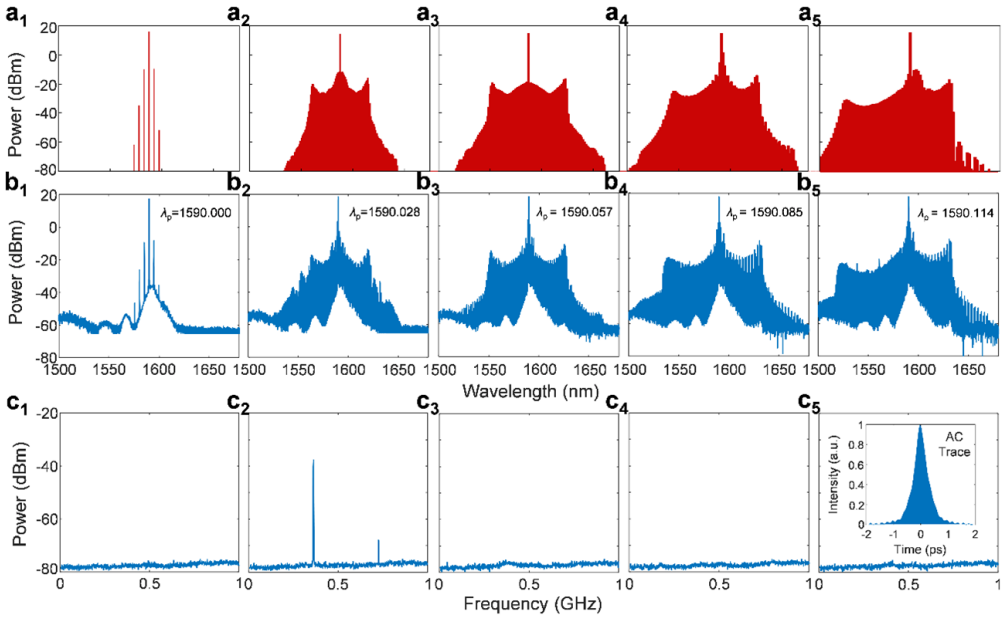

Figure D.2: Broadband platicon frequency microcomb and coherent mode-locked pulse generation metrology. a, Modeled platicon frequency microcomb at different pump-resonance detunings through the Lugiato-Lefever equation, starting from the primary microcomb lines aided by the AMX to platicon frequency microcomb, with the tunable optical bandwidth and different spectral asymmetry. b, Corresponding measured platicon frequency microcomb at the different pump-resonance detunings where the measurements agree well with the modeling. c, Intensity noise of the generated platicon mode-locked pulse.

Figure D.3 depicts the different simulated platicon frequency microcomb evolution dynamics with the high noise and breathing state. Figure D.3a depicts the 2D spectral evolution and Figure D.1b shows the total microcomb power with respect to pump-resonance detuning, from which we identify different comb states. In this simulation, the AMX frequency shift is set at 720 MHz. In this evolution, the microcomb starts from primary comb line of 4-FSR away from the pump, then transits into high noise state, and later accesses a breathing state. Eventually it transits into a low noise state with extending comb bandwidth as

the detuning increases. Figure D.3c and D.3d are the selected optical spectral and temporal profiles, respectively, depicting the four comb states discussed above.

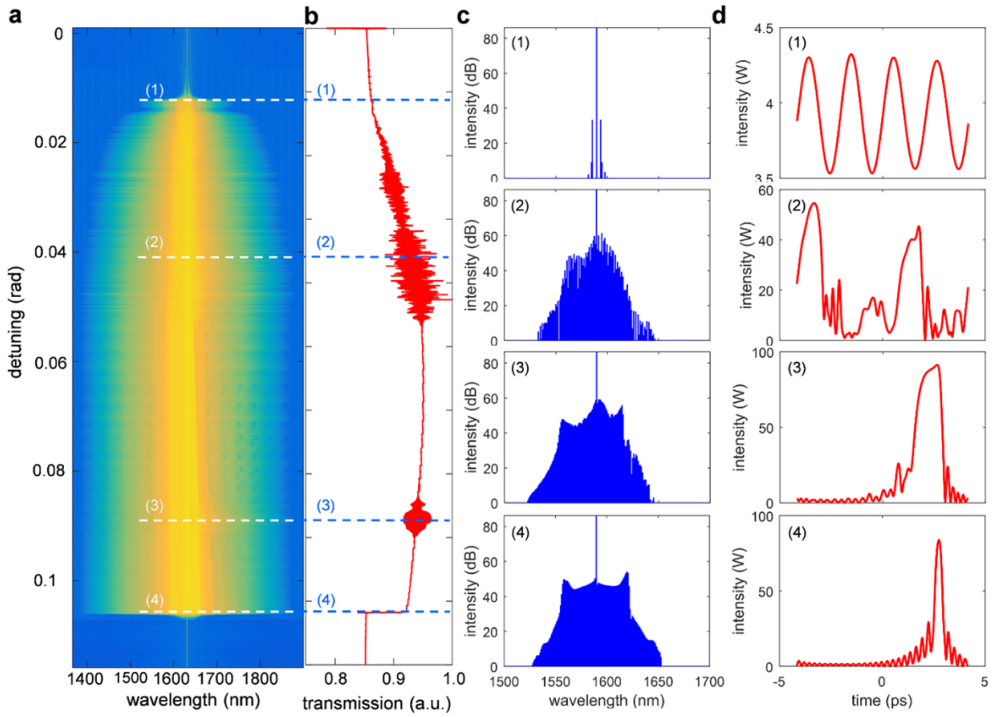

Figure D.3: The simulated platicon frequency microcomb dynamics when the avoided mode frequency shift is larger. a, The simulated optical spectral evolution with respect to the pump-resonance detuning. b, Total microcomb power. c, The representatively optical spectral microcomb spectra. d, The temporal profiles corresponding to c.

D.2 Free-space optical link implementation

The free-space link setup is denoted in Figure Figure D.4, which includes two beam expanders, steering mirrors and an active feedback control system. Different collimators are used for the transmitter and receiver to avoid spurious reflections in the link optical signal. To expand the testing range, a flat folding mirror is placed in the building II. In the free-space atmospheric link, the random fluctuating sources include beam pointing and

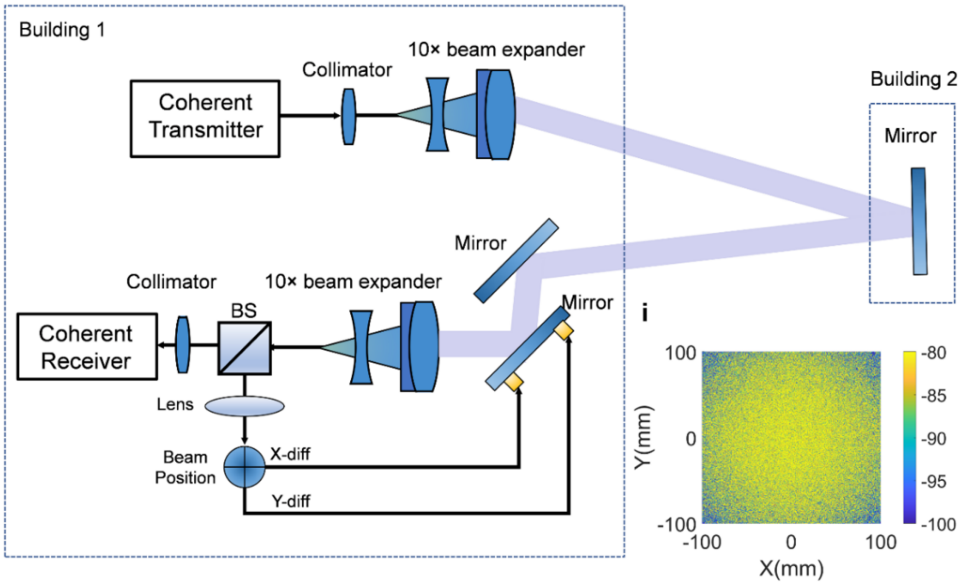

Figure D.4: Free-space link setup. Free-space atmospheric link setup. Inset: modeled optical Gaussian beam wavefront using measured C_n^2.

atmospheric refractive index fluctuations described by refractive index power spectrum. Turbulence degraded wavefronts can be simulated and compensated by pre- or post-detection processing, ideal lossless adaptive optics including a spatial mode digital coherent receiver and a multimode pre-amplifier, few mode fiber and modes diversity coherent receipt. To effectively suppress the pointing error of the free-space link and power fading induced by the atmospheric turbulence, we developed the active feedback control locking system. Figure D.5a-f show the free-running scenario and the active tracking scenario with beam stabilization. Figures D.5c and 9d show the beam position of the received light beam along x-axis and y-axis for the free-running and stabilized cases. A quadrant positional detector (Thorlabs PDQ30C) with a 150 kHz servo bandwidth (KPA101) is used for the beam feedback stabilization. We run this in closed-loop by controlling the piezoelectric adjusters of the kinematic mirror mounts (POLARIS-K2S2P), with an active feedback control bandwidth of 1 kHz. (The link distance is 160 m which gives a traveling time delay of $\approx$ 520 ns and a maximum corresponding bandwidth of 1.93 MHz.) Before beam stabilization, the x- and

y-axis pixel fluctuations are respectively ± 0.697 and ± 0.553 mm (1σ). With active feedback locking system, the x- and y-axis transmission beam pointing errors are suppressed respectively to ± 0.052 and ± 0.042 mm (1σ).

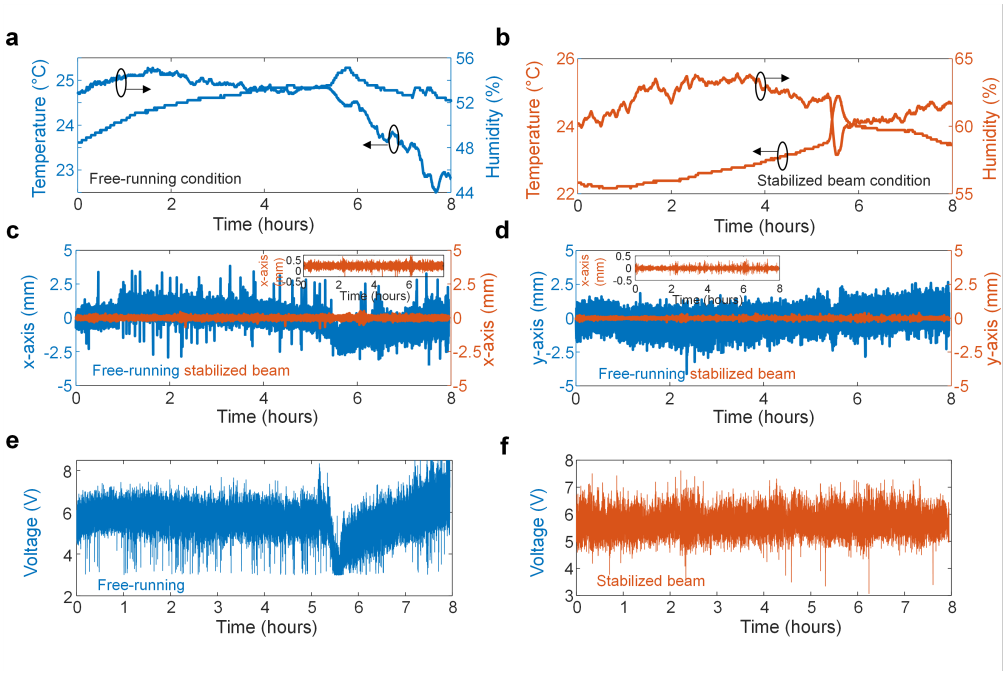

Figure D.5: Free-space link beam stabilization. a and b, Weather condition for the stabilized and free-running link. c and d, Beam position distribution along x-axis and y-axis before and after beam stabilization respectively. Insets: amplitude zoom-in, after beam stabilization. e and f, Received optical power fluctuations before and after free-space beam stabilization.

Figures D.5e and f show the received optical power fluctuations before and after free-space beam stabilization, respectively. Even with beam positional feedback stabilization, the received power still fluctuates by 79%, which arises from residual pointing error, turbulence, and laser intensity noise. In our link demonstration, the beam size is expanded 10 times via an achromatic Galilean beam expander to 4 cm. Consequently, the power density of our link is about 0.004 W/cm^2, much lower than the IEC 60825 eye-safety requirements. In IEC 60825 standards, the maximum permissible exposure (MPE) – the highest power or energy density (in W/cm^2 or J/cm^2) of a light source – at 1550 nm for 0.25 seconds (human blink

reflex time) is 1 J/cm^2. This corresponds to 4 W/cm^2, for negligible probability of damage.

REFERENCES

[1] T. W. Hänsch, "Nobel Lecture: Passion for precision," *Rev. Mod. Phys.*, vol. 78, pp. 1297–1309, nov 2006.

[2] J. L. Hall, "Nobel Lecture: Defining and measuring optical frequencies," *Rev. Mod. Phys.*, vol. 78, pp. 1279–1295, nov 2006.

[3] A. A. Savchenkov, A. B. Matsko, D. Strekalov, M. Mohageg, V. S. Ilchenko, and L. Maleki, "Low Threshold Optical Oscillations in a Whispering Gallery Mode CaF2 Resonator," *Phys. Rev. Lett.*, vol. 93, p. 243905, dec 2004.

[4] T. J. Kippenberg, S. M. Spillane, and K. J. Vahala, "Kerr-Nonlinearity Optical Parametric Oscillation in an Ultrahigh- Q toroid Microcavity," *Phys. Rev. Lett.*, vol. 93, p. 083904, aug 2004.

[5] T. J. Kippenberg, R. Holzwarth, and S. A. Diddams, "Microresonator-Based Optical Frequency Combs," *Science (80-.).*, vol. 332, pp. 555–559, apr 2011.

[6] P. Del'Haye, T. Herr, E. Gavartin, M. L. Gorodetsky, R. Holzwarth, and T. J. Kippenberg, "Octave Spanning Tunable Frequency Comb from a Microresonator," *Phys. Rev. Lett.*, vol. 107, p. 063901, aug 2011.

[7] Y. Okawachi, K. Saha, J. S. Levy, Y. H. Wen, M. Lipson, and A. L. Gaeta, "Octave-spanning frequency comb generation in a silicon nitride chip," *Opt. Lett.*, vol. 36, p. 3398, sep 2011.

[8] W. Liang, D. Eliyahu, V. S. Ilchenko, A. A. Savchenkov, A. B. Matsko, D. Seidel, and L. Maleki, "High spectral purity Kerr frequency comb radio frequency photonic oscillator," *Nat. Commun.*, vol. 6, p. 7957, nov 2015.

[9] S.-W. Huang, J. Yang, J. Lim, H. Zhou, M. Yu, D.-L. Kwong, and C. W. Wong, "A low-phase-noise 18 GHz Kerr frequency microcomb phase-locked over 65 THz," *Sci. Rep.*, vol. 5, p. 13355, oct 2015.

[10] J. Li, H. Lee, T. Chen, and K. J. Vahala, "Low-Pump-Power, Low-Phase-Noise, and Microwave to Millimeter-Wave Repetition Rate Operation in Microcombs," *Phys. Rev. Lett.*, vol. 109, p. 233901, dec 2012.

[11] S. B. Papp and S. A. Diddams, "Spectral and temporal characterization of a fused-quartz-microresonator optical frequency comb," *Phys. Rev. A*, vol. 84, p. 053833, nov 2011.

[12] P. Del'Haye, O. Arcizet, A. Schliesser, R. Holzwarth, and T. J. Kippenberg, "Full Stabilization of a Microresonator-Based Optical Frequency Comb," *Phys. Rev. Lett.*, vol. 101, p. 053903, jul 2008.

[13] S.-W. Huang, J. Yang, M. Yu, B. H. McGuyer, D.-L. Kwong, T. Zelevinsky, and C. W. Wong, "A broadband chip-scale optical frequency synthesizer at 2.7×10^{-16} relative uncertainty," *Sci. Adv.*, vol. 2, p. e1501489, apr 2016.

[14] S. B. Papp, K. Beha, P. Del'Haye, F. Quinlan, H. Lee, K. J. Vahala, and S. A. Diddams, "Microresonator frequency comb optical clock," *Optica*, vol. 1, p. 10, jul 2014.

[15] X. Xue, Y. Xuan, Y. Liu, P.-H. Wang, S. Chen, J. Wang, D. E. Leaird, M. Qi, and A. M. Weiner, "Mode-locked dark pulse Kerr combs in normal-dispersion microresonators," *Nat. Photonics*, vol. 9, pp. 594–600, sep 2015.

[16] T. Herr, V. Brasch, J. D. Jost, C. Y. Wang, N. M. Kondratiev, M. L. Gorodetsky, and T. J. Kippenberg, "Temporal solitons in optical microresonators," *Nat. Photonics*, vol. 8, pp. 145–152, feb 2014.

[17] S.-W. Huang, H. Zhou, J. Yang, J. F. McMillan, A. Matsko, M. Yu, D.-L. Kwong, L. Maleki, and C. W. Wong, "Mode-Locked Ultrashort Pulse Generation from On-Chip Normal Dispersion Microresonators," *Phys. Rev. Lett.*, vol. 114, p. 053901, feb 2015.

[18] K. Saha, Y. Okawachi, B. Shim, J. S. Levy, R. Salem, A. R. Johnson, M. A. Foster, M. R. E. Lamont, M. Lipson, and A. L. Gaeta, "Modelocking and femtosecond pulse generation in chip-based frequency combs," *Opt. Express*, vol. 21, p. 1335, jan 2013.

[19] X. Yi, Q.-F. Yang, K. Y. Yang, M.-G. Suh, and K. Vahala, "Soliton frequency comb at microwave rates in a high-Q silica microresonator," *Optica*, vol. 2, p. 1078, dec 2015.

[20] V. Brasch, M. Geiselmann, T. Herr, G. Lihachev, M. H. P. Pfeiffer, M. L. Gorodetsky, and T. J. Kippenberg, "Photonic chip-based optical frequency comb using soliton Cherenkov radiation," *Science (80-.).*, vol. 351, pp. 357–360, jan 2016.

[21] T. J. Kippenberg, A. L. Gaeta, M. Lipson, and M. L. Gorodetsky, "Dissipative Kerr solitons in optical microresonators," *Science (80-.).*, vol. 361, p. eaan8083, aug 2018.

[22] D. J. Moss, R. Morandotti, A. L. Gaeta, and M. Lipson, "New CMOS-compatible platforms based on silicon nitride and Hydex for nonlinear optics," *Nat. Photonics*, vol. 7, pp. 597–607, aug 2013.

[23] L. Maleki, V. S. Ilchenko, A. A. Savchenkov, and A. B. Matsko, "Crystalline Whispering gallery mode resonators in optics and photonics," in *Pract. Appl. Microresonators Opt. Photonics*, ch. 3, pp. 133–209, CRC Press, 2009.

[24] H. Jung, C. Xiong, K. Y. Fong, X. Zhang, and H. X. Tang, "Optical frequency comb generation from aluminum nitride microring resonator," *Opt. Lett.*, vol. 38, p. 2810, aug 2013.

[25] B. J. M. Hausmann, I. Bulu, V. Venkataraman, P. Deotare, and M. Lončar, "Diamond nonlinear photonics," *Nat. Photonics*, vol. 8, pp. 369–374, may 2014.

[26] P. Del'Haye, A. Schliesser, O. Arcizet, T. Wilken, R. Holzwarth, and T. J. Kippenberg, "Optical frequency comb generation from a monolithic microresonator," *Nature*, vol. 450, pp. 1214–1217, dec 2007.

[27] T. Herr, V. Brasch, J. D. Jost, I. Mirgorodskiy, G. Lihachev, M. L. Gorodetsky, and T. J. Kippenberg, "Mode Spectrum and Temporal Soliton Formation in Optical Microresonators," *Phys. Rev. Lett.*, vol. 113, p. 123901, sep 2014.

[28] M. Pu, L. Ottaviano, E. Semenova, and K. Yvind, "Efficient frequency comb generation in AlGaAs-on-insulator," *Optica*, vol. 3, p. 823, aug 2016.

[29] Y. He, Q.-F. Yang, J. Ling, R. Luo, H. Liang, M. Li, B. Shen, H. Wang, K. Vahala, and Q. Lin, "Self-starting bi-chromatic $LiNbO_3$ soliton microcomb," *Optica*, vol. 6, p. 1138, sep 2019.

[30] Y. Liu, Y. Xuan, X. Xue, P.-H. Wang, S. Chen, A. J. Metcalf, J. Wang, D. E. Leaird, M. Qi, and A. M. Weiner, "Investigation of mode coupling in normal-dispersion silicon nitride microresonators for Kerr frequency comb generation," *Optica*, vol. 1, p. 137, sep 2014.

[31] A. A. Savchenkov, A. B. Matsko, W. Liang, V. S. Ilchenko, D. Seidel, and L. Maleki, "Kerr frequency comb generation in overmoded resonators," *Opt. Express*, vol. 20, no. 24, p. 27290, 2012.

[32] S. Ramelow, A. Farsi, S. Clemmen, J. S. Levy, A. R. Johnson, Y. Okawachi, M. R. E. Lamont, M. Lipson, and A. L. Gaeta, "Strong polarization mode coupling in microresonators," *Opt. Lett.*, vol. 39, p. 5134, sep 2014.

[33] H. Zhou, S.-W. Huang, Y. Dong, M. Liao, K. Qiu, and C. W. Wong, "Stability and Intrinsic Fluctuations of Dissipative Cavity Solitons in Kerr Frequency Microcombs," *IEEE Photonics J.*, vol. 7, pp. 1–13, jun 2015.

[34] S.-W. Huang, H. Liu, J. Yang, M. Yu, D.-L. Kwong, and C. W. Wong, "Smooth and flat phase-locked Kerr frequency comb generation by higher order mode suppression," *Sci. Rep.*, vol. 6, p. 26255, sep 2016.

[35] Y. Li, S.-W. Huang, B. Li, H. Liu, J. Yang, A. K. Vinod, K. Wang, M. Yu, D.-L. Kwong, H.-T. Wang, K. K.-Y. Wong, and C. W. Wong, "Real-time transition dynamics and stability of chip-scale dispersion-managed frequency microcombs," *Light Sci. Appl.*, vol. 9, p. 52, dec 2020.

[36] Y.-S. Jang, H. Liu, J. Yang, M. Yu, D.-L. Kwong, and C. W. Wong, "Nanometric Precision Distance Metrology via Hybrid Spectrally Resolved and Homodyne Interferometry in a Single Soliton Frequency Microcomb," *Phys. Rev. Lett.*, vol. 126, p. 023903, jan 2021.

[37] P. Grelu and N. Akhmediev, "Dissipative solitons for mode-locked lasers," *Nat. Photonics*, vol. 6, pp. 84–92, feb 2012.

[38] K. Luke, A. Dutt, C. B. Poitras, and M. Lipson, "Overcoming Si_3N_4 film stress limitations for high quality factor ring resonators," *Opt. Express*, vol. 21, p. 22829, sep 2013.

[39] D. Hillerkuss, R. Schmogrow, T. Schellinger, M. Jordan, M. Winter, G. Huber, T. Vallaitis, R. Bonk, P. Kleinow, F. Frey, M. Roeger, S. Koenig, A. Ludwig, A. Marculescu, J. Li, M. Hoh, M. Dreschmann, J. Meyer, S. Ben Ezra, N. Narkiss, B. Nebendahl, F. Parmigiani, P. Petropoulos, B. Resan, A. Oehler, K. Weingarten, T. Ellermeyer, J. Lutz, M. Moeller, M. Huebner, J. Becker, C. Koos, W. Freude, and J. Leuthold, "26 Tbit/s line-rate super-channel transmission utilizing all-optical fast Fourier transform processing," *Nat. Photonics*, vol. 5, pp. 364–371, jun 2011.

[40] C.-H. Li, A. J. Benedick, P. Fendel, A. G. Glenday, F. X. Kärtner, D. F. Phillips, D. Sasselov, A. Szentgyorgyi, and R. L. Walsworth, "A laser frequency comb that enables radial velocity measurements with a precision of 1 cm/s," *Nature*, vol. 452, pp. 610–612, apr 2008.

[41] T. Bååk, "Silicon oxynitride; a material for GRIN optics," *Appl. Opt.*, vol. 21, p. 1069, mar 1982.

[42] J. K. Jang, M. Erkintalo, S. G. Murdoch, and S. Coen, "Observation of dispersive wave emission by temporal cavity solitons," *Opt. Lett.*, vol. 39, p. 5503, oct 2014.

[43] S. Coen, H. G. Randle, T. Sylvestre, and M. Erkintalo, "Modeling of octave-spanning Kerr frequency combs using a generalized mean-field Lugiato–Lefever model," *Opt. Lett.*, vol. 38, p. 37, jan 2013.

[44] C. Y. Wang, T. Herr, P. Del'Haye, A. Schliesser, J. Hofer, R. Holzwarth, T. W. Hänsch, N. Picqué, and T. J. Kippenberg, "Mid-infrared optical frequency combs at 2.5 μm based on crystalline microresonators," *Nat. Commun.*, vol. 4, p. 1345, dec 2013.

[45] X. Liu, X. Yao, and Y. Cui, "Real-Time Observation of the Buildup of Soliton Molecules," *Phys. Rev. Lett.*, vol. 121, p. 023905, jul 2018.

[46] P. Ryczkowski, M. Närhi, C. Billet, J.-M. Merolla, G. Genty, and J. M. Dudley, "Real-time full-field characterization of transient dissipative soliton dynamics in a mode-locked laser," *Nat. Photonics*, vol. 12, pp. 221–227, apr 2018.

[47] G. Herink, F. Kurtz, B. Jalali, D. R. Solli, and C. Ropers, "Real-time spectral interferometry probes the internal dynamics of femtosecond soliton molecules," *Science (80-.).*, vol. 356, pp. 50–54, apr 2017.

[48] K. Krupa, K. Nithyanandan, U. Andral, P. Tchofo-Dinda, and P. Grelu, "Real-Time Observation of Internal Motion within Ultrafast Dissipative Optical Soliton Molecules," *Phys. Rev. Lett.*, vol. 118, p. 243901, jun 2017.

[49] B. G. Bale, S. Boscolo, and S. K. Turitsyn, "Dissipative dispersion-managed solitons in mode-locked lasers," *Opt. Lett.*, vol. 34, p. 3286, nov 2009.

[50] T. Yu, E. A. Golovchenko, A. N. Pilipetskii, and C. R. Menyuk, "Dispersion-managed soliton interactions in optical fibers," *Opt. Lett.*, vol. 22, p. 793, jun 1997.

[51] H. Haus, K. Tamura, L. Nelson, and E. Ippen, "Stretched-pulse additive pulse mode-locking in fiber ring lasers: theory and experiment," *IEEE J. Quantum Electron.*, vol. 31, pp. 591–598, mar 1995.

[52] B. Yao, S.-W. Huang, Y. Liu, A. K. Vinod, C. Choi, M. Hoff, Y. Li, M. Yu, Z. Feng, D.-L. Kwong, Y. Huang, Y. Rao, X. Duan, and C. W. Wong, "Gate-tunable frequency combs in graphene–nitride microresonators," *Nature*, vol. 558, pp. 410–414, jun 2018.

[53] A. Pasquazi, M. Peccianti, L. Razzari, D. J. Moss, S. Coen, M. Erkintalo, Y. K. Chembo, T. Hansson, S. Wabnitz, P. Del'Haye, X. Xue, A. M. Weiner, and R. Morandotti, "Micro-combs: A novel generation of optical sources," *Phys. Rep.*, vol. 729, pp. 1–81, jan 2018.

[54] D. T. Spencer, T. Drake, T. C. Briles, J. Stone, L. C. Sinclair, C. Fredrick, Q. Li, D. Westly, B. R. Ilic, A. Bluestone, N. Volet, T. Komljenovic, L. Chang, S. H. Lee, D. Y. Oh, M. G. Suh, K. Y. Yang, M. H. Pfeiffer, T. J. Kippenberg, E. Norberg, L. Theogarajan, K. Vahala, N. R. Newbury, K. Srinivasan, J. E. Bowers, S. A. Diddams, and S. B. Papp, "An optical-frequency synthesizer using integrated photonics," *Nature*, vol. 557, no. 7703, pp. 81–85, 2018.

[55] A. Dutt, C. Joshi, X. Ji, J. Cardenas, Y. Okawachi, K. Luke, A. L. Gaeta, and M. Lipson, "On-chip dual-comb source for spectroscopy," *Sci. Adv.*, vol. 4, p. e1701858, mar 2018.

[56] P. Marin-Palomo, J. N. Kemal, M. Karpov, A. Kordts, J. Pfeifle, M. H. P. Pfeiffer, P. Trocha, S. Wolf, V. Brasch, M. H. Anderson, R. Rosenberger, K. Vijayan, W. Freude, T. J. Kippenberg, and C. Koos, "Microresonator-based solitons for massively parallel coherent optical communications," *Nature*, vol. 546, pp. 274–279, jun 2017.

[57] P. Trocha, M. Karpov, D. Ganin, M. H. P. Pfeiffer, A. Kordts, S. Wolf, J. Krockenberger, P. Marin-Palomo, C. Weimann, S. Randel, W. Freude, T. J. Kippenberg, and

C. Koos, "Ultrafast optical ranging using microresonator soliton frequency combs," *Science (80-.).*, vol. 359, pp. 887–891, feb 2018.

[58] M.-G. Suh and K. J. Vahala, "Soliton microcomb range measurement.," *Science (80-.).*, vol. 359, pp. 884–887, feb 2018.

[59] E. Lucas, G. Lihachev, R. Bouchand, N. G. Pavlov, A. S. Raja, M. Karpov, M. L. Gorodetsky, and T. J. Kippenberg, "Spatial multiplexing of soliton microcombs," *Nat. Photonics*, vol. 12, pp. 699–705, nov 2018.

[60] C. Godey, I. V. Balakireva, A. Coillet, and Y. K. Chembo, "Stability analysis of the spatiotemporal Lugiato-Lefever model for Kerr optical frequency combs in the anomalous and normal dispersion regimes," *Phys. Rev. A*, vol. 89, p. 063814, jun 2014.

[61] S. Coen and M. Erkintalo, "Universal scaling laws of Kerr frequency combs," *Opt. Lett.*, vol. 38, no. 11, p. 1790, 2013.

[62] S.-W. Huang, J. Yang, S.-H. Yang, M. Yu, D.-L. Kwong, T. Zelevinsky, M. Jarrahi, and C. W. Wong, "Globally Stable Microresonator Turing Pattern Formation for Coherent High-Power THz Radiation On-Chip," *Phys. Rev. X*, vol. 7, p. 041002, oct 2017.

[63] A. F. J. Runge, N. G. R. Broderick, and M. Erkintalo, "Observation of soliton explosions in a passively mode-locked fiber laser," *Optica*, vol. 2, p. 36, jan 2015.

[64] G. Herink, B. Jalali, C. Ropers, and D. R. Solli, "Resolving the build-up of femtosecond mode-locking with single-shot spectroscopy at 90 €...MHz frame rate," *Nat. Photonics*, vol. 10, pp. 321–326, may 2016.

[65] Y. Yu, B. Li, X. Wei, Y. Xu, K. K. Tsia, and K. K. Wong, "Spectral-temporal dynamics of multipulse mode-locking," *Appl. Phys. Lett.*, vol. 110, p. 201107, may 2017.

[66] M. A. Foster, R. Salem, D. F. Geraghty, A. C. Turner-Foster, M. Lipson, and A. L. Gaeta, "Silicon-chip-based ultrafast optical oscilloscope," *Nature*, vol. 456, pp. 81–84, nov 2008.

[67] B. Li, S.-W. Huang, Y. Li, C. W. Wong, and K. K. Y. Wong, "Panoramic-reconstruction temporal imaging for seamless measurements of slowly-evolved femtosecond pulse dynamics," *Nat. Commun.*, vol. 8, p. 61, dec 2017.

[68] E. Lucas, M. Karpov, H. Guo, M. L. Gorodetsky, and T. J. Kippenberg, "Breathing dissipative solitons in optical microresonators," *Nat. Commun.*, vol. 8, p. 736, dec 2017.

[69] X. Yi, Q.-F. Yang, K. Y. Yang, and K. Vahala, "Imaging soliton dynamics in optical microcavities," *Nat. Commun.*, vol. 9, p. 3565, dec 2018.

[70] C. Bao and C. Yang, "Stretched cavity soliton in dispersion-managed Kerr resonators," *Phys. Rev. A*, vol. 92, p. 023802, aug 2015.

[71] Y. Song, K. Jung, and J. Kim, "Impact of pulse dynamics on timing jitter in mode-locked fiber lasers," *Opt. Lett.*, vol. 36, p. 1761, may 2011.

[72] J. Capmany and D. Novak, "Microwave photonics combines two worlds," jun 2007.

[73] C. Manzoni, O. D. Mücke, G. Cirmi, S. Fang, J. Moses, S.-W. Huang, K.-H. Hong, G. Cerullo, and F. X. Kärtner, "Coherent pulse synthesis: towards sub-cycle optical waveforms," *Laser Photon. Rev.*, vol. 9, pp. 129–171, mar 2015.

[74] A. B. Matsko and L. Maleki, "On timing jitter of mode locked Kerr frequency combs," *Opt. Express*, vol. 21, p. 28862, nov 2013.

[75] P. Del'Haye, O. Arcizet, M. L. Gorodetsky, R. Holzwarth, and T. J. Kippenberg, "Frequency comb assisted diode laser spectroscopy for measurement of microcavity dispersion," *Nat. Photonics*, vol. 3, pp. 529–533, sep 2009.

[76] A. G. Griffith, R. K. Lau, J. Cardenas, Y. Okawachi, A. Mohanty, R. Fain, Y. H. D. Lee, M. Yu, C. T. Phare, C. B. Poitras, A. L. Gaeta, and M. Lipson, "Silicon-chip mid-infrared frequency comb generation," *Nat. Commun.*, vol. 6, pp. 1–5, feb 2015.

[77] M. Kues, C. Reimer, P. Roztocki, L. R. Cortés, S. Sciara, B. Wetzel, Y. Zhang, A. Cino, S. T. Chu, B. E. Little, D. J. Moss, L. Caspani, J. Azaña, and R. Morandotti, "On-chip generation of high-dimensional entangled quantum states and their coherent control," *Nature*, vol. 546, pp. 622–626, jun 2017.

[78] X. Guo, C.-L. Zou, H. Jung, Z. Gong, A. Bruch, L. Jiang, and H. X. Tang, "Efficient Generation of a Near-visible Frequency Comb via Cherenkov-like Radiation from a Kerr Microcomb," *Phys. Rev. Appl.*, vol. 10, p. 14012, 2018.

[79] M. Zhang, C. Wang, R. Cheng, A. Shams-Ansari, and M. Lončar, "Monolithic ultra-high-Q lithium niobate microring resonator," *Optica*, vol. 4, p. 1536, dec 2017.

[80] D. Yoon Oh, K. Y. Yang, C. Fredrick, G. Ycas, S. A. Diddams, and K. J. Vahala, "Coherent ultra-violet to near-infrared generation in silica ridge waveguides," *Nat. Commun.*, vol. 8, p. 13922, apr 2017.

[81] B. Kuyken, T. Ideguchi, S. Holzner, M. Yan, T. W. Hänsch, J. Van Campenhout, P. Verheyen, S. Coen, F. Leo, R. Baets, G. Roelkens, and N. Picqué, "An octave-spanning mid-infrared frequency comb generated in a silicon nanophotonic wire waveguide," *Nat. Commun.*, vol. 6, p. 6310, may 2015.

[82] K. Y. Yang, K. Beha, D. C. Cole, X. Yi, P. Del'Haye, H. Lee, J. Li, D. Y. Oh, S. A. Diddams, S. B. Papp, and K. J. Vahala, "Broadband dispersion-engineered microresonator on a chip," *Nat. Photonics*, vol. 10, pp. 316–320, may 2016.

[83] S. A. Diddams, K. Vahala, and T. Udem, "Optical frequency combs: Coherently uniting the electromagnetic spectrum," *Science (80-.).*, vol. 369, jul 2020.

[84] T. Udem, R. Holzwarth, and T. W. Hänsch, "Optical frequency metrology," *Nature*, vol. 416, pp. 233–237, mar 2002.

[85] M. Lezius, T. Wilken, C. Deutsch, M. Giunta, O. Mandel, A. Thaller, V. Schkolnik, M. Schiemangk, A. Dinkelaker, A. Kohfeldt, A. Wicht, M. Krutzik, A. Peters, O. Hellmig, H. Duncker, K. Sengstock, P. Windpassinger, K. Lampmann, T. Hülsing, T. W. Hänsch, and R. Holzwarth, "Space-borne frequency comb metrology," *Optica*, vol. 3, p. 1381, dec 2016.

[86] J. Lee, K. Lee, Y.-S. Jang, H. Jang, S. Han, S.-H. Lee, K.-I. Kang, C.-W. Lim, Y.-J. Kim, and S.-W. Kim, "Testing of a femtosecond pulse laser in outer space," *Sci. Rep.*, vol. 4, p. 5134, may 2015.

[87] I. Coddington, W. C. Swann, L. Nenadovic, and N. R. Newbury, "Rapid and precise absolute distance measurements at long range," *Nat. Photonics*, vol. 3, pp. 351–356, jun 2009.

[88] T. M. Fortier, M. S. Kirchner, F. Quinlan, J. Taylor, J. C. Bergquist, T. Rosenband, N. Lemke, A. Ludlow, Y. Jiang, C. W. Oates, and S. A. Diddams, "Generation of ultrastable microwaves via optical frequency division," *Nat. Photonics*, vol. 5, pp. 425–429, jul 2011.

[89] X. Xie, R. Bouchand, D. Nicolodi, M. Giunta, W. Hänsel, M. Lezius, A. Joshi, S. Datta, C. Alexandre, M. Lours, P.-A. Tremblin, G. Santarelli, R. Holzwarth, and Y. Le Coq, "Photonic microwave signals with zeptosecond-level absolute timing noise," *Nat. Photonics*, vol. 11, pp. 44–47, jan 2017.

[90] A. Tikan, J. Riemensberger, K. Komagata, S. Hönl, M. Churaev, C. Skehan, H. Guo, R. N. Wang, J. Liu, P. Seidler, and T. J. Kippenberg, "Emergent nonlinear phenomena in a driven dissipative photonic dimer," *Nat. Phys.*, vol. 17, pp. 604–610, may 2021.

[91] J. Liu, E. Lucas, A. S. Raja, J. He, J. Riemensberger, R. N. Wang, M. Karpov, H. Guo, R. Bouchand, and T. J. Kippenberg, "Photonic microwave generation in the X- and K-band using integrated soliton microcombs," *Nat. Photonics*, vol. 14, pp. 486–491, aug 2020.

[92] Z. Gong, A. Bruch, M. Shen, X. Guo, H. Jung, L. Fan, X. Liu, L. Zhang, J. Wang, J. Li, J. Yan, and H. X. Tang, "High-fidelity cavity soliton generation in crystalline AlN micro-ring resonators," *Opt. Lett.*, vol. 43, p. 4366, sep 2018.

[93] Y. He, J. Ling, M. Li, and Q. Lin, "Perfect soliton crystals on demand," sep 2019.

[94] L. Chang, A. Boes, X. Guo, D. T. Spencer, M. J. Kennedy, J. D. Peters, N. Volet, J. Chiles, A. Kowligy, N. Nader, D. D. Hickstein, E. J. Stanton, S. A. Diddams, S. B. Papp, and J. E. Bowers, "Heterogeneously Integrated GaAs Waveguides on Insulator for Efficient Frequency Conversion," *Laser Photon. Rev.*, vol. 12, p. 1800149, oct 2018.

[95] B. Stern, X. Ji, Y. Okawachi, A. L. Gaeta, and M. Lipson, "Battery-operated integrated frequency comb generator," *Nature*, vol. 562, pp. 401–405, oct 2018.

[96] A. S. Raja, A. S. Voloshin, H. Guo, S. E. Agafonova, J. Liu, A. S. Gorodnitskiy, M. Karpov, N. G. Pavlov, E. Lucas, R. R. Galiev, A. E. Shitikov, J. D. Jost, M. L. Gorodetsky, and T. J. Kippenberg, "Electrically pumped photonic integrated soliton microcomb," *Nat. Commun.*, vol. 10, p. 680, dec 2019.

[97] B. Shen, L. Chang, J. Liu, H. Wang, Q.-F. Yang, C. Xiang, R. N. Wang, J. He, T. Liu, W. Xie, J. Guo, D. Kinghorn, L. Wu, Q.-X. Ji, T. J. Kippenberg, K. Vahala, and J. E. Bowers, "Integrated turnkey soliton microcombs," *Nature*, vol. 582, pp. 365–369, jun 2020.

[98] W. Jin, Q.-F. Yang, L. Chang, B. Shen, H. Wang, M. A. Leal, L. Wu, M. Gao, A. Feshali, M. Paniccia, K. J. Vahala, and J. E. Bowers, "Hertz-linewidth semiconductor lasers using CMOS-ready ultra-high-Q microresonators," *Nat. Photonics*, vol. 15, pp. 346–353, may 2021.

[99] A. Fülöp, M. Mazur, A. Lorences-Riesgo, Ó. B. Helgason, P.-H. H. Wang, Y. Xuan, D. E. Leaird, M. Qi, P. A. Andrekson, A. M. Weiner, and V. Torres-Company, "High-order coherent communications using mode-locked dark-pulse Kerr combs from microresonators," *Nat. Commun.*, vol. 9, p. 1598, dec 2018.

[100] B. Corcoran, M. Tan, X. Xu, A. Boes, J. Wu, T. G. Nguyen, S. T. Chu, B. E. Little, R. Morandotti, A. Mitchell, and D. J. Moss, "Ultra-dense optical data transmission over standard fibre with a single chip source," *Nat. Commun.*, vol. 11, p. 2568, dec 2020.

[101] J. Riemensberger, A. Lukashchuk, M. Karpov, W. Weng, E. Lucas, J. Liu, and T. J. Kippenberg, "Massively parallel coherent laser ranging using a soliton microcomb," *Nature*, vol. 581, pp. 164–170, may 2020.

[102] E. Obrzud, M. Rainer, A. Harutyunyan, M. H. Anderson, J. Liu, M. Geiselmann, B. Chazelas, S. Kundermann, S. Lecomte, M. Cecconi, A. Ghedina, E. Molinari, F. Pepe, F. Wildi, F. Bouchy, T. J. Kippenberg, and T. Herr, "A microphotonic astrocomb," *Nat. Photonics*, vol. 13, pp. 31–35, jan 2019.

[103] M.-G. Suh, X. Yi, Y.-H. Lai, S. Leifer, I. S. Grudinin, G. Vasisht, E. C. Martin, M. P. Fitzgerald, G. Doppmann, J. Wang, D. Mawet, S. B. Papp, S. A. Diddams, C. Beichman, and K. Vahala, "Searching for exoplanets using a microresonator astrocomb," *Nat. Photonics*, vol. 13, pp. 25–30, jan 2019.

[104] M.-G. Suh, Q.-F. Yang, K. Y. Yang, X. Yi, and K. J. Vahala, "Microresonator soliton dual-comb spectroscopy," *Science (80-.).*, vol. 354, pp. 600–603, nov 2016.

[105] M. Yu, Y. Okawachi, A. G. Griffith, N. Picqué, M. Lipson, and A. L. Gaeta, "Silicon-chip-based mid-infrared dual-comb spectroscopy," *Nat. Commun.*, vol. 9, p. 1869, dec 2018.

[106] E. Lucas, P. Brochard, R. Bouchand, S. Schilt, T. Südmeyer, and T. J. Kippenberg, "Ultralow-noise photonic microwave synthesis using a soliton microcomb-based transfer oscillator," *Nat. Commun.*, vol. 11, p. 374, dec 2020.

[107] D. Jeong, D. Kwon, I. Jeon, I. H. Do, J. Kim, and H. Lee, "Ultralow jitter silica microcomb," *Optica*, vol. 7, p. 1108, sep 2020.

[108] X. Xu, M. Tan, B. Corcoran, J. Wu, A. Boes, T. G. Nguyen, S. T. Chu, B. E. Little, D. G. Hicks, R. Morandotti, A. Mitchell, and D. J. Moss, "11 TOPS photonic convolutional accelerator for optical neural networks," *Nature*, vol. 589, pp. 44–51, jan 2021.

[109] J. Feldmann, N. Youngblood, M. Karpov, H. Gehring, X. Li, M. Stappers, M. Le Gallo, X. Fu, A. Lukashchuk, A. S. Raja, J. Liu, C. D. Wright, A. Sebastian, T. J. Kippenberg, W. H. Pernice, and H. Bhaskaran, "Parallel convolutional processing using an integrated photonic tensor core," *Nature*, vol. 589, pp. 52–58, jan 2021.

[110] E. Lucas, H. Guo, J. D. Jost, M. Karpov, and T. J. Kippenberg, "Detuning-dependent properties and dispersion-induced instabilities of temporal dissipative Kerr solitons in optical microresonators," *Phys. Rev. A*, vol. 95, p. 043822, apr 2017.

[111] J. R. Stone, T. C. Briles, T. E. Drake, D. T. Spencer, D. R. Carlson, S. A. Diddams, and S. B. Papp, "Thermal and Nonlinear Dissipative-Soliton Dynamics in Kerr-Microresonator Frequency Combs," *Phys. Rev. Lett.*, vol. 121, p. 063902, aug 2018.

[112] X. Yi, Q.-F. Yang, X. Zhang, K. Y. Yang, X. Li, and K. Vahala, "Single-mode dispersive waves and soliton microcomb dynamics," *Nat. Commun.*, vol. 8, p. 14869, apr 2017.

[113] Q.-F. Yang, Q.-X. Ji, L. Wu, B. Shen, H. Wang, C. Bao, Z. Yuan, and K. Vahala, "Dispersive-wave induced noise limits in miniature soliton microwave sources," *Nat. Commun.*, vol. 12, p. 1442, dec 2021.

[114] Y. Bai, M. Zhang, Q. Shi, S. Ding, Y. Qin, Z. Xie, X. Jiang, and M. Xiao, "Brillouin-Kerr Soliton Frequency Combs in an Optical Microresonator," *Phys. Rev. Lett.*, vol. 126, p. 063901, feb 2021.

[115] J. R. Stone and S. B. Papp, "Harnessing Dispersion in Soliton Microcombs to Mitigate Thermal Noise," *Phys. Rev. Lett.*, vol. 125, p. 153901, oct 2020.

[116] T. E. Drake, J. R. Stone, T. C. Briles, and S. B. Papp, "Thermal decoherence and laser cooling of Kerr microresonator solitons," *Nat. Photonics*, vol. 14, pp. 480–485, aug 2020.

[117] C. Bao, M.-G. Suh, B. Shen, K. Şafak, A. Dai, H. Wang, L. Wu, Z. Yuan, Q.-F. Yang, A. B. Matsko, F. X. Kärtner, and K. J. Vahala, "Quantum diffusion of microcavity solitons," *Nat. Phys.*, jan 2021.

[118] J. Taylor, S. Datta, A. Hati, C. Nelson, F. Quinlan, A. Joshi, and S. Diddams, "Characterization of Power-to-Phase Conversion in High-Speed P-I-N Photodiodes," *IEEE Photonics J.*, vol. 3, pp. 140–151, feb 2011.

[119] D. Kwon, C.-G. Jeon, J. Shin, M.-S. Heo, S. E. Park, Y. Song, and J. Kim, "Reference-free, high-resolution measurement method of timing jitter spectra of optical frequency combs," *Sci. Rep.*, vol. 7, p. 40917, mar 2017.

[120] D. C. Cole, E. S. Lamb, P. Del'Haye, S. A. Diddams, S. B. Papp, P. Del'Haye, S. A. Diddams, and S. B. Papp, "Soliton crystals in Kerr resonators," *Nat. Photonics*, vol. 11, pp. 671–676, oct 2017.

[121] X. Yi, Q.-F. Yang, K. Y. Yang, and K. Vahala, "Theory and measurement of the soliton self-frequency shift and efficiency in optical microcavities," *Opt. Lett.*, vol. 41, p. 3419, aug 2016.

[122] Z. Liu, M. Ouali, S. Coulibaly, M. G. Clerc, M. Taki, and M. Tlidi, "Characterization of spatiotemporal chaos in a Kerr optical frequency comb and in all fiber cavities," *Opt. Lett.*, vol. 42, p. 1063, mar 2017.

[123] S. Huang, T. Zhu, M. Liu, and W. Huang, "Precise measurement of ultra-narrow laser linewidths using the strong coherent envelope," *Sci. Rep.*, vol. 7, p. 41988, feb 2017.

[124] W. Weng, E. Lucas, G. Lihachev, V. E. Lobanov, H. Guo, M. L. Gorodetsky, and T. J. Kippenberg, "Spectral Purification of Microwave Signals with Disciplined Dissipative Kerr Solitons," *Phys. Rev. Lett.*, vol. 122, p. 013902, jan 2019.

[125] G. Huang, E. Lucas, J. Liu, A. S. Raja, G. Lihachev, M. L. Gorodetsky, N. J. Engelsen, and T. J. Kippenberg, "Thermorefractive noise in silicon-nitride microresonators," *Phys. Rev. A*, vol. 99, p. 061801, jun 2019.

[126] R. Paschotta, "Noise of mode-locked lasers (Part II): timing jitter and other fluctuations," *Appl. Phys. B*, vol. 79, pp. 163–173, jul 2004.

[127] T. Herr, K. Hartinger, J. Riemensberger, C. Y. Wang, E. Gavartin, R. Holzwarth, M. L. Gorodetsky, and T. J. Kippenberg, "Universal formation dynamics and noise of Kerr-frequency combs in microresonators," *Nat. Photonics*, vol. 6, pp. 480–487, jul 2012.

[128] Q.-F. Yang, X. Yi, K. Y. Yang, and K. Vahala, "Counter-propagating solitons in microresonators," *Nat. Photonics*, vol. 11, pp. 560–564, aug 2017.

[129] M. Yu, J. K. Jang, Y. Okawachi, A. G. Griffith, K. Luke, S. A. Miller, X. Ji, M. Lipson, and A. L. Gaeta, "Breather soliton dynamics in microresonators," *Nat. Commun.*, vol. 8, pp. 1–7, feb 2017.

[130] M. Karpov, M. H. P. Pfeiffer, H. Guo, W. Weng, J. Liu, and T. J. Kippenberg, "Dynamics of soliton crystals in optical microresonators," *Nat. Phys.*, vol. 15, pp. 1071–1077, oct 2019.

[131] X. Ji, X. Yao, A. Klenner, Y. Gan, A. L. Gaeta, C. P. Hendon, and M. Lipson, "Chip-based frequency comb sources for optical coherence tomography," *Opt. Express*, vol. 27, p. 19896, jul 2019.

[132] P. J. Marchand, J. C. Skehan, J. Riemensberger, J.-j. Ho, M. H. P. Pfeiffer, J. Liu, C. Hauger, T. Lasser, and T. J. Kippenberg, "Soliton microcomb based spectral domain optical coherence tomography," feb 2019.

[133] J. Kiessling, I. Breunig, P. G. Schunemann, K. Buse, and K. L. Vodopyanov, "High power and spectral purity continuous-wave photonic THz source tunable from 1 to 4.5 THz for nonlinear molecular spectroscopy," *New J. Phys.*, vol. 15, p. 105014, oct 2013.

[134] J. Hu, J. He, J. Liu, A. S. Raja, M. Karpov, A. Lukashchuk, T. J. Kippenberg, and C.-S. Brès, "Reconfigurable radiofrequency filters based on versatile soliton microcombs," *Nat. Commun.*, vol. 11, p. 4377, dec 2020.

[135] H. Zhou, Y. Geng, W. Cui, S.-W. Huang, Q. Zhou, K. Qiu, and C. Wei Wong, "Soliton bursts and deterministic dissipative Kerr soliton generation in auxiliary-assisted microcavities," *Light Sci. Appl.*, vol. 8, p. 50, dec 2019.

[136] Y. Zhao, L. Chen, C. Zhang, W. Wang, H. Hu, R. Wang, X. Wang, S. T. Chu, B. Little, W. Zhang, and X. Zhang, "Soliton Burst and Bi-Directional Switching in the Platform with Positive Thermal-Refractive Coefficient Using an Auxiliary Laser," *Laser Photon. Rev.*, vol. 15, p. 2100264, sep 2021.

[137] H. Guo, E. Lucas, M. H. Pfeiffer, M. Karpov, M. Anderson, J. Liu, M. Geiselmann, J. D. Jost, and T. J. Kippenberg, "Intermode Breather Solitons in Optical Microresonators," *Phys. Rev. X*, vol. 7, p. 041055, dec 2017.

[138] Ó. B. Helgason, F. R. Arteaga-Sierra, Z. Ye, K. Twayana, P. A. Andrekson, M. Karlsson, J. Schröder, and Victor Torres-Company, "Dissipative solitons in photonic molecules," *Nat. Photonics*, vol. 15, pp. 305–310, apr 2021.

[139] S. Miller, K. Luke, Y. Okawachi, J. Cardenas, A. L. Gaeta, and M. Lipson, "On-chip frequency comb generation at visible wavelengths via simultaneous second- and third-order optical nonlinearities," *Opt. Express*, vol. 22, p. 26517, nov 2014.

[140] A. E. Dorche, S. Abdollahramezani, H. Taheri, A. A. Eftekhar, and A. Adibi, "Extending chip-based Kerr-comb to visible spectrum by dispersive wave engineering," *Opt. Express*, vol. 25, p. 22362, sep 2017.

[141] Y. Xuan, Y. Liu, L. T. Varghese, A. J. Metcalf, X. Xue, P.-H. Wang, K. Han, J. A. Jaramillo-Villegas, A. Al Noman, C. Wang, S. Kim, M. Teng, Y. J. Lee, B. Niu, L. Fan, J. Wang, D. E. Leaird, A. M. Weiner, and M. Qi, "High-Q silicon nitride microresonators exhibiting low-power frequency comb initiation," *Optica*, vol. 3, p. 1171, nov 2016.

[142] A. Kordts, M. H. P. Pfeiffer, H. Guo, V. Brasch, and T. J. Kippenberg, "Higher order mode suppression in high-Q anomalous dispersion SiN microresonators for temporal dissipative Kerr soliton formation," *Opt. Lett.*, vol. 41, p. 452, feb 2016.

[143] J. Liu, A. S. Raja, M. Karpov, B. Ghadiani, M. H. P. Pfeiffer, B. Du, N. J. Engelsen, H. Guo, M. Zervas, and T. J. Kippenberg, "Ultralow-power chip-based soliton microcombs for photonic integration," *Optica*, vol. 5, p. 1347, oct 2018.

[144] G. Lihachev, J. Liu, W. Weng, L. Chang, J. Guo, J. He, R. N. Wang, M. H. Anderson, J. E. Bowers, and T. J. Kippenberg, "Platicon microcomb generation using laser self-injection locking," mar 2021.

[145] J. Liu, G. Huang, R. N. Wang, J. He, A. S. Raja, T. Liu, N. J. Engelsen, and T. J. Kippenberg, "High-yield, wafer-scale fabrication of ultralow-loss, dispersion-engineered silicon nitride photonic circuits," *Nat. Commun.*, vol. 12, p. 2236, dec 2021.

[146] a. B. Matsko, a. a. Savchenkov, and L. Maleki, "Normal group-velocity dispersion Kerr frequency comb," *Opt. Lett.*, vol. 37, p. 43, jan 2012.

[147] W. Liang, A. a. Savchenkov, V. S. Ilchenko, D. Eliyahu, D. Seidel, A. B. Matsko, and L. Maleki, "Generation of a coherent near-infrared Kerr frequency comb in a monolithic microresonator with normal GVD," *Opt. Lett.*, vol. 39, p. 2920, may 2014.

[148] A. Rizzo, A. Novick, V. Gopal, B. Y. Kim, X. Ji, S. Daudlin, Y. Okawachi, Q. Cheng, M. Lipson, A. L. Gaeta, and K. Bergman, "Integrated Kerr frequency comb-driven silicon photonic transmitter," sep 2021.

[149] A. Lukashchuk, J. Riemensberger, A. Tusnin, J. Liu, and T. Kippenberg, "Chaotic micro-comb based parallel ranging," dec 2021.

[150] V. Lobanov, G. Lihachev, T. J. Kippenberg, and M. Gorodetsky, "Frequency combs and platicons in optical microresonators with normal GVD," *Opt. Express*, vol. 23, p. 7713, mar 2015.

[151] X. Xue, Y. Xuan, P.-H. Wang, Y. Liu, D. E. Leaird, M. Qi, and A. M. Weiner, "Normal-dispersion microcombs enabled by controllable mode interactions," *Laser Photon. Rev.*, vol. 9, pp. L23–L28, jul 2015.

[152] H. Shu, L. Chang, Y. Tao, B. Shen, W. Xie, M. Jin, A. Netherton, Z. Tao, X. Zhang, R. Chen, B. Bai, J. Qin, S. Yu, X. Wang, and J. E. Bowers, "Bridging microcombs and silicon photonic engines for optoelectronics systems," oct 2021.

[153] V. E. Lobanov, A. V. Cherenkov, A. E. Shitikov, I. A. Bilenko, and M. L. Gorodetsky, "Dynamics of platicons due to third-order dispersion," *Eur. Phys. J. D*, vol. 71, p. 185, jul 2017.

[154] V. E. Lobanov, A. E. Shitikov, R. R. Galiev, K. N. Min'kov, and N. M. Kondratiev, "Generation and properties of dissipative Kerr solitons and platicons in optical microresonators with backscattering," *Opt. Express*, vol. 28, p. 36544, nov 2020.

[155] A. M. Kaplan, G. P. Agrawal, and D. N. Maywar, "Optical Square-Wave Clock Generation Based on an All-Optical Flip-Flop," *IEEE Photonics Technol. Lett.*, vol. 22, pp. 489–491, apr 2010.

[156] L. Oxenlowe, R. Slavik, M. Galili, H. Mulvad, A. Clausen, Yongwoo Park, J. Azana, and P. Jeppesen, "640 Gb/s Timing Jitter-Tolerant Data Processing Using a Long-Period Fiber-Grating-Based Flat-Top Pulse Shaper," *IEEE J. Sel. Top. Quantum Electron.*, vol. 14, no. 3, pp. 566–572, 2008.

[157] E. Palushani, L. Oxenlowe, M. Galili, H. Mulvad, A. Clausen, and P. Jeppesen, "Flat-Top Pulse Generation by the Optical Fourier Transform Technique for Ultrahigh Speed Signal Processing," *IEEE J. Quantum Electron.*, vol. 45, pp. 1317–1324, nov 2009.

[158] V. V. Lozovoy, G. Rasskazov, A. Ryabtsev, and M. Dantus, "Phase-only synthesis of ultrafast stretched square pulses," *Opt. Express*, vol. 23, p. 27105, oct 2015.

[159] M. H. Anderson, G. Lihachev, W. Weng, J. Liu, and T. J. Kippenberg, "Zero-dispersion Kerr solitons in optical microresonators," jul 2020.

[160] V. E. Lobanov, G. Lihachev, and M. L. Gorodetsky, "Generation of platicons and frequency combs in optical microresonators with normal GVD by modulated pump," *EPL (Europhysics Lett.*, vol. 112, p. 54008, dec 2015.

[161] H. Liu, S.-W. Huang, J. Yang, M. Yu, D.-L. Kwong, and C. W. Wong, "Bright square pulse generation by pump modulation in a normal GVD microresonator," in *Conf. Lasers Electro-Optics*, vol. 2017-Janua, (Washington, D.C.), p. FTu3D.3, OSA, oct 2017.

[162] A. Antikainen and G. P. Agrawal, "Dual-pump frequency comb generation in normally dispersive optical fibers," *J. Opt. Soc. Am. B*, vol. 32, p. 1705, aug 2015.

[163] C. Finot, B. Kibler, L. Provost, and S. Wabnitz, "Beneficial impact of wave-breaking for coherent continuum formation in normally dispersive nonlinear fibers," *J. Opt. Soc. Am. B*, vol. 25, p. 1938, nov 2008.

[164] J. Fatome, C. Finot, G. Millot, A. Armaroli, and S. Trillo, "Observation of Optical Undular Bores in Multiple Four-Wave Mixing," *Phys. Rev. X*, vol. 4, p. 021022, may 2014.

[165] D. Massonnet, M. Rossi, C. Carmona, F. Adragna, G. Peltzer, K. Feigl, and T. Rabaute, "The displacement field of the Landers earthquake mapped by radar interferometry," *Nature*, vol. 364, pp. 138–142, jul 1993.

[166] P. Giacomo, "News from the BIPM," *Metrologia*, vol. 20, pp. 25–30, jan 1984.

[167] S. A. Diddams, J. C. Bergquist, S. R. Jefferts, and C. W. Oates, "Standards of Time and Frequency at the Outset of the 21st Century," *Science (80-.).*, vol. 306, pp. 1318–1324, nov 2004.

[168] N. Bobroff, "Recent advances in displacement measuring interferometry," *Meas. Sci. Technol.*, vol. 4, pp. 907–926, sep 1993.

[169] P. L. Bender, D. G. Currie, S. K. Poultney, C. O. Alley, R. H. Dicke, D. T. Wilkinson, D. H. Eckhardt, J. E. Faller, W. M. Kaula, J. D. Mulholland, H. H. Plotkin, E. C. Silverberg, and J. G. Williams, "The Lunar Laser Ranging Experiment," *Science (80-.).*, vol. 182, pp. 229–238, oct 1973.

[170] I. Fujima, S. Iwasaki, and K. Seta, "High-resolution distance meter using optical intensity modulation at 28 GHz," *Meas. Sci. Technol.*, vol. 9, pp. 1049–1052, jul 1998.

[171] J. Lee, Y.-J. Kim, K. Lee, S. Lee, and S.-W. Kim, "Time-of-flight measurement with femtosecond light pulses," *Nat. Photonics*, vol. 4, pp. 716–720, oct 2010.

[172] W. Gao, S. Kim, H. Bosse, H. Haitjema, Y. Chen, X. Lu, W. Knapp, A. Weckenmann, W. Estler, and H. Kunzmann, "Measurement technologies for precision positioning," *CIRP Ann.*, vol. 64, pp. 773–796, jan 2015.

[173] D. J. Jones, S. A. Diddams, J. K. Ranka, A. Stentz, R. S. Windeler, J. L. Hall, and S. T. Cundiff, "Carrier-envelope phase control of femtosecond mode-locked lasers and direct optical frequency synthesis," *Science (80-.).*, vol. 288, pp. 635–639, apr 2000.

[174] S. A. Diddams, D. J. Jones, J. Ye, S. T. Cundiff, J. L. Hall, J. K. Ranka, R. S. Windeler, R. Holzwarth, T. Udem, and T. W. Hänsch, "Direct link between microwave and optical frequencies with a 300 THz femtosecond laser comb," *Phys. Rev. Lett.*, vol. 84, pp. 5102–5105, may 2000.

[175] S. W. Kim, "Metrology: Combs rule," *Nat. Photonics*, vol. 3, pp. 313–314, jun 2009.

[176] T.-A. Liu, N. R. Newbury, and I. Coddington, "Sub-micron absolute distance measurements in sub-millisecond times with dual free-running femtosecond Er fiber-lasers," *Opt. Express*, vol. 19, p. 18501, sep 2011.

[177] K. Minoshima and H. Matsumoto, "High-accuracy measurement of 240-m distance in an optical tunnel by use of a compact femtosecond laser," *Appl. Opt.*, vol. 39, p. 5512, oct 2000.

[178] N. R. Doloca, K. Meiners-Hagen, M. Wedde, F. Pollinger, and A. Abou-Zeid, "Absolute distance measurement system using a femtosecond laser as a modulator," *Meas. Sci. Technol.*, vol. 21, p. 115302, nov 2010.

[179] Y.-S. Jang, W. Kim, H. Jang, and S.-W. Kim, "Absolute Distance Meter Operating on a Free-Running Mode-Locked Laser for Space Mission," *Int. J. Precis. Eng. Manuf.*, vol. 19, pp. 975–981, jul 2018.

[180] K.-N. Joo, Y. Kim, and S.-W. Kim, "Distance measurements by combined method based on a femtosecond pulse laser," *Opt. Express*, vol. 16, p. 19799, nov 2008.

[181] K.-N. Joo and S.-W. Kim, "Absolute distance measurement by dispersive interferometry using a femtosecond pulse laser," *Opt. Express*, vol. 14, p. 5954, jun 2006.

[182] S. A. van den Berg, S. T. Persijn, G. J. P. Kok, M. G. Zeitouny, and N. Bhattacharya, "Many-Wavelength Interferometry with Thousands of Lasers for Absolute Distance Measurement," *Phys. Rev. Lett.*, vol. 108, p. 183901, may 2012.

[183] A. Lešundák, D. Voigt, O. Cip, and S. van den Berg, "High-accuracy long distance measurements with a mode-filtered frequency comb," *Opt. Express*, vol. 25, p. 32570, dec 2017.

[184] N. Schuhler, Y. Salvadé, S. Lévêque, R. Dändliker, and R. Holzwarth, "Frequency-comb-referenced two-wavelength source for absolute distance measurement," *Opt. Lett.*, vol. 31, p. 3101, nov 2006.

[185] G. Wang, Y.-S. Jang, S. Hyun, B. J. Chun, H. J. Kang, S. Yan, S.-W. Kim, and Y.-J. Kim, "Absolute positioning by multi-wavelength interferometry referenced to the frequency comb of a femtosecond laser," *Opt. Express*, vol. 23, p. 9121, apr 2015.

[186] Y.-S. Jang, G. Wang, S. Hyun, H. J. Kang, B. J. Chun, Y.-J. Kim, and S.-W. Kim, "Comb-referenced laser distance interferometer for industrial nanotechnology," *Sci. Rep.*, vol. 6, p. 31770, aug 2016.

[187] H. Shi, Y. Song, F. Liang, L. Xu, M. Hu, and C. Wang, "Effect of timing jitter on time-of-flight distance measurements using dual femtosecond lasers," *Opt. Express*, vol. 23, p. 14057, jun 2015.

[188] J. Liu, H. Tian, E. Lucas, A. S. Raja, G. Lihachev, R. N. Wang, J. He, T. Liu, M. H. Anderson, W. Weng, S. A. Bhave, and T. J. Kippenberg, "Monolithic piezoelectric control of soliton microcombs," *Nature*, vol. 583, pp. 385–390, jul 2020.

[189] Y.-S. Jang and S.-W. Kim, "Compensation of the refractive index of air in laser interferometer for distance measurement: A review," *Int. J. Precis. Eng. Manuf.*, vol. 18, pp. 1881–1890, dec 2017.

[190] J. Schwider and L. Zhou, "Dispersive interferometric profilometer," *Opt. Lett.*, vol. 19, p. 995, jul 1994.

[191] A. Fercher, C. Hitzenberger, G. Kamp, and S. El-Zaiat, "Measurement of intraocular distances by backscattering spectral interferometry," *Opt. Commun.*, vol. 117, pp. 43–48, may 1995.

[192] Z. L. Newman, V. Maurice, T. Drake, J. R. Stone, T. C. Briles, D. T. Spencer, C. Fredrick, Q. Li, D. Westly, B. R. Ilic, B. Shen, M.-G. Suh, K. Y. Yang, C. Johnson, D. M. S. Johnson, L. Hollberg, K. J. Vahala, K. Srinivasan, S. A. Diddams, J. Kitching, S. B. Papp, and M. T. Hummon, "Architecture for the photonic integration of an optical atomic clock," *Optica*, vol. 6, p. 680, may 2019.

[193] J. Lim, W. Liang, A. A. Savchenkov, A. B. Matsko, L. Maleki, and C. W. Wong, "Probing 10 μK stability and residual drifts in the cross-polarized dual-mode stabilization of single-crystal ultrahigh-Q optical resonators," *Light Sci. Appl.*, vol. 8, p. 1, dec 2019.

[194] J. Lim, A. A. Savchenkov, E. Dale, W. Liang, D. Eliyahu, V. Ilchenko, A. B. Matsko, L. Maleki, and C. W. Wong, "Chasing the thermodynamical noise limit in whispering-gallery-mode resonators for ultrastable laser frequency stabilization," *Nat. Commun.*, vol. 8, p. 8, dec 2017.

[195] T. Nagatsuma, G. Ducournau, and C. C. Renaud, "Advances in terahertz communications accelerated by photonics," *Nat. Photonics*, vol. 10, pp. 371–379, jun 2016.

[196] S. Koenig, D. Lopez-Diaz, J. Antes, F. Boes, R. Henneberger, A. Leuther, A. Tessmann, R. Schmogrow, D. Hillerkuss, R. Palmer, T. Zwick, C. Koos, W. Freude, O. Ambacher, J. Leuthold, and I. Kallfass, "Wireless sub-THz communication system with high data rate," *Nat. Photonics*, vol. 7, pp. 977–981, dec 2013.

[197] Y. Salamin, B. Baeuerle, W. Heni, F. C. Abrecht, A. Josten, Y. Fedoryshyn, C. Haffner, R. Bonjour, T. Watanabe, M. Burla, D. L. Elder, L. R. Dalton, and J. Leuthold, "Microwave plasmonic mixer in a transparent fibre–wireless link," *Nat. Photonics*, vol. 12, pp. 749–753, dec 2018.

[198] H. Kaushal and G. Kaddoum, "Optical Communication in Space: Challenges and Mitigation Techniques," *IEEE Commun. Surv. Tutorials*, vol. 19, no. 1, pp. 57–96, 2017.

[199] Y.-A. Chen, Q. Zhang, T.-Y. Chen, W.-Q. Cai, S.-K. Liao, J. Zhang, K. Chen, J. Yin, J.-G. Ren, Z. Chen, S.-L. Han, Q. Yu, K. Liang, F. Zhou, X. Yuan, M.-S. Zhao, T.-Y. Wang, X. Jiang, L. Zhang, W.-Y. Liu, Y. Li, Q. Shen, Y. Cao, C.-Y. Lu, R. Shu, J.-Y. Wang, L. Li, N.-L. Liu, F. Xu, X.-B. Wang, C.-Z. Peng, and J.-W. Pan, "An integrated space-to-ground quantum communication network over 4,600 kilometres," *Nature*, vol. 589, pp. 214–219, jan 2021.

[200] L. Kang and B. H. Kolner, "Characterization of AM-to-PM Conversion in Silicon p-i-n Photodiodes," *IEEE Photonics Technol. Lett.*, vol. 31, pp. 1001–1004, jul 2019.

[201] M. P. J. Lavery, M. M. Abadi, R. Bauer, G. Brambilla, L. Cheng, M. A. Cox, A. Dudley, A. D. Ellis, N. K. Fontaine, A. E. Kelly, C. Marquardt, S. Matlhane, B. Ndagano, F. Petruccione, R. Slavík, F. Romanato, C. Rosales-Guzmán, F. S. Roux, K. Roux, J. Wang, and A. Forbes, "Tackling Africa's digital divide," *Nat. Photonics*, vol. 12, pp. 249–252, may 2018.

[202] A. Dochhan, J. Poliak, J. Surof, M. Richerzhagen, H. F. Kelemu, and R. M. Calvo, "13.16 Tbit/s Free-space Optical Transmission over 10.45 km for Geostationary Satellite Feeder-links," in *Photonic Networks; 20th ITG-Symposium*, pp. 1–3, 2019.

[203] E. Ciaramella, Y. Arimoto, G. Contestabile, M. Presi, A. D'Errico, V. Guarino, and M. Matsumoto, "1.28 terabit/s (32x40 Gbit/s) wdm transmission system for free space optical communications," *IEEE J. Sel. Areas Commun.*, vol. 27, pp. 1639–1645, dec 2009.

[204] J. Wang, J.-Y. Yang, I. M. Fazal, N. Ahmed, Y. Yan, H. Huang, Y. Ren, Y. Yue, S. Dolinar, M. Tur, and A. E. Willner, "Terabit free-space data transmission employing orbital angular momentum multiplexing," *Nat. Photonics*, vol. 6, pp. 488–496, jul 2012.

[205] T. Harter, C. Füllner, J. N. Kemal, S. Ummethala, J. L. Steinmann, M. Brosi, J. L. Hesler, E. Bründermann, A.-S. S. Müller, W. Freude, S. Randel, and C. Koos, "Generalized Kramers–Kronig receiver for coherent terahertz communications," *Nat. Photonics*, vol. 14, pp. 601–606, oct 2020.

[206] N. Zhao, X. Li, G. Li, and J. M. Kahn, "Capacity limits of spatially multiplexed free-space communication," *Nat. Photonics*, vol. 9, pp. 822–826, dec 2015.

[207] L. Lundberg, M. Mazur, A. Mirani, B. Foo, J. Schröder, V. Torres-Company, M. Karlsson, and P. A. Andrekson, "Supplementary: Phase-coherent lightwave communications with frequency combs," *Nat. Commun.*, vol. 11, p. 201, dec 2020.

[208] D. Kong, A. A. Jørgensen, M. R. Henriksen, F. Klejs, Z. Ye, Ò. B. Helgason, H. E. Hansen, H. Hu, M. Yankov, S. Forchhammer, P. Andrekson, A. Larsson, M. Karlsson, J. Schröder, Y. Sasaki, K. Aikawa, J. Thomsen, T. Morioka, M. Galili, V. Torres-Company, and L. K. Oxenløwe, "Single Dark-Pulse Kerr Comb Supporting 1.84 Pbit/s Transmission over 37-Core Fiber," in *Conf. Lasers Electro-Optics*, vol. Part F181-, (Washington, D.C.), p. JTh4A.7, OSA, 2020.

[209] B. J. Puttnam, R. S. Luis, W. Klaus, J. Sakaguchi, J.-M. Delgado Mendinueta, Y. Awaji, N. Wada, Y. Tamura, T. Hayashi, M. Hirano, and J. Marciante, "2.15 Pb/s transmission using a 22 core homogeneous single-mode multi-core fiber and wideband optical comb," in *2015 Eur. Conf. Opt. Commun.*, pp. 1–3, IEEE, sep 2015.

[210] J. Pfeifle, V. Brasch, M. Lauermann, Y. Yu, D. Wegner, T. Herr, K. Hartinger, P. Schindler, J. Li, D. Hillerkuss, R. Schmogrow, C. Weimann, R. Holzwarth, W. Freude, J. Leuthold, T. J. Kippenberg, and C. Koos, "Coherent terabit communications with microresonator Kerr frequency combs," *Nat. Photonics*, vol. 8, pp. 375–380, may 2014.

[211] Ó. B. Helgason, Z. Ye, K. Twayana, P. A. Andrekson, and J. Schroder, "Dark-pulse Kerr combs in linearly coupled microring structures," in *Conf. Lasers Electro-Optics*, (Washington, D.C.), p. STu3H.5, OSA, 2020.

[212] X. Xue, P.-H. Wang, Y. Xuan, M. Qi, and A. M. Weiner, "Microresonator Kerr frequency combs with high conversion efficiency," *Laser Photon. Rev.*, vol. 11, p. 1600276, jan 2017.

[213] E. Nazemosadat, A. Fülöp, Ó. B. Helgason, P.-H. Wang, Y. Xuan, D. E. Leaird, M. Qi, E. Silvestre, A. M. Weiner, and V. Torres-Company, "Switching dynamics of dark-pulse Kerr frequency comb states in optical microresonators," *Phys. Rev. A*, vol. 103, p. 013513, jan 2021.

[214] B. Y. Kim, Y. Okawachi, J. K. Jang, M. Yu, X. Ji, Y. Zhao, C. Joshi, M. Lipson, and A. L. Gaeta, "Turn-key, high-efficiency Kerr comb source," *Opt. Lett.*, vol. 44, no. 18, p. 4475, 2019.

[215] H. Bao, A. Cooper, M. Rowley, L. Di Lauro, J. S. Totero Gongora, S. T. Chu, B. E. Little, G.-L. Oppo, R. Morandotti, D. J. Moss, B. Wetzel, M. Peccianti, and A. Pasquazi, "Laser cavity-soliton microcombs," *Nat. Photonics*, vol. 13, pp. 384–389, jun 2019.

[216] A. A. Farid and S. Hranilovic, "Outage Capacity Optimization for Free-Space Optical Links With Pointing Errors," *J. Light. Technol.*, vol. 25, pp. 1702–1710, jul 2007.

[217] B. T. Vu, N. T. Dang, T. C. Thang, and A. T. Pham, "Bit Error Rate Analysis of Rectangular QAM/FSO Systems Using an APD Receiver Over Atmospheric Turbulence Channels," *J. Opt. Commun. Netw.*, vol. 5, p. 437, may 2013.

[218] A. Prokes, "Atmospheric effects on availability of free space optics systems," *Opt. Eng.*, vol. 48, p. 066001, jun 2009.

[219] V. Torres-Company, J. Schroder, A. Fulop, M. Mazur, L. Lundberg, O. B. Helgason, M. Karlsson, and P. A. Andrekson, "Laser Frequency Combs for Coherent Optical Communications," *J. Light. Technol.*, vol. 37, pp. 1663–1670, apr 2019.